UNIVERSITY OF
LIVERPOOL

Novel Sol-Gel Materials for Advanced Glass Products: Structure, Dynamics and Stability

Thesis Submitted in accordance with the requirements of the
University of Liverpool for the degree of Doctor in Philosophy by
Paul Vincent Wiper

August 2012

Dedication

...to my loving and supportive parents

Acknowledgements

To obtain a PhD an individual must have some of the following traits; an inquisitive mind, focused, eager to learn, cope with pressure, overcome difficulties and have a propensity for alcohol[citation needed!]. However, these attributes must be combined with a dedicated support network of family and friends in order to cope with four years of academia. Indeed, I like to think that I have some of the aforementioned traits but I could not have reached this point without the following people...

Firstly, my profound thanks to my primary industrial and academic supervisors, Dr. S. Varma and Prof. Y. Z. Khimyak; for allowing me to undertake an exciting and challenging PhD program. They have provided me with support and knowledge over the duration of the research. Particularly, I would like to thank Yaroslav for his strict and somewhat unorthodox work ethic that has driven me to better myself and achieve goals that I would never had thought been possible four years ago. I am also grateful to him for the informal chats and cultural indoctrinations; *from Mahler to Britten.*

I am indebted to Dr. B. Thomas, without his weekly advice, guidance and drying of the plates this research would not have been possible. I have learned so much from him, especially in the world of silica. I also hope he has learned from me some aspects of the fascinating world of NMR.

I would like to acknowledge Drs. A. Fogg, J. Claridge, D. Bradshaw and J. Iggo for the regular discussions/suggestions in group meetings and for help with TGA, XRD and solution-NMR. Also, I acknowledge Prof. P. Myers for his advice with the GC analysis (sorry for blocking up 7 syringes!). I'd also like to thank the following departmental staff, Sandra, Manda, Anne, Debbie and Nadeen for hours of entertainment and help with forms also to Tony for keeping the magnets alive.

I am very fortunate to have a circle of wonderful and forgiving friends whose characters range from the conservative housewife to a liberal, bohemian throw back (not mentioning names!). To Jimmy, Adrian, Helen and Victoria; Good Morning! This group of reprobates have given me so many fantastic memories, support and guidance; we shall always be in touch. Alex, Laura, Carly and Gemma for all the laughs, nightouts, arguments and banter that have provided me with many distractions from work! A special mention to Andrea; over the past year you have given me motivation, crab sticks and scouse banter that hasn't half made me chuckle girl. Oh, just do me a favour though? Stop panicking!!

Cate; she deserves a new paragraph. She is like a sister to me, albeit slightly tapped, she has been there right from the start and she knows how much I think of her and her family. Thank you for the discussions regarding NMR, particularly with nuclear magnetic relaxation; we shall definitely write a book! My dear, I will miss you terribly.

Finally, to my family. For all the phone calls; be it sober or drunken, for all the moral and financial support, for my genes, for all the visits to Liverpool and help with accommodation. For this, and for so much more, I am truly thankful.

Abstract

Flame retardants are composite materials or chemicals used in thermoplastics, thermosets, textiles, coatings and glasses that inhibit or resist the spread of fire. In 2014 the global market for flame retardants is expected to reach \$6.10 billion[2] with a drive in research for designing and developing new fire resistant materials. A commercially available product based on a hydrogel/glass composite is an effective fire and heat resistant glazing that is employed in the commercial and domestic sector. The macroscopic effects of these materials have been investigated; however no information exists on the molecular level properties. Therefore, the aim of this research is to fully characterise a series of hydrogels with the ultimate goal of understanding structure-property relationships.

The hydrogels discussed herein are made by drying commercially available sodium-silicate solutions onto traditional float glass to create a sandwich glazing. The materials present a unique challenge to characterise at the molecular level because of their amorphous and metastable nature. NMR spectroscopy has been extensively used in this research because it is shown to be an ideal technique for the elucidation of structures and dynamics in disordered systems.

The complete “life-cycle” of the product is investigated; firstly, using solid-state NMR, a thorough and detailed analysis of the hydrogels are presented. The thermal stability of the hydrogels are then investigated by means of short and long term ageing effects, which shows that the product crystallises into the layered silicate makatite. The ability to improve the longevity of the product by inhibiting makatite formation follows with a final section dedicated to understanding different composites of the materials.

Publications

Published:

- **“**A water-stable porphyrin-based metal-organic framework active for visible light photocatalysis” Alexandra Fateeva, Philip A. Chater, Christopher P. Ireland, Asif A. Tahir, Yaroslav Z. Khimyak, **Paul V. Wiper,** James R. Darwent, and Matthew J. Rosseinsky *Angew. Chem. Int. Ed*. 2012, 51, 1 – 6
- “The coordinatively saturated vanadium MIL-47 as a low leaching heterogeneous catalyst in the oxidation of cyclohexene” Karen Leus, Matthias Vandichel, Ying-Ya Liu, Ilke Muylaert, Jan Musschoot, Steven Pyl, Henk Vrielinck, Freddy Callens, Guy B. Marin, Christophe Detavernier, **Paul V. Wiper,** Yaroslav Z. Khimyak, Michel Waroquier, Veronique Van Speybroeck and Pascal Van Der Voort *J. Cata.* 2012 285 196-207
- “An Adaptable Peptide-Based Porous Material” J. Rabone, Y.-F. Yue, S. Y. Chong, K. C. Stylianou, J. Bacsa, D. Bradshaw, G. R. Darling, N. G. Berry, Y. Z. Khimyak, A. Y. Ganin, **P. V. Wiper,** J. B. Claridge and M. J. Rosseinsky *Science 2010,* 329 1053
- “Solid acid catalysts based on $H_3PW_{12}O_{40}$ heteropoly acid: Acid and catalytic properties at a gas–solid interface” Ali M. Alsalme, **Paul V. Wiper,** Yaroslav Z. Khimyak, Elena F. Kozhevnikova and Ivan V. Kozhevnikov *J. Cata.* 2010, 276, 181–189
- “Ethenylene-Bridged Periodic Mesoporous Organosilicas: *From E to Z*” Carl Vercaemst, Matthias Ide, **Paul V. Wiper,** James T. A. Jones, Yaroslav Z. Khimyak, Francis Verpoort, and Pascal Van Der Voort *Chem. Mater.* 2009, 21, 5792–5800

In Preparation:

- “Solid-state NMR characterisation of makatite crystallisation” **Paul V. Wiper,** B. Thomas, S. Varma and Y. Z. Khimyak

- “Incorporation of Aluminium into -CH_2CH_2-/-CH=CH-PMOs: probing the location of Al using solid state NMR” James T. A. Jones, **Paul V. Wiper** and Yaroslav Z. Khimyak

Contents

Chapter 1 -- 1

Introduction -- 1

1.1 The Chemistry of Silicon and Silica -- 3

1.2 Structure of Silica and Silicate Glass -- 4

1.3 Silicate Glasses -- 5

1.4 Definition of Glasses and Amorphous Materials --- 7

1.5 Preparation of Glassy and Amorphous Solids -- 8

1.6 The Vitrification Method -- 9

1.7 The Glass Transition in Materials -- 10

1.8 The Nature of T_g *--- 11*

1.9 Sol-gel Processing -- 11

1.10 Solubility of Silica -- 15

1.11 Alkaline silicate solutions -- 17
  1.11.1 Nomenclature and Properties --- 17
  1.11.2 Production and Applications -- 19
  1.11.3 The Constituents of Sodium-Silicate Solutions ------------------------------------ 21

1.12 Layered Silicates -- 25

1.13 Aims of the Project -- 28
  1.13.1 Temperature Regimes -- 29

Chapter 2 --- 32

Characterisation --- 32

2.1 Nuclear Magnetic Resonance -- 33

2.2 Basics of Nuclear Spin and Resonance[215-223] *--- 33*

2.3 Bulk Magnetisation -- 36

2.4 The Rotating Frame of Reference -- 37

2.5 Excitation and Detection -- 40

2.6 Chemical Shift -- 42

2.7 Relaxation -- 43
  2.7.1 Assessing Molecular Mobility using Relaxation Measurements[224-227] ------------- 45
  2.7.2 Calculation of τ_c -- 48
  2.7.3 Spin Diffusion[230-233] -- 48

2.8 Solid-state NMR (SSNMR) -- 49
  2.8.1 The Spin Hamiltonian -- 50
  2.8.2 Chemical Shift Anisotropy -- 51
  2.8.3 Dipole-dipole Coupling --- 53
  2.8.4 Magic Angle Spinning (MAS) -- 56
  2.8.5 Decoupling Sequences -- 58

2.8.6 Cross-polarisation ---------- 60

2.9 Quadrupolar Coupling[254-258] ---------- 61
2.9.1 Frame Transformations ---------- 66
2.9.2 Methodologies to reduce the quadrupolar interaction ---------- 68
2.9.2.1 High B_0 ---------- 68
2.9.2.2 Magic Angle Spinning: ---------- 68
2.9.2.3 Double Rotation (DOR) and Dynamic Angle Spinning (DAS) ---------- 69
2.9.2.4 Multiple Quantum MAS (MQMAS)[267-271] ---------- 70
2.9.2.5 MQMAS for Amorphous or Disorder Materials[268, 280] ---------- 74

2.10 Techniques Available for Structural Studies of Glassy Systems ---------- 76

2.11 Crystallography[304-306] ---------- 79
2.11.1 Principles of X-diffraction ---------- 79

2.12 Optical Measurements ---------- 81

Chapter 3 ---------- 83

3 Experimental ---------- 83

3.1 Solid-state NMR ---------- 84
3.1.1 One dimensional magic angle spinning (MAS) ---------- 84
3.1.2 ^{1}H-X Cross Polarisation Magic Angle Spinning (CP/MAS) ---------- 85
3.1.3 Two dimensional ^{1}H-^{13}C Heteronuclear Correlation (HETCOR) ---------- 86
3.1.4 Multiple-quantum magic angle spinning (MQMAS) ---------- 87
3.1.5 Spin-lattice relaxation in the laboratory frame, T_1 ---------- 88
3.1.6 Spin-spin relaxation, T_2 ---------- 89
3.1.7 Spin-lattice relaxation in the rotating frame; $T_{1\rho}^{H/C}$ ---------- 89
3.1.8 Variable Temperature Experiments ---------- 90

3.2 Solution-state NMR ---------- 90

3.3 Powder X-Ray Diffraction (pXRD) ---------- 90

3.4 Environmental Scanning Electron Microscopy (E-SEM) ---------- 90

E-SEM was conducted at the University of Liverpool by Dr. P. Hill. The images were obtained on a FEI Quanta ESEM 200 instrument using low vacuum (0.75 Torr), 60°C stage operating at 15.0 keV. ---------- 90

3.5 Data processing ---------- 90

Chapter 4 ---------- 92

4 Solid-state NMR characterisation of organic-inorganic hydrogels ---------- 92

4.1 Introduction ---------- 93

4.2 Experimental Part ---------- 94
4.2.1 Production of the Hydrogel Interlayer ---------- 94

4.3 Results and Discussion ---------- 96

4.4 Structure and composition of the hydrogels ---------- 96
4.4.1 Quantification of silicon environments using cross-polarisation ---------- 96
4.4.2 ^{1}H-^{29}Si CP/MAS NMR ---------- 99
4.4.3 ^{23}Na MAS NMR ---------- 101
4.4.4 ^{23}Na{^{1}H} MQMAS NMR ---------- 102

4.4.4.1 Relationship between local sodium environment and ^{23}Na isotropic chemical shift and the quadrupolar product ---------- 103
4.4.4.2 Assigning the local sodium environments in the CS2 hydrogels ---------- 107
4.4.6 ^{1}H MAS NMR ---------- 111

4.5 Structure and Dynamics of Water ---------- 115
4.5.1 Variable Temperature ^{1}H T_1 Relaxation Measurements ---------- 116
4.5.1.1 Dynamics of the water and polyol molecules ---------- 117
4.5.1.2 Nature of the water hydrogen bonding networks ---------- 118
4.5.2 Variable Temperature ^{1}H T_2 Relaxation Measurements ---------- 121

4.6 Distribution of polyols in hydrogels ---------- 125

4.7 Conclusions ---------- 127

5 Investigation into the thermal stability of the CS2 hydrogels ---------- 130

5.1 Introduction ---------- 131

5.2 Short term ageing ---------- 132
5.2.1 Temperature-dependent transparency and structural changes in the hydrogels ---------- 132

5.3 Differential Scanning Calorimetry ---------- 140

5.4 Long term ageing ---------- 142
5.4.1 Tracking makatite crystallisation ---------- 142
5.4.2 Powder X-ray Diffraction ---------- 142
5.4.3 Environmental-SEM ---------- 144

5.5 Optical Properties ---------- 146

5.6 The Structure of Makatite ---------- 148

5.7 Monitoring changes at the molecular level as a function of ageing ---------- 153
5.7.1 ^{1}H-^{29}Si CP MAS NMR ---------- 153
5.7.2 ^{23}Na MAS and MQMAS NMR ---------- 154
5.7.3 ^{23}Na{^{1}H} MQMAS NMR ---------- 156
5.7.4 Comparison of ^{23}Na sites present within the CS2 and CS2EG hydrogels during the phase transformation: ^{23}Na MQMAS NMR ---------- 160

5.8 Discussion ---------- 161
5.8.1 Makatite Crystallisation ---------- 161
5.8.2 Origin of the Change in Optical Properties; Short and Long Term Ageing ---------- 162

5.9 Conclusions ---------- 163

6 Inhibiting Makatite Formation ---------- 164

6.1 Introduction ---------- 165

6.2 Experimental Part ---------- 166
6.2.1 Commerical Solutions, CS1, CS2 and CS3 ---------- 166
6.2.2 Synthesis of the sCS2 analogue ---------- 166
6.2.3 Lentz-GC Analysis ---------- 166
6.2.4 Trimethylsilation procedure ---------- 166
6.2.5 Gas-Chromatography ---------- 167

6.3 Analysis of Sodium-Silicate Solutions ---------- 168
6.3.1 Commercial Sodium-Silicate Solutions ---------- 168
6.3.2 Commercial vs. Synthetic Sodium-Silicate Solutions ---------- 170

6.4 Lentz-GC Analysis ---------- 171

6.5 Ageing Performance ---------- 174
  6.5.1 Visual Observations ---------- 174
  6.5.2 Hazing Measurements ---------- 175
  6.5.3 Powder X-ray Diffraction ---------- 176

6.6 Comparison of the local environments in the commercial and synthetic hydrogels ---------- 177
  6.6.1 ^{29}Si SP MAS NMR ---------- 177
  6.6.2 ^{23}Na{^{1}H} MQMAS NMR ---------- 178

6.7 Discussion ---------- 180
  6.7.1 The Effect of SiO_2 : Na_2O ratio on silica speciation ---------- 184

6.8 Conclusions ---------- 185

7 Investigating makatite/glycerol interactions ---------- 186

7.1 Introduction ---------- 187

7.2 Experimental Part ---------- 187
  7.2.1 Makatite Synthesis ---------- 187
  7.2.2 Synthesis of makatite/glycerol composite ---------- 188

7.3 Results ---------- 189
  7.3.1 Composition of the Materials ---------- 189
  7.3.2 TGA ---------- 190
  7.3.3 Powder X-ray diffraction ---------- 191

7.4 Probing the local structure ---------- 192
  7.4.1 ^{1}H-^{29}Si CP MAS NMR ---------- 192
  7.4.2 ^{1}H MAS NMR ---------- 193
  7.4.3 ^{13}C{^{1}H} MAS NMR ---------- 194
  7.4.4 ^{23}Na{^{1}H} MQMAS NMR ---------- 195

7.5 Discussion ---------- 197
  7.5.1 Structural representation of the MKG composite ---------- 197
  7.5.2 Makatite Synthesis ---------- 198
  7.5.3 Intercalation Chemistry ---------- 199

7.6 Conclusions ---------- 199

8.1 General Conclusions and Outlook ---------- 201

Chapter 1

Introduction

Silicon dioxide (SiO_2) or *silica* is the basic building block for a variety of materials. Silica materials are divided into amorphous and crystalline substances. The amorphous substances include mesoporous silicas[3-6], aerogels[7, 8], xerogels[9], hydrogels[10, 11] and inorganic glasses[12-14]. Crystalline materials include zeolites[15-17], layered silicates[18-21] as well 'dense silicas' *i.e.* quartz[22].

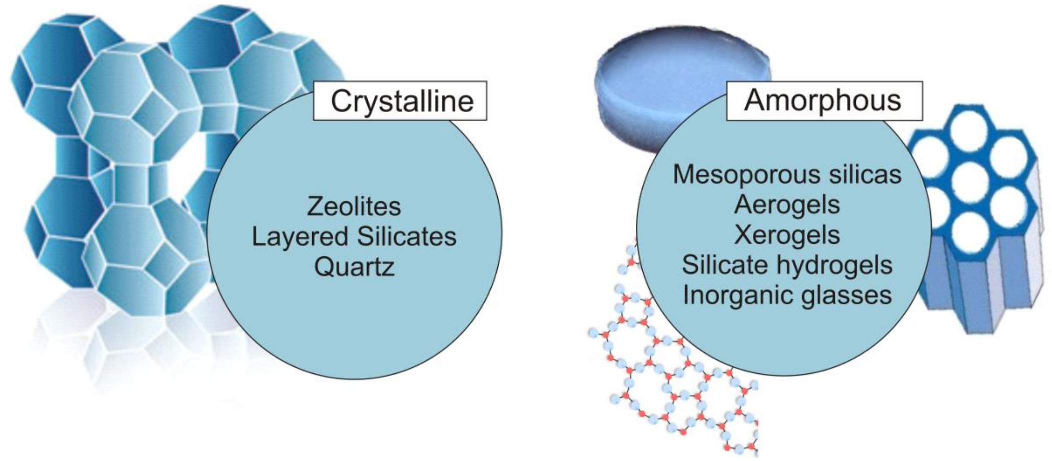

Figure 1.1 Crystalline and amorphous silica based materials

Traditional applications of these materials include, catalysis, gas sensing, chemical separation, drug delivery and chromatography[23-25]. Novel applications have seen aerogels used by NASA to insulate the Mars Rover buggy and also to collect comet debris[26, 27]. Commercially available sodium-silicate hydrogels are used as fire resistant materials. Introducing "silica based materials" to a reader is a difficult task due not only to the various different types of silica compounds but also because of the wealth of information that is available. The subject of this project was to investigate commercially available sodium-silicate hydrogels, of which there are very few reports in the literature. In light of this, the introductory section consists of topics directly related to the hydrogels. Genesis of the hydrogels begins with the dissolution of a sodium-silicate glass into a sodium-silicate solution. The solution is then dried to a specific water content to produce the desired hydrogel. Therefore, topics of silica, alkaline-silicate glasses, solutions and layered silicates are covered ranging from their structure, formation and production with relevant literature reviews.

1.1 The Chemistry of Silicon and Silica

Silicon is the second most abundant element in the earth's crust, accounting for approximately 27% by mass.[28] Silicon is mainly in the form of silica. Over millions of years it has been deposited from rocks, by the action of water, into either it's crystalline or amorphous form. Quartz, cristobalite, tridymite and coesite are just a few examples of the crystalline polymorphs of silica whilst opal constitutes its amorphous phase.[29] Synthetic amorphous silica can exist in various forms: fumed silica (formed from the reaction of $SiCl_4$, H_2 and O_2 in a flame), precipitated silica or silica gel (formed *via* the sol-gel process) and silica glass or vitreous silica (obtained melting quartz and cooling rapidly). The amorphous form can also be biological in origin. Unicellular organisms and some plants uptake Si in the form of silicic acid ($Si(OH)_4$) from water and deposit it as amorphous silica for use in cell walls.[30-32] The SiO_4 tetrahedron is the primary building unit of silica, as shown in **Figure 1.2**. Silicate structures are built up by sharing of the oxygen atoms between SiO_4 tetrahedra: sharing with two oxygen atoms per unit yields a chain, three oxygen atoms a sheet, and four oxygen atoms a three-dimensional network.

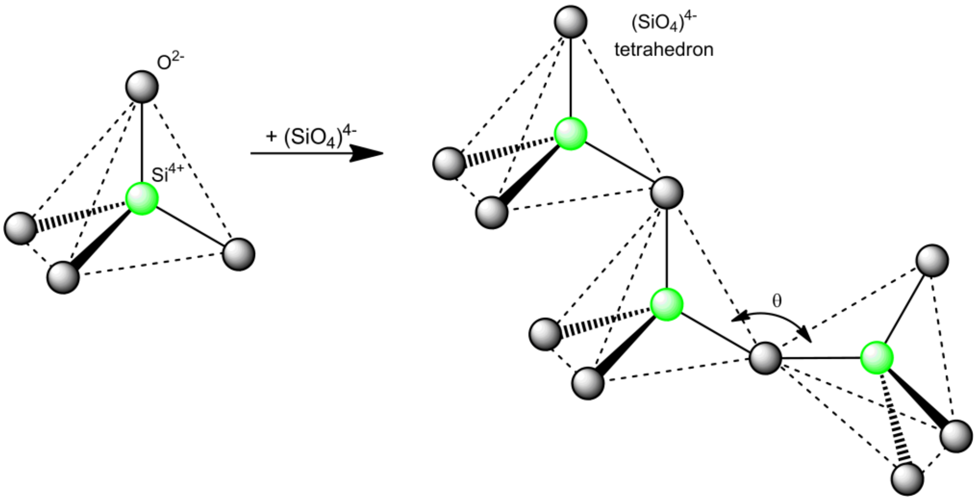

Figure 1.2 The SiO_4 subunit and linkages with other SiO_4 units to form sheet like silicate structures. In amorphous silica, the basic tetrahedral structural subunit remains largely intact. However, long range order is lost as the arrangement between adjacent tetrahedra introduces flexibility between second, third *etc.* nearest neighbours.

The siloxane (Si-O-Si) linkages are very stable with a bond energy of about 432 kJ mol^{-1} which is the most stable of all Si-X element bonds[33] and form the basic frameworks for amorphous and crystalline silicate materials. Depending on the silica material, the Si-O-Si bond angle can range from 120° to 180° with a mean value of about 145°. The silicon-oxygen distance has a mean value of 0.162 nm.[34] The four-coordinate centre remains by far the most common in both the solid and solution state. However, there are exceptions; in the solid state, the coordination of Si is predominantly four-fold but five and six-fold coordination environments are also reported. For example, Si exists in a six-fold octahedral coordination sphere in thaumasite[35] ($Ca_3Si(OH)_6SO_4CO_3 \cdot 12H_2O$) and stishovite[36] (high pressure polymorph of SiO_2). Silicate glasses can contain Si coordinated to four, five, or six oxygens, even when formed at atmospheric pressure.[37] In the solution state, the existence of five and sixfold Si coordination is very rare. However, Kinrade *et al.*[38] showed that the addition of aliphatic polyols (xylitol, mannitol *etc.*) to aqueous silicate solutions yielded high concentrations of stable polyolate complexes containing Si in five or six-fold coordination confirmed by $^{29}Si\{^1H\}$ NMR.

1.2 Structure of Silica and Silicate Glass

Three hypotheses have been proposed for a generalised silica glass structure and are summarised in the following:

1. Crystalline hypothesis proposed by Lebedev[39] and later experiments of Rangall[40]; glass consists of an accumulation of microcrystals in disordered medium.
2. Continuous Random Network (CRN) structure proposed by Zachariasen[41] and experimentally supported by Warren[42] compares crystalline silicate units of cristobalite to amorphous glass structures. Basic unit is SiO_4 tetrahedron sharing corner oxygen atoms known as bridging oxygen atoms (BOs) between two adjacent atoms of silicon. See **Figure 1.3. (a).**
3. Discrete ion hypothesis is based on the notion that glass is closely related to the liquid from which it has been cooled.[34]

The consensus of research suggests that the "Zachariasen-Warren" model is commonly used to describe the structure of glass. Henderson[43] (2005) provides an excellent review of additional experimental and computational methods over the past years used to investigate these theories. The Zachariasen-Warren model also extends to other commercial glasses based on the following oxides of GeO_2, B_2O_3, P_2O_5, As_2O_3 and TiO_2. SiO_2, B_2O_3, GeO_2 and P_2O_5 are known as network formers and readily form glasses. As_2O_3 and TiO_2 are intermediate formers *i.e.* they can substitute for network formers but cannot form glasses independently. The glass formers, according to Zachariasen, establish a random network of corner-bound polyhedra, which, if required, can be broken up by so-called modifier oxides (alkali/alkaline cations): Na_2O, Li_2O, CaO *etc*.

1.3 Silicate Glasses

The addition of network-modifying alkali and/or alkaline-earth ions (Na^+/K^+/Ca^{2+} *etc.*) into SiO_2 breaks up the connectivity of BOs with the creation of non-bridging oxygens (NBOs) that are linked to only one Si atom.[44, 45] Each alkali cation introduces one NBO whereas alkaline-earth cations introduce two NBOs. The structure of silicate glasses can usually be pictured as a combination of a partially depolymerised network interspaced by oxides based on the Modified Random Network (MRN) model proposed by Greaves (see **Figure 1.3 (b).**). Essentially, Greaves used X-ray absorption fine structure (EXAFS) and ^{29}Si solid-state NMR experiments to analyse sodium-silicate glasses with varying molar compositions.[46]

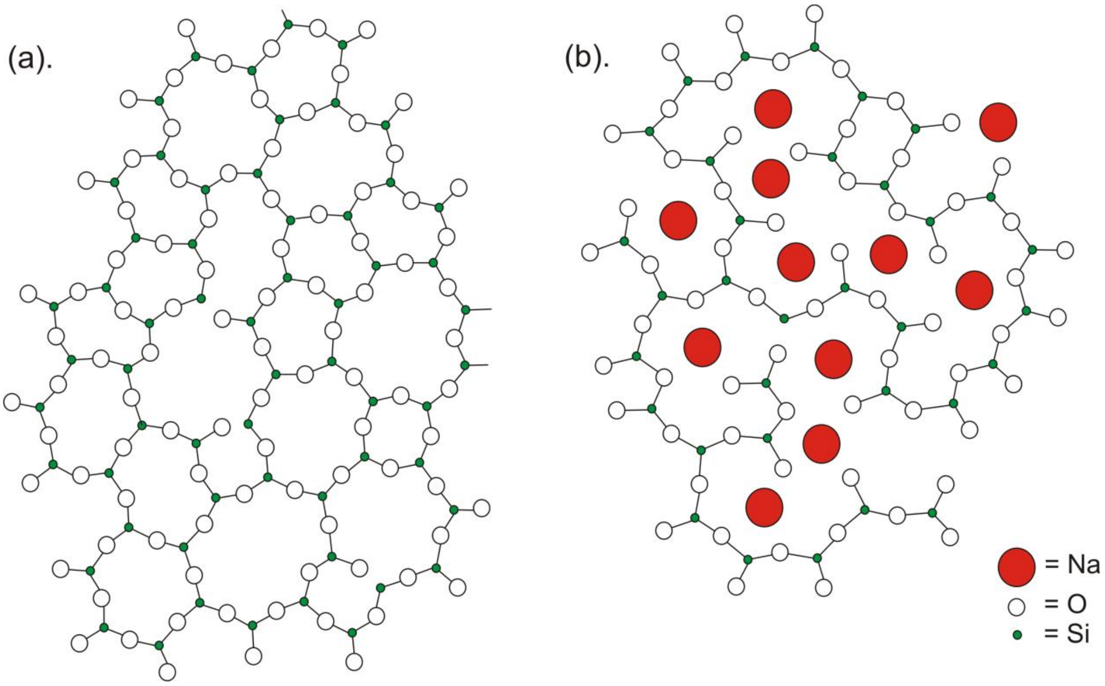

Figure 1.3 Structural representation of (a). CRN models for SiO_2 glass and (b). MRN model for the structure of a sodium-silicate glass. Si atoms are shown as small green circles, O atoms as open circles and large red circles refer to Na cations. BO atoms are located within the network and NBO atoms along the modifier channels. For clarity the coordination number of Si is reduced to 3. Notice that the Na^+ generate "holes" or percolation channels in the silica, which are discussed.

Electrical conduction in silicate glasses is thought to arise from cations jumping along holes in the glass network, like those represented in **Figure 1.3 (b).** For example, Eldin *et al.*[47] report conductance values of 4.97×10^{-11} S for a 60:40 *wt.* % SiO_2:Na_2O anhydrous glass. As the Na_2O content is reduced to 25 *wt.* % there is an accompanied decrease in conductance to 6.95×10^{-14} S. The reduction in conductivity is simply a linear decrease as a function of Na_2O content. However, if we replace say, 50 % of the Na^+ for Li^+, the conductivity would be several orders of magnitude lower than in the original material. This is known as the 'mixed alkali effect' (MAE)[48-50]. The non-linear decrease in ionic transport remains an unsolved problem, however, current theories suggest that each cation has different "jump pathways" within glass. It is an interesting subject area which warrants mention, but a full description of this phenomenon is beyond of the scope of this report (see Habasaki *et al.*[51] for a recent review).

1.4 Definition of Glasses and Amorphous Materials

Non-crystalline solids can be divided into two classes: glasses and amorphous solids. Amorphous solids are without long range order, but contain significant *local* chemical and topological order i.e. the coordination state, bond lengths and bond angles with nearest neighbours are quite similar. Unlike a crystal, the order rapidly decays with distance: distances of second neighbours are more uncertain than for first neighbours, and so on. If asked to define a glass, one instantaneously thinks of window glass prepared from the rapid cooling of a sand-soda melt (vitrification). This is broadly correct, formally however, a glass is defined as an amorphous solid that exhibits a *glass transition* (T_g). The glass transition is a phenomenon in which a solid amorphous phase exhibits an abrupt change in thermodynamic properties (*e.g.*, heat capacity or thermal expansivity) with a change in temperature.[52-56] Therefore, ‘‘glassy’’ materials need not be prepared only by quenching from the melt.

1.5 Preparation of Glassy and Amorphous Solids

Non-crystalline materials may be generated using a variety of techniques and can be divided into chemical and physical methods, as shown in **Figure 1.4**.

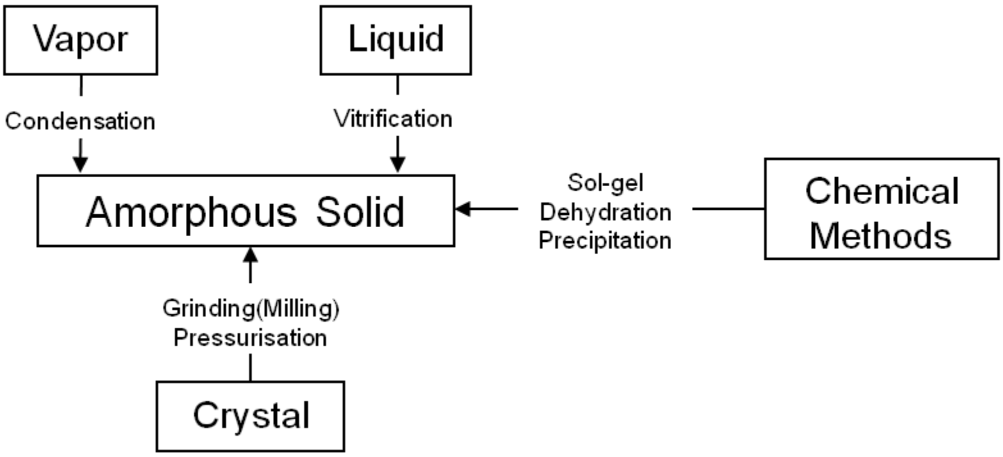
Vapor
Liquid
Condensation
Vitrification
Amorphous Solid
Sol-gel
Dehydration
Precipitation
Chemical Methods
Grinding(Milling)
Pressurisation
Crystal

Figure 1.4 Methods for preparing amorphous solids, adapted from Hiroshi *et al.*[53]

Chemical methods include sol-gel synthesis, dehydration and precipitation. The sol-gel route to produce amorphous materials will be covered later. Dehydration is simply the removal of water from a crystal structure. For example, Saleki-Gerhardt *et al.*[57] showed that heating crystalline raffinose pentahydrate (a carbohydrate) at 60°C in a vacuum converted the material into an amorphous form. Precipitation methods using spray or freeze drying can yield amorphous solids; these techniques are usually employed in the pharmaceutical industry.[58-61] Physical methods include, vapour condensation[55], liquid quenching or vitrification to form a glass, grinding/milling[62] or pressurisation of crystals[63]. The vitrification process is the most common route to produce an amorphous/glassy material.

1.6 The Vitrification Method

In order to obtain silica or alkaline-silicate glasses the rapid cooling from a melt is the method of choice. The volume, enthalpy, entropy *vs.* temperature diagram, as shown in **Figure 1.5**, is often used to discuss the interrelationships between the liquid, glass and crystalline states.

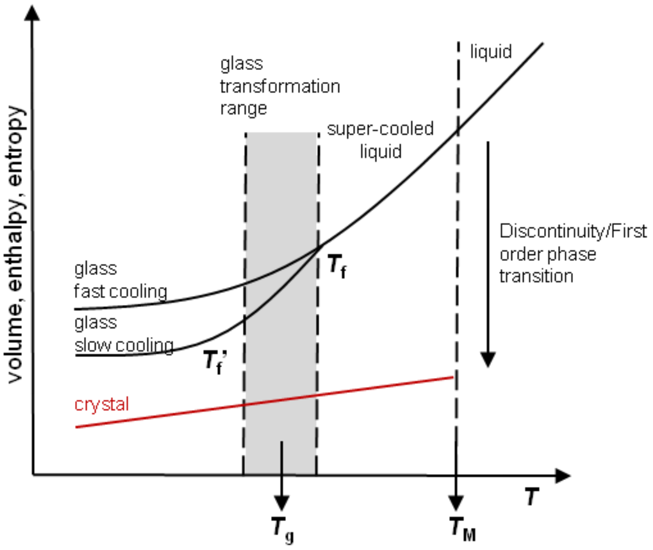
volume, enthalpy, entropy
glass transformation range
liquid
super-cooled liquid
Discontinuity/First order phase transition
glass fast cooling
glass slow cooling
T_f
T_f'
crystal
T
T_g
T_M

Figure 1.5 First-order thermodynamic properties of enthalpy, entropy, and volume as a function of temperature. Glasses with different frictive temperatures, T_f, $T_{f'}$ are derived from the liquid by decreasing the cooling rate. T_m and T_g denote the melting point of the crystal and the glass-transition temperature of the liquid, respectively.

Firstly, we consider how to form a crystalline material. As we decrease the temperature from the liquid state to the melting point (T_m) a sharp, decrease or discontinuity results (dotted line) indicating a transition to the crystalline form (red line). The crystalline-state is thermodynamically stable state with respect to non-crystalline forms. The crystallisation process leads to a sudden contraction of the system due to a decrease in free enthalpy, entropy and volume and corresponds to a first-order phase transition[61] (this is not always case; freezing of water sees an increase in volume on cooling reflecting the open ice structure).[64] Conversely, glasses and other non-crystalline materials generally possess excess volume, enthalpy and entropy compared to their crystalline counterparts. Therefore, one must avoid establishing thermodynamic equilibrium; this can be achieved by rapid cooling.[65] No discontinuity in thermodynamic properties is seen on cooling the material below T_m and the system forms a super-cooled liquid. As the material is cooled further, a change in the slope is usually observed at a characteristic temperature, known as the glass transition temperature. The most commonly measured signature of a glass transition is the rapid increase in specific heat capacity, C_p, across a relatively narrow temperature range when a glass is reheated into the super-cooled liquid state in a scanning calorimeter. The characteristic temperature associated with this jump, ΔC_p, is also known as the calorimetric glass transition temperature. The atomic structure of the glass is representative of that of its parent liquid, frozen in time, and is characteristic of the temperature at which the liquid thermally equilibrated for the last time. This temperature is also known as the 'frictive' temperature (T_f) and depends on the cooling rate of the liquid.[44, 65-67] In an ordinary oxide glass, a fast-cooled glass (higher T_f) has a greater specific volume, as shown in **Figure 1.5**. It is important to note, that silica glass is unique and exhibits the opposite trend. At this temperature, the bonding between molecules remains essentially the same as that of the liquid but the translational and rotational motions of those molecules are dramatically reduced.[66] Motions in glasses are over a period in excess of 100 s, and viscosities are usually greater than 10^{13} Poise (P).[68] (Water has a viscosity of 0.009 P at 25 °C and 1 atm[69]).

1.7 The Glass Transition in Materials

At temperatures below T_g polymeric materials are hard and glassy. As temperature increases towards T_g, the material becomes soft and rubbery[70]. This is a result of the polymer backbone and chain ends acquiring energy to overcome intermolecular restraints and undergo rotational and translational motions. In polymeric materials, the T_g is referred to as the onset of large scale cooperative motion of chain segments (20-50 carbon atoms in length)[71] and accounts for the glassy/rubbery transition. In silicate glasses T_g is related to the energy required to break and re-form covalent bonds from the melt-glass state[72].

1.8 The Nature of T_g

In 1996, Ediger *et al.* commented, "Although there have been attempts to understand the nature of the glass transition, *no theory has yet been proposed that captures all the salient features of this phenomenon."*[73] and to date this statement is still valid. The change in enthalpy, entropy and volume suggests that the glass transition is a second-order thermodynamic phase transition. A second order transition is rate independent whereas the T_g is dependent on the cooling rate. Therefore, the T_g is not ideally second order. The transition from a liquid to a glass or glass to a liquid is primarily a kinetic phenomenon.[44, 61] Notable theories on glass formation include Kauzmann, Adams and Gibbs, energy landscape, mode coupling and spin glasses which have been proposed for glass-forming liquids. The theories proposed are beyond the scope of this report but can be found in the following review papers, respectively.[73-77] There is also an excellent presentation on the subject matter available from the website of Korea's Advanced Institute of Science and Technology (KAIST).

1.9 Sol-gel Processing

Sol-gel processing is an alternative route to produce glasses[78-82], glass ceramics[83, 84] (glass containing areas of crystallinity) and silica hybrid materials.[3, 6, 85, 86] Advantages of using the sol-gel route include:

1. ability to prepare glasses of materials that cannot be obtained as amorphous solids by vitrification;
2. capability of obtaining fully-dense amorphous solids at temperatures lower by hundreds of degrees compared to traditional processes;
3. obtaining fully-condensed crystalline ceramics;
4. ability to obtain novel materials with organic-inorganic distributions;
5. controlled porosity.[87]

According to IUPAC[88], a *Sol* is a colloidal suspension of solid particles, with diameters of ~1-100 nm, in a liquid. The solid particles in the colloidal phase are stable due to short-range forces such as Van der Waals and surface charges. A *Gel* consists of continuous solid and fluid phases of colloidal dimensions. In sol-gel processing, a sol of a given precursor is prepared, which undergoes some chemical or physical changes, grows in size and forms a gel. This gel when dried, under high temperatures and set time (hours/weeks), yields an inorganic composite.[89-92] At this point, it is necessary to distinguish between gels formed from (1). sols (*i.e.* destabilisation/aggregation of sols) and (2). polymeric gels (gels prepared only from the hydrolysis and condensation of metal alkoxides).[87] The two routes are represented in **Figure 1.6**.

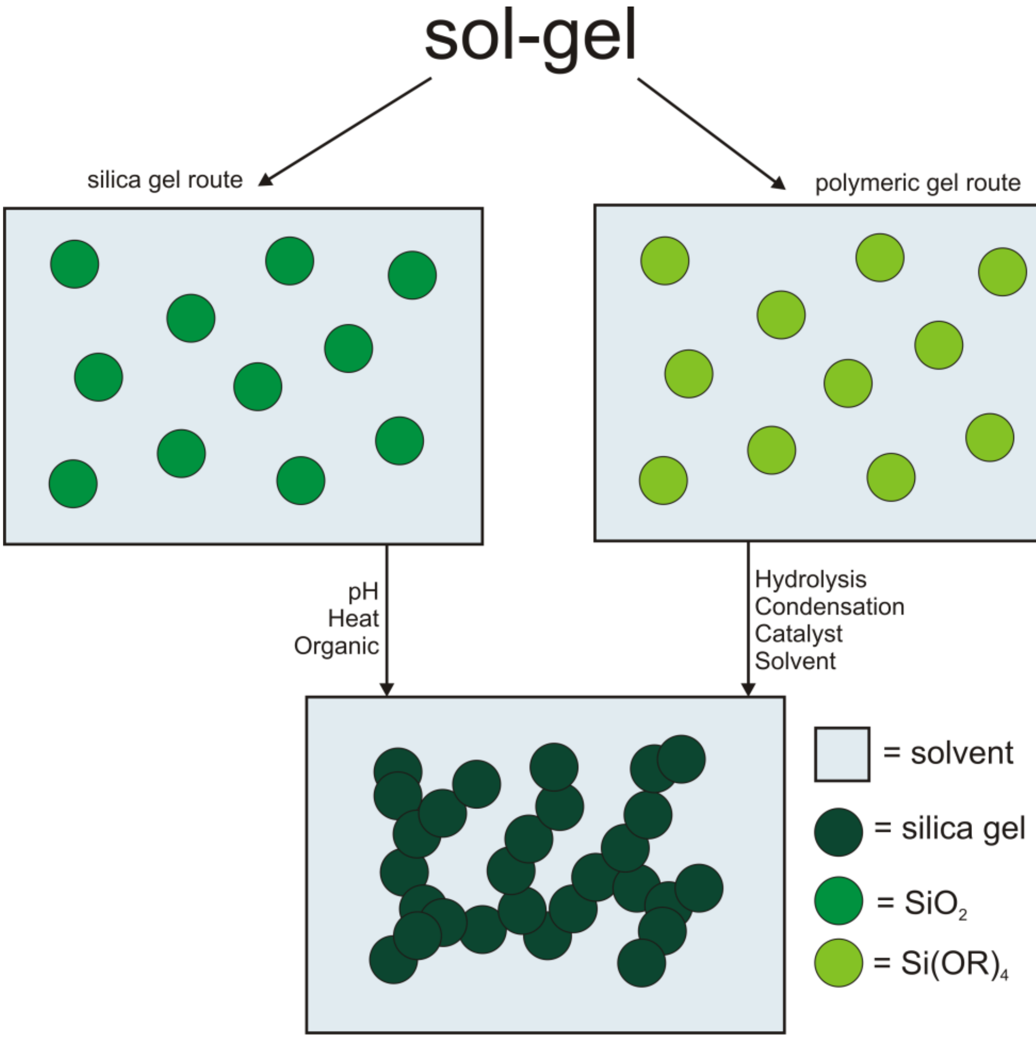
sol-gel
silica gel route
polymeric gel route
pH
Heat
Organic
Hydrolysis
Condensation
Catalyst
Solvent
= solvent
= silica gel
= SiO₂
= Si(OR)₄

Figure 1.6 Methodologies to obtain silica gels based on sol-gel reactions

Let us consider the right hand route in **Figure 1.6** in more detail. Chemically, the sol-gel route to form polymeric gels can be represented by six reactions:

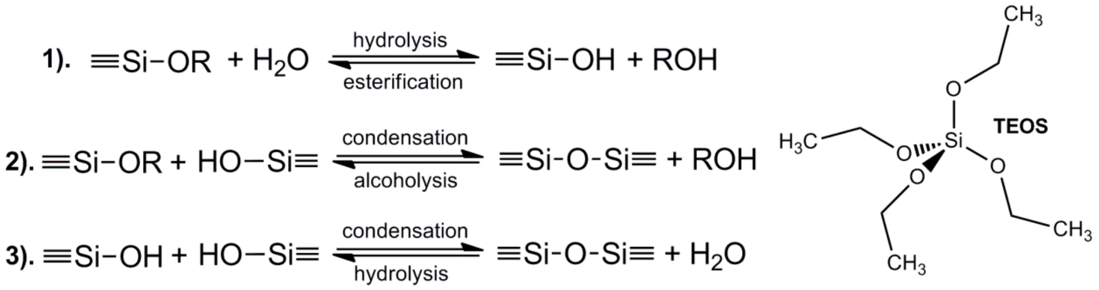
1). ≡Si−OR + H2O ⇌ ≡Si−OH + ROH
hydrolysis
esterification
2). ≡Si−OR + HO−Si≡ ⇌ ≡Si-O-Si≡ + ROH
condensation
alcoholysis
3). ≡Si−OH + HO−Si≡ ⇌ ≡Si-O-Si≡ + H2O
condensation
hydrolysis
TEOS
CH3
H3C
O
Si

Scheme 1.1 Series of reactions representing the sol-gel process. Reaction 1. *Hydrolysis:* Using $H_2{}^{18}O$,[93] it was found that the hydrolysis of a metal alkoxide (for example, tetraethylorthosilicate, TEOS) follows nucleophilic S_n2 substitution yielding a silanol group, $(OH)Si(OR)_3$. Reactions 2 & 3: *Condensation:* The silanol groups can react with each other or with alkoxide groups to form siloxane bonds; the basis of the gel networks.

The process can proceed at pH 7, but gellation can take several weeks. The rate of hydrolysis and condensation can be accelerated by the addition of an acid or base and subsequently the reaction mechanisms are different. For example, in acid catalysis, a water molecule attacks the metal centre whereas in base catalysis, a hydroxyl anion acts as the nucleophile.[89-93] The subsequent gel that forms is strongly dependent on the $M(OR)_4$: solvent : catalyst : H_2O ratios. A variety of gels and subsequent glasses can be formed. For example, Beckett *et al.*[78] demonstrated the synthesis of a binary SiO_2-B_2O_3 glass, confirmed using X-ray diffraction, optical transmission and IR absorption spectroscopy. Deng *et al.*[79] reported on a series of TiO_2-SiO_2 glasses comprising >9% TiO_2 *via* sol-gel processing. The sols gelled in 2-4 days followed by drying for 6-8 days at 1500°C to produce clear, dense, microstructure-free glasses. Gosh *et al.*[80] reported semiconducting V_2O_5-SiO_2 glasses. In the past decade, research has focused on producing SiO_2-CaO-P_2O_5 based ‘bioglasses.’ These materials are good candidates for medical applications used for bone repair/growth and as drug releasing agents.[94-96] There are also subdivisions of silica gels that can be derived from silicon alkoxides or sodium-silicate solutions:

- *Xerogels* are obtained from drying a gel by evaporation and are often reduced in volume by a factor of 5 to 10 compared to the original wet gel.[9, 29]
- *Areogels* are obtained by replacing the solvent in a gel system with gas and exhibit porosities up to 99.8 % and surface areas *ca.* 1500 m^2 g^{-1}. [7, 8, 29]
- *Hydrogels* are materials with three-dimensional, water swollen structures composed of mainly hydrophilic polymers or oligomers. They are insoluble due to the presence of chemical or physical crosslinks. The physical crosslinks can be entanglements, crystallites, or weak associations formed by Van der Waals interactions, π-π stackings or hydrogen bonds. The crosslinks provide the network structure and physical integrity[97]. The majority of hydrogels in the literature are hybrids based on networks of organic polymers and silica. Applications include drug delivery[98, 99], enzyme encapsulation[100, 101] and as a wound-healing composites.[10]

1.10 Solubility of Silica

The reported solubilities of silica (SiO_2) in water (pH 7 and at 298 K) range from 5 ppm (8 x 10^{-5} mol L^{-1}) to 11 ppm for quartz and 100-130 ppm for amorphous silica.[102-104] Therefore, silica is sparingly soluble in water. Fournier *et al.*[105] have shown that the solubilities of amorphous silica and quartz can be increased to 1200 and *ca.* 380 ppm, respectively, with temperature. At pH 7 the silica in solution is present primarily as monomeric uncharged silicic acid, $Si(OH)_4$.[106] Solubility of silica increases slightly below pH 7, but the increase is dramatic above pH values of *ca.* 9.5, and silica concentrations of several mol L^{-1} are feasible at very high pH.[107] **Figure 1.7** shows the stability diagram for amorphous silica as a function of pH.

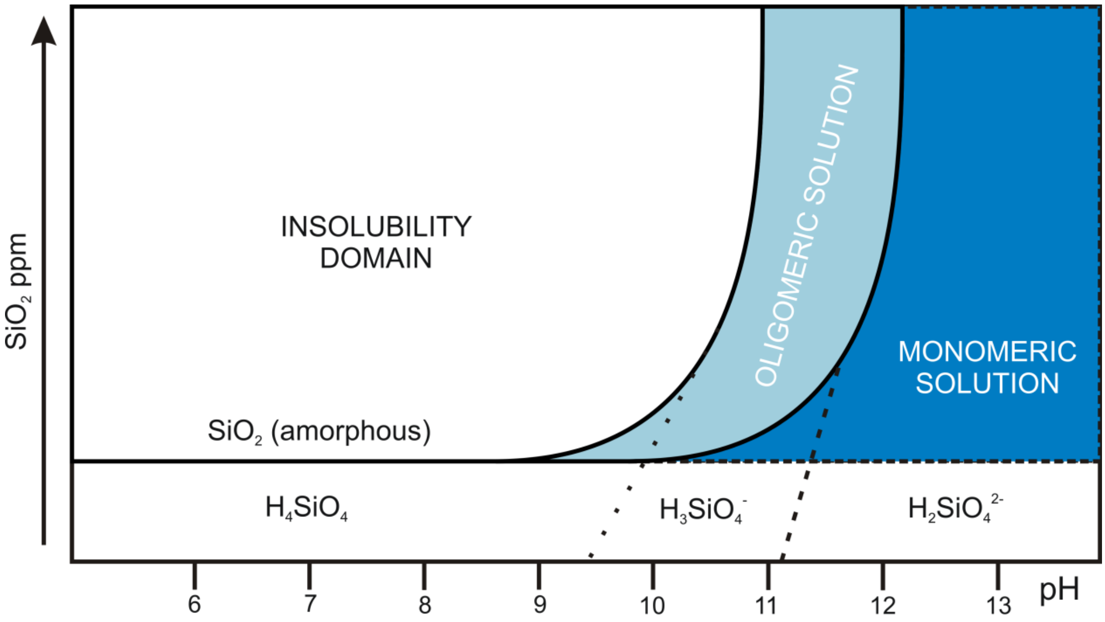

Figure 1.7 Stability diagram for soluble silicates at 298 K. The heavy solid line is the solubility curve for amorphous silica. The dotted and dashed lines represent the first and second pKa's of silicic acid.

In the region below and to the right of the solid line, the silicate anions are in solution. Between pH 9.5 to 11.5, there is a sharp rise in SiO_2 solubility and a variety of oligomers are generated (see next section). The degree of polymerisation, concentration and type of silicate anions increases as Si concentration increases, or pH is decreased. According to Iler[108], the monomer reacts with another monomer to form a dimer. The dimer reacts to form cyclic and larger 3D structures. The monomer is always in equilibrium with higher species, which is governed by two sets of independent reactions:

Acid-base:

$\equiv Si\text{-}OH + H_2O \leftrightarrow \equiv Si\text{-}O^- + H_3O^+$

Polymerisation-depolymerisation:

$\equiv Si\text{-}OH + HO\text{-}Si\equiv \leftrightarrow \equiv Si\text{-}O\text{-}Si\equiv + H_2O$ or

$\equiv Si\text{-}OH + {}^-O\text{-}Si\equiv \leftrightarrow \equiv Si\text{-}O\text{-}Si\equiv + {}^-OH$

As pH continues to increase the dominant anion will be the monomer. The silicate solutions (sodium-silicate solutions) used in this work are in the region of the oligomeric domain.

1.11 Alkaline silicate solutions

1.11.1 *Nomenclature and Properties*

Alkaline silicate solutions, soluble silicates or waterglass describe solutions which are essentially combinations of alkali metal oxide and silica, usually dissolved in water. The general formula is:

$x\text{SiO}_2\text{:M}_2\text{O}$

where, M is an alkali metal (Li^+, Na^+, K^+ *etc.*) and x is the modulus. The modulus can be expressed by either the *mole* or *weight* ratio. The molar ratio (R_M) is defined as the number of moles of silica (SiO_2) per mole of alkali metal oxide (M_2O). The weight ratio (R_W) is defined as the weight of silica per weight of alkali metal oxide. For example, a sodium silicate solution containing 27.7% SiO_2 and 8.40 % Na_2O have R_M and R_W values of 3.40 and 3.30 respectively. The total amount of SiO_2 and Na_2O determines the % solids content. (The molecular weights of Na_2O, 62, and SiO_2, 60, are similar; hence small differences between molar and weight ratio for sodium silicates) The weight ratio is used to describe commercial solutions.[107, 109, 110] Sodium silicates are commonly produced followed by potassium[111-113] and lithium[111, 114]. However, rubidium[115], caesium[116], tetramethyl/ethylammonium (TM/EA)[117] ions, and more recently, tetraoctylammonium[118] ions can also be used. The viscosity of sodium-silicate solutions is dependent on the concentration, density, ratio, and temperature (**Figure 1.8**). Viscosities are usually measured in poise or centipoises. We can see from **Figure 1.8** that at constant solids content the solutions are at a minimum viscosity at 2.00 *wt.*

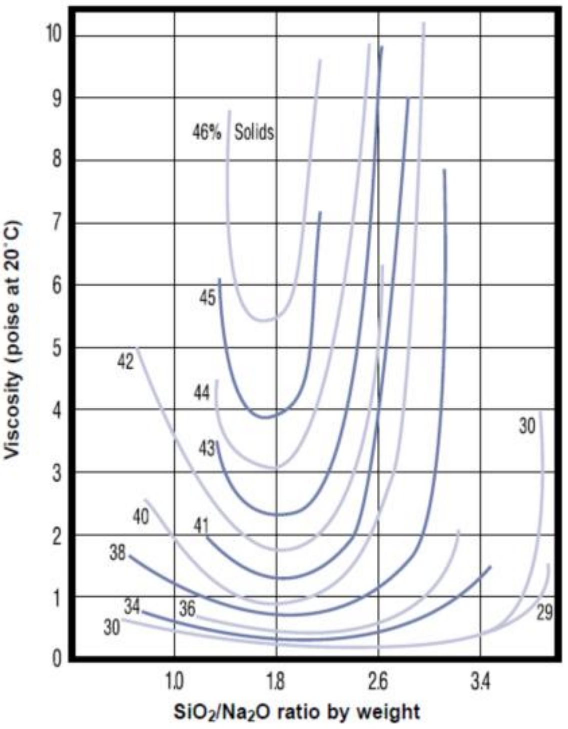

Figure 1.8 Viscosity of sodium-silicate solutions as a function of *wt.* ratio and solids content[1].

ratio. Viscosity increases as the *wt.* ratio of the sodium silicate becomes either more siliceous or more alkaline. All silicate solutions are alkaline, the pH of commercial silicate solutions ranges from approximately 10 to 13. The pH is a function of SiO_2 : Na_2O *wt.* ratio and decreases with increasing silica content.

1.11.2 *Production and Applications*

The two common methods for producing sodium-silicate solutions are schematically represented in **Figure 1.9**:

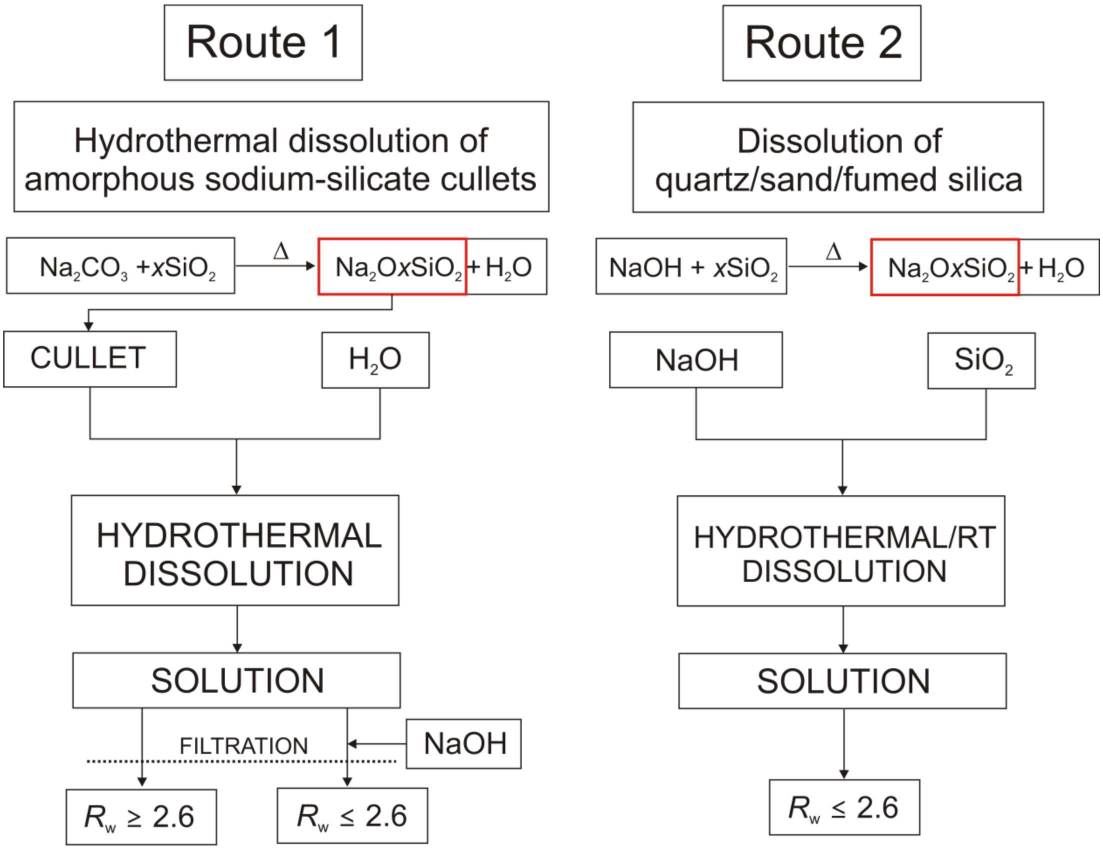
Route 1
Route 2
Hydrothermal dissolution of amorphous sodium-silicate cullets
Dissolution of quartz/sand/fumed silica
Na2CO3 +xSiO2
Δ
Na2OxSiO2 + H2O
NaOH + xSiO2
CULLET
H2O
NaOH
SiO2
HYDROTHERMAL DISSOLUTION
HYDROTHERMAL/RT DISSOLUTION
SOLUTION
FILTRATION
NaOH
Rw ≥ 2.6
Rw ≤ 2.6

Figure 1.9 Traditional methods of producing sodium-silicate solutions

In route 1 the dissolution of the cullet is achieved by ion exchange between the alkali ions in the glass and the hydrogen ions of the surrounding water. This forms a protective layer of silanol groups on the glass surface, while the pH of the solution rises. In the second step, the alkalinity drives the depolymerisation of the silicate particles. The same dissolution process also occurs in route 2.[119] The solutions are passed through various filtration methods to yield (generally) clear solutions. Filtration methods are employed to remove hydrated sodium metasilicate crystals that can precipitate from the solutions.[120, 121] Route 1 is used predominantly to produce higher modulus silicates, however lower R_W ratios can be achieved by adding additional NaOH (the name “waterglass” was derived because of this route). Route 2 produces solutions with R_W of *ca.* 2.00 and solid levels of 48 % but higher ratios can also be prepared this way. The choice of which method to use in industry is dependent upon raw material and energy costs. The solutions are used mainly as a feedstock for the synthesis of Zeolites[122-124] (detergents) and mesoporous silicas.[4, 125-127] This method is also used for anticorrosive coatings[128, 129], a sealant in the oil industries[130-132] and for direct use in extinguishing fires.[133] A novel use of sodium silicate solutions is the ability to grow chemical gardens (see **Figure 1.10**). Chemical gardens are plantlike structures produced by a variety of different metal-ion salts (Ca/Mn/$CoCl_2$) when immersed in a solution of sodium silicate.[134-138] The physical and chemical variables that control the morphology of the structures are yet to be established and gaining greater insight into these processes would potentially be of value for materials sciences. Also, the attractive visuals of these systems can be used for educational purposes explaining chemical processes of dissolution, precipitation, and crystallisation.[136]

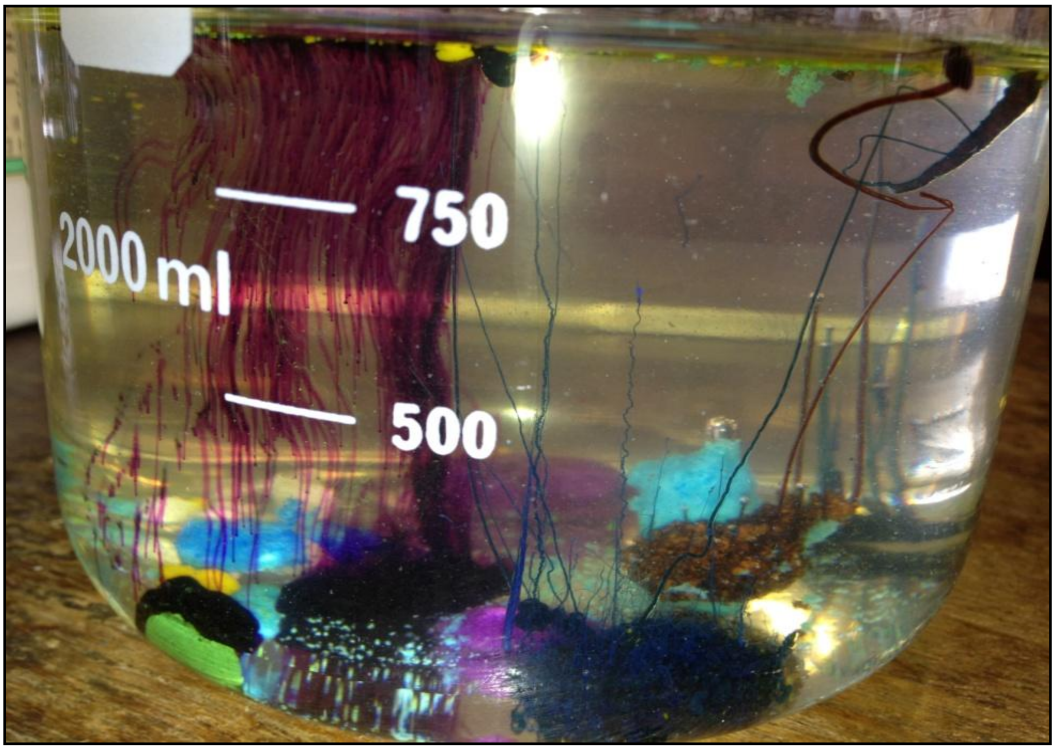

Figure 1.10 Picture of a typical chemical garden of with a variety of transition metal salts in a SiO_2:Na_2O R_W of 1:1 solution. Courtesy of Dr. C. Cropper; the University of Liverpool.

1.11.3 *The Constituents of Sodium-Silicate Solutions*

Sodium silicate solutions were first reported by Van Helmont in 1640 as a fluid substance made by melting sand with excess alkali.[139, 140] Falcone[109] states that these solutions were also experimented with in 1768 by Goethe, (unfortunately, my attempts to find the original manuscript by Goethe proved unsuccessful). From the 18th to 19th Century the production of sodium-silicate was based in Europe. North America imported the solutions during the Civil War for anticorrosion coatings in cannons.

It was only during the 1920s that attention focused on the behaviour and establishing bulk properties of the solutions with varying R_w ratios and concentrations. For example, Harman[141] in 1925 stated: "...at the time this work was undertaken our knowledge of the alkali silicates was meagre, vague, and in large part contradictory...the solutions at this time can be summed up as largely hydrolysed and in which most of the silica exists in the colloidal state..." Harman then published seven papers regarding bulk properties such as (1) conductivity,[141] (2) transport numbers[142] (electrolysis), (3) sodium ion activity,[143] (4) hydrolysis,[144] (5) lowering of vapour pressure and of freezing points,[145] (6) heterogeneous equilibria[146] and (7) silicate ions[147] on R_W of 1:00, 1.50, 2.00, 3.00 and 4.00 at concentrations ranging from 0.005 to 2 M with respect to SiO_2 content. The results are surmised in his eighth paper in which the bulk properties are used to explain the constitution and behaviour of the solutions. He stated that depending upon the $SiO_2 : Na_2O$ ratio the silica in the solutions exist as partially or wholly "crystallodial silica." This is explained as being analogous to crystalline silicate compounds in equilibrium with silicate ions (they knew of the existence of silicic acid), or electrically charged aggregates of silicate ions and silica i.e. ionic micelles, or pure colloidal aggregates. His theory that simple silicate ions were in equilibrium with larger colloidal or crystallodial components would not be proven for another 40 years. Other macroscopic properties such as pH[148], viscosity[149], turbidity[150] and refractive indexes[151] were investigated during the thirties, forties and fifties. It was in 1964 that the first direct evidence of the structure of silicate anions in alkaline solution was provided by Lentz. The reaction consists of two steps:

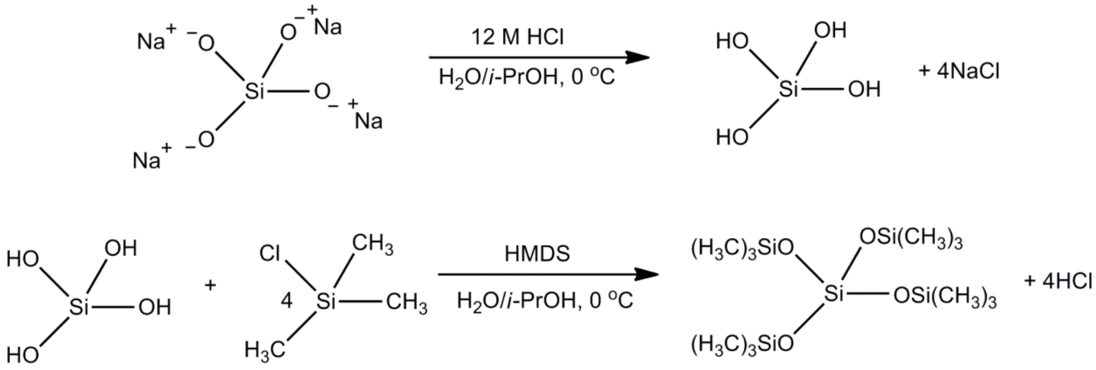

Scheme 1.2 Lentz reaction. Top: acidification of the sodium-silicate anions in solution to their silicic acid derivatives. Bottom: trimethylchlorosilyation of the silicic acid to form the TMS-derivatives. This example shows the Lentz reaction on the monomeric silicate anion and is represented by QM_4

The first step is the exchange of sodium ions in the solution for hydrogen ions to give the corresponding silicic acid. The second step is the reaction of silicic acid with silylating agents to block the reactive-acid groups, which gives the stable TMS derivatives. The true silylating agent is probably trimethylchlorosilane, which is produced by hydrochloric acid cleavage from hexamethyldisiloxane (HMDS).[152-155] The products can be analysed using thin-layer[156, 157] or gas-phase chromatography[152, 154, 155, 158-161], or combined with mass spectrometry.[153] In the original paper Lentz isolated the monomer and oligomer species including the dimer, trimers and tetramers. Chemical methods such as molybdic acid and ultrafiltration methods were employed by Iler[162] and Dietzel[163] *et al.* to study a 3.10 *wt.* ratio sodium-silicate solution (25.2 *wt*. % SiO_2). The results indicated that the solution consists of 10 *wt.* % monomer, 15 *wt.* % oligomers and 75 *wt.* % colloids. These methods and features associated with the colloidal fraction of the solutions are addressed in more detail in **Chapter 6**. The emerging use of ^{29}Si NMR during the 1970s shed light on additional silicate anions present in solutions and confirmed the findings by Lentz. Initially, ^{29}Si NMR was shown to differentiate between different types of silicon environments[164, 165] and Engelhardt[166, 167] adopted the 'Q' notation to designate the connectivity of Si atoms under consideration. There was, however, no reliable way of assigning the ^{29}Si NMR peaks of individual anion structures. This was because (1) ^{29}Si has a natural abundance of 4.7 % therefore the NMR spectra show no ^{29}Si-^{29}Si *J*-coupling;

(2) rapid exchange of the hydroxyl protons modulates ^{1}H-^{29}Si *J*-coupling and (3) due to the concentration and equilibrium in solutions overlapping or broad signals are observed. Towards the 80s spectral assignments were made possible through the use of higher magnetic fields, ^{29}Si isotropic enrichment and dilution methodologies. Notable pioneers of this research area from the 1980s to mid 2000s have been Stephen D. Kinrade[168-170], Christopher T. G. Knight [171, 172], and Robin K. Harris[173-176], whom either jointly or individually have characterised, to date (last publication on the subject matter; 2007), at least 48 structures.[177]

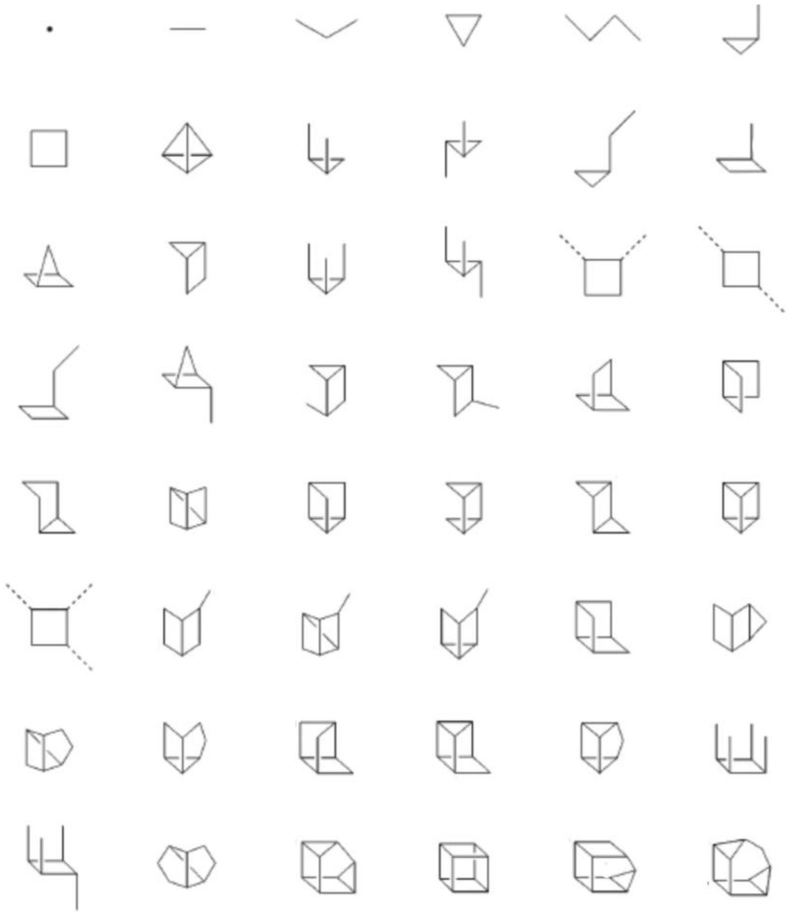

Figure 1.11 48 silicate structure positively identified using ^{29}Si-^{29}Si COSY on $^{29}SiO_2$ enriched $1SiO_2 : 1KOH$ solution[177] starting with the monomer; $Si(OH)_4$.

Recent investigations revisit the identification of the units in **Figure 1.11** in sodium-silicate solutions using higher field strengths and improved NMR experiments. For example, Haouas *et al.*[178] use ^{29}Si-^{29}Si INADEQUATE (incredible natural abundance double quantum transfer experiments)

experiments in order to gain connectivity information and aid spectral assignment of enriched ^{29}Si 96 % $SiO_2 : Na_2O$ solutions of R_w: 3.30 at several dilution factors. The results confirm those reported in the 1980s and also show new Si-Si correlations. Cho *et al.*[179] use ^{29}Si-^{29}Si correlation NMR spectroscopy (COSY) combined with molecular modelling calculations to show evidence for at least nine new silicate anions in $SiO_2 : Na_2O$ solutions (they do not state the $R_{w/m}$ ratios or dilutions used). In the past two years the majority of research has focused on the oligomerisation of silica *via* the condensation of TEOS using ^{29}Si NMR, Raman and molecular modelling calculations.[180-182] In conclusion, sodium-silicate solutions are complex systems in which monomeric, oligomeric and colloidal silica are in dynamic equilibrium. The macroscopic and molecular level properties are dependent upon $SiO_2 : Na_2O$ ratio, concentration and temperature.

1.12 Layered Silicates

Layered hydrous sodium-silicates are naturally occurring minerals found in alkaline/silica-carbonate rich environments, for instance Lake Magadi in Kenya.[183, 184] Layered silicates can be classified into two categories; single and multilayered silicates. Single layered silicates are kanemite and makatite. Multilayered silicates are octosilicate, magadiite and kenyaite:

Table 1.1 Formulae and basal spacing for layered sodium-silicates[185]

Silicate	Formula	Basal Spacing /Å	Connectivity ratio Q^3/Q^4
makatite	$Na_2O{\cdot}4SiO_2{\cdot}5H_2O$	9.0	1:0
kanemite	$Na_2O{\cdot}4SiO_2{\cdot}7H_2O$	10.3	1:0
octosilicate*	$Na_2O{\cdot}8SiO_2{\cdot}9H_2O$	11.0	1:1
magadiite	$Na_2O{\cdot}14SiO_2{\cdot}10H_2O$	15.6	1:3
kenyaite	$Na_2O{\cdot}22SiO_2{\cdot}10H_2O$	20.0	1:5

*Octosilicate is synthetic[186] (Other names Illertie or RUB[187]).

The crystal structure of makatite and kanemite is resolved fully. The structures consist of silicate layers, separated by hydrated sodium ions with characteristic gallery or basal spacing. The thickness of the silicate sheets increases from makatite to kenyaite and is also consistent with an increase in Q^3:Q^4 ratio from ^{29}Si NMR.[188]

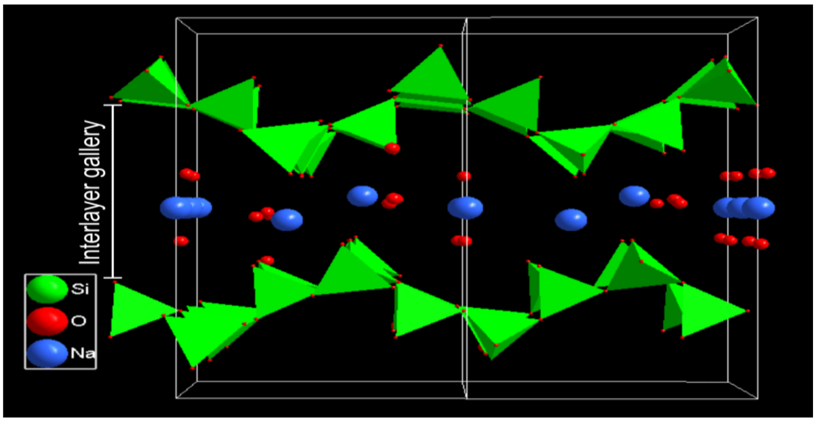

Figure 1.12 General structure of layered silicates

The interlayer gallery of layered silicates can be intercalated or grafted with organic guest species to produce nanocomposite materials. These guest species may be grafted covalently to the outer layer surface of the host and/or can reside in the interlayer region as neutral species bound to the host material by hydrogen bonds. The applications of these composites range from adsorbents[189], catalysts[190, 191], exfoliated nanoparticles[192], fire retardants[193, 194] and compounds for the removal of toxic substances from aquatic environments[195, 196]. In the late 1970s Beneke and Lagaly studied the synthesis and intercalation compounds of kenyaite[197], kanemite[198] and magadiite[199, 200] extensively. The organic species used for intercalation varied from n-alkylammonium and pryidinium ions to N/P/S-oxides (trimethylamine oxide, trimethylphosphate, dimethylsulfoxide, respectively). Successful inclusion of the organic moieties is shown by an increase in gallery spacing (or basal spacing) derived from X-ray diffraction measurements. Mercier *et al*.[201] was the first to report an intercalated and grafted ethylene glycol-magadiite hybrid. The material was studied using TGA, ^{1}H-^{29}Si and ^{1}H-^{13}C CP MAS NMR spectroscopy. The intercalate (ethylene glycol associated with magadiite through hydrogen bonding) showed a mass loss between 100 and 180°C, whereas the grafted analogue showed an additional mass loss between 450 and 590°C; evidence for the formation of Si-O-C bonds. Dipolar dephasing was implemented during ^{1}H-^{13}C CP/MAS acquisition to show rigid and mobile ethylene glycol components in the grafted material. Additionally, the ^{1}H-^{29}Si CP MAS NMR spectrum indicated a reduction in the Q^3 resonance *i.e.* interlayer region, resonance compared to the intercalated material. Mitamura *et al*.[202] intercalated aliphatic alcohols ($C_nH_{2n+1}OH$ (n = 2 - 16) into H-magadiite. (H-magadiite is simply the acid treated product of the host). They reported that alcohols with chain lengths up to 4 (butanol) would react readily with the interlayer region. This was confirmed by an increase in the basal spacing but also from ^{2}H NMR. The ^{2}H NMR spectrum of CD_3OD-treated H-magadiite showed Pake doublets with quadrupole coupling constants of 43 and 48 kHz and asymmetry factors of 0, indicating the fixation of the C-O axis. There was no increase in the basal spacing of this material when using the longer chained alcohols suggesting that the chains were lying parallel to the layers.

More recently, Hirsemann *et al*.[203] used advanced solid-state NMR techniques, such as ^{27}Al MQMAS (Multiple Quantum Magic Angle Spinning) and ^{13}C-^{27}Al REAPDOR (Rotational Echo Adiabatic Passage DOuble Resonance) experiments to unequivocally prove the presence of covalently bound ethylene glycol in Kaolinite. ^{27}Al MQMAS showed that the chemical surroundings of the octahedrally coordinated aluminum nuclei in the layer were significantly changed as a result of a covalent bond. REAPDOR measurements are used for the determination of the distances between heteronuclei. The experiment gave a $d(^{13}\text{C-}^{27}\text{Al})$ bond distance of 3.1 Å which further proved the existence of a covalent bond.

The literature is rife with examples of intercalation compounds of naturally occurring silicates *i.e*. magadiite, kenyaite and kanemite, however, there are no reports regarding makatite. It was Sheppard *et al.*[204] who were first to discover makatite in Lake Magadi, Kenya in 1970 (magadiite is also found here, hence the name). Annehed *et al*.[205] solved the crystal structure (see **Chapter 5** for full crystal structure), Schwieger *et al*.[206] studied the silicate structure of synthetic makatite and an acidified form, H-makatite, using ^{1}H-^{29}Si CP MAS NMR. The group gave a molar ratio to prepare makatite and stated that hydrothermal treatment is required to prepare the synthetic version. However, they did not to provide details on the length of time required for hydrothermal treatment, or state the nature of the silica precursor used for the synthesis. Towards the late 1990s Harris and co-workers[185, 207-209] published several articles on the use of solid-state NMR; in particular ^{23}Na MQMAS NMR experiments on makatite and other layered silicates. At this point, only the crystal structure of makatite had been resolved. Harris' group aimed to gain additional structural information on magadiite, kenyaite and kanemite using NMR experiments inferred from that of makatite. Subsequently, the crystal structure of kanemite were solved[210]. To date, the crystal structures of magadiite and kenyaite remain unsolved. The last research paper to report on makatite was published in 2007 by Hiroaki *et al*.[211] They report the use of makatite as a silica source which is reacted with hexadecyltrimethylammonium (C_{16}TMA) chloride to form mesoporous silicas.

1.13 Aims of the Project

The Fire Statistics Monitor (a body within Communities and Local Government) estimates that 312 people are killed and 7,400 are injured in fires in England alone (April ’10 to March ’11). In 2008 the economic cost of fire damage was estimated at £8.30 billion.[212] The majority of these deaths, injuries and losses occur in buildings where fire and smoke protection measures are inadequate. The installation of effective fire resistant glasses can save lives and reduce the costs associated with fire damage. Several global manufactures produce complex fire products that are installed in the commercial and industrial sector. These are clear materials, which are laminated structures comprising a transparent sodium-silicate/polyol hydrogel interlayer sandwiched by sheets of ordinary float glass:

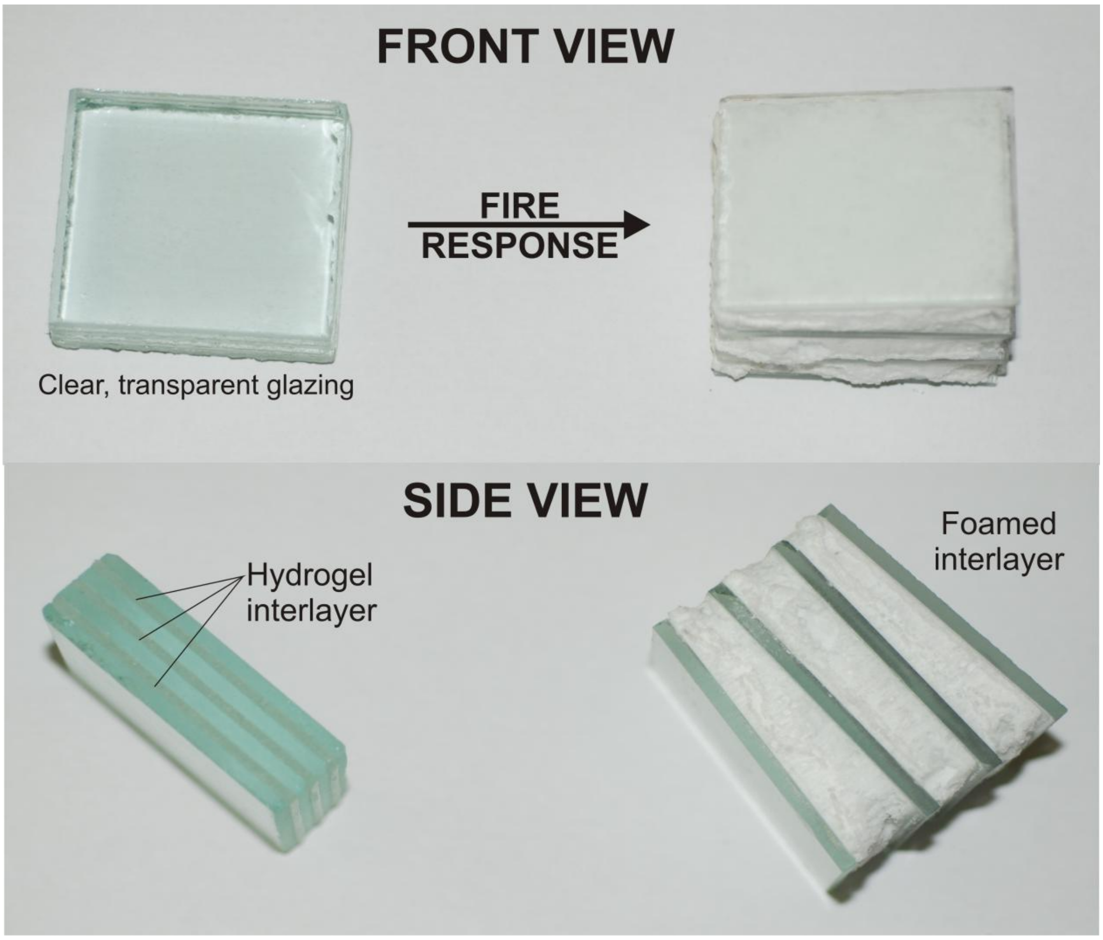

Figure 1.13 Images of the product before and after a firing test. From a front view, the product appears to be ordinary glass but tilted on its side, one can see the hydrogel/float glass laminates making up the product.

The mechanism of fire protection is based on the foaming and swelling of the hydrogel when exposed to temperatures in excess of 100°C, thereby producing endothermic cooling and physically impeding the transverse transfer of radiant heat, smoke and fire through the structure. The advantage of this product range over other fire resistant materials is that it stops the spread of flames, hot gases and heat and can offer up to 120 minutes of integrity and insulation during a fire.

1.13.1 *Temperature Regimes*

Figure 1.14 represents the structural and visual changes that occur within the hydrogel as a function of temperature. There are essentially two temperature regimes.

1. High temperature: excess of 150°C induces the fire response as mentioned above
2. Lower temperature regime, 40-100°C leading to crystallisation of the hydrogel into makatite. The crystallisation process generates a hazing throughout the product that becomes progressively worse with time. The rate of crystallisation is dependent upon temperature and the composition of the hydrogel. More importantly the crystallisation process is detrimental to the performance of the product.

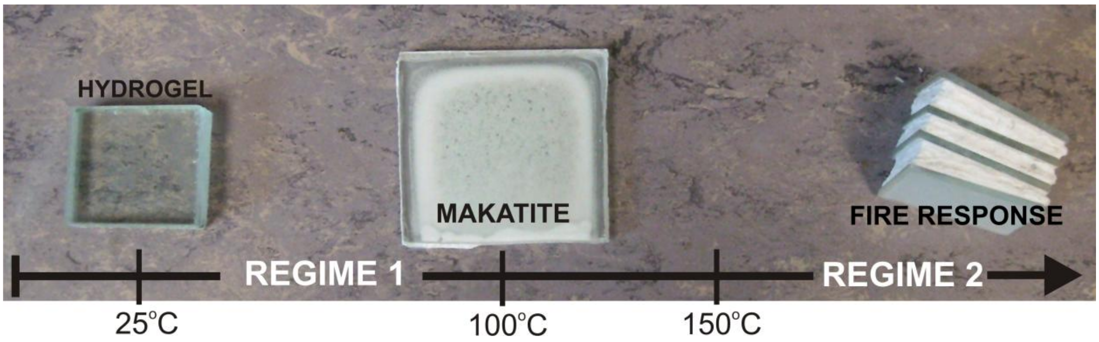

Figure 1.14 Effect of temperature on the structural changes occurring within the hydrogel interlayer and corresponding visual observations

The formation of an organic-inorganic hydrogel is a complex process requiring a careful control over synthesis conditions. The hydrogels are amorphous, structurally heterogeneous and show a lack of long range order, which precludes the use of standard diffraction techniques making their characterisation more challenging. Solid-state NMR has shown to be an ideal technique in the study of amorphous systems and is therefore the primary spectroscopic tool used throughout the project. The overall aim of the project is to characterise the local environment of the hydrogel and correlate this to the products longevity and thermal stability. In order to achieve this goal, the project has been divided into four areas:

(1). molecular characterisation of the materials
(2). investigation into the crystallisation of makatite as a result of thermal treatment
(3). methodologies to improve the product i.e. retardation of makatite formation
(4). insight into makatite formation and interlayer reactivity *via* the synthesis of a makatite/glycerol hydrogel

In chapter 4 the molecular level characterisation of a series of hydrogels with different weight ratios are investigated by means of 1D MAS NMR experiments. This includes a detailed analysis of the local structure of silicon, sodium and proton environments. As water is a major constituent in the hydrogels, variable temperature relaxation methodologies are employed to characterise water mobility and domains. The influence of ethylene glycol or glycerol on directing properties on the molecular level is investigated. The homogeneity of glycerol is also studied using spin-lattice relaxation measurements. The results are used to generate structural models for the systems and allow for a greater understanding of the materials.

The formation of makatite is detrimental to the performance of the product, therefore it is important to understand the mechanism of its formation in the potentially motionally restricted hydrogel environment. The crystallisation of makatite from the hydrogel with or without polyol is followed using optical measurements and X-ray diffraction techniques. With the aid of ^{1}H-^{29}Si CP MAS, ^{23}Na MQMAS and variable temperature heteronuclear correlation NMR experiments we aim to show the change in silica and sodium speciation, the thermal instability of the ethylene glycol hydrogel over the glycerol counterpart and relate this to differences in crystallisation rates.

Chapter 6 deals with methodologies to inhibit makatite nucleation and growth by modifying the starting sodium-silicate solutions. A synthetic analogue to one of the commercial solutions is prepared and dried to form a hydrogel, with and without glycerol. The synthetic system greatly inhibits makatite formation. The constitution of the synthetic and commercial solutions are analysed using ^{29}Si NMR and Lentz-GC analysis. The local environments of the hydrogels are investigated using ^{1}H-^{29}Si CP MAS and ^{23}Na MQMAS NMR experiments. A discussion follows as to possible reasons as to why the synthetic systems significantly inhibits makatite nucleation and growth.

In the final chapter we ‘reverse’ the hydrogel process, that is we synthesise a makatite hydrogel containing the same water and glycerol contents to those in the initial amorphous based hydrogel. The local structure of this composite is compared to the initial hydrogels as to gain a deeper understanding between the interactions occurring between silica, water and glycerol. On a separate theme, we also demonstrate the difficulty in synthesising makatite hydrothermally and its resilience towards intercalation chemistry.

Chapter 2

Characterisation Techniques

2.1 Nuclear Magnetic Resonance

Nuclear Magnetic Resonance is the study of matter through measurement of the interaction of an oscillating radiofrequency electromagnetic field with a collection of nuclei immersed in an external magnetic field. The phenomenon can be described to an extent by classical physics. To fully appreciate the phenomenon of NMR and advanced pulse sequences, quantum mechanics and the product operator formulism[213, 214] are required. However, a semi-classical approach can be used and is often adequate to describe NMR.

2.2 Basics of Nuclear Spin and Resonance[215-223]

Protons and neutrons possess a number of intrinsic properties such as charge, mass and angular momentum, $\vec{I}$. Angular momentum, or nuclear spin, is a vector quantity and is therefore denoted using the arrow superscript: $\vec{X}$. Nuclei that have spin angular momentum give rise to a magnetic moment, $\vec{\mu}$, just as an electric charge moving in a circle creates a magnetic field (see **Figure 2.1**). The magnetic moment is also a vector, defined by its axis of spin, which is parallel to its spin angular momentum, see below:

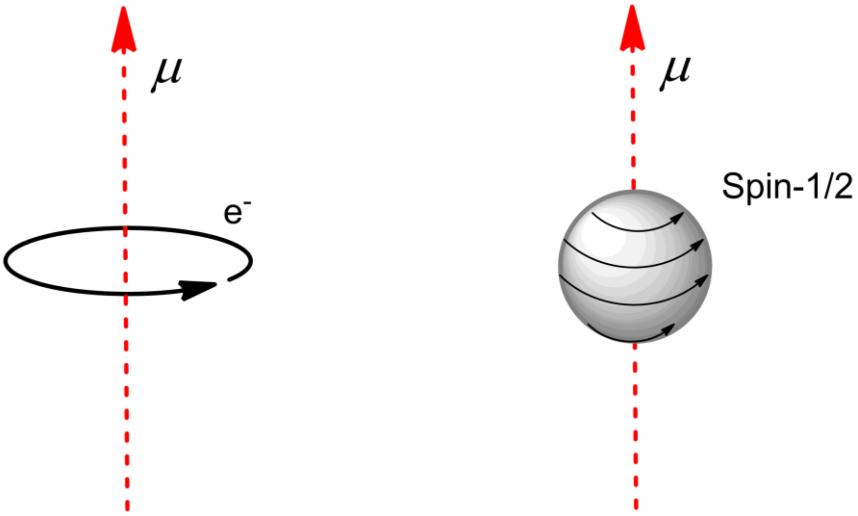

Figure 2.1 Analogy between electrons in a wire generating a magnetic moment and that of a spin-1/2 nucleus. The black arrows of the nucleus represent the movement of charge associated with the nucleus

The magnetic moment of a nucleus is given by:

$$\vec{\boldsymbol{\mu}} = \boldsymbol{\gamma\hbar I} \qquad \textbf{Eq. 2.1}$$

where, γ, is a constant of the nucleus called the *gyromagnetic ratio, $\hbar$,* is Planks constant divided by 2π and I is the spin quantum number of the nucleus. The spin angular momentum is related to the spin quantum number by:

$$\vec{\boldsymbol{I}}^{\mathbf{2}} = \left(\mathbf{I}(\mathbf{I}+\mathbf{1})\boldsymbol{\hbar}^{\mathbf{2}}\right) \qquad \textbf{Eq. 2.2}$$

Nuclei with a spin quantum number not equal to zero *i.e.* I = 1/2, 1, 3/2, 5/2... are NMR active. In the absence of an external magnetic field, all $2\mathrm{I}+1$ orientations of a spin have the same energy. However, if a strong external magnetic field is applied, $\vec{B}_0$, which is arbitrarily chosen to be along the z-axis, degeneracy is removed and the magnetic moment of a spin acquires the following energy:

$$\boldsymbol{E} = -\vec{\boldsymbol{\mu}} \cdot \vec{\boldsymbol{B}}_{\mathbf{0}} \qquad \textbf{Eq. 2.3}$$

As $\vec{B}_0$ is set along the z-axis, the vectors systems of $\vec{\mu}$ and $\vec{B}_0$ coincide to give:

$$\boldsymbol{E} = -\boldsymbol{\mu}_{\boldsymbol{z}} \cdot \boldsymbol{B}_{\mathbf{0}} = -\boldsymbol{m\hbar\gamma B}_{\mathbf{0}} \qquad \textbf{Eq. 2.4}$$

Where m is the magnetic quantum number which takes 2I + 1 values in integer steps between $+I$ and $-I$. This is known as the *Zeeman* interaction or *Zeeman* splitting. The selection rule is, $\Delta m = \pm 1$ and the difference between the two levels is;

$$\Delta\boldsymbol{E} = \boldsymbol{\hbar\gamma B}_{\mathbf{0}} \qquad \textbf{Eq. 2.5}$$

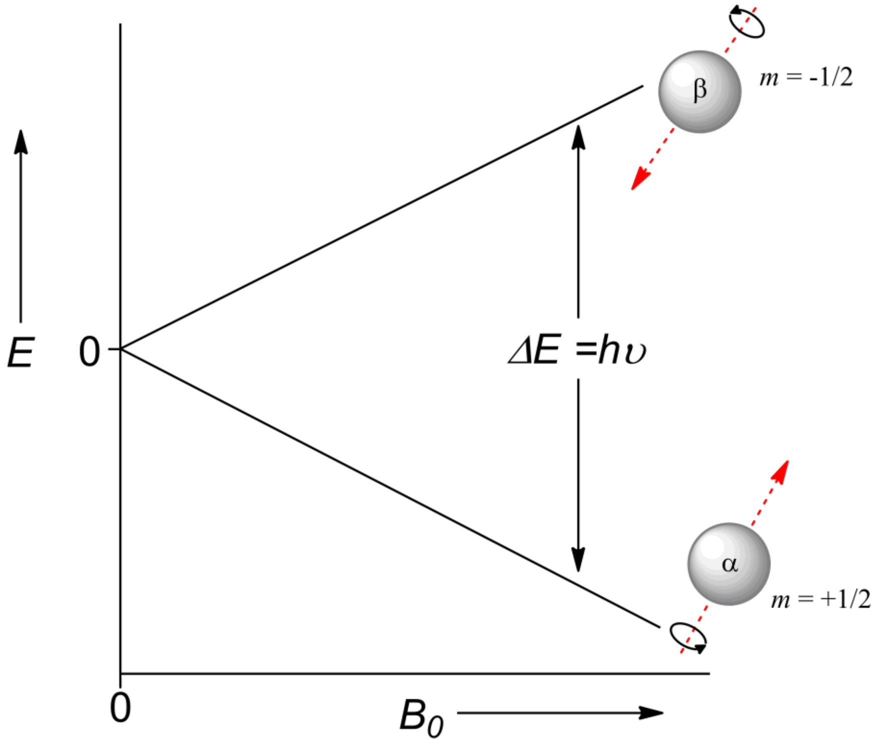

Figure 2.2 Relative energy of both magnetic spin states for a spin-1/2 nuclei as a function of increasing external magnetic field strength. The two states are also referred to as α or β

In the presence of an external magnetic field the nucleus experiences a torque due to its magnetic moment perpendicular to its direction causing it to rotate about an axis. The frequency of this motion is specific to each type of nucleus and is referred to as the nuclear Larmor frequency ω_0, see **Figure 2.3**.

$$\boldsymbol{\omega_0 = -\gamma B_0} \qquad \textbf{Eq. 2.6}$$

Therefore, if we apply **Eq 2.5** to a ^{1}H nucleus in a 9.7 Tesla (T) B_0 field whose γ= 267.5 rad T^{-1} s^{-1}, we obtain an energy difference between the α and β spin states of 2.74 x 10^{-25} J = 400 MHz. Therefore, excitation between the spin-states can be achieved using radiowaves (*rf* pulses) oscillating close to that of the Larmor frequency of the nucleus under consideration.

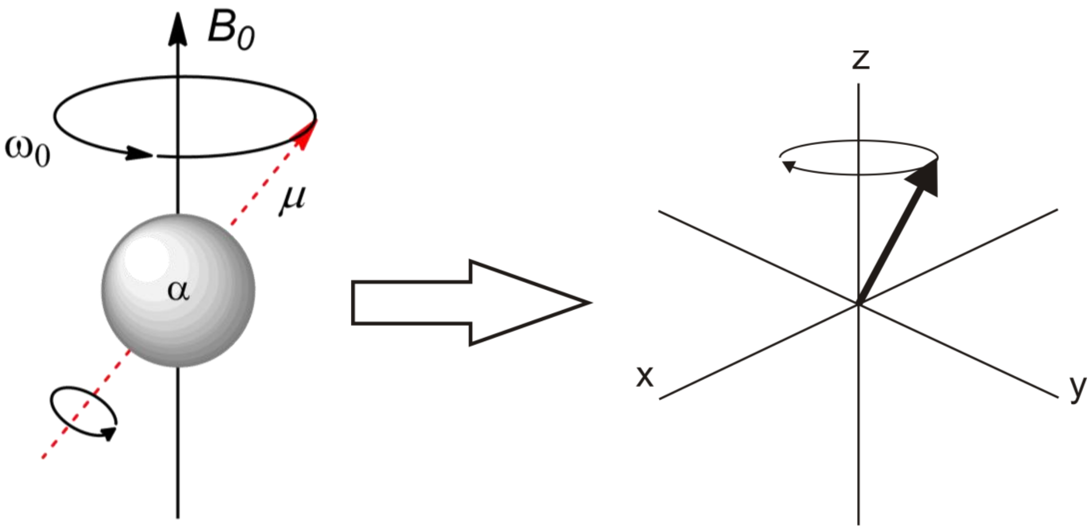

Figure 2.3 The torque experienced by a nucleus in a strong external field, rotating about an axis at its Lamor frequency. This is inferred into a coordinate systems where the arrow indicates the magnet moments spinning about like a gyroscope

2.3 Bulk Magnetisation

So far, we have only considered a single spin, but in reality we deal with a collection of spins within a sample. When an ensemble of spins are placed into an external magnetic field, the spin states will establish thermal equilibrium according to Boltzmann:

$$\frac{\boldsymbol{n}(+\frac{1}{2})}{\boldsymbol{n}(-\frac{1}{2})} = \mathbf{exp}\left(\frac{\Delta \boldsymbol{E}}{\boldsymbol{kT}}\right) \qquad \textbf{Eq. 2.7}$$

Where *n* is the population of a spin state, k, is Boltzmann's constant, T, is absolute temperature, and ΔE is the energy difference between the spin states. Using **Eq. 2.7** ($B_0 = 9.4$ T) we calculate that for every million spins, there are only about 50 more in the α state than the β spin state. This slight excess is added vectorially and results in a net vector along the +z direction. The sum of all the individual spins is called *bulk magnetization* ($\mathbf{M}_0$), and the boldface arrow pointing along the +z direction in the figure represents this (**Figure 2.4** and **Figure 2.6**). Because the spins are distributed randomly around the z-axis, there is no net *x* or *y*-magnetization; that is, $M_x = M_y = 0$, and hence, $\mathbf{M}_0 = M_z$ which is schematically shown in **Figure 2.4**.

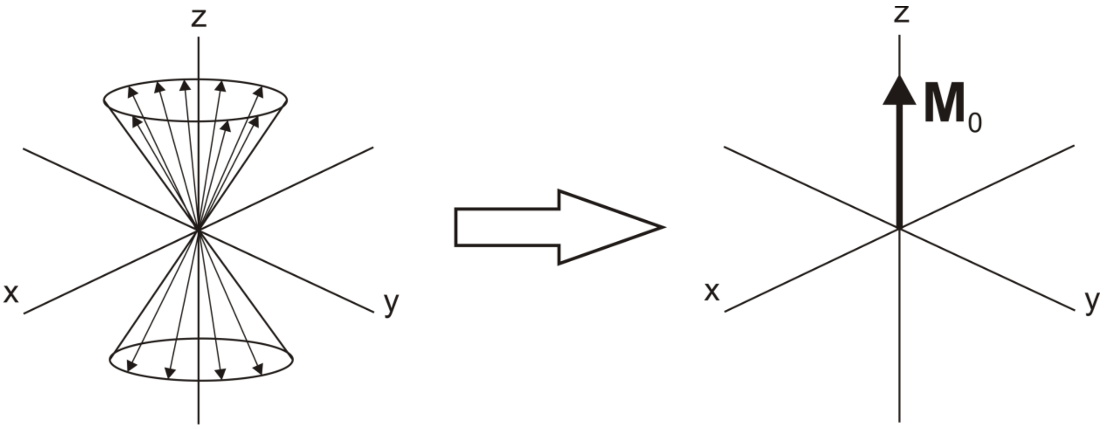

Figure 2.4 Vector model representing a collection of spin-1/2 nuclei precessing at $\boldsymbol{\omega_0}$. Summation of individual spins leads to a bulk magnetisation $\mathbf{M}_0$ aligned parallel to the external field, $\boldsymbol{B_0}$. This is known as the laboratory frame of reference whereby there is a slight excess of α spins.

This representation is referred to as the 'vector model' and is used to describe bulk $\mathbf{M}_0$ and is effective for describing simple pulse-acquire experiments.

2.4 The Rotating Frame of Reference

As mentioned previously, the energy difference between the α and β states is equal to the *rf*-range, therefore by applying an *rf*-pulse to the spins close to the Larmor frequency the energy difference can be satisfied. Similarly to all electromagnetic radiation, radiowaves have an associated time-dependent magnetic field. This field is designated as the B_1 field to distinguish it from the stronger, external B_0 field. The *rf*-pulse is transmitted *via* a coil surrounding the sample, in the transverse plane, perpendicular to the static field. To aid the visualisation of how this oscillating field operates on the bulk magnetisation vector, a simplified formalism, known as the rotating frame of reference, can be used. The oscillating B_1 field is considered to be composed of two counter-rotating magnetic vectors in the x–y plane (**Figure 2.5**):

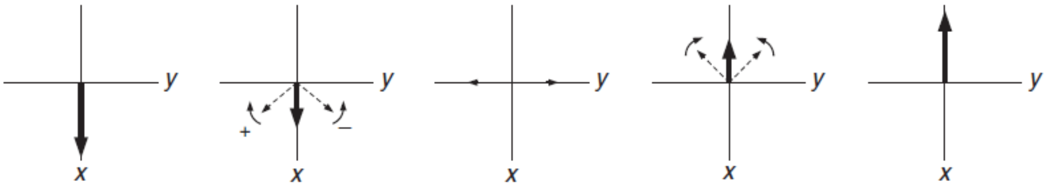

Figure 2.5 The *rf*-pulse provides an oscillating magnetic field along one axis (here the x axis), which is equivalent to two counter-rotating vectors in the transverse plane

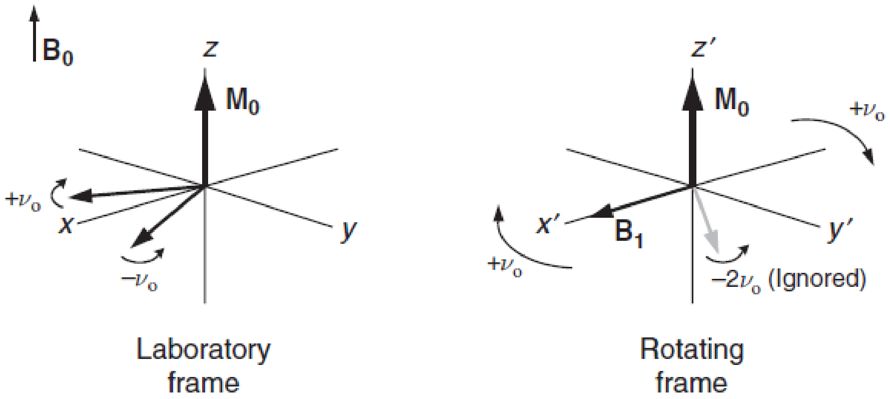

Figure 2.6 The laboratory and rotating frame representations

In **Figure 2.6**, the left represents the laboratory frame; the co-ordinate system (x,y,z) is viewed as being static, whereas in the rotating frame it rotates at a rate *equal* to the applied *rf* frequency, v_o. In this representation, the motion of one component of the applied *rf* is frozen whereas the other is rotating at twice the Lamor frequency and can be ignored. This provides a simplified model for the description of pulsed NMR experiments and removes the time dependency of the *rf*-field. The carousel analogy is often used in many NMR texts to explain the different frames, see **Figure 2.7**.

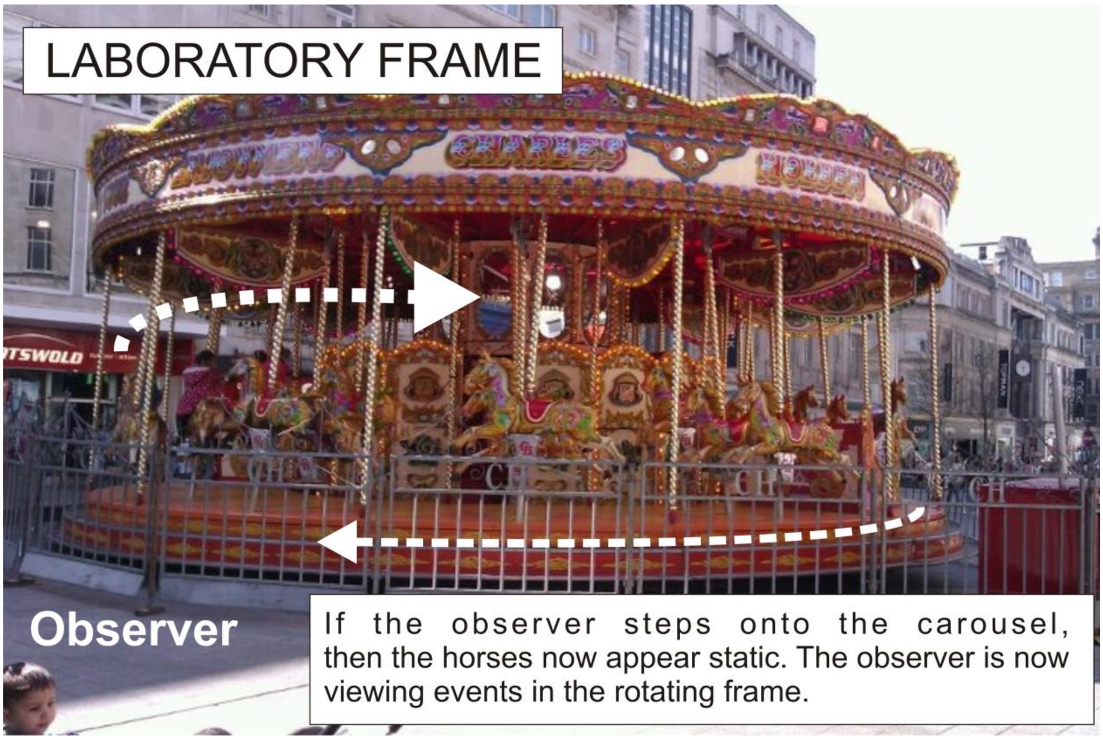
LABORATORY FRAME
Observer
If the observer steps onto the carousel, then the horses now appear static. The observer is now viewing events in the rotating frame.

Figure 2.7 A fairground carousel, Liverpool City Centre, is not just fun but can be used to view and explain the laboratory or the rotating frame of references.

2.5 Excitation and Detection

Once bulk magnetisation equilibrium has been established, the system is ready to be perturbed and acquisition of an NMR spectrum can occur. The of what happens when a 90° or a 180° pulse is applied to a collection of identical spins using both the vector model and quantum mechanically (i.e. spin-state) can now be considered:

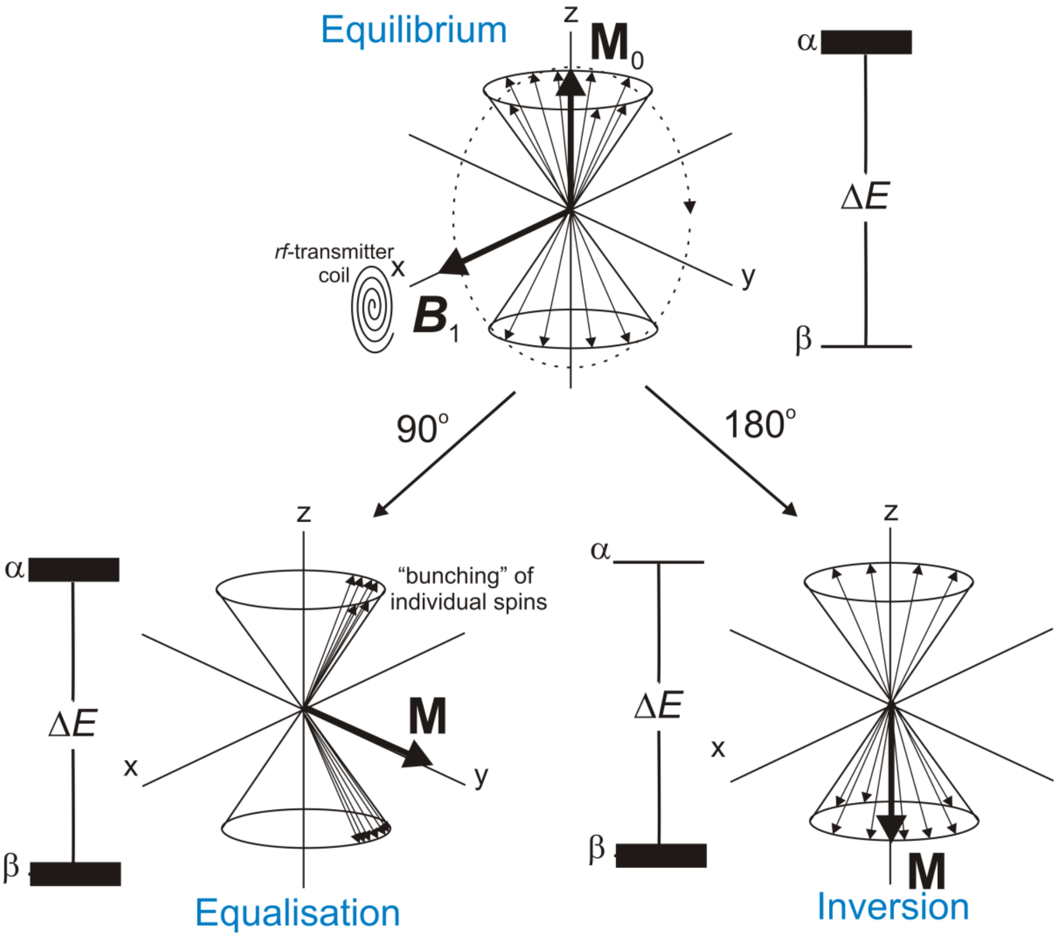
Equilibrium
z
M_0
α
ΔE
β
rf-transmitter coil
x
y
B_1
90°
180°
z
α
ΔE
β
"bunching" of individual spins
x
y
M
Equalisation
α
ΔE
β
z
x
y
M
Inversion

Figure 2.8 Excitation of a spin system and the subsequent tilt on the magnetisation vector into the xy-plane upon the application of $\boldsymbol{B}_1$

An *rf*-pulse is generated from a transmitter coil in the *xy* (transverse) plane. We choose the field, $\boldsymbol{B}_1$, to be "on resonance" i.e. to match the Larmor frequency of the spins. For a 90° +x pulse it causes a torque on the $\mathbf{M}_0$ vector in a direction that is perpendicular to the direction of the $\boldsymbol{B}_1$ field and is rotated from the +z axis toward the +y axis. Simultaneously, the populations of the α and β states are equalised, as there is now no net z-magnetisation but magnetisation “bunched” together in the xy-plane and we say that the system has “phase coherence.” Conversely, a 180° pulse inverts the α and β states so **M** is now aligned in the –z direction with no magnetisation in the xy-plane. In the above example, we applied a 90° +x pulse, however, we can apply pulses along any +x, +y, -y and –x axes resulting in different starting positions of the excited magnetisation vector. Applying a sequence of pulses of different phase angles is very important when devising pulse sequences and is central to phase cycling and coherence order selection. Following a 90° +x pulse, the bulk magnetisation vector simply remains static along the +y axis because events are being viewed in the rotating frame of reference. In reality, in the laboratory frame, magnetisation begins to precess about the xy-axis at its Larmor frequency:

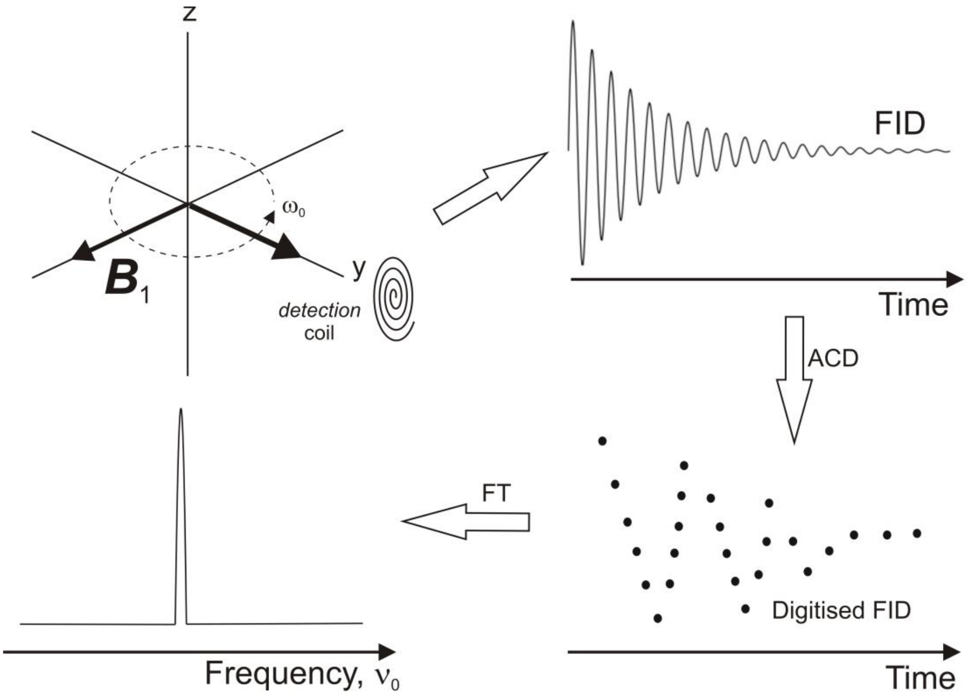

Figure 2.9 Representation of how an NMR signal is recorded

The rotating magnetic moment in the transverse plane gives rise to an oscillating magnetic field, which in turn induces an electric current in the detection coil, which also lies along the xy-plane. This weak electric signal oscillates and decays over time just like the transverse magnetization, and is called a Free Induction Decay (FID). The FID is amplified, digitized (ADC) and transformed to the frequency domain *via* a Fourier transformation (FT).

The resulting NMR spectrum is a plot of signal intensity as a function of frequency with a peak centered at the Larmor frequency.

2.6 Chemical Shift

NMR would be a rather limited technique if it were to observe just a single resonance for each type of nuclei or sample. In reality, multiple resonances are observed because the local magnetic field, B, experienced by a nucleus is dependent upon its chemical environment. This is due to the external field, B_0, which causes the electrons around a nucleus to circulate within their orbitals and induces motion that generates small magnetic fields, B'. The nucleus is shielded from the external field by its surrounding electrons. Therefore, the actual magnetic field experienced by a nucleus is given by:

$$\boldsymbol{B = B_0 - B' = B_0(1 - \sigma)} \qquad \textbf{Eq. 2.8}$$

Where, σ is a dimensionless quantity called the *shielding constant* (σ is usually positive, but can be negative). This interaction changes the resonance frequency of the nucleus thus giving rise to *chemical shift*, δ, the *shielding constant* is not used to calculate chemical shift, as absolute shifts are rarely needed and difficult to determine. Experimentally, the chemical shift is measured as difference in resonance frequencies between the nucleus in question (υ) and a reference nucleus (υ_{ref}), eg. (tetramethylsilane, TMS, for ^{1}H, ^{29}Si, and ^{13}C):

$$\boldsymbol{\delta = 10^6 \left(\frac{\upsilon - \upsilon_{ref}}{\upsilon_{ref}}\right)} \qquad \textbf{Eq. 2.9}$$

This gives the chemical shift in *parts per million (ppm).*

2.7 Relaxation

Once an *rf*-pulse has perturbed the system, magnetisation will seek to re-establish equilibrium *via* two relaxation pathways:

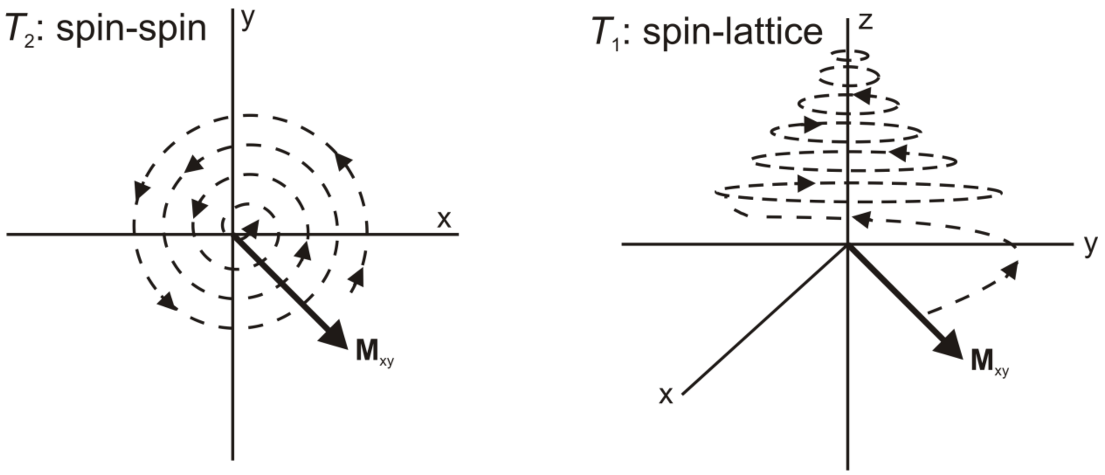

Figure 2.10 Following on from a 90° pulse, (left) looking down the z-axis at the decay of $\mathbf{M}_{xy}$ magnetisation through T_2 relaxation whilst (right) re-establishing $\mathbf{M}_0$, magnetization via T_1 relaxation.

The decay of $\mathbf{M}_{xy}$ occurs through spin-spin relaxation, T_2. The process is the mutual exchange of energy between the α and β states which causes a change in phase and a loss of coherence with no net change in energy *via* through space dipole-dipole interactions. Repetition of this process will randomise the phase, driving $\mathbf{M}_{xy}$ to zero and with it the NMR signal. Additionally, inhomogeneities in the $\boldsymbol{B}_0$ field will alter the magnetic field of nuclei causing them to precess at slightly different frequencies (fanning out), again with no net change in energy but a loss of phase coherence. As $\mathbf{M}_{xy}$ decays, $\mathbf{M}_0$ magnetisation begins to re-establish and a loss of energy from the spins is transferred into the surroundings in the form of heat, although the energies involved are so small that temperature changes in the bulk sample are undetectable. This is known as spin-lattice relaxation, whereby the lattice represents the environment around the target nucleus. The pathway for T_1 relaxation also involve dipole-dipole interactions and is strongly dependent upon molecular motion (other pathways include chemical shift anisotropy, quadrupolar relaxation and spin rotation, but will not be covered here as the main pathway relies on dipolar interactions).

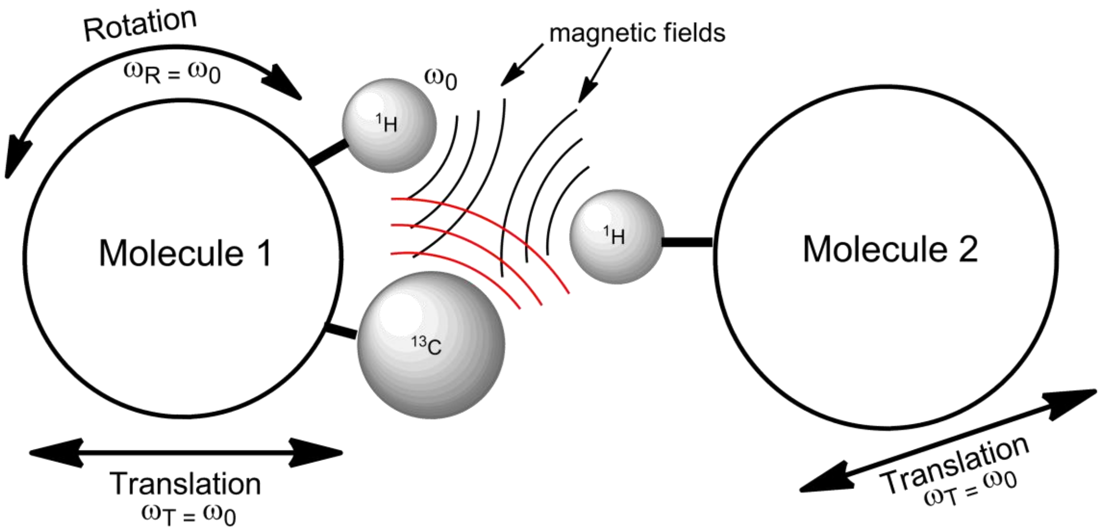
Rotation
ωR = ω0
magnetic fields
ω0
1H
Molecule 1
1H
Molecule 2
13C
Translation
ωT = ω0
Translation
ωT = ω0

Figure 2.11 Effect of motions of molecules on the dipolar interactions between spins allowing pathways for relaxation to occur

For example, in **Figure 2.11** we are interested in the relaxation of the ^{1}H nucleus in molecule 1. The lattice nuclei (being the ^{13}C and also the ^{1}H on molecule 2) are undergoing constant rotational and translation motion resulting in the oscillation of local magnetic fields (black and red lines). When the frequency of this motion is comparable to the Larmor frequency i.e. ($\omega_{R/}\omega_T = \omega_0$) for the ^{1}H nucleus, there can be mutual spin flips. However, since these nuclei are non-identical, there will be a net change in energy accompanying the exchange. These exchanges continue at a rate governed by T_1 until equilibrium is re-established.

2.7.1 *Assessing Molecular Mobility using Relaxation Measurements*[224-227]

Most dipole-dipole relaxation mechanisms rely on molecular movement by translation or rotation to modulate the magnetic fields in nearby molecules, as seen in **Figure 2.11**. This motion is assigned to a function $h(t)$ which can be associated with the fluctuation of the local magnetic fields and can be expressed in terms of an autocorrelation function, $G(t)$, defined as:

$$\boldsymbol{G(t)} = < h(\boldsymbol{t})\boldsymbol{h}(\boldsymbol{t} + \boldsymbol{\tau}) > \qquad \textbf{Eq. 2.10}$$

It reflects the degree to which the molecule reorients in a given time interval. If the motion is random (Brownian), the autocorrelation function is modelled as an exponential decay:

$$\boldsymbol{G(t)} = \mathbf{exp}\left(\frac{-\boldsymbol{t}}{\boldsymbol{\tau_c}}\right) \qquad \textbf{Eq. 2.11}$$

Where, τ_c, is the correlation time. The rotational correlation time is the time for a molecule to rotate 1 radian. Fourier transform of $G(t)$ into frequency domain yields *spectral density* $J(\omega)$ given by:

$$\boldsymbol{J_{(\omega)}} = \frac{\boldsymbol{\tau_c}}{\boldsymbol{1+\omega_0^2\tau^2}} \qquad \textbf{Eq. 2.12}$$

Where, ω, is the Larmor frequency of the target nucleus. The relationship between relaxation times and spectral densities was derived through time-dependent perturbation theory by Bloembergen, Purcell and Pound (BPP theory) and is represented graphically in **Figure 2.12 (a).** For a spin-½ nucleus, the relaxation rates are:

$$\frac{1}{T_1} = \frac{3\gamma^4\hbar^2}{10r^6}\left[\frac{\tau_c}{1+\omega_0^2\tau_c^2} + \frac{4\tau_c}{1+\omega_0^2\tau_c^2}\right] \qquad \textbf{Eq. 2.13}$$

$$\frac{1}{T_2} = \frac{3\gamma^4\hbar^2}{20r^6}\left[3\tau_c + \frac{5\tau_c}{1+\omega_0^2\tau_c^2} + \frac{2\tau_c}{1+4\omega_0^2\tau_c^2}\right] \qquad \textbf{Eq. 2.14}$$

$$\frac{1}{T_{1\rho}} = \frac{3\gamma^4\hbar^2}{20r^6}\left[\frac{3\tau_c}{1+4\omega_1^2\tau_c^2} + \frac{5\tau_c}{1+\omega_0^2\tau_c^2} + \frac{2\tau_c}{1+4\omega_0^2\tau_c^2}\right] \qquad \textbf{Eq. 2.15}$$

Where, γ is the nuclear gyromagnetic ratio, r is the internuclear separation between a spin pair, ω_0 is the nuclear Larmor frequency, ω_1 is the frequency of the *rf*-pulse and $\hbar$ is the reduced Plank's constant.

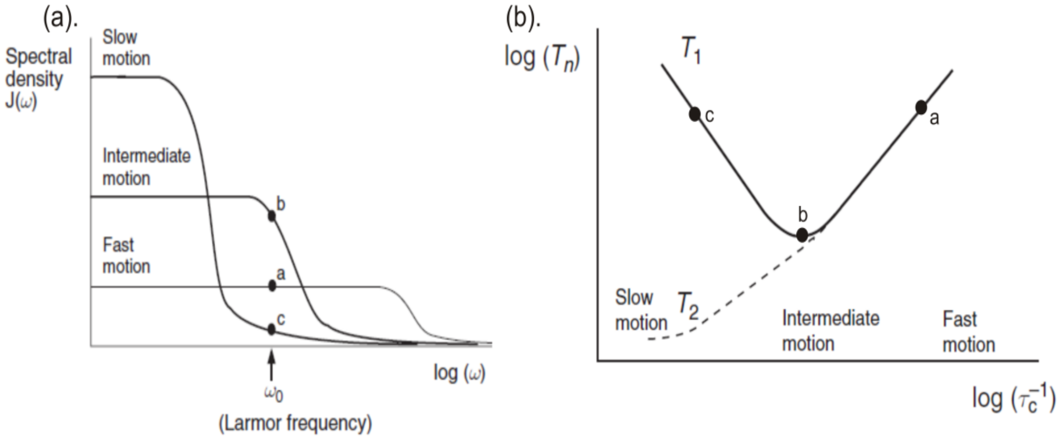

Figure 2.12 (a). Spectral density as a function of increasing frequency for molecules exhibiting fast, intermediate and slow motions. (b). The dependence of T_1 and T_2 on the rate of molecular tumbling.

For slowly tumbling molecules (τ_c long) $\omega_0^2\tau_c^2 >> 1$ a small fraction of spectral density at ω_0 is present. This results in long T_1 relaxation times which can be seen in Figure 2.12 (b). As molecular motion increases to the point at which $\omega_0^2\tau_c^2 \sim 1$, the largest fraction of spectral density is present at ω_0 in which efficient relaxation occurs as characterised by the T_1 dip i.e. short T_1 relaxation. As molecular motion increases further (fast motion, τ_c short) whereby $\omega_0^2\tau_c^2 << 1$ a small fraction of spectral density at ω_0 is present and results in long T_1 times. The case is more complex for T_2 relaxation; as molecular motion decreases (τ_c increases) the value of T_2 becomes smaller than T_1. This is the case for solids, whereby rotational and translational mobilities are restricted, resulting in T_1 in the order of seconds to minutes, with T_1>>T_2. Therefore, solid-state measurements of T_1 relaxation times can provide information on *fast* molecular dynamics that is on the order of MHz *i.e.* methyl rotations, water mobility. T_2 relaxation can probe *slower* motions (kHz) and is best suited to study surface interactions.

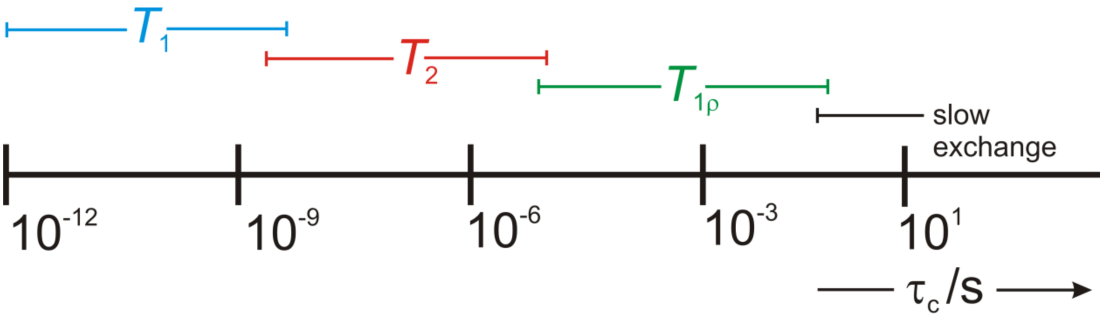

Figure 2.13 Relationship between correlation times and NMR relaxation methods to probe motions at different time scales

An alternative approach to investigate kHz motions in the solid-state is *via* spin-locking pulse sequences, and is called spin-lattice relaxation in the rotating frame, $T_{1\rho}$. It is dependent upon the spin-lock field (order of kHz) and therefore relies on motions which resonate at such frequencies, like cooperative polymer backbone motions. From **Figure 2.12 (b).** it is clear that a single relaxation time can be in any of the three $\omega_0^2\tau_c^2$ regimes. Therefore, it is important to find out where and in what motional regime the time belongs. This can be achieved by varying the strength of the external magnetic field which modulates the Larmor frequencies as to resonate with the motions in the sample. This can also be achieved by varying the temperature. This is because molecular motions are modulated by temperature and hence affect the τ_c. It is accepted that τ_c follows an Arrhenius type law, given by:

$$\boldsymbol{\tau_c = \tau_0 \exp\left(\frac{E_a}{RT}\right)} \qquad \textbf{Eq. 2.16}$$

Where, E_a, is the activation energy of molecular motions (in KJ mol^{-1}) R is the gas constant, T is 298K, and τ_0 is the correlation time constant (τ_0~ 10^{-13} s). In conclusion, measurements of T_1, T_2 and $T_{1\rho}$ relaxation times can provide information into motions at different time scales. Using the theory above, the methodology in place to achieve this is to first plot natural $T_{1/2}$ *vs* temperature to show in which motional regime the target nucleus is in. Secondly, a plot of In$T_{1/2}$ *vs* 10^3/Temperature (in Kelvin) yields a slope equal to $-E_a/RT$ which enables the extraction of the E_a for motional processes.

2.7.2 *Calculation of τ_c*

There appears to be no universally adopted methodology for calculating τ_c in the literature. For example, Andrews *et al.*[228] uses ^{1}H T_1 relaxation measurements between 80 to 350 K to study the methyl group in polycrystalline progesterone. From plots of natural T_1 vs 10^3 K they calculate an $E_a = 10.9 \pm 0.8$ kJ/mol^{-1} but then simply state that the intercept is equal to $\tau_0 = 2.3 \pm 0.2$ s^{-1} and do not mention τ_c. Whereas Taylor *et al.*[229] uses T_1 and $T_{1\rho}$ measurements to study the random hopping about the threefold axis of the –NH$_3$ group in glycine. Plots of In$T_1/T_{1\rho}$ *vs* 10^3/K show a minimum for both T_1 and $T_{1\rho}$ from which they take the correlation time, τ_c, to be equal to inverse of the Larmor frequency. Therefore, this suggests that only when a clear minimum is observed can τ_c be extracted.

2.7.3 *Spin Diffusion*[230-233]

Spin diffusion is defined as the transport of spin energy within the lattice by mutual energy conservative spin flips mediated by the dipolar interaction. It is often used to obtain information about spatial proximity of nuclei in solids. For example, in semi-crystalline polymers, crystalline phases show different T_1 and $T_{1\rho}$ relaxation compared to amorphous ones, so spin diffusion will be different in the different phases. This can also be used to estimate the lower and upper limit of domains sizes based on:

$$\boldsymbol{L = \sqrt{6Dt}} \qquad \textbf{Eq. 2.17}$$

where, L is the effective diffusion length, D is the spin diffusion coefficient and t the diffusion time. Therefore, if the average domain size in a polymer blend is smaller than *ca.* 1 nm, ^{1}H-^{1}H spin diffusion averages out T_1 and

$T_{1\rho}$ relaxation differences. In that case, all protons decay with the same effective T_1 and $T_{1\rho}$. In contrast, if the domain size is larger than *ca.* 50 nm, spin diffusion is too slow to average out such differences and the phases will decay each with their intrinsic T_1 and $T_{1\rho}$ times.

2.8 Solid-state NMR (SSNMR)

The development of NMR spectroscopy for solids has been much slower than that of liquids due to the different behavior of nuclear spin interactions. In the solution state these interactions are averaged to zero or reduced to the isotropic (orientation independent) values by rapid molecular motions. Conversely, in solids the reduction in molecular motion gives rise to anisotropic broadening (orientation dependent terms). However, it is possible to obtain high-resolution spectra that can routinely probe polymers, porous silicas, minerals and insoluble compounds *etc*. As mentioned, the broad solid-state resonances are primarily the result of interactions that are present (but rarely observed) in liquid-state NMR. The main broadening mechanisms, (in increasing order of spectral broadening) are chemical-shift anisotropy, heteronuclear and homonuclear dipole-dipole interactions and quadrupolar coupling. J-couplings are present in the solid-state but the interaction is so small in comparison to those above, that is can be ignored. The nuclear spin Hamiltonian for a powdered solid sample is given by:

$$\widehat{H}_{TOTAL=} + \widehat{H}_z + \widehat{H}_{CSA} + \widehat{H}_D + \widehat{H}_Q + \widehat{H}_J \qquad \textbf{Eq. 2.18}$$

The Hamiltonian of each interaction and how this leads to line broadening in solid-state NMR will be explained. The methodologies that are used to reduce or eliminate these interactions are also discussed.

2.8.1 *The Spin Hamiltonian*

Nuclei in a magnetic field experience many different types of interactions. Some are stronger than others but each interaction contains valuable structural or dynamic insight into a system. The interactions between a nuclear spin and a local magnetic field can be expressed as a tensor product using the general equation:

$$\hat{H} = \vec{I} \cdot \boldsymbol{A} \cdot \vec{B} \qquad \textbf{Eq. 2.19}$$

Where, $\hat{H}$ is the Hamiltonian operator which represents the energy in the system. The NMR interaction tensor, $\boldsymbol{A}$, describes the orientation of an NMR interaction with respect to the Cartesian axis system of the molecule. These tensors are represented by 3x3 matrices and can be diagonalised to yield tensors that have three principal components which describe the interaction in its own principal axis system (PAS):

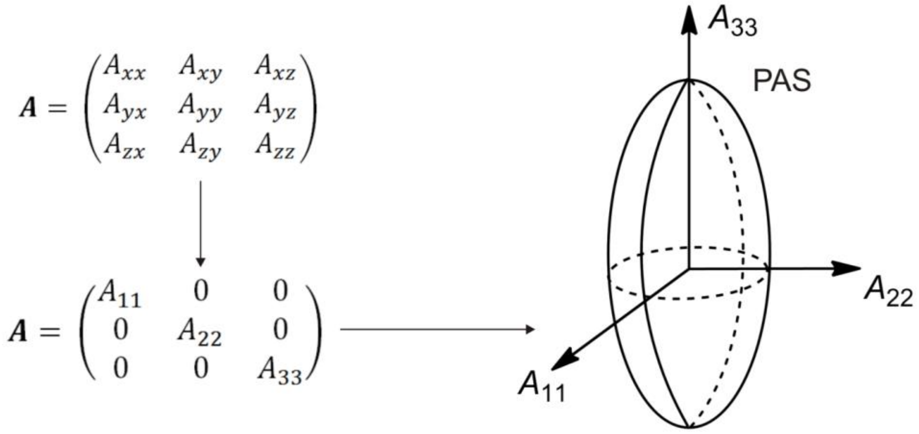

$$\boldsymbol{A} = \begin{pmatrix} A_{xx} & A_{xy} & A_{xz} \\ A_{yx} & A_{yy} & A_{yz} \\ A_{zx} & A_{zy} & A_{zz} \end{pmatrix}$$

$$\boldsymbol{A} = \begin{pmatrix} A_{11} & 0 & 0 \\ 0 & A_{22} & 0 \\ 0 & 0 & A_{33} \end{pmatrix}$$

Figure 2.14 3x3 matrix representing the NMR interaction tensor which is diagonalised to yield the interaction in its own PAS.

The Zeeman interaction is the strongest and far most important interaction in NMR. We can modify Eq. 2.19 and write the Zeeman Hamiltonian, $\hat{H}_z$, as:

$$\hat{\boldsymbol{H}}_{\boldsymbol{z}} = \vec{\boldsymbol{I}}\boldsymbol{Z}\overrightarrow{\boldsymbol{B}}_{\boldsymbol{0}} \qquad \textbf{Eq. 2.20}$$

All other interactions of the nucleus with its surroundings are several orders of magnitude smaller than the Zeeman splitting and can therefore be treated as perturbations of this interaction.

2.8.2 *Chemical Shift Anisotropy*

The orientation dependence of a molecule on the chemical shift in an external magnetic field is known as chemical shift anisotropy (CSA). The CSA is determined by the symmetry of electronic charge distribution around a nucleus. The CSA interaction increases linearly with the strength of the external magnetic field, given by the Hamiltonian:

$$\boldsymbol{\hat{H}_{CSA} = \vec{I}\sigma\vec{B}_0} \qquad \textbf{Eq. 2.21}$$

Where, $\boldsymbol{\sigma}$, is the chemical shielding tensor, which can be represented in the PAS frame:

$$\boldsymbol{\sigma} = \begin{pmatrix} \boldsymbol{\sigma_{11}} & \mathbf{0} & \mathbf{0} \\ \mathbf{0} & \boldsymbol{\sigma_{22}} & \mathbf{0} \\ \mathbf{0} & \mathbf{0} & \boldsymbol{\sigma_{33}} \end{pmatrix}$$

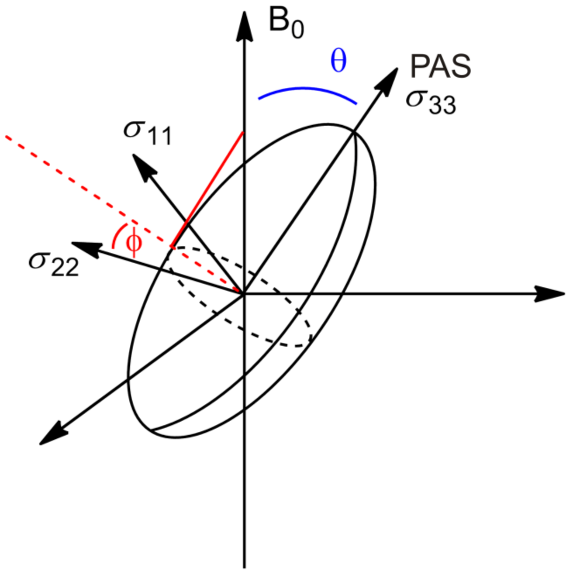

Figure 2.15 Matrix and graphical representation of the chemical shift tensor in PAS.

The angles θ and ϕ are the polar angles that define the orientation of the B_0 field in the PAS of the shielding tensor. The principle components of the chemical shielding tensor can be expressed as σ_{11}, σ_{22} and σ_{33} where σ_{11} is the least shielded and σ_{33} is the highest shielded. The average of the shielding tensor is known as the isotropic chemical shift, δ_{iso}, given by:

$$\boldsymbol{\delta_{iso} = (\sigma_{11} + \sigma_{33} + \sigma_{33})/3} \qquad \textbf{Eq. 2.22}$$

The anisotropic part of the shielding tensor (we will omit the full equation as it requires considerable deviation) contains a geometric term; $(3\cos^2\theta - 1)$. This term appears frequently when describing spin interactions and will be discussed in more detail in the next section. Line broadening occurs because in a powdered sample, all molecular orientations are present. Referring to **Figure 2.16**, all values of the polar angles are possible; each different molecular orientation has a different PAS with respect to the external field resulting in slightly different chemical shifts:

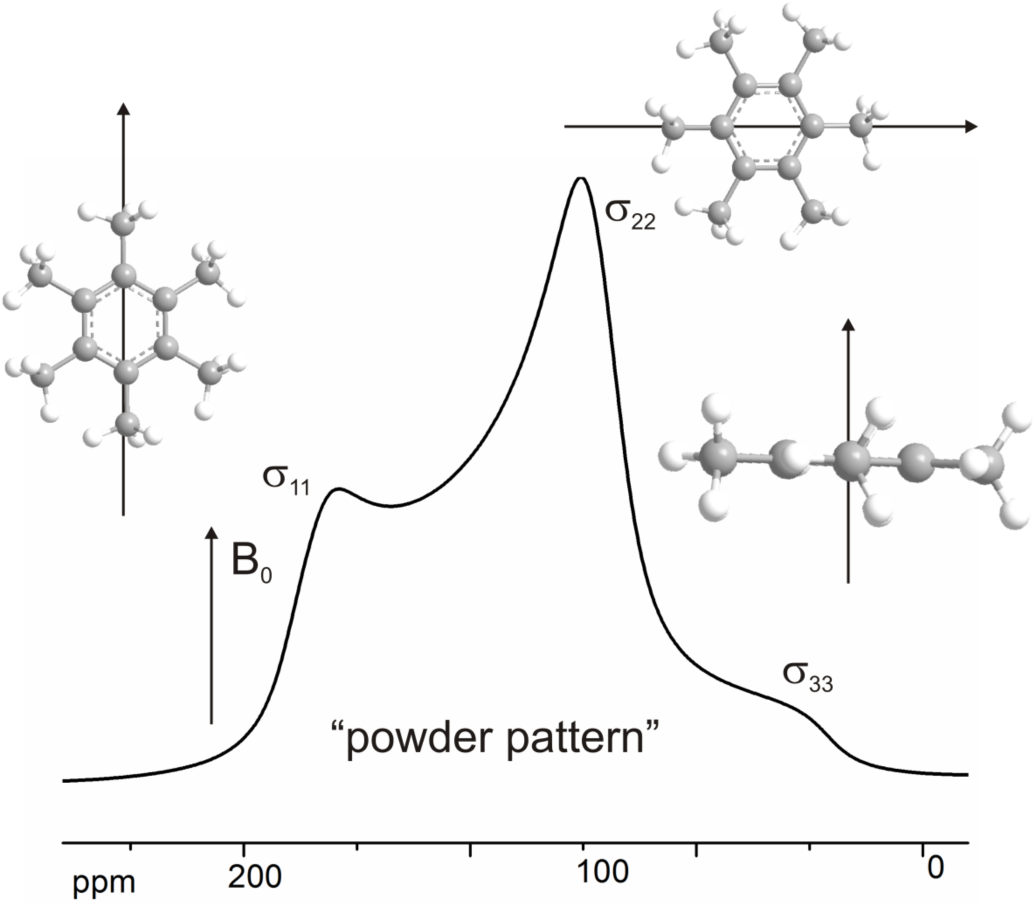

Figure 2.16 Static powder pattern of hexamethylbenzene resulting from all possible orientations from the methyl groups aligned with B_0 (σ_{11}) to the molecule lying perpendicular to the external field (σ_{33}).

The lineshape observed in **Figure 2.16**, is the sum of individual lines for all possible molecular orientations of hexamethylbenzene with a characteristic shape called a powder pattern.

2.8.3 *Dipole-dipole Coupling*

Dipole-dipole coupling is the through space interaction between the magnetic moments of the same (*homo*nuclear, *I-I*) or of dissimilar nuclei (*hetero*nuclear *I-S*). Classically, the energy of interaction between two magnet moments, $\vec{\mu}_1$ and $\vec{\mu}_2$ separated by a distance, *r*, is given by:

$$\boldsymbol{U} = \left\{\frac{\vec{\boldsymbol{\mu}}_1 \cdot \vec{\boldsymbol{\mu}}_2}{\boldsymbol{r}^3} - \mathbf{3}\,\frac{(\vec{\boldsymbol{\mu}}_1 \cdot \boldsymbol{r})(\vec{\boldsymbol{\mu}}_2 \cdot \boldsymbol{r})}{\boldsymbol{r}^5}\right\}\frac{\boldsymbol{\mu}_0}{4\boldsymbol{\pi}} \qquad \textbf{Eq. 2.23}$$

where, μ_0 is the permeability of free space. We can express this quantum mechanically by substitution of **Eq. 2.23** for two spins, $\vec{I}_1$ and $\vec{I}_2$ to give the Hamiltonian:

$$\widehat{\boldsymbol{H}}_D = \frac{\boldsymbol{\mu}_0}{4\boldsymbol{\pi}} \cdot \frac{\gamma_1\gamma_2\hbar^2}{\boldsymbol{r}^3}\left(\vec{\boldsymbol{I}}_1 \cdot \vec{\boldsymbol{I}}_2\,\frac{3(\vec{\boldsymbol{I}}_1 \cdot \vec{\boldsymbol{r}})(\vec{\boldsymbol{I}}_2 \cdot \vec{\boldsymbol{r}})}{\boldsymbol{r}^2}\right) \qquad \textbf{Eq. 2.24}$$

In the literature this equation is expanded and rearranged, to obtain the dipolar "alphabet" given as:

$$\widehat{\boldsymbol{H}}_D = \frac{\boldsymbol{\mu}_0}{4\boldsymbol{\pi}} \cdot \frac{\gamma_1\gamma_2\hbar^2}{\boldsymbol{r}^3}[\boldsymbol{A} + \boldsymbol{B} + \boldsymbol{C} + \boldsymbol{D} + \boldsymbol{E} + \boldsymbol{F}] \qquad \textbf{Eq. 2.25}$$

Terms A and B are only important for this discussion; the Hamiltonians of these terms are:

$$\boldsymbol{A} = \hat{\boldsymbol{I}}_{1z}\hat{\boldsymbol{I}}_{2z}(\mathbf{3}\cos^2\boldsymbol{\theta} - \mathbf{1}) \qquad \textbf{Eq. 2.26}$$

$$\boldsymbol{B} = -\frac{\mathbf{1}}{\mathbf{4}}\left[\hat{\boldsymbol{I}}_{1+}\hat{\boldsymbol{I}}_{2-} + \hat{\boldsymbol{I}}_{1-}\hat{\boldsymbol{I}}_{2+}\right](\mathbf{3}\cos^2\boldsymbol{\theta} - \mathbf{1}) \qquad \textbf{Eq. 2.27}$$

Where, $\hat{I}_{1+}\hat{I}_{2-} \rightarrow \hat{I}_{1-}\hat{I}_{2+}$ represent raising and lowering operators of the two spins. Raising operator increases the angular momentum of a spin causing the flipping of a spin from the "down" to "up" orientation. Simultaneously, the lowering operator decreases the angular momentum causing a spin flip from "up" to "down". Hence term B is called the "flip-flop" operator and is an energy conserving process. If the spins are of different elements, then the B-term in the dipolar Hamiltonian vanishes. Hence, we obtain the homonuclear and heteronuclear Hamiltonians given by:

Homonuclear Dipolar Hamiltonian for a set of like spins; $\hat{I}_{i,j}$*:*

$$\hat{\boldsymbol{H}}_{\boldsymbol{D}}^{\boldsymbol{II}} = \frac{\boldsymbol{\mu_0}}{\boldsymbol{4\pi}} \sum_{i,j} \frac{1}{2}\frac{\gamma_I^2\hbar^2}{r^3}\left[2\hat{\boldsymbol{I}}_{iz}\hat{\boldsymbol{I}}_{jz} - \frac{1}{2}\left[\hat{\boldsymbol{I}}_{1+}\hat{\boldsymbol{I}}_{2-} + \hat{\boldsymbol{I}}_{1-}\hat{\boldsymbol{I}}_{2+}\right]\right]\left(3\cos^2\boldsymbol{\theta}_{ij} - 1\right) \qquad \textbf{Eq. 2.28}$$

Heteronuclear Dipolar Hamiltonian for a set of different spins; $\hat{I}$ and $\hat{S}$*:*

$$\hat{H}_D^{IS} = \frac{\mu_0}{8\pi} \sum_{i,j} \frac{1}{2}\frac{\gamma_I^2\hbar^2}{r^3} 2\hat{I}_z\hat{S}_z\left(3\cos^2\theta_{IS} - 1\right) \qquad \textbf{Eq. 2.29}$$

What do these equations actually mean, how do they relate to common nuclei like ^{1}H and ^{13}C and what is the effect on the resulting NMR spectra? To answer these questions we can break down the $\hat{H}_D^{II}$ and schematically describe each term:

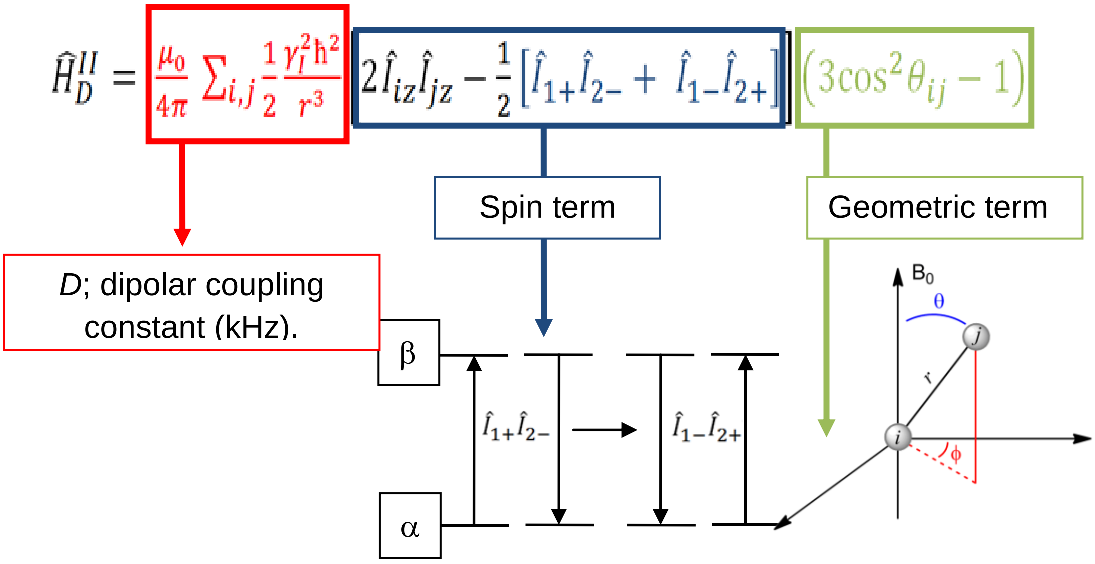
$\hat{H}_D^{II} = \frac{\mu_0}{4\pi}\sum_{i,j}\frac{1}{2}\frac{\gamma_I^2\hbar^2}{r^3}$
$2\hat{I}_{iz}\hat{I}_{jz} - \frac{1}{2}[\hat{I}_{1+}\hat{I}_{2-} + \hat{I}_{1-}\hat{I}_{2+}]$
$(3\cos^2\theta_{ij} - 1)$
Spin term
Geometric term
D; dipolar coupling constant (kHz).
β
α
$\hat{I}_{1+}\hat{I}_{2-}$
$\hat{I}_{1-}\hat{I}_{2+}$
B$_0$
θ
j
r
i
ϕ

Figure 2.17 Breaking down the homonuclear Hamiltonian into three parts.

The red term is dependent upon the gyromagnetic ratio and inverse cube of the distance between the *i* and *j* spins. The blue term is concerned with the "flip-flop" transitions, or more commonly known as spin diffusion that depends upon the abundance of the spin. The green term corresponds to the orientation dependence of a spin pair; which we have already come across in the CSA interaction. This term is dependent upon the angles of θ and ϕ specifying the orientation of *i-j* internuclear vector with respect to B_0. The heteronuclear Hamiltonian also has a similar form but the spin term is reduced.

Table 2.1 Properties of ^{1}H and ^{13}C nuclei

Nucleus	**Spin**	**Abundance**	$\boldsymbol{\gamma / (rad.\ s^{-1}\ T^{-1})}$
^{1}H	½	99%	267:522 x 10^6
^{13}C	½	1.1%	67.283 x 10^6

The natural abundance and γ values for ^{1}H and ^{13}C nuclei are given in **Table 2.1**. If we relate these parameters to **Eq. 2.28** we can see that because of the ^{1}H's high abundance and high γ value strong homonuclear couplings are present. Conversely ^{13}C exhibits very weak homonuclear couplings because the chances of two ^{13}C nuclei being close together are remote and the nucleus also has a reduced γ value *c.f.* ^{1}H. Therefore, (generally) the spectra for ^{1}H are much broader than for ^{13}C nuclei. These couplings also manifest in a spectrum as a doublet pattern called the "Pake Doublet":

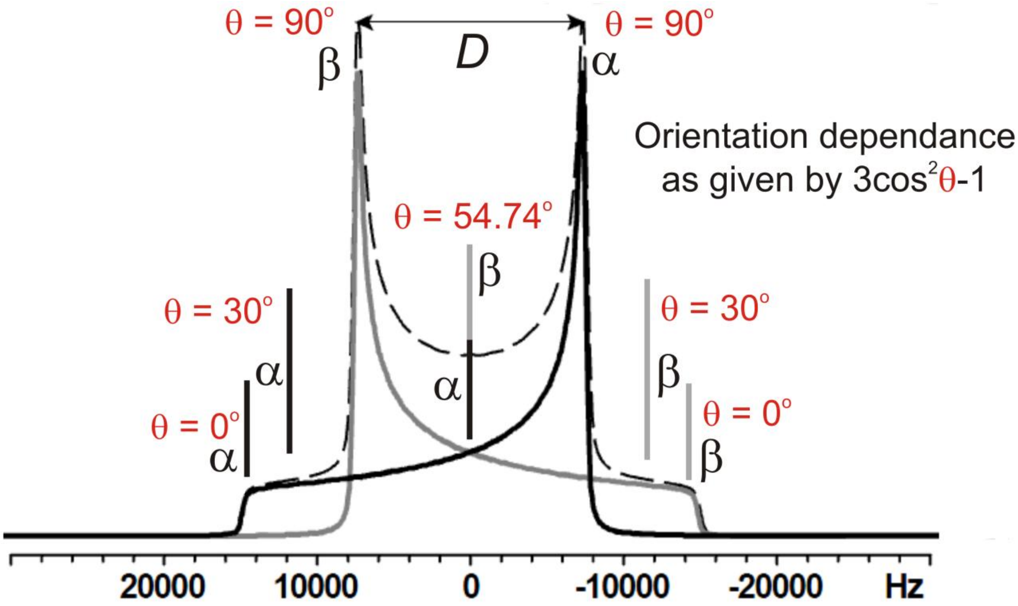

Figure 2.18 Schematic powder pattern of two coupled spin-½ nuclei

This pattern, first seen for the ^{1}H spectrum of Gypsum, $CaSO_4 \cdot 2H_2O$ was discovered by Pake. It is composed of two subspectra arising from the α and β spin states with orientations of the molecule lying at 0 to 90°. The splitting of the "horns" is equal to the dipolar coupling constant, *D*, in kHz. Notice how the two states converge when θ = 54.74°, this angle is referred to as the magic-angle and, as will be shown, can effectively reduce if not totally remove the geometric interaction.

2.8.4 *Magic Angle Spinning (MAS)*

Andrew *et al.*[234] first proposed that the geometric term, $3\cos^2\theta - 1$, present in the CSA, homonuclear and heteronuclear Hamiltonians could be exploited mechanically. If the sample is spun at an angle of 54.74° with respect to the applied magnetic field B_0, the term $3\cos^2\theta - 1 = 0$, removing the orientation dependence and artificially creating a "solution-like state".

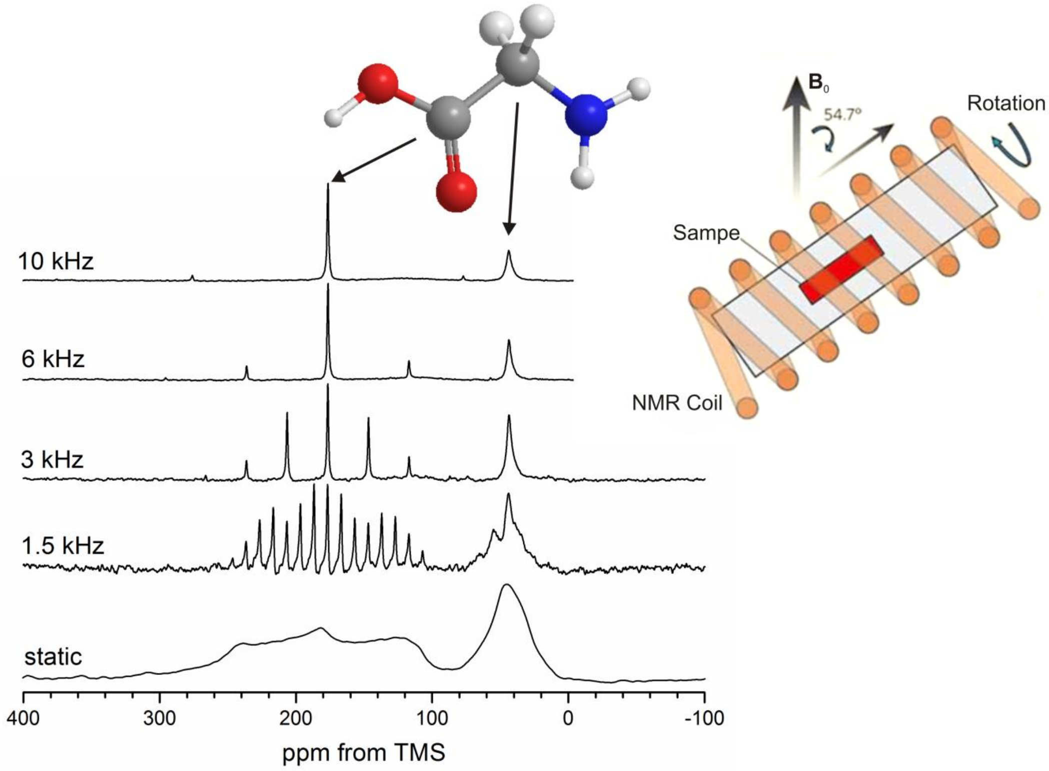

Figure 2.19 $^{13}C\{^{1}H\}$ NMR spectra of glycine powder sample at static and varying MAS rates. To the right of the figure, schematic showing a sample packed into a rotor inclined at the magic angle within the NMR coil.

The rate of spinning must be at a frequency higher than the strength of the interaction which we are trying to remove (at least 3 or 4 times). For example, **Figure 2.19**, shows the effect of increasing MAS rate on the ^{13}C spectra of glycine. Without spinning (static), a broad, featureless pattern is observed resulting from CSA and heteronuclear couplings. As MAS rate increases the broadening is reduced however a set of spinning side bands manifest as a manifold which is separated by the spinning speed. Above 3 kHz, it becomes clear which resonances correspond to the CO and C_{α} carbons within glycine. At 10 kHz, the side bands have almost been removed and a well resolved spectrum of glycine is afforded. Generally, the CSA interaction can be fully removed by slow spinning. However, heteronuclear and homonuclear interactions require higher spinning rates for complete averaging. Although it is possible to spin at 80 kHz[235] ^{1}H-^{1}H interactions can still dominate a spectrum.

2.8.5 *Decoupling Sequences*

Haeberlen and Waugh[236] first introduced the concept that dipole-dipole coupling effects could also be averaged in spin space using multiple *r.f.* pulses. One of the first heteronuclear dipolar decoupling schemes uses a continuous radio-frequency wave (CW)[237] to rotate the proton nuclear spins between their spin-up and spin-down states averaging the ^{1}H to X nucleus interaction to zero. An alternative scheme is Two Phase Pulse Modulation (TPPM) which uses two high-power pulses differing in phase by 10 to 70°.[238, 239] Homonuclear dipolar decoupling schemes are more complicated as there is an additional spin term in the Hamiltonian, **Eq. 2.28**. There have been at least fourteen decoupling sequences proposed and each is detailed and grouped in a review by Subhradip *et al.*[240] The most common sequences are based on Lee-Goldburg (LG)[241] or the (decoupling using mind boggling optimisation) DUMBO[242] schemes. In the simplest LG sequence, an *r.f.* pulse is set to be off-resonance given by:

$$\boldsymbol{\Delta\omega = \omega_1 tan(\theta_m)} \qquad \textbf{Eq. 2.30}$$

where, $\Delta\omega$, ω_1 and θ_m represent the off-resonance value, *r.f.* amplitude and the magic angle respectively. The duration of the pulse creates a rotation of 360° for the resonant spins around the effective axis averaging part of the homonuclear interaction see **Figure 2.20 (a).**

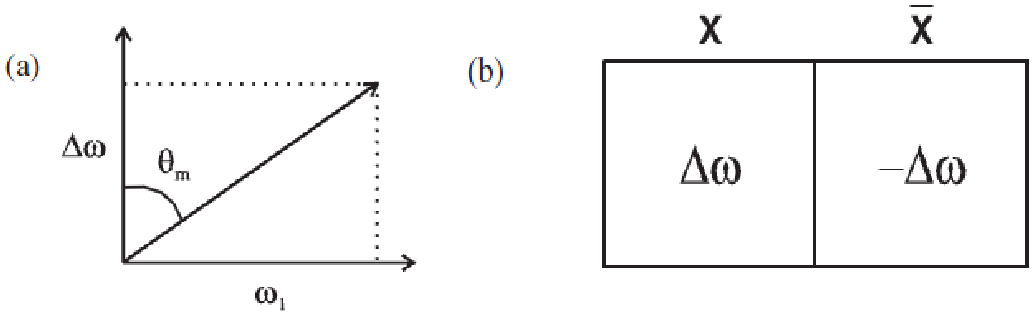

Figure 2.20 LG irradiation. The amplitude ($\boldsymbol{\omega_1}$) and the offset ($\boldsymbol{\Delta\omega = \omega_1\sqrt{2}}$) of the *r.f.* pulse result in creating an effective field that coincides with the magic angle, which averages parts of homonuclear interaction (b). Pulse sequence of FSLG.[243]

This LG sequence only averages some parts of the homonuclear interaction. The sequence was subsequently adapted by switching the offset between $\Delta\omega$ and $-\Delta\omega$ and simultaneously changing the phase of the *r.f.* pulse by 180°, see **Figure 2.20 (b).** This is known Frequency-Switched Lee-Goldburg (FSLG)[243]. Later sequences use a series of on-resonance pulses with discreet phases called Phase-Modulated Lee-Goldburg (PMLG).[244] DUMBO is also a phase modulated sequence. These sequences are recorded under MAS as 2D NMR spectra ("windowed") but can be made "windowless" that is they can be collected as simple 1D experiments[245] and are called combined rotation and pulse sequences (CRAMPS). The main drawback of homonuclear pulse sequences is that as the MAS rate increases, the cycle time of the *r.f.* pulses get closer to the rotor period and the benefit of high-order averaging of the homonuclear interaction diminishes. According to Gan *et al.*[246] as the spinning frequency reaches 65 kHz there is just enough room to fit in certain pulse sequences before interference between the two regimes causes severe resonant broadening. To date, both PMLG and DUMBO have been implemented at 65 kHz and both give comparable resolution[247]:

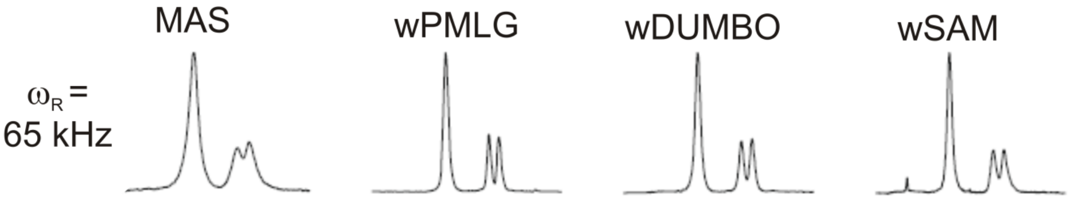

Figure 2.21 Proton spectra of glycine acquired at an MAS rate of 65 kHz with different decoupling schemes. wSAM is a symmetry based scheme.[248] Adapted from Lekes *et al.*[247]

The problem is compounded for disordered materials whereby strong homonuclear couplings and distributions of chemical shifts dominate a spectrum using even the most advanced NMR experiments. The future of SSNMR will undoubtedly be researching new pulse based schemes that afford resolution when MAS rates exceed 65 kHz.

2.8.6 *Cross-polarisation*

Dilute spins, (^{13}C, ^{29}Si), *etc.* have small γ values, low natural abundances and therefore long T_1 times, giving rise to poor signal-to-noise and weak NMR resonances[221, 249]. In order to improve the signal-to-noise ratio for these nuclei, either isotopic enrichment or long experimental times are required, with the former being extremely expensive with the latter often impracticable. These problems can be circumvented by using cross-polarization (CP) introduced by Pines *et al*[250]. In this technique, magnetisation from abundant spins, *I*, such as ^{1}H or ^{19}F, is transferred to dilute spins, *S*, such as ^{13}C or ^{29}Si. Therefore, CP enhances the signal-to-noise ratio of low abundant nuclei and shortens experimental times. This is achieved by applying two spin-locking fields, B_1^I, and B_1^S to both spins simultaneously, along the direction of the magnetization of spin *I*[251]. The spin locking powers on both channels must meet the Hartmann–Hahn condition[252]:

$$\boldsymbol{\gamma_I B_1^I = \gamma_S B_1^S} \qquad \textbf{Eq. 2.31}$$

Once this is achieved a doubly rotating frame is generated whereby the *I* and *S* nuclei precessess in the rotating frame at the same rate *i.e.* the energy gaps become equal irrespective of their Zeeman splitting energies of the laboratory frame. The magnetization is now transferred in the rotating frame *via* heteronuclear dipolar interactions between the *I* and *S* spins. The locking fields are switched off, the FID is recorded of on the *S*-channel with heteronuclear decoupling on the *I*-channel. The main drawback of CP is that it is not quantitative,[253] this is explained in more detail in **Chapter 4**.

2.9 Quadrupolar Coupling[254-258]

75% of NMR active nuclei are quadrupolar and can be characterised by the spin quantum number, I = >½. For example, ^{7}Li, ^{11}B, ^{23}Na, ^{39}K (I = 3/2), ^{17}O, ^{25}Mg, ^{27}Al (I = 5/2), ^{51}V, ^{59}Co (I = 7/2) and ^{93}Nb (I = 9/2). In addition to a magnetic moment (similar to their spin-1/2 counterparts) they also possess an asymmetric charge distribution of nucleons giving rise to a non-spherical electric charge distribution:

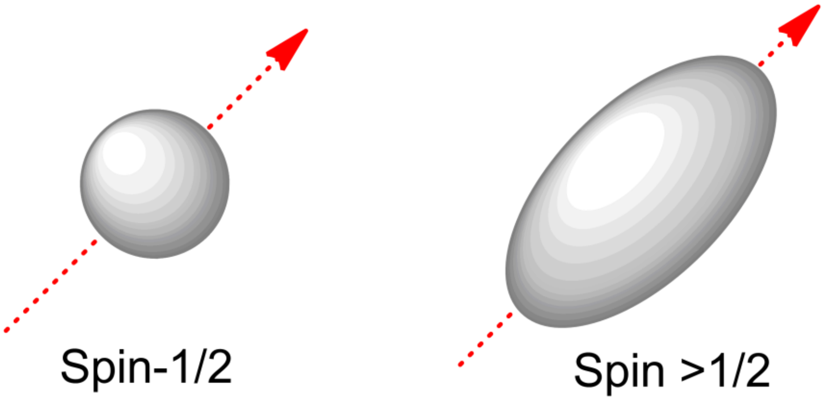

Figure 2.22 Schematic representation of the difference between spherical and non-spherical charge distribution (grey) for a spin-1/2 and quadrupolar nucleus.

This asymmetric charge distribution is described by the *nuclear electric quadrupole moment, eQ* and is an intrinsic property of the nucleus. *eQ* can interact with *electric field gradients*, EFGs, which arise from particular distributions of electrons and other nuclei around the nucleus in question, present in most solids:

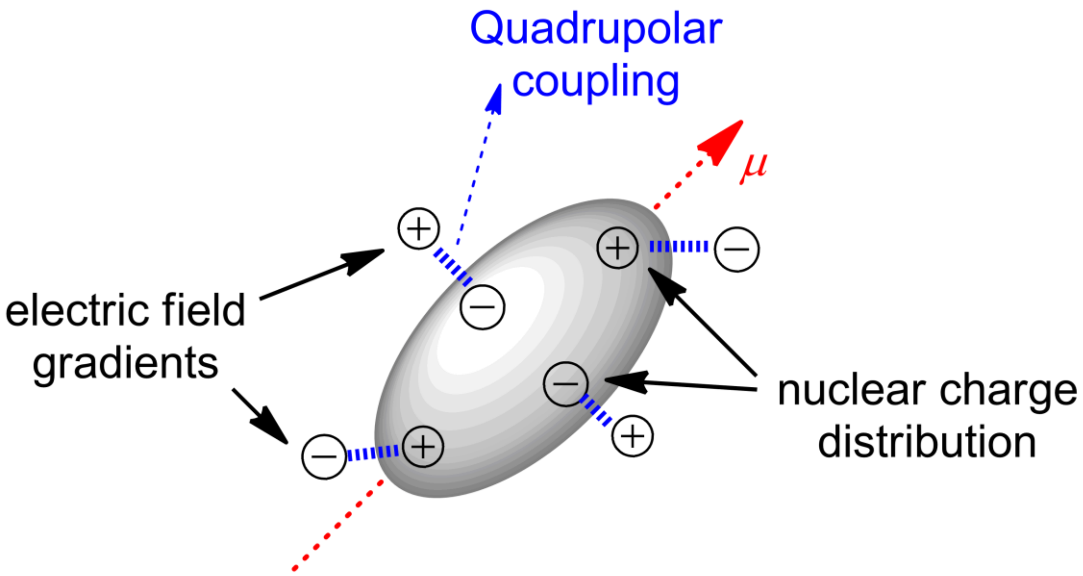

Figure 2.23 Schematic representing the quadrupolar coupling interaction between the asymmetric charge distribution and electric field gradients (represented by positive and negative signs) present in neighbouring atoms or molecules

The nuclear electric quadrupole moment/electric field gradient interaction is called the *quadrupolar coupling interaction*; it can be rather large, causing powder patterns of several MHz. The size of the interaction depends on the size of eQ (constant) and the symmetry of the EFG, which is determined by the molecular and electronic structure around the nucleus. To explain quadrupolar coupling effects on the NMR spectrum, we must define and dissect the Hamiltonian, which takes the general form:

$$\hat{H}_Q = \underbrace{\boxed{\frac{v_Q}{3}}}_{\text{Magnitude of the interaction}} \sum_{k=-2}^{2} (-1)^k \underbrace{\boxed{V_{-q}^{(2)}}}_{\text{Spatial tensor (geometric)}} \underbrace{\boxed{T_{-q}^{(2)}}}_{\text{Spin tensor}}$$

$$v_Q = \underbrace{\frac{3e^2qQ}{2I(2I-1)\hbar}}_{\text{Magnitude in radians/s}} = \underbrace{2\pi\frac{3Q_{cc}}{2I(2I-1)}}_{\text{Magnitude in Hz}}$$

Figure 2.24 General form of the quadrupolar Hamiltonian

At first glance the Hamiltonian looks dissimilar to those describing the CSA or dipolar interactions; however, it simply takes on more terms with different notations, where:

1. v_Q and Q_{cc} denote the quadrupolar frequency and the quadrupolar coupling constant expressed in radians/s or hertz respectively. These terms describe the magnitude of the interaction
2. $V_{-q}^{(2)}$ is the geometric or spatial tensor of the EFG. For now, it can be represented in the PAS. The subscript "-*q*" gives the coefficients of the tensor:

$$\boldsymbol{V_0^{(2)}} = \sqrt{\frac{3}{2}}\ \boldsymbol{V_1^{(2)}} = \ \mathbf{0}\ \boldsymbol{V_2^{(2)}} = \frac{\mathbf{1}}{\mathbf{2}}\boldsymbol{\eta} \qquad \textbf{Eq. 2.32}$$

   where, η is the asymmetry parameters and characterises the EFG around the nucleus. It can adopt values from 0 to 1.
3. Finally, the $T_{2,k}$ is the spin tensor with *K* representing a series of coefficients, which will be detailed later.

Now that we have defined the terms, the quadrupolar Hamiltonian can be treated as a perturbation to the Zeeman field, given by:

$$\widehat{H}_Q = \widehat{H}_Q^1 + \widehat{H}_Q^2$$

$$\widehat{H}_Q^1 = \frac{v_Q}{3} T_0^{(2)} V_0^{(2)} = \frac{hv'_Q}{6} [3I_z^2 - I(I+1)$$

$$\widehat{H}_Q^2 = \frac{hv_Q^2}{9v_0} \left\{ 2I_z \left[2I_z^2 - I(I+1) + \frac{1}{4} \right] V_{-1}^{(2)} V_1^{(2)} + I_z \left[I_z^2 - I(I+1) + \frac{1}{2} \right] V_{-2}^{(2)} V_2^{(2)} \right\} \quad \textbf{Eq. 2.33}$$

The effects of first and second order perturbations on the Zeeman splitting and how this affects an NMR spectrum are shown below in **Figure 2.25**. Using $2\mathrm{I} + 1$ rule, a spin-3/2 nucleus can adopted four spin states; -3/2, -1/2, +1,2 and +3/2. The energy levels between ǀ-3/2↔1/2ǀ and ǀ+1/2↔+3/2ǀ are known as satellite transitions, whereas the ǀ-1/2↔+1/2ǀ energy level is known as the central transition. Under Zeeman splitting these levels are degenerate separated by a frequency, v_0. The first-order quadrupolar interaction affects only the satellite transitions:

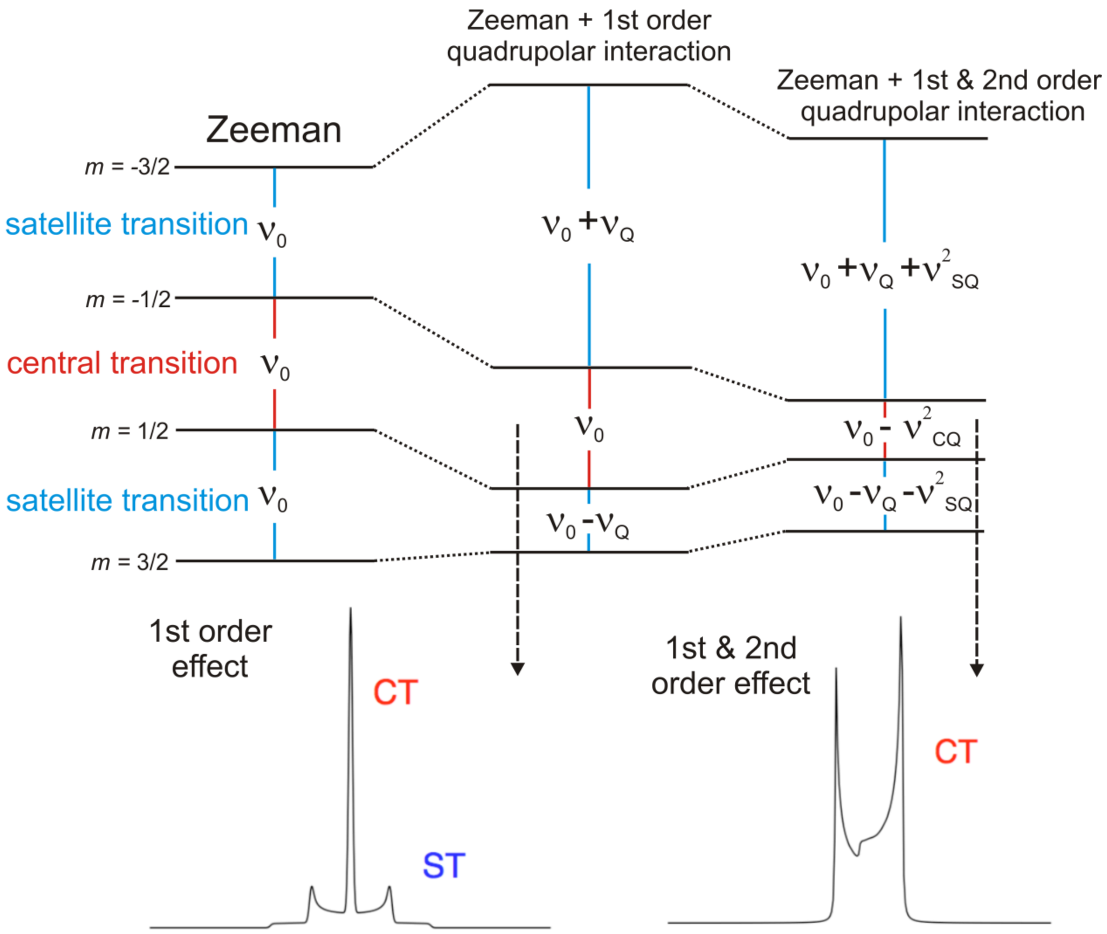
Zeeman
Zeeman + 1st order quadrupolar interaction
Zeeman + 1st & 2nd order quadrupolar interaction
m = -3/2
m = -1/2
m = 1/2
m = 3/2
satellite transition ν0
central transition ν0
satellite transition ν0
ν0 +νQ
ν0
ν0 -νQ
ν0 +νQ +ν²SQ
ν0 - ν²CQ
ν0 -νQ -ν²SQ
1st order effect
CT
ST
1st & 2nd order effect
CT

Figure 2.25 Top: Energy levels of a spin-3/2 *i.e.* in the presence of Zeeman field, first-order and second-order quadrupolar interactions. Bottom: Simulated NMR spectra for a spin-3/2 nucleus under first and second order quadrupolar interactions

The result is that we see three transitions in the NMR spectrum corresponding to the CT and ST. The frequency of the CT is unaffected by first-order perturbation. (First-order effects are more pronounced for integer spins where the observable satellite transitions are broadened extensively (up to several MHz), making their detection difficult). We are more concerned with second-order effects; in **Figure 2.25** both the ST and the CT energy levels are shifted and the resulting NMR spectrum is distorted and broad. The CT provides information on the chemical environment of the nucleus *i.e.* the isotropic chemical shift, δ_{iso}, quadrupole coupling constant, Q_{CC}, and the asymmetry of the quadrupolar interaction tensor, η. Therefore in order to determine these parameters accurately one must implement techniques to reduce or eliminate 2nd order effects on the central transition.

2.9.1 *Frame Transformations*

In **Figure 2.24**, The spatial tensor, $V_{-q}^{(2)}$, in the general form of $\widehat{H}_Q$ is represented in its PAS. However, in **Eq. 2.33**, it is given under MAS conditions i.e. in the ROTOR frame relative to the LAB frame. In order to represent the quadrupolar interaction, it requires two consecutive transformations:

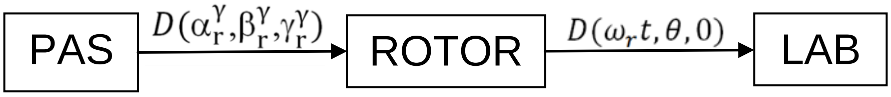

Figure 2.26 Schematic representing frame transformations using "Wigner matrix elements;" $D(\alpha,\beta,\gamma)$.

The angles, (α,β,γ), (Euler angles) describe the location of the rotor axis in the PAS of the quadrupolar tensor. Only when we are in the ROTOR frame the transformation into the LAB frame is performed using another Wigner matrix, where, $\omega_r t$ is the phase angle experienced by the rotor while spinning at a frequency, ω_r and θ is the rotor axis with respect to the external field. Note: these transformations do not result in the PAS coinciding with either the ROTOR or LAB frames but describe them relative to each other.

Under MAS the spatial part of the second order Hamiltonian becomes a sum of Legendre polynomials with ranks 0, 2 and 4 and we can write for an *m* to *m*’ transition:

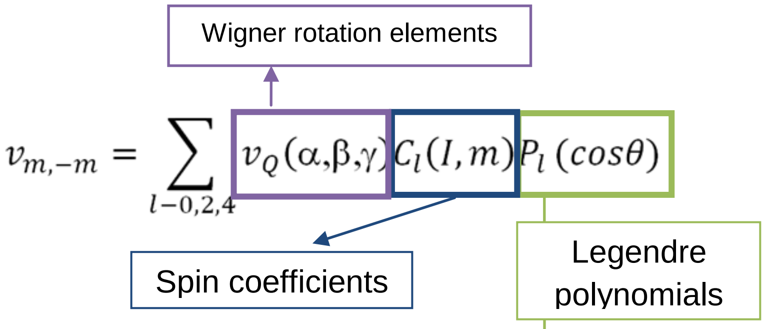

$$v_{m,-m} = \sum_{l-0,2,4} \boxed{v_Q(\alpha,\beta,\gamma)}\boxed{C_l(I,m)}\boxed{P_l\,(cos\theta)}$$

$$C_0(I,m) = 2m[I(I+1) - 3m^2]$$
$$C_2(I,m) = 2m[8I(I+1) - 12m^2 - 3]$$
$$C_4(I,m) = 2m[18I(I+1) - 34m^2 - 5]$$

$$P_0 = (cos\theta) = 1$$
$$P_2 = (cos\theta) = \frac{1}{2}(3cos^2\theta - 1)$$
$$P_4 = (cos\theta) = \frac{1}{8}(35cos^4\theta - 30cos^2\theta + 3)$$

Figure 2.27 Break down of the frequency between two m to m’ transitions including the spin and geometric (Legendre polynomials) terms

From the equation above in **Figure 2.27**, we can calculate the transition frequency between any m to m’ level like those depicted in **Figure 2.25** for a spin-3/2. The breakdown of this equation is important because it gives clues as to how we can eliminate (in the case of geometric terms) and change (in the case of the spin coefficients) these terms in order to reduce spectral broadening.

2.9.2 *Methodologies to reduce the quadrupolar interaction*

2.9.2.1 High B_0

The second-order quadrupolar coupling is inversely dependent upon the external field, $1/B_0$. Therefore by increasing the strength of the external field greater resolution can be achieved.[259]

2.9.2.2 Magic Angle Spinning:

The Legendre polynomials are plotted as a function of θ, the angle between the rotor axis and the external field:

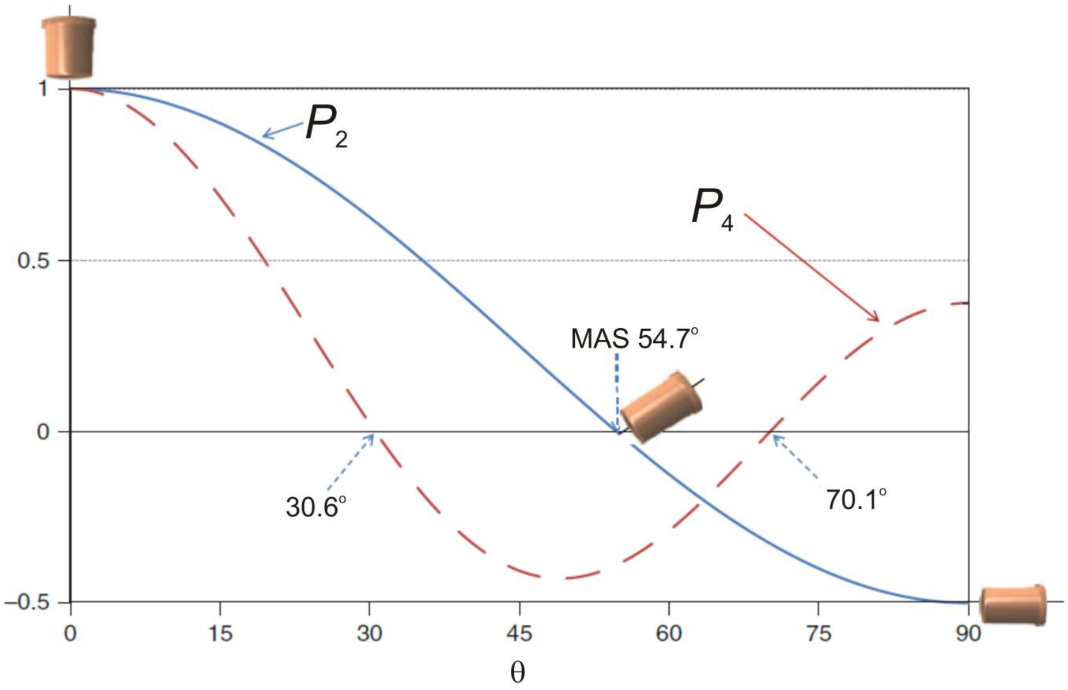

Figure 2.28 The values of second-order P_2 and fourth-order P_4 Legendre polynomials as functions of rotor axis, θ. Adapted from Fernandez *et al.*[255]

As shown in **Figure 2.28**, the Legendre polynomials indicate the complexity of the geometric terms for quadrupolar nuclei. The P_0 term is isotropic and therefore is independent of orientation. The P_2 term cancels when $\theta = 54.7^\circ$. The P_4 term cancels when $\theta = 30.6$ or 70.1°. However, the two polynomials do not have a common root, *i.e.* the anisotropic terms in the second-order quadrupolar Hamiltonian cannot both be cancelled at once, regardless of the orientation of the rotor axis. Therefore, even under very fast MAS a broad powder pattern will still exist.

2.9.2.3 Double Rotation (DOR) and Dynamic Angle Spinning (DAS)

In double rotation (DOR) NMR, the sample is spun inside a small inner rotor inclined at either 30.6 or 70.1° which is itself spun about the magic angle in a larger outer rotor. The combination of the two rotors acts to average out the second and fourth rank polynomials in the second-order interaction.[260, 261] DOR yields high-resolution ('solution-like') spectra for quadrupolar nuclei in one dimension from a simple "pulse-acquire" experiment. The main limitations with DOR are that the probe heads are usually expensive and spinning rates are slow because of the large size of the outer rotor. This generally leads to a large number of spinning sidebands which can overlap with other resonances.[262] Although Perras *et al.*[263] have recently presented DOR-TOSS (Total Suppression of Spinning Side Bands) sequence which can eliminate the unwanted side band manifold. The DAS experiment works by spinning separately about two angles and is preformed as a 2D experiment.[264, 265] According to Ashbrook and Duer[256], it can be a tedious experiment to implement because (1) no pair of spinning angles includes the magic angle. Thus, the effects of dipolar coupling and chemical shift anisotropy remain in the two dimensional spectrum (2). spinning angles need to be changed during the experiment which is technically difficult as it must be performed in a time that is short compared with the T_1 time for the observed spins. Quadrupolar nuclei can have short relaxation times and can limit this type of experiment. MAS, DOR and DAS are mechanical averaging techniques acting on the geometric/spatial tensor. The spin coefficients can also be manipulated under MAS to yield high resolution NMR spectra and was realised in 1995 by Frydman.[266]

2.9.2.4 Multiple Quantum MAS (MQMAS)[267-271]

MQMAS is a 2D experiment that affords resolution of the central transition by using both spin and spatial averaging techniques. The experiment can be conducted on most MAS probe heads and is relatively straightforward to implement.

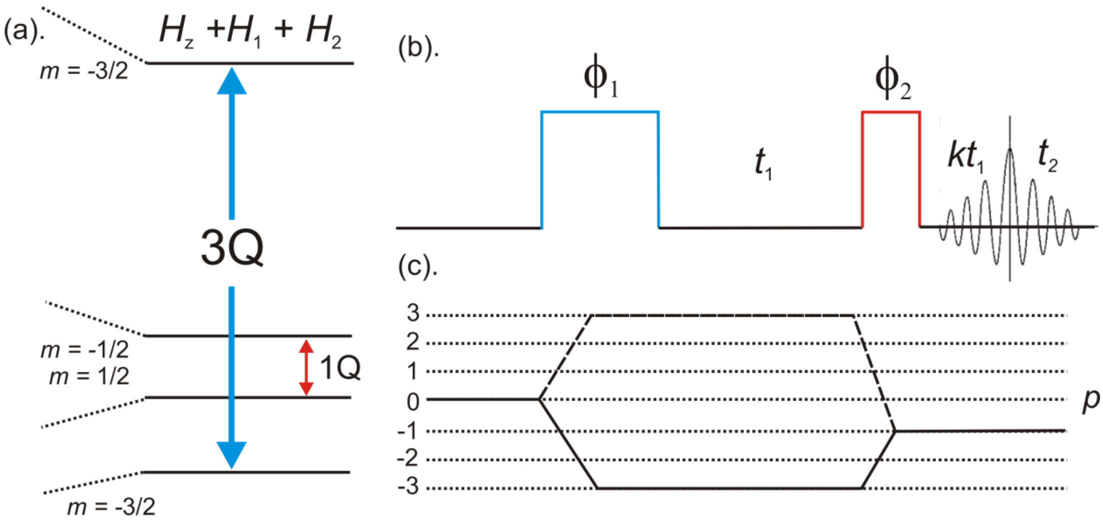

Figure 2.29 (a). Energy level diagram for spin-3/2 nucleus. (b). Pulse sequence (c). coherence transfer pathways diagram for a basic 3QMAS experiment. Blue and red boxes, ϕ_1, ϕ_2, indicate the selective and hard pulses to excite triple quantum (3Q) and transfer this into single quantum (1Q) coherences respectively. Recall that the selection rule for NMR is *m* ±1, therefore we can only directly observe the 1Q coherence Phase cycling ensures that we detect the *p* = 0 to -3 to -1 pathway.[267]

Firstly, the l-3/2↔3/2l energy level, 3Q coherence, is excited using a selective pulse, ϕ_1. The frequency of this transition can be written, under MAS, from the equation in **Figure 2.27** as:

$$\Delta v_{3Q} = -v_Q\{(C_0P_0) + (C_2P_2) + (C_4P_4)\} \qquad \textbf{Eq. 2.34}$$

Under MAS, the second rank term (C_2P_2) in **Eq. 2.34** vanishes and during the first evolution period, t_1, the coherences evolves under the zero (C_0P_0) and fourth-rank (C_4P_4) terms. At the end of t_1, 3Q coherence is transferred into the l-1/2↔1/2l energy level i.e. 1Q coherence. We can write the frequency of the central transition as:

$$\Delta \boldsymbol{v}_{\boldsymbol{1Q}} = -\boldsymbol{v}_{\boldsymbol{Q}}(\mathbf{3} - \mathbf{4}\boldsymbol{I}(\boldsymbol{I} + \mathbf{1})\left\{\left(\frac{\mathbf{1}}{\mathbf{2}}\boldsymbol{P}_{\mathbf{0}}\right) + (\mathbf{4}\boldsymbol{P}_{\mathbf{2}}) + (\mathbf{9}\boldsymbol{P}_{\mathbf{4}})\right\} \qquad \textbf{Eq. 2.35}$$

Again, the second-rank term is averaged under MAS leaving the evolution of 1Q coherence under the zero and fourth rank-terms. 1Q coherence is allowed to evolve for a time, kt_1, where k is equal to the ratio of the fourth-rank terms in both the 3Q and 1Q frequencies, given by (C_4 term is expanded to make it clearer)

$$\boldsymbol{k} = \mathbf{4}\boldsymbol{m}\left(\frac{\mathbf{18}\boldsymbol{I}(\boldsymbol{I}+\mathbf{1}) - \mathbf{34}\boldsymbol{m}^{\mathbf{2}} - \mathbf{5}}{\mathbf{9}(\mathbf{3} - \mathbf{4}\boldsymbol{I}(\boldsymbol{I}+\mathbf{1}))}\right) \qquad \textbf{Eq. 2.36}$$

Therefore, k for a spin-3/2 nuclei = 7/9 and is known as the MQMAS ratio. When k = 7/9, (the ratio can be positive or negative and depends on which coherence pathway we want to select[267]) the evolution of the 3Q coherence under fourth rank-terms is undone or refocused by the evolution of the 1Q coherence under its fourth rank-term and occurs at the end of kt_1. At the end of time $t_1 + kt_1$ the net evolution of the remaining 1Q coherence is governed only by the zero term i.e. the isotropic quadrupolar terms (The isotropic term is identical for every crystalline orientation in the powder hence we do not have to mechanically spin at two angles!) and is then recorded as an FID in the t_2 period. A double Fourier transformation of the time domains signals; t_1 and t_2 into their respective frequency domains, f_1 and f_2 produces an NMR spectrum.

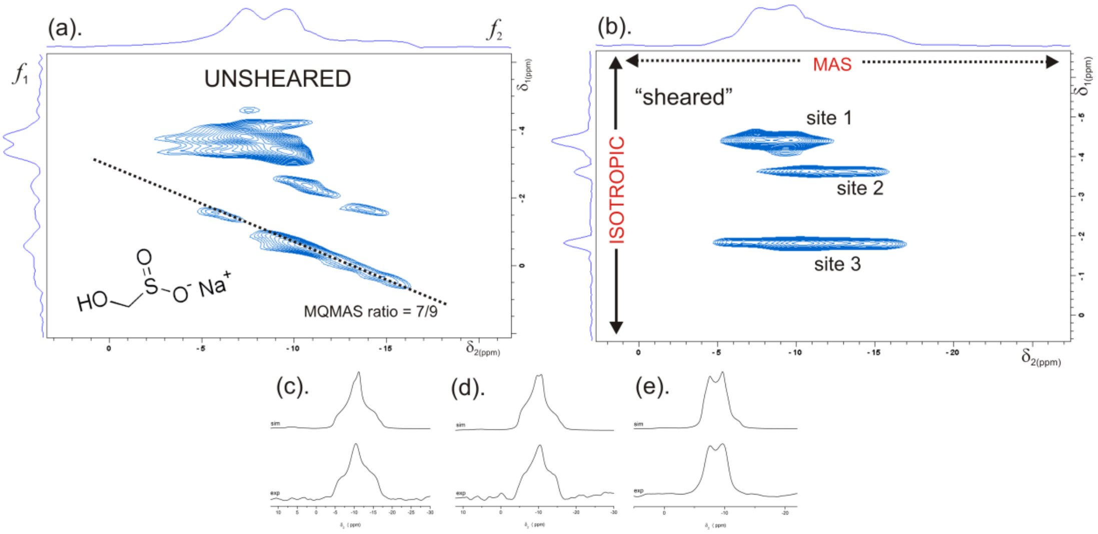

Figure 2.30 (a). ^{23}Na MQMAS unsheared spectrum (b). ^{23}Na MQMAS spectrum with shearing (c). to (e). extracted line shapes from $\boldsymbol{f_2}$ dimension with simulated spectra giving the quadrupolar parameters for each sodium site

For example, **Figure 2.30 (a).** shows the ^{23}Na MQMAS NMR spectrum of Rongalite ($HOCH_2SO_2^{-+}Na$) which has three distinct sodium environments.[272] The resulting NMR projection lies at a ridge governed by the MQMAS ratio. It is still not clear as to how many sites are present as the spectrum requires a shearing transformation (a phase correction) to ensure isotropic line shapes, **Figure 2.30 (b).** Once sheared, the f_1 side corresponds to the isotropic dimension whilst f_2 is the MAS (anisotropic) dimension. Extraction of sites from the MAS dimension can be simulated using dmfit[273] or TopSpin to give the δ_{iso}, Q_{CC} and η quadrupolar parameters; **Figure 2.30 (c) to (e).** These parameters give insight into the local atomic environment and symmetry of the nucleus in question. The main limitation of the MQMAS experiment is that site populations are not quantitative as the intensities (area) depends on the ability to excite and convert 3Q coherence into 1Q coherence, which, in turn, is dependent upon the strength of the quadrupolar interaction:

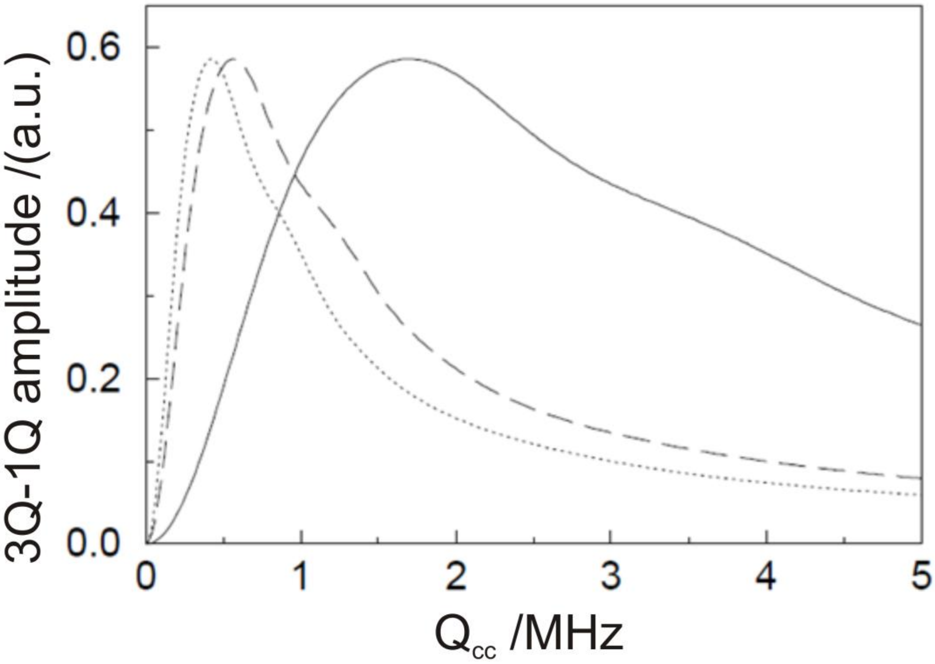

Figure 2.31 The dependence of the 3Q to 1Q conversion (selecting the p = –3 to p = –1 pathway), of the spin I = 3/2 central transition amplitude on the quadrupolar coupling constant, $\boldsymbol{C_Q}$, is the same as $\boldsymbol{Q_{cc}}$, where the pulse, $\boldsymbol{\omega_1/2\pi}$, power is equal to 300 kHz (solid line), 100 kHz (dashed line), and 75 kHz (dotted line). In each case, the flip angles of the on-resonance excitation and reconversion pulses were 240° and 60°, respectively. Reproduced from S. Brown's PhD thesis.[274]

Clearly, we can see from **Figure 2.31** that as the quadrupolar interaction increases there is a decrease in signal amplitude. In our work, excitation powers comparable to that of the dashed line are used to excite and convert 3Q-1Q coherence states and indeed, our results reported chapter 4, are in agreement with those in **Figure 2.31**. In light of this, Gan[275] introduced a similar experiment known as satellite transition (ST) MAS NMR. In this experiment satellite transitions l±3/2 ↔±1/2l are correlated with the central transition l-1/2↔+1/2l in a 2D experiment under MAS. The form of the refocusing of the fourth-rank terms in the ST and CT takes on different ratios to that in the MQMAS experiment to yield the isotropic CT[276]. However, because the STs are 1Q coherence states, excitation can be achieved much more efficiently resulting in an improvement in resolution:

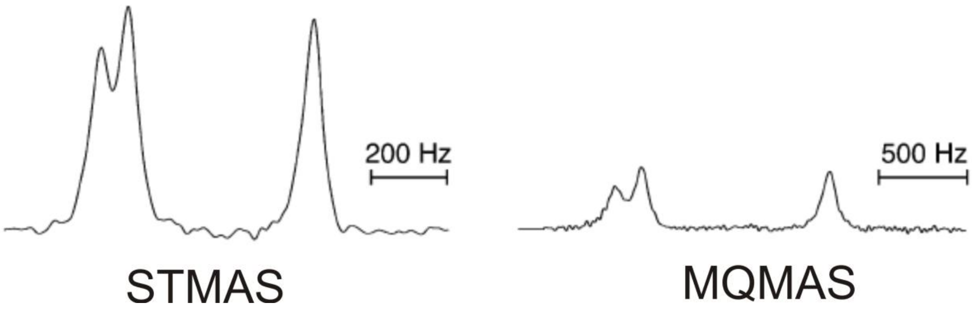

Figure 2.32 Comparing the isotropic projections obtained from STMAS and MQMAS on ^{87}Rb (spin-3/2) in $RbNO_3$. In each experiment in 192 scans were used with a recycle interval of 250 ms. The MAS rate was 20 kHz. Experiments were performed using a conventional 2.5 mm Bruker MAS probe with a maximum radiofrequency field strength of $\boldsymbol{\omega_1/2\pi}$ = 180 kHz. Adapted from Askbrook *et al*.[277]

Application of heteronuclear decoupling schemes during MQ or STMAS acquisition can also significantly improve resolution.[208, 278] To date, the newest method of obtaining high resolution NMR spectra for spin-3/2 nuclei was reported in 2008 by Thrippleton *et al.*[279] with the experiment called satellite transitions acquired in real time by magic angle spinning (STARTMAS). It involves modifying the STMAS pulse sequence by transferring the STs into double-quantum (DQ) coherence states and then finally back to 1Q coherence. Essentially, it allows for ultrafast acquisition of isotropic NMR spectra similar to that obtained from DOR.

2.9.2.5 MQMAS for Amorphous or Disorder Materials[268, 280]

For crystalline solids, the MAS NMR resonances along the f_1 dimension are very narrow, see **Figure 2.30**. However, this is not the case for amorphous or disordered materials. A distribution of bond angles and bond lengths are present, resulting in distributions of isotropic chemical shift and quadrupolar parameters (P_Q) which considerably broaden the resonances in the f_1 dimension. Therefore, extraction of line shapes and simulations to obtain δ_{iso}, Q_{CC}, and, η is not possible. However, δ_{iso} and P_Q can be calculated from a sheared MQMAS spectrum using:

$$\boldsymbol{\delta_{iso} = \frac{10}{27}\langle\delta_{F2}\rangle + \frac{17}{27}\langle\delta_{F1}\rangle} \qquad \textbf{Eq. 2.37}$$

$$\boldsymbol{P_Q = \sqrt{\frac{680v_0^2\cdot 10^6}{27}(\langle\delta_{F1}\rangle - \langle\delta_{F2}\rangle)}} \qquad \textbf{Eq. 2.38}$$

where $\langle\delta_{F2}\rangle$ and $\langle\delta_{F1}\rangle$are the position (ppm in unit) of the signal in the f_1 and f_2 dimension of the corresponding 2D MQMAS spectrum. v_0 is the Lamor frequency (MHz units) and P_Q is related to Q_{CC} and η by:

$$\boldsymbol{P_Q = Q_{CC}(1+\eta^2)^{1/2}} \qquad \textbf{Eq. 2.39}$$

The parameters, δ_{iso}, Q_{CC}, η and $\boldsymbol{P_Q}$ can give insight into the structural environment, ligands and coordination sphere around a quadrupolar nucleus. The relationship between these parameters and the local atomic environment are discussed in **Chapter 4.**

2.10 Techniques Available for Structural Studies of Glassy Systems

X-ray diffraction of glasses give broad diffractograms as a result of the distribution of undefined spacing between atomic planes. Therefore X-ray diffraction studies of glasses are based upon radial distribution function curves (RDF). RDF gives parameters concerned with the first coordination shell, the average distance between atom pairs, and the coordination number. This is extremely useful for determining the short range order around an atom but little information is obtained when the relative position of atoms are more than three or four neighbours apart.[281, 282]

Vibrational spectroscopy techniques are used to probe the atomic-scale structure of silica species in aqueous solution[182, 283-286] and hydrous silica glasses.[285, 287, 288] As all vibrations of all the atoms are considered in a random network it is difficult to unambiguously assign vibrational modes. However, a combination of Raman and IR can give a unique insight into glasses and has the advantage of being an in-situ technique *c.f.* the grinding of a glass for SSNMR analysis: For example, Aguiar *et al.*[289] reported a detailed structural study on SiO_2:CaO:P_2O_5 glasses using IR and Raman spectroscopy:

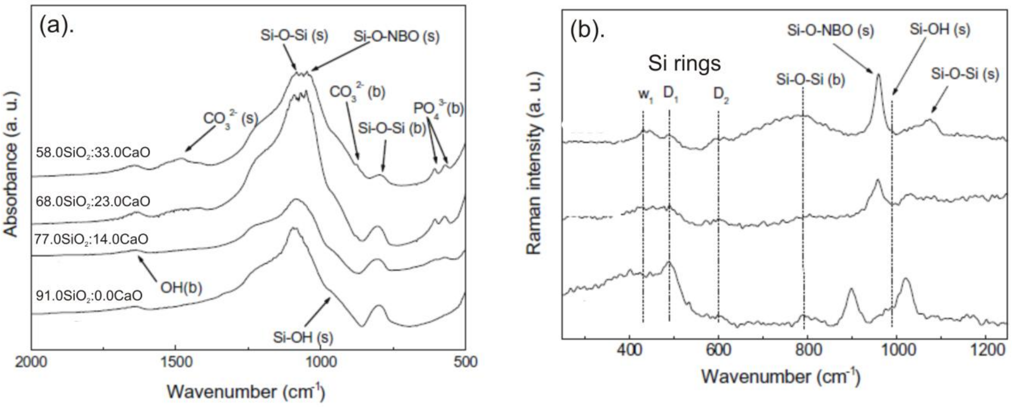

Figure 2.33 (a). IR and (b). Raman spectra of sol-gel derived SiO_2:CaO:P_2O_5 glasses. The P_2O_5 mol % is fixed at 9.0 in each case. (The authors do not include the lowest SiO_2 containing glass in the Raman spectra).

The two techniques can give complimentary structural information regarding 3,4 and 5 Si containing rings, Si-O-Si bending modes and on the different types of Si-OH (silanol) groups.

Mössbauer spectroscopy (nuclear gamma resonance) is a tool to obtain quantitative information on both the structural environment and oxidation state of iron in silicate glasses and melts as it is a common impurity in commercial glass.[290, 291]

Solid-state Nuclear Magnetic Resonance: without doubt this technique has been particularly effective in unveiling atomic structures, dynamics and connectivity of multi-component glasses. Over the past ten years, research has focused on detailing the atomic configurations, degree of network connectivity and disorder in glasses and melts with varying composition to provide atomistic links between structure-properties reletionships.[292]

In this work, silica based hydrogels were studied and present a challenging class of materials for structural analysis. Solid-state NMR was chosen as the primary spectroscopic tool as it can provide a wealth of information on the systems over the aforementioned techniques. The hydrogels contain the following NMR active nuclei, ^{1}H, ^{17}O, ^{23}Na and ^{29}Si. The choice of NMR experiment depends upon the nature of the system and also on the applicability of the experiment on the nuclei in question. For example, for phosphate based glasses, typically INADEQUATE experiments are used. This method utilises the homonuclear indirect ^{31}P–^{31}P through bond (^{2}J) interactions between phosphate species linked *via* oxygen bridges for creating double quantum coherences. Applying this method as a spectral filter, it can be used for the selective detection of only those phosphate species involved in P-O-P linkages. Also, different oxygen-bridged phosphate species can be exposed by monitoring the double-quantum build curves.[293] However, the natural abundance of ^{31}P is 100 % *c.f.* 4.7 % for ^{29}Si. Therefore, these experiments cannot be conducted on silicate glasses without isotropic enrichment. Typically, single-pulse (SP) or CP ^{29}Si SSNMR experiments are used to characterise the local silicon environments within glasses. Owing to the nuclei's low natural abundance Wiench *et al.*[294] recently demonstrated a significant enhancement in ^{29}Si sensitivity when a Carr-Purcell-Meiboom-Gill (CPMG) train of rotor-synchronised 180° pulses is used during acquisition. Advanced experiments such as heteronuclear dipolar correlation experiments can determine the proximity of ^{1}H to ^{29}Si nuclei.[85, 295] (see next chapter) Recoupling techniques, (Rotational Echo Double Resonance; REDOR). have also been used between to determine internuclear distances and/or clustering between ^{29}Si and ^{7}Li nuclei.[296]

Oxygen is a major constituent in glasses. ^{17}O is the NMR active isotope, I = 5/2, with a natural abundance of ~ 0.037% hence limiting NMR investigations.[297] However, enrichment is possible and the BO and NBOs in glasses can be resolved using ^{17}O MQMAS NMR experiments.[298, 299]

The combination of a large nuclear magnetic moment and high natural abundance (99.99%) renders the ^{1}H easily accessible for NMR studies. However, as we have already addressed, broad and featureless spectra are observed for glassy systems. Robert *et al.*[300] has reported using spin-counting and ^{1}H-^{1}H double-quantum Nuclear Overhauser (NOSEY) type experiments. However, the ^{1}H linewidths are so broad that any conclusions made should be treated tentatively. (In fact, the majority of publications regarding any glass-oxide system omit ^{1}H spectra).

^{23}Na is 100 % abundant but is I = 3/2 therefore MQMAS experiments are required for insight into its local structure. It is possible to cross-polarise from ^{1}H to ^{23}Na but it has only been demonstrated on crystalline materials.[301, 302] The mechanism of quadrupolar cross-polarisation is poorly understood.[256, 302, 303]

2.11 Crystallography[304-306]

A crystal is a solid that is characterised by periodic repetition of a certain pattern of atoms. These patterns are located upon the points of a lattice, which is an array of points repeating periodically in three dimensions. The points can be thought of as forming identical tiny boxes, called unit cells, that fill the space of the lattice. The form of the unit cell is described in terms of three translational vectors a, b and c and the intervector angles α, β, and γ:

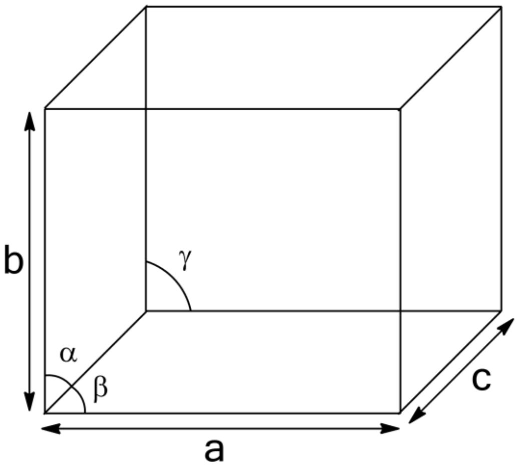

Seven Crystal Systems:

Cubic
Hexagonal
Monoclinic
Orthorhombic
Rhombohedral
Tetragonal
Triclinic

Figure 2.34 Unit cell parameters and the seven crystal systems

The unit cell can have seven possible shapes, known as the Seven Crystal Systems and are given in **Figure 2.33**. Unit cells can be classified into one of the following: Primitive (P), Body-Centred (I), Face-Centred (F) and End-Centred (C). The classification is dependent on the number of lattice points per unit cell.

2.11.1 *Principles of X-diffraction*

X-ray diffraction (XRD) is an analytical technique utilising X-ray scattering from crystalline materials. Each material produces a unique X-ray "fingerprint" of X-ray intensity versus scattering angle that is characteristic of its crystalline atomic structure. A monochromatic beam of X-rays (ADI) is directed at a crystal lattice, which is represented by the array of black dots in **Figure 2.35**. These are arranged so that they form a series of parallel planes with Miller indices *hkl* and interplanar spacing d_{hkl}. The ray A is scattered by the atom B and the ray D is scattered by an atom at F *etc*. For the reflected beams to emerge as a single beam, they must arrive in phase with one another. This is known as constructive interference.

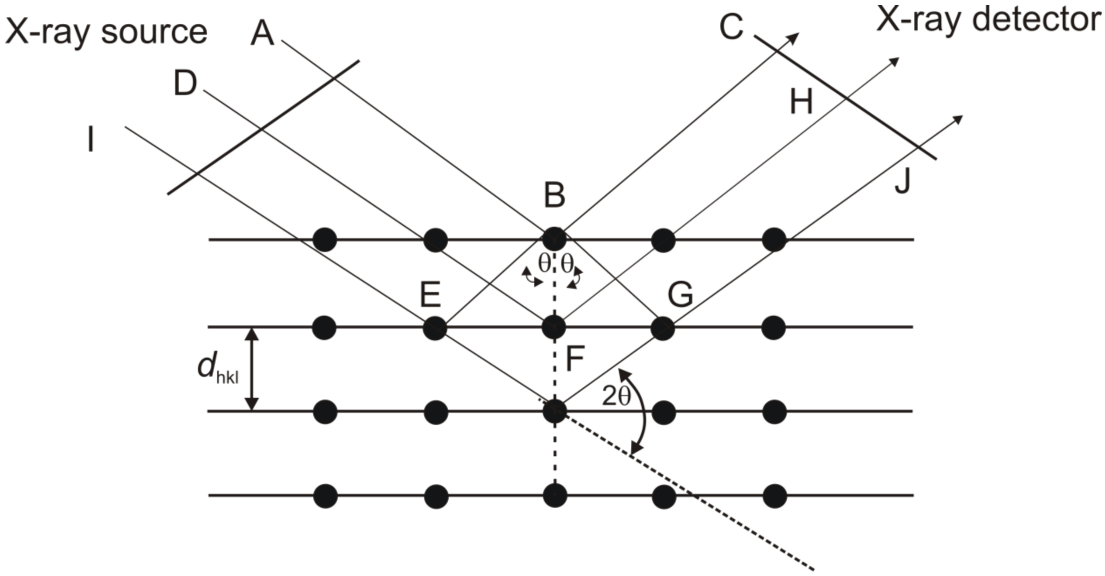

Figure 2.35 Diffraction condition for parallel X-ray beam incident on a set of lattice planes

The path difference between the waves scattered by atoms from adjacent lattice planes is given by:

$$\boldsymbol{EFG = 2dsin\theta} \qquad \textbf{Eq. 2.40}$$

For constructive interference:

$$\boldsymbol{n\lambda = 2dsin\theta} \text{ (Braggs Law)} \qquad \textbf{Eq. 2.41}$$

Where n must be equal to an integral number of wavelengths. When Braggs law is satisfied the reflected beams are in phase and interfere constructively. Angles other than the Bragg angle result in the beams out of phase, which interfere destructively and thus cancel. The reflections observed on x-ray patterns are generally indexed according to the plane at which they diffract with the planes being labeled using Miller indices (100), (110), (111) *i.e.* they describe the faces/planes of a crystal. Miller indices, h, k and l of the crystal face or planes are defined by:

$$\boldsymbol{h = \frac{a}{X} \quad k = \frac{b}{Y} \quad l = \frac{c}{Z}}$$ **Eq. 2.42**

where, X, Y and Z are the axial intercepts along the a, b and c axis. For example, consider a cubic crystal, **Figure 2.36**. The intercepts Y and Z of face A on the axes y and z are at infinity, so the Miller indices h, k and l for this face will be $a/1$, b/∞ and c/∞ or (100). Hence, faces B and C are designated (010) and (001). Conversely, for an octahedron, all faces cut the X, Y and Z intercepts therefore all faces are (111):

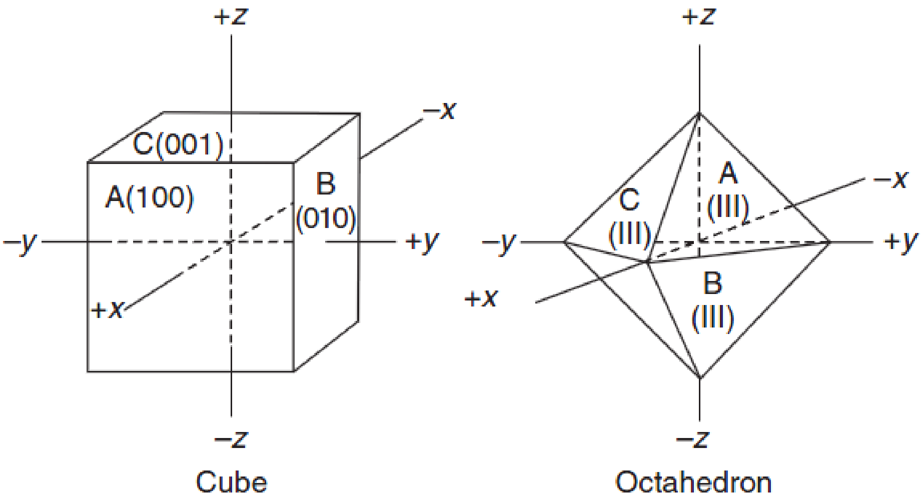

Figure 2.36 Miller indices for cubic and octahedral crystal structures

2.12 Optical Measurements

Optical properties involve visual inspection of the hydrogels and haze (H) measurements using a haze-gard *dual* spectrophotometer. This equipment (BYK-Gardner GmbH, Germany) employs two international standards ISO 13468 and ASTM D1003[307]. The light wavelength used was 589 nm. ASTM D1003 is an international standard that is typically used to characterise the transparency of plastic films. Haze can be described as the cloudy or turbid appearance of an otherwise transparent specimen caused by light scattered from within the material or from its surfaces.[308-310] The measurement of haze is represented in **Figure 2.36**.

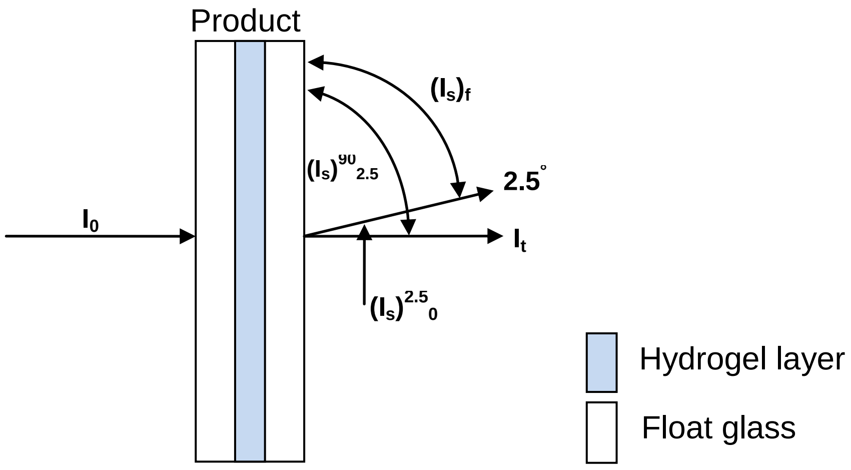

Figure 2.37 Schematic of how haze is measured within the fire-resistant product

Here, I_0 is the incident light flux, I_t, is the direct transmitted flux, $(I_s)_f$ is the forward scattered flux, *i.e.* the scattered intensity between 0° and 90°. $(I_s)^{90}_{2.5}$ is the scattered flux that is deviated from the incident beam between 2.5° and 90°. Therefore haze is calculated from:

$$\boldsymbol{H} = \frac{\boldsymbol{I_{s}}^{\mathbf{90}}_{\mathbf{2.5}}}{\boldsymbol{I_t} + (\boldsymbol{I_s})_{\boldsymbol{f}}} \qquad \textbf{Eq. 2.43}$$

Haze is defined as the percentage of transmitted light that in passing through a specimen deviates from the incident beam by more than 2.5° from the normal incident beam.[308-310] When H is below 5 % the material is considered to be transparent. The material is opaque when H is 100 %. The material is considered to be translucent when the when H is between 5-99 %.

Chapter 3

Experimental

3.1 Solid-state NMR

All Solid-state NMR experiments were conducted at 9.4 T using a Bruker DSX-400 spectrometer operating at 79.49, 100.61, 105.85 and 400.13 MHz for ^{29}Si, ^{13}C, ^{23}Na and ^{1}H respectively. The chemical shifts of ^{1}H, ^{29}Si and ^{13}C are quoted in ppm from external TMS whilst ^{23}Na is quoted from external 1M $NaCl_{(aq)}$. Samples were spun in zirconia rotors driven by N_2 gas using either a 4 mm ^{1}H/X/Y or 2.5 mm ^{1}H/^{19}F/X commercial probeheads.

3.1.1 *One dimensional magic angle spinning (MAS)*

All one dimensional MAS NMR experiments were acquired using a simple pulse acquire program displayed in **Figure 3.1**:

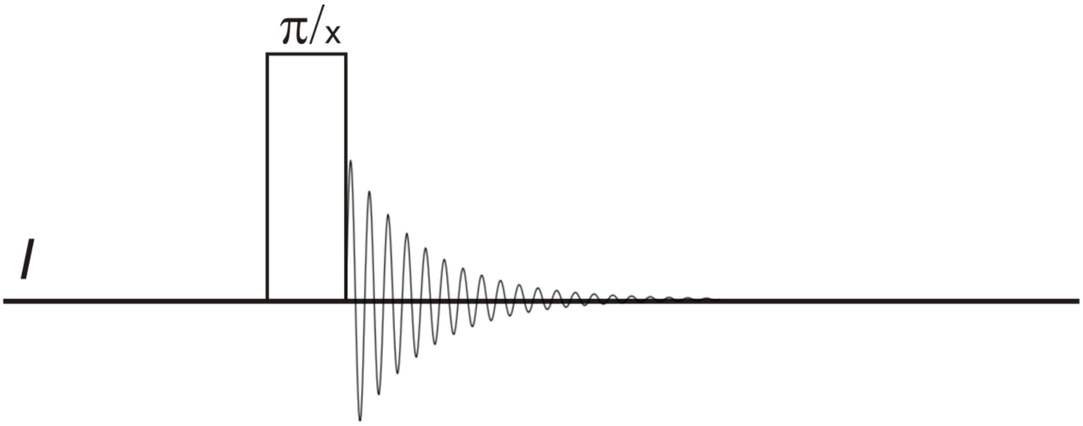

Figure 3.1 Symbolic representation of the pulse acquire MAS experiment

- ^{1}H MAS NMR spectra were acquired using a $\pi/2$ pulse length of 3.0 or 2.5 μs at an MAS rate of 10 or 30 kHz respectively and a recycle delay of 8 s.
- ^{29}Si MAS NMR spectra were acquired with a ^{29}Si $\pi/3$ pulse length of 2.6 μs at an MAS rate of 4.0 kHz and a recycle delay of 240 s without ^{1}H decoupling.
- ^{23}Na MAS NMR spectra were acquired with a $\pi/9$ pulse length of 0.8 μs at an MAS rate of 10 kHz and a recycle delay of 2 s.

3.1.2 *^{1}H-X Cross Polarisation Magic Angle Spinning (CP/MAS)*

All CP/MAS NMR experiments were conducted using ramp amplitude (RAMP[311]) implemented on the ^{1}H channel during the contact step. TPPM15[238] heteronuclear dipolar decoupling with 15° phase difference between the two pulses was used during acquisition.

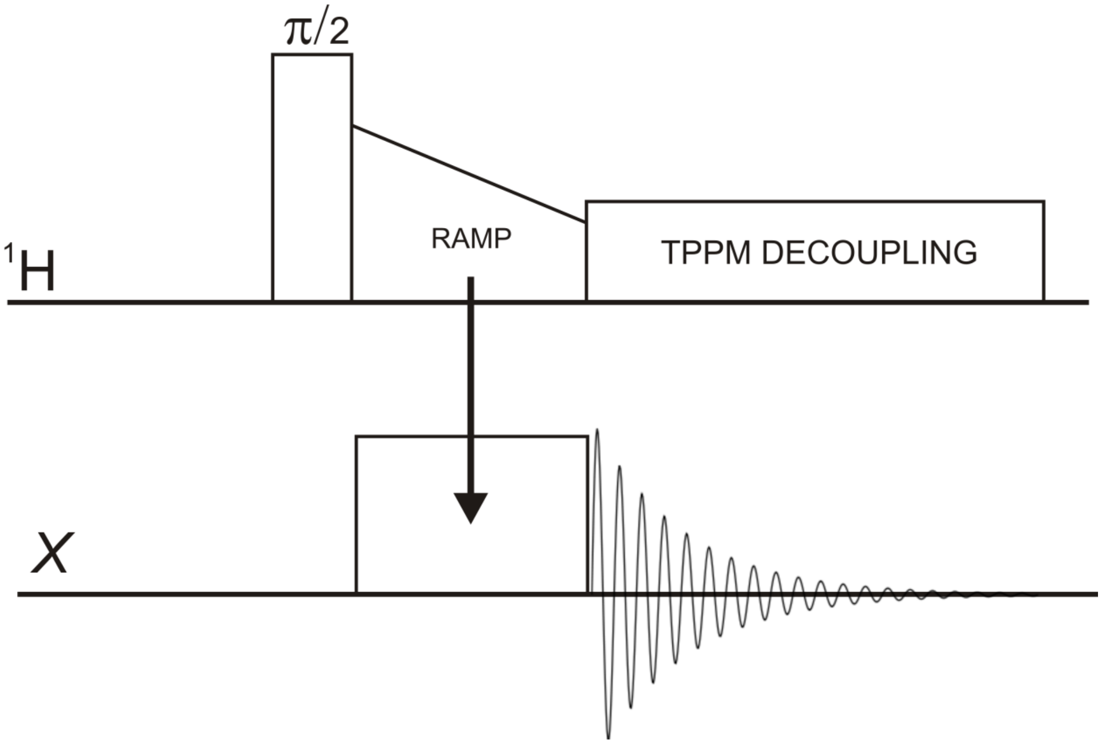

Figure 3.2 ^{1}H-X CP/MAS pulse program, where X refers to ^{13}C or ^{29}Si

- ^{1}H-^{13}C CP/MAS NMR spectra were acquired at a MAS rate of 10 kHz. A ^{1}H π/2 pulse length was 3.0 μs and the recycle delay was 8.0 s was used during acquisition. The CP contact time was 0.5 ms with the Hartman–Hahn matching condition set using Hexamethylbenzene (HMB).
- ^{1}H-^{29}Si CP/MAS NMR spectra were acquired at a MAS rate of 4.0 kHz. A ^{1}H π/2 pulse length of 3.0 μs and the recycle delay of 8 s was used during acquisition. The CP contact time was 2.0 ms with the Hartmann–Hahn matching condition set using kaolinite.

3.1.3 *Two dimensional ^{1}H-^{13}C Heteronuclear Correlation (HETCOR)*

2D ^{1}H-^{13}C HETCOR NMR is a technique that correlates the ^{1}H chemical shifts recorded in the indirect dimension to ^{13}C nuclei chemical shifts in the direct dimension. In the t_1 evolution period the ^{1}H's are decoupled from each other using FSLG[241] homonuclear dipolar decoupling sequence thus ^{1}H magnetisation evolves only under the influence of their chemical shift Hamiltonian.

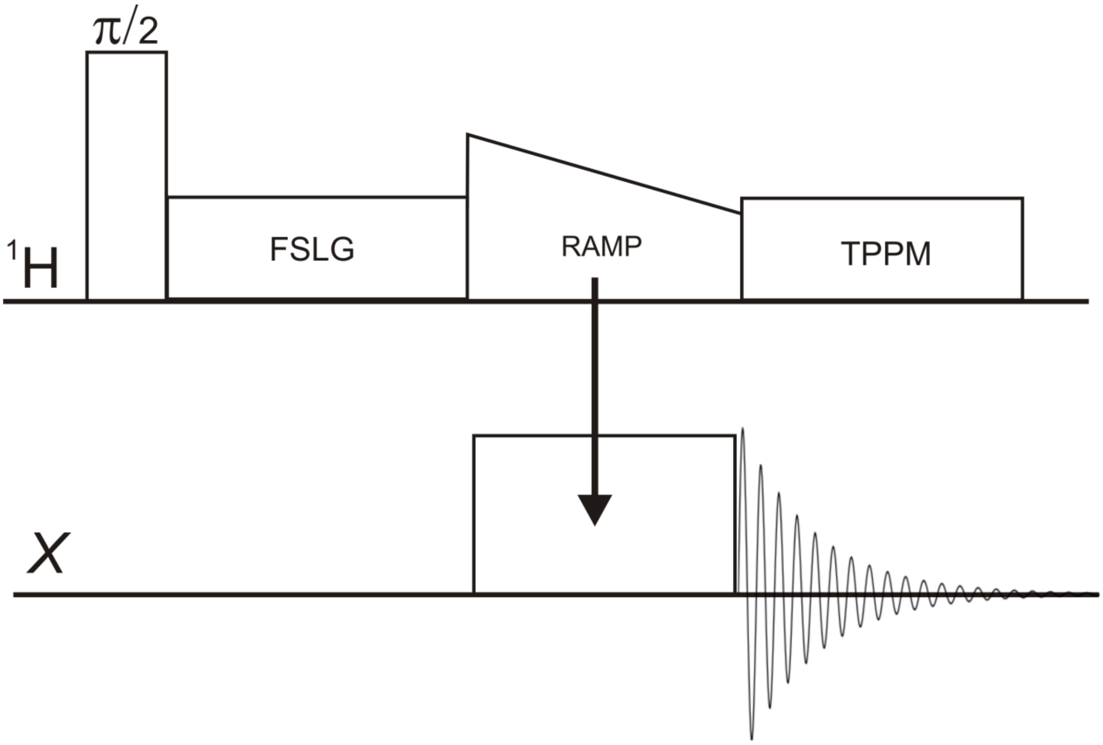

Figure 3.3 ^{1}H-X HETCOR pulse program, where X refers to ^{13}C or ^{29}Si

- 2D ^{1}H-^{13}C HETCOR MAS NMR spectra were acquired at an MAS rate of 10 kHz. The 2D HETCOR experiments used FSLG[241] homonuclear decoupling with ^{1}H *rf* field of *ca.* 90 kHz in t_1 and RAMP ^{1}H-^{13}C cross-polarization with a contact time of 0.5 ms. TPPM decoupling was used during acquisition at a decoupling strength of *ca.* 80.6 kHz. States Time Proportional Phase Incrimination (TPPI) was employed for phase sensitive detection.[312, 313] The recycle delay was set at 2.0 s. 256 increments were recorded in t_1 to cover the full ^{1}H spectral width of 23048.023 Hz corresponding to a dwell time of 43.4 µs. 800 scans acquired in t_2 per increment.

3.1.4 *Multiple-quantum magic angle spinning (MQMAS)*

Several pulse schemes are available from the basic two pulse sequence described in the chapter 2 to more complicated versions utilising cross-polarisation.[314] In this work, the z-filter MQMAS pulse sequence proposed by Amoureux *et al.*[315] is implemented throughout; it is a robust technique and easy to implement. The pulse sequence and coherence pathways are shown in **Figure 3.4**.

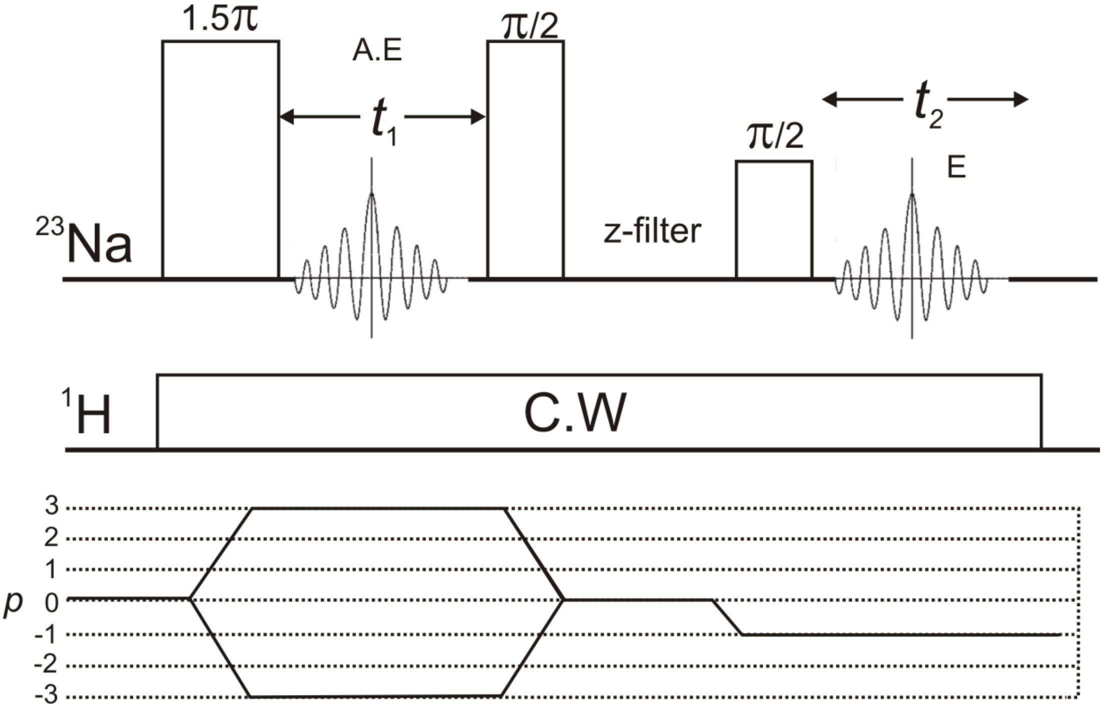

Figure 3.4 Pulse sequence and coherence transfer pathway for 3QMAS NMR experiments

In this three-pulse scheme the first hard pulse excites 3Q coherence followed by another hard pulse into 0Q coherence (i.e. stored along the z-axis). After a short delay (z-filter) 0Q coherence is then transferred into observable 1Q coherence using a selective soft pulse. Unlike the two-pulse scheme, symmetrisation of the echo (-3) and antiecho (+3) pathways during the two hard pulses (p=0→±3→0) forces an equal intensity of the signals, leading to pure absorption spectra i.e. free from phase twists although a shearing transformation is still required.

- The pulse lengths were optimised each time a MQMAS experiment was preformed. Typically, pulse lengths of 4.5, 1.6, and 30 μs were employed for 3Q excitation, conversion and selective central transition excitation, respectively. The recycle delay was 2 s using a z-filter delay time of 20 μs. 360 transients acquired in t_2 per 256 t_1 increment. The spectral width in the indirection dimension was rotor synchronised at 10 kHz. ^{1}H continuous wave decoupling was implemented during the entire X-pulse sequence. To produce pure absorption-mode line-shapes in the two-dimensional spectra, STATES-TPPI[312, 313] was employed.

3.1.5 *Spin-lattice relaxation in the laboratory frame, T_1*

All T_1 experiments were collected using the standard inversion recovery sequence:

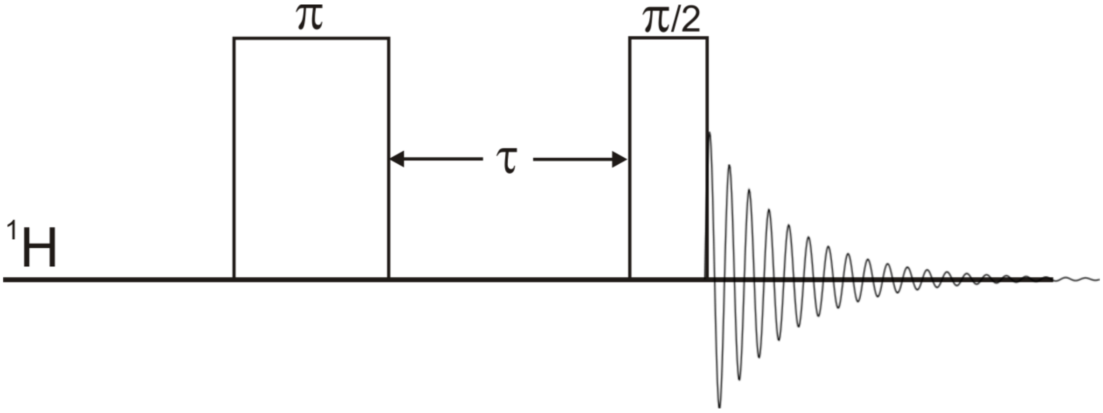

Figure 3.5 Inversion recovery pulse sequence

A 180° rotates magnetisation down into the –z plane which evolves for a certain time, τ before a 90° rotates the remaining magnetisation into the –xy plane, FID is then recorded. To obtain a T_1 recovery curve, 18 experiments were conducted with τ set from 0.01 to 6 ms.

3.1.6 *Spin-spin relaxation, T_2*

All T_2 experiments were collected using Carr-Purcell-Meiboom-Gill[316] (CPMG) pulse sequence

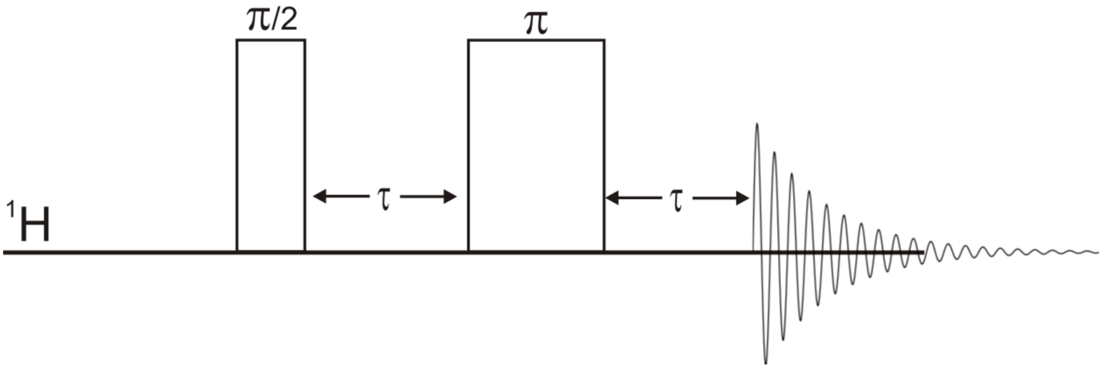

Figure 3.6 CPMG pulse sequence

A 90° rotates magnetisation into the –xy plane which evolves for a time τ. A 180° has the effect of refocusing magnetisation i.e. coherence is resorted and allowed to evolve for τ before being recorded. To obtain a T_2 decay curve, 22 experiments were conducted with τ delays from 0.01 to 4 ms. In both T_1 and T_2 90 and 180° pulse lengths of 3 and 6 μs were used.

3.1.7 *Spin-lattice relaxation in the rotating frame; $T_{1\rho}^{H/C}$*

$T_{1\rho}$ experiments utilise the CP pulse sequence in **Figure 3.7** but a spin-locking pulse is added:

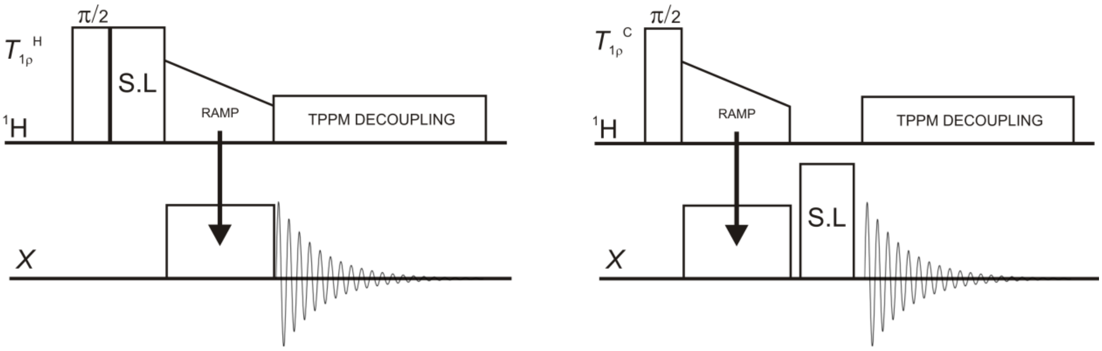

Figure 3.7 $T_{1\rho}^{H}$ and $T_{1\rho}^{C}$ pulse sequences

For $T_{1\rho}^{H}$ experiments, a 90° pulse rotates magnetisation into the –xy plane but is allowed to evolve via spin-locking pulse for a predetermined time. After this time, remaining magnetisation is transferred to the X nucleus as in the CP experiment. A similar situation exists for $T_{1\rho}^{C}$ experiments however; the spin-locking pulse is applied after ^{1}H magnetisation transfer. In order to obtain $T_{1\rho}$ decay curves 14 experiments were conducted with spin-locking times from 0.01 to 3 ms.

3.1.8 *Variable Temperature Experiments*

Typically, variable temperature NMR temperature experiments were conducted from 25 to 100°C at 10°C intervals. A filament within the probe is used to heat the N_2 gas bearing gas.

3.2 Solution-state NMR

Originally, ^{29}Si{^{1}H} NMR experiments were conducted at 9.4 T using a Bruker AVANCE 400 spectrometer operating at 79.49 MHz for ^{29}Si. The probehead contained a ^{29}Si background signal. This was removed using a T_2-filtering or FID subtraction methods. However, this led to problems with phase corrections. Therefore, ^{29}Si{^{1}H} were ran on the Bruker solid-state NMR DSX-400 spectrometer. Solutions were injected into zirconia rotors and placed into a 7 mm probehead.

- ^{29}Si{^{1}H} NMR spectra were acquired with a ^{29}Si $\pi/2$ pulse length of 13.0 μs using ^{1}H WALTZ decoupling

3.3 Powder X-Ray Diffraction (pXRD)

Powder X-ray diffraction (PXRD) patterns were measured using a BRUKER diffractometer with Co-$K_{\alpha1}$ radiation with a wavelength λ = 1.789 Å. Patterns were recorded in Bragg-Brentano reflection geometry and measured between 5 - 60 2θ ranges.

3.4 Environmental Scanning Electron Microscopy (E-SEM)

E-SEM was conducted at the University of Liverpool by Dr. P. Hill. The images were obtained on a FEI Quanta ESEM 200 instrument using low vacuum (0.75 Torr), 60°C stage operating at 15.0 keV.

3.5 Data processing

All powder XRD data were processed using PANalytical High Score plus software. All solid and solution NMR spectra were acquired using XWINNMR 3.5 and processed using Bruker Topspin 2.1. Deconvolution of

^{1}H-^{29}Si CP/SP MAS spectra and relaxation data was processed using OriginLab 8.5 software. Line-shape simulations of the ^{23}Na sites extracted from MQMAS experiments was conducted using dmfit.

Chapter 4

Solid-state NMR characterisation of organic-inorganic hydrogels

4.1 Introduction

This chapter covers the results obtained from a variety of solid-state NMR experiments on three commercial silicate hydrogels. The silicates range from weight ratio x SiO_2 : 1.00 Na_2O values of high (X = 3.90), medium (X = 3.30) and low (X = 2.00). The effect on the molecular level structure and dynamics upon the addition of ethylene glycol or glycerol on the 3.30 *wt.* ratio hydrogel are also investigated. The hydrogels are designated as CS1, CS2 and CS3 corresponding to 2.00, 3.30 and 3.90 *wt.* ratio respectively. The ethylene glycol and glycerol containing hydrogels are denoted as CS2EG and CS2G, respectively. The local structure and composition of the silica networks have been elucidated using ^{1}H-^{29}Si CP MAS NMR. We used ^{23}Na MAS NMR in conjunction with MQMAS to gain a unique insight into the sodium environments present. ^{1}H MAS NMR experiments highlight the difficulty in obtaining high resolution spectra for materials that are amorphous and contain high amounts of water. The ability to improve the sensitivity of ^{1}H NMR experiments is addressed. As water is a major component in these systems, it is important to understand its dynamics and structure at a molecular level. Variable temperature spin-lattice (T_1) and spin-spin (T_2) relaxation times measurements were conducted on the CS2 hydrogels with and without polyols. Spin-lattice relaxation measurements in the rotating frame ($T_{1p}^{H/C}$) address the heterogeneity of glycerol in the CS2G hydrogel. Finally, proposed models of the CS2 hydrogels are presented.

4.2 Experimental Part

4.2.1 *Production of the Hydrogel Interlayer*

The hydrogel interlayer is a product of the sol-gel process whereby a commercially available sodium-silicate solution (CS) is dried down to a hydrogel form. The compositions of the solutions are given in Table 4.1.

Table 4.1 Composition of commercially available solutions

Solutions	SiO_2:Na_2O *wt.* ratio	SiO_2:Na_2O mol. ratio	*wt.* % SiO_2	*wt.* % Na_2O	*wt.* % H_2O	pH at 20°C
CS3	3.90	4.00	23.20	6.00	70.8	10.8
CS2	3.30	3.40	27.70	8.40	63.9	11.4
CS1	2.00	2.06	30.55	15.27	54.2	12.2

The solution is poured onto a sealed piece of float glass; this is known as a bilayer, and placed into a specialised drying chamber (see Figure 4.1). The drying process involves three stages; degassing, drying and conditioning.

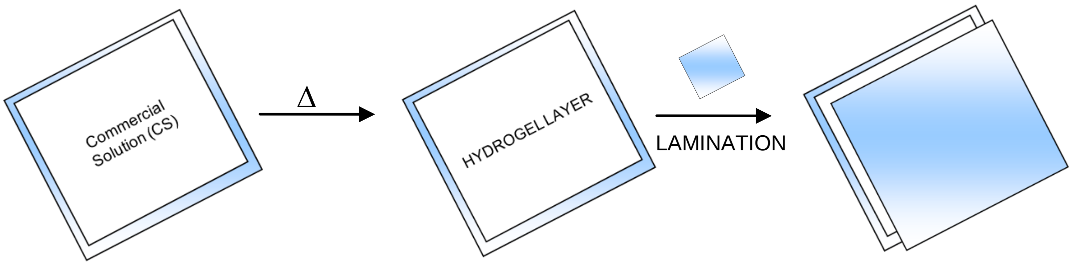

Figure 4.1 Processing the fire-resistant product. The blue squares indicate float glass sandwiching the (white) hydrogel layer

In the drying stage a maximum temperature of 120°C is reached which gradually reduces the water content in the solution from 60-65 to 20-25 *wt* % over a period of 9 hours. The loss of water induces silica condensation producing a sodium-silicate hydrogel with polyol i.e. an organic-inorganic hydrogel. After the conditioning phase, the bilayer is created into a full laminate by placing another piece of float glass ontop and is fixed in place through a rolling press. The product is mounted into custom made window frames to serve as an effective fire-resistant material. Polyols are added to the CS2 solution to achieve a viscosity in which the hydrogel can be effectively attached to the float glass. Typically, the CS2 solution (92.76 wt %) is mixed with either glycerol or ethylene glycol (7.24 wt %) and then dried to produce the CS2G and CSEG hydrogels. For solid-state NMR analysis the hydrogel is removed from the laminate using a drill to produce a fine white powder.

4.3 Results and Discussion

4.4 Structure and composition of the hydrogels

4.4.1 *Quantification of silicon environments using cross-polarisation*

Single-pulse (SP) NMR experiments on dilute nuclei such as ^{29}Si and ^{13}C often suffer from low sensitivity because of (1) low natural abundance and (2) long T_1 times resulting in the need for recycle delays lasting from minutes to hours.[220, 221, 317] The CP method can overcome these disadvantages and has been covered in **Chapter 2**. However, the main drawback of CP is that it is not quantitative as silicon atoms in closest proximity to protons are preferentially enhanced. Therefore, the signal intensity of the Q^{1-3} sites, which contain ≡Si-OH groups, will be greater than the fully condensed Q^4 sites; this is highlighted in **Figure 4.2**:

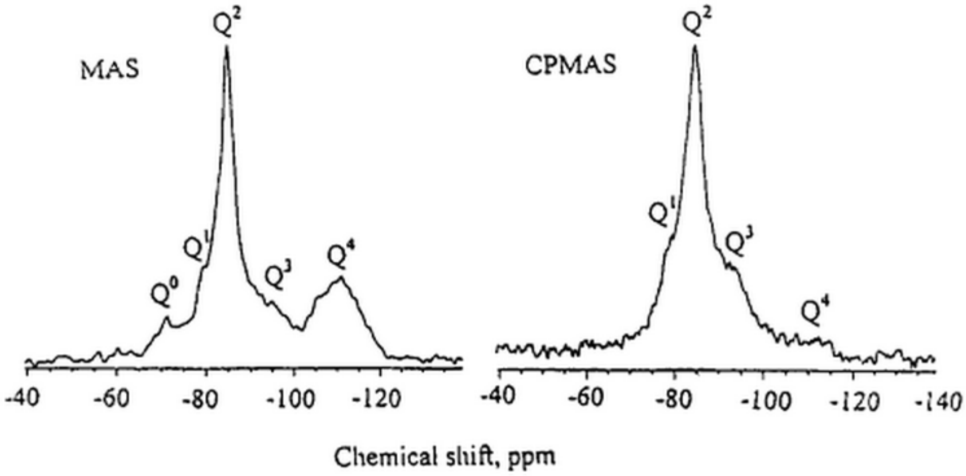

Figure 4.2 Left: ^{29}Si SP MAS and right: ^{1}H-^{29}Si CP MAS NMR spectra of Ca_3SiO_5 paste hydrated in the presence of fumed silica for nine months. There are clear differences between the signal intensities and therefore peak areas depending upon the nature of the Q-sites and the NMR method employed. Figure taken from Harrison *et al.*[318]

The CP experiment can yield semi-quantitative data if a variable contact time (VCT) experiment is conducted. For example, the signal intensity of each Q site is plotted against varying contact time for the CS2G hydrogel; **Figure 4.3**:

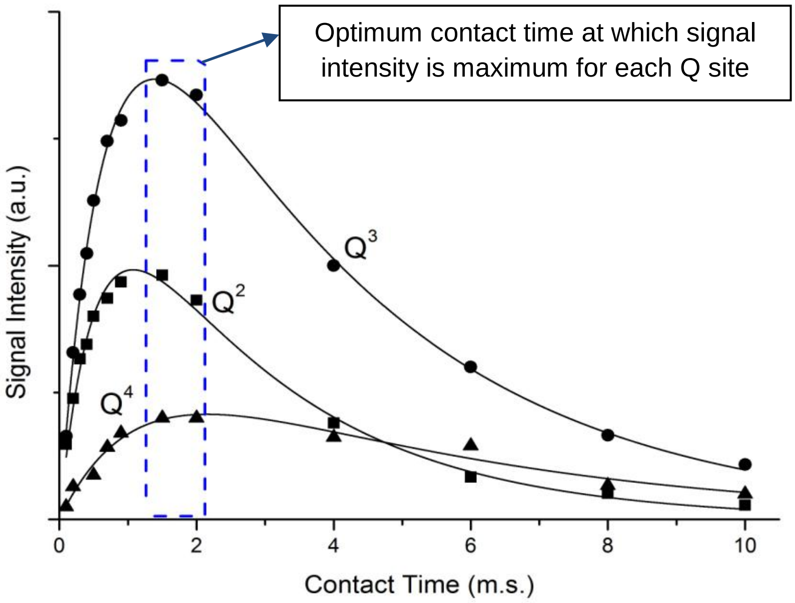
Optimum contact time at which signal intensity is maximum for each Q site

Figure 4.3 Signal intensity of the Q^{2-4} sites (Q^1 is omitted for clarity) against increasing contact time for the CS2G hydrogel. Blue dashed area indicates the area in which the maximum signal intensity is achieved for each Q site.

From **Figure 4.3** a contact time between 1.5 and 3 ms should be used to ensure the maximum signal for each Q site. Following on from this, a comparison of peak areas obtained from a ^{29}Si SP and CP experiment was conducted on the CS2G hydrogel.

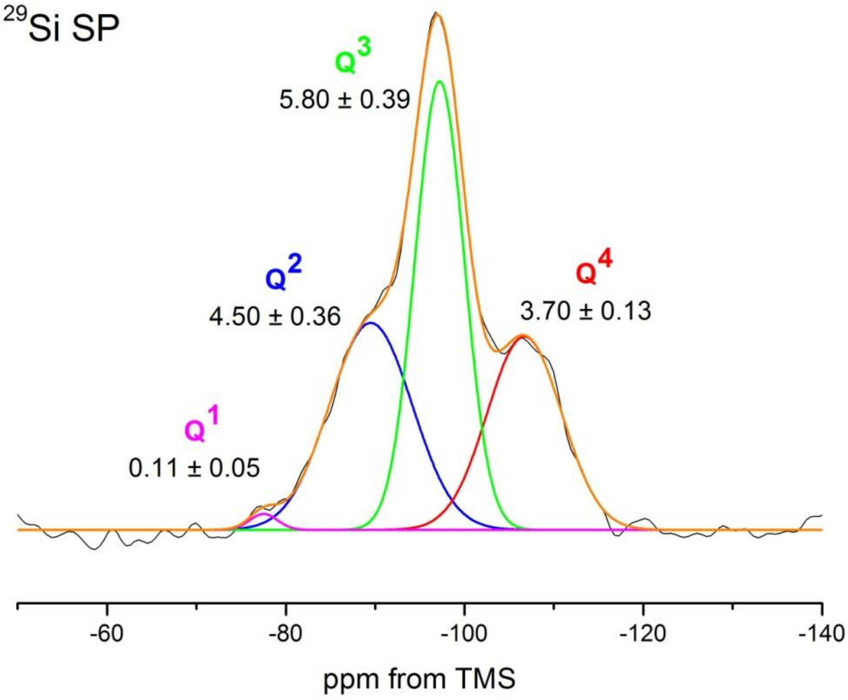

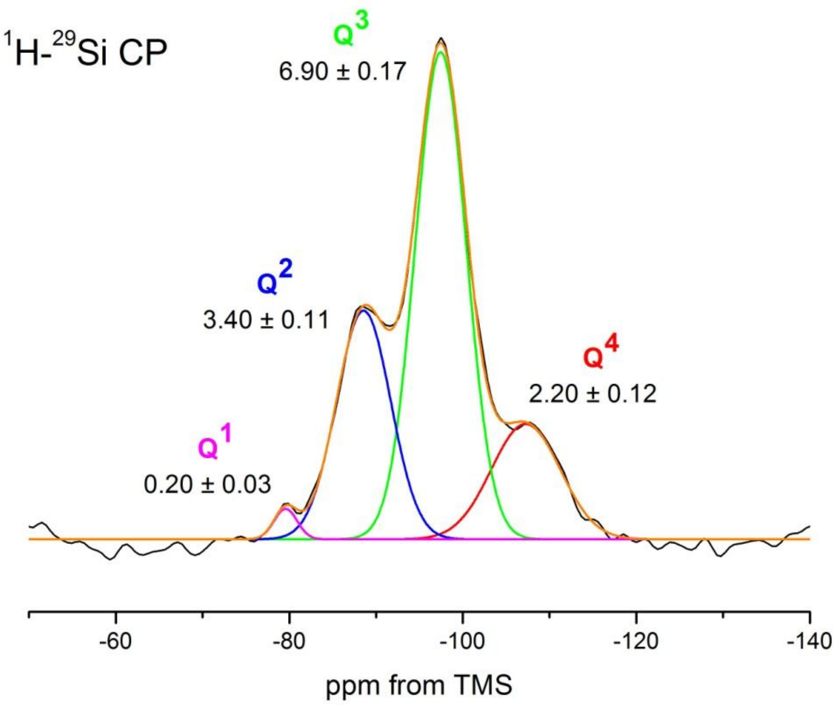

Figure 4.4 Top: ^{29}Si SP MAS and bottom: ^{1}H-^{29}Si CP MAS NMR spectra of the CS2G hydrogel. Peak areas obtained from Gaussian deconvolution are also shown. The CP experiment implements a recycle delay of 8 s, contact time of 2 ms (obtained from the VCT experiment) and a total acquisition time of *ca*. 6 hours. The SP experiment uses a recycle delay of 240 s with a total acquisition time of 24 hours.

There is a clear improvement in ^{29}Si spectral resolution using CP over the SP method. The peak areas for the $Q^{1\text{-}3}$ units are slightly higher in CP compared to the SP experiment. This is to be expected due to association of these sites with a close proximity proton. The peak area of the Q^4 site acquired using CP is lower than that derived from the SP experiment. Although the Q^4 site is slightly underestimated in the CP experiment, generally both NMR experiments yield representative Q distributions. Therefore, the silica environments and distributions in the hydrogels were all probed using ^{1}H-^{29}Si CP MAS NMR experiments.

4.4.2 *^{1}H-^{29}Si CP/MAS NMR*

^{1}H-^{29}Si CP/MAS NMR spectra of the hydrogels indicate the degree of condensation of the silica units and confirm the silicon environments present.

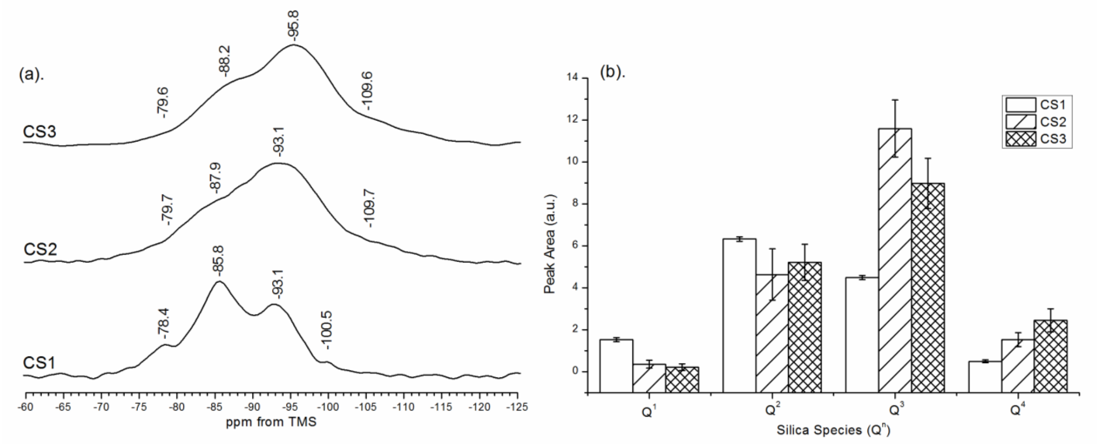

Figure 4.5 ^{1}H-^{29}Si CP/MAS NMR spectra and (b). Bar chart with errors showing the normalised peak areas for silica Q-sites obtained from Gaussian deconvolution.

The ^{1}H-^{29}Si CP/MAS NMR spectra for the commercial silicates display broad resonances typical for amorphous silica based gels. The resonances can be assigned to the following Q^{n} silica environments[319-321]:

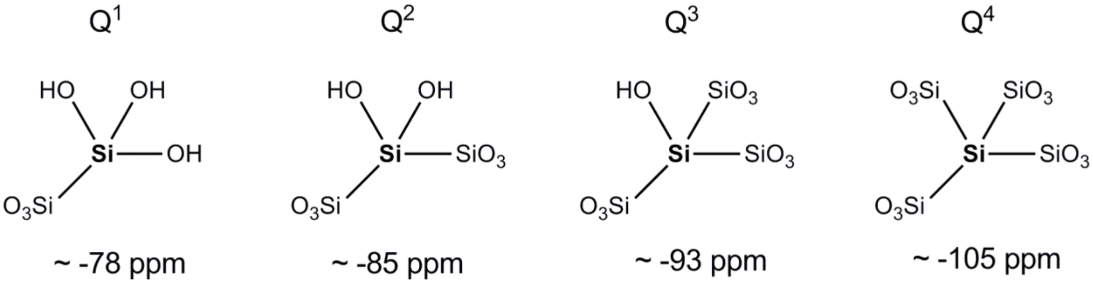

Figure 4.6 Q^{n} silica environments in the hydrogels. The number of siloxane bonds (Si-O-Si) attached to the Si centre under consideration is denoted by a superscript.[33]

In the CS1 hydrogel the Q^{2} units dominate followed by Q^{3}, Q^{1} and Q^{4}. The CS2 and CS3 hydrogels display similar distributions, with a general trend being that the Q^{3} site dominates followed by Q^{4}, Q^{2} and Q^{1}. The latter hydrogels display broad, ill-defined resonances which are difficult to deconvolute accurately. Therefore, higher error values are obtained for the

Q^3 and Q^4 sites. (It will be shown in **Chapter 6** that the CS3 hydrogel contains higher amounts of Q^3 and Q^4 compared to the CS2 hydrogel). The difference in the degree of condensation between the hydrogels is related to the pH, Si/Na *wt.* ratio and temperature of the starting solutions used for hydrogel formation. As the Si/Na *wt.* ratio decreases the extent of silica polycondensation also decreases, which in turn leads to higher amounts of Q^1 and Q^2 species being observed, this is consistent with literature and is discussed further in **Chapter 6**. [322-324]

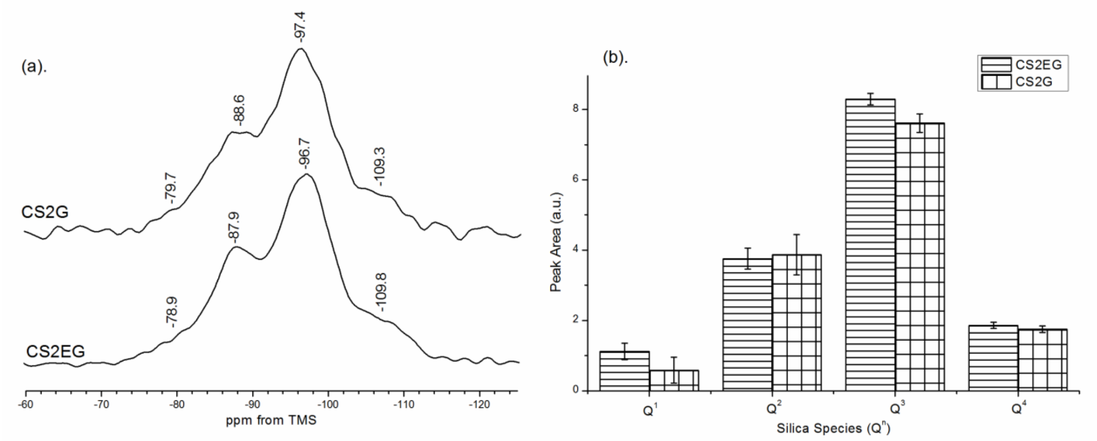

Figure 4.7 (a). ^1H-^{29}Si CP/MAS NMR spectra and (b). Bar chart with errors of population of silica species obtained from deconvolution of peak areas for each hydrogel.

The ^1H-^{29}Si CP/MAS NMR spectra for the polyol containing CS2 hydrogels show similar chemical shifts and peak areas respectively, when compared to those in the CS2 hydrogel. This indicates that the silica environments and Q-distributions are not affected by the presence of polyols. The ^{29}Si lines are narrower for the polyol containing hydrogels compared to their polyol free analogues. This observation suggests that some of polyols are in close proximity to the silica/water interface and is investigated in more detail later.

4.4.3 ^{23}*Na MAS NMR*

Solid-state NMR spectra of quadrupolar nuclei, often exhibit low resolution owing to the presence of significant anisotropic quadrupolar broadening due to the quadrupolar interaction.[325] This, combined with the amorphous nature of the materials, leads to distributions in the isotropic chemical shifts and/or quadrupolar parameters of the nucleus further complicating the spectra.[280]

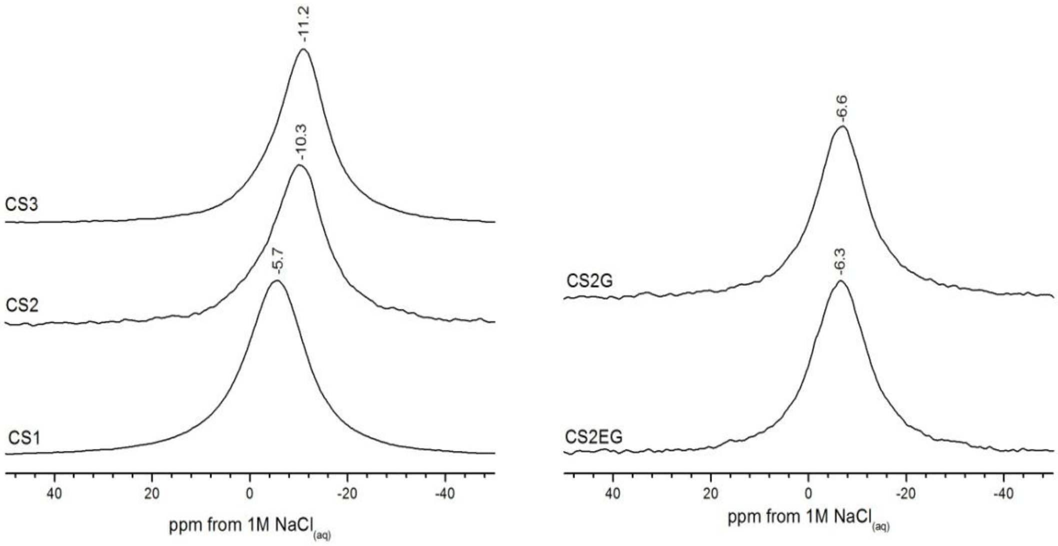

Figure 4.8 ^{23}Na MAS NMR spectra of the hydrogels.

The ^{23}Na MAS NMR spectra of the five hydrogels (**Figure 4.8**) display broad and asymmetric line shapes absent of the effects of strong, second-order quadrupolar coupling. The line shapes are typical for ^{23}Na sites in disordered materials such as glasses and gels.[324-330] The polyol free hydrogel show an increase in the observed chemical shift values from -11.2, -10.3 to -5.7 ppm as a function of decreasing weight ratio. The addition of the polyols results in a shift from -10.3 to -6.4 ppm. The width of the ^{23}Na resonances indicates a distribution of chemical shifts and quadrupolar parameters. In order to probe the ^{23}Na local structure further, ^{23}Na MQMAS experiments were conducted on the CS2 hydrogels.

4.4.4 *^{23}Na{^{1}H} MQMAS NMR*

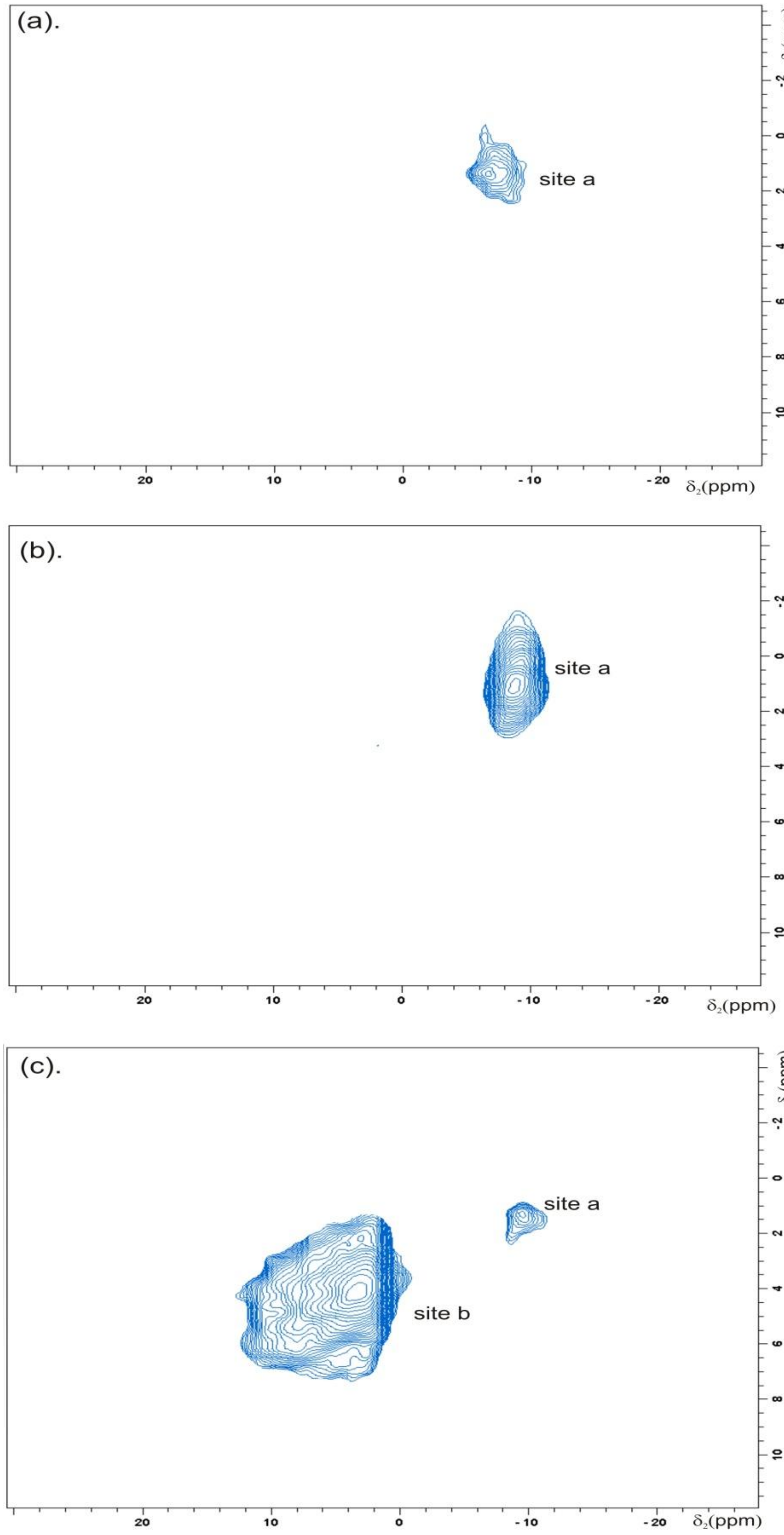

Figure 4.9 ^{23}Na{^{1}H} MQMAS NMR spectra of (a). CS2EG (b) CS2G and (c). CS2

Figure 4.9 shows the ^{23}Na{^{1}H} MQMAS NMR spectra for the CS2 series hydrogels. Values of δ_{iso} and P_Q have been calculated from **Eq. 2.37** and **2.38** for each Na-site and are given in **Table 4.2**. The CS2EG and CS2G hydrogels show a single Na site, Na(**a**), with an average δ_{iso} and P_Q values of -2.4 ppm and 5.3 MHz. The CS2 hydrogel, which contains no polyol also shows this same Na site, Na(**a**). However, an additional Na site, Na(**b**), with an δ_{iso} of 3.8 ppm and P_Q of 1.6 MHz is also observed. The MQMAS technique is generally not quantitative as site intensities are dependent upon the strength of P_Q. This is because the ability to create 3Q coherence and convert it into detectable 1Q coherence decreases with increasing P_Q values.[331, 332] This is true in the case of the Na sites **a** and **b**. Site **a**, with P_Q values between 5.0 and 5.6 MHz, shows a relatively weak signal intensity. The opposite trend is observed for site **b**.

Table 4.2 Isotropic chemical shift (δ_{iso}) and quadrupolar product (P_Q) obtained from **Eq. 2.37** and **2.38** using $F_1/_2$ values for ^{23}Na in the CS2 hydrogels

Hydrogel	Site	F_1 /ppm	F_2 /ppm	δ_{iso} /ppm	P_Q /MHz
CS2	**a**	1.3	-9.7	-2.8	5.6
	b	4.1	3.2	3.8	1.6
CS2EG	**a**	1.4	-7.4	-1.8	5.0
CS2G	**a**	1.0	-8.8	-2.7	5.3

4.4.4.1 Relationship between local sodium environment and ^{23}Na isotropic chemical shift and the quadrupolar product

In the early 1990s several groups independently reported trends between ^{23}Na isotropic chemical shifts and its local atomic environment (bond distances, coordination number and geometry; assuming Na is coordinating with O). Notably, Koller[333], George[328], Angeli[327] and Xue[329] studied a variety of silicate based minerals and correlated coordination number, Na-O distance and geometry to ^{23}Na chemical shifts and, to a lesser extent, the quadrupolar coupling constant. However, it is accepted that interpretation of chemical shifts and inferring it to local atomic environments is by no means straightforward or unambiguous. The observed ^{23}Na chemical shift range is *ca.* 50 ppm with common coordination numbers of 5- and 6- reported for crystalline sodium silicates (4, 7 and 8-fold coordination numbers are also reported but for different materials[258]). The chemical shift ranges for the 5- and 6-fold coordinations overlap heavily and lie between -20 to +20 ppm.[258] For this reason, X-ray crystallography data is used to aid structural assignment. In the absence of such data, for example in amorphous systems, the P_Q can be used in combination with the δ_{iso} to infer structural information. In general, the P_Q value depends upon both the number of coordinated ligands and the geometry upon which the metal-ligand complex adopts. Koller *et al.*[333] provides a pictorial guideline for a qualitative interpretation of the quadrupole interaction in structural terms calculated by the point charge model for different sodium-oxygen complexes.

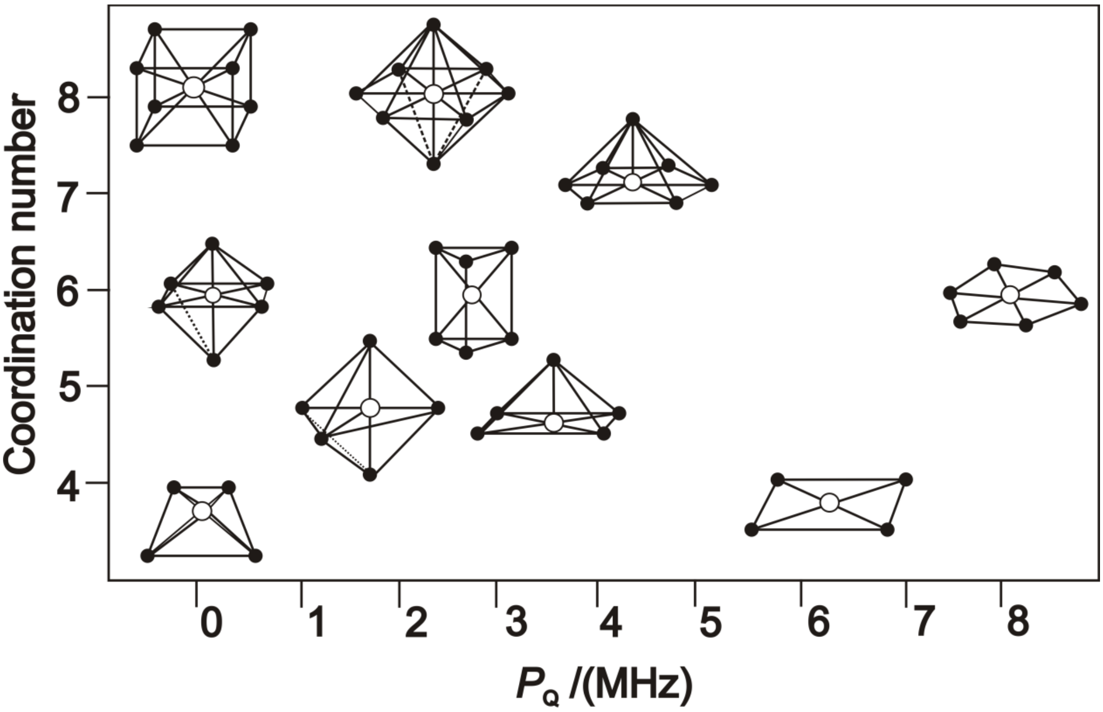

Figure 4.10 The relationship between the quadrupolar parameters and the sodium (white circles) oxygen (black circles) coordinations with different symmetries and coordination numbers. The figure has been adapted from Koller.[333]

Figure 4.10 shows that for a perfect tetrahedral or octahedral complex the P_Q adopts a value around zero. The P_Q increases for trigonal bipyramidal or quadratic pyramidal symmetry, and is the largest for planar coordinations of four or six oxygen ions around sodium. Any distortions from regular coordination symmetries and differences in the actual ligands will further affect the size of P_Q. The theory provided by Koller[333] has been used by various groups in an attempt to gain a better understanding of the local environment of sodium in various silicate gels, glasses and minerals.

Table 4.3 δ_{iso} and P_Q values for sodium sites within sodium-silicate based gels, hydrous glasses, and a hydrated layered silicate, montmorillonite

Author	**Material**	**No. of Na Sites**	**δ_{iso} /ppm**	**P_Q /MHz**
Tambelli[320]	Alkali-silica based gel	I	0.3	0.4
		II	-0.5 – 1.0	1.0 – 1.5
		III	1.5 - 2.9	1.8 - 1.9
Masui[334]	Anhydrous $3.00SiO_2{:}Na_2O$ glass	I	4.2	0.6
	Hydrous (39 wt %) $3.00SiO_2{:}Na_2O$ glass	I	4.2	0.6
		II	10.2	1.3
Yang[324]	Zeolite A: $Al_2O_3{:}2SiO_2{:}3.06{:}NaOH{:}128H_2O$ Amorphous gel precursor isolated from 0 to 12 hours into reaction	I	-1.6 – 2.1	1.3 - 2.0
Ohkubo[335]	Dry montmorillonite	I	-14.0	1.5
	Hydrated (12.5 wt %) montmorillonite	I	-2.0	3.8

Table 4.3 contains the reported δ_{iso} and P_Q values for a variety of sodium-silicate based materials. Tambelli *et al.*[320] investigated the deleterious ‘alkali-silica’ reaction that can occur in concrete. The products of the reaction are silicate based gels containing semi-crystalline trona. They resolved at least 3 different Na-sites within one gel. Trona has two crystallographic Na-sites per

unit cell; one site is 6-coordinate forming a slightly distorted octahedron and the other site has a 5-fold coordination. The latter site can also be described as pseudo 6-coordinate as there is an interaction with a distant O atom at 2.60 Å. This site is considerably less symmetric than the 'true' 6-fold site and hence a higher P_Q value was expected. Therefore, they assign site II to the 6-fold complex and site III to the 5-fold complex. The authors suggest that the remaining Na site I could be due to symmetric crystal domains of some sodium hydrate or rapidly diffusing Na ions within the amorphous gel structure. Masui *et al.*[334] studied alkali-silicate glasses a function of hydration using ^{23}Na MAS/MQMAS NMR. They showed that at low hydration levels (<8.4 *wt.* % water) one sodium site was present and that two sites could be resolved upon higher water levels. Additionally, they elaborate on work undertaken by Angeli *et al.*[327] who showed a relationship between the Na-O bond distance d(Na-O) and δ_{iso}:

$$d\text{Na-O}(\text{Å}) = -0.0119\ \delta_{iso} + 2.5912 \qquad \textbf{Eq. 4.1}$$

Using **Eq. 4.1**, they calculated the Na-O distance for Na(I) and Na(II) to be 2.54 and 2.47 Å respectively. However, they concluded that the difference in P_Q values was not sufficient to distinguish between the two chemical Na sites; instead they discussed the origin of the two sites by considering the variation of the ^{23}Na MAS spectra with increasing water content. Na(1) is present in both the anhydrous and hydrous glasses suggesting that the site is coordinated to a non-bridging oxygen, $\equiv$Si-O$^-$. The second site, which is only present in the hydrated glasses, is then assigned to Na existing in a water microphase having relatively high mobility. They rationalise this by suggesting (1) that Na-OH$_2$ bond lengths are shorter than that of Si-O-Na and (2) the site disappears with decreasing temperature suggesting that the sodium ions segregate from the water phase and ion exchange for Si-OH. Yang *et al.*[324] investigated the local atomic environments of both aluminium and sodium during the crystallization of Zeolite A. They concluded that during crystallisation 5- and/or 6-fold sodium ions in hydrated spheres were present due to the range of δ_{iso}. However, they did not elaborate on the P_Q values. Finally, Ohkubo *et al.*[335] studied the hydration behaviour of montmorillonite; a hydrated layered sodium-silicate containing aluminium, iron and magnesium. The sodium ions are located between the sheets of Si/Al layers. In the 'dry' material, one sodium site is observed with δ_{iso} = -14.0 ppm and P_Q = 1.5 MHz. At 12.5 *wt.* % hydration level, the P_Q value rises dramatically to 3.8 MHz but then decreases gradually upon further hydration. The δ_{iso} changes to -2.0 ppm but then remains constant for all hydration levels. From the model proposed by Koller, the authors suggest that the Na ions are located in hexagonal cavaties due to the relatively low P_Q values. As the level of hydration increases the Na ions coordinate with water and a change in chemical shift is observed. Additionally, the geometry changes from octahedral to planar and then back to octahedral, which would explain the rise and fall in P_Q values.

4.4.4.2 Assigning the local sodium environments in the CS2 hydrogels

Using equation **Eq. 4.2** the Na-O distances for Na(**a**) and Na(**b**) are estimated to be 2.62 (taking an average δ_{iso} of -2.43 ppm) and 2.55 Å. There is a general trend of increasing chemical shift with decreasing coordination number and interatomic distance. For example, for reported 5-coordinated sodium complexes the d(Na-O) values range from 2.34 to 2.40 Å. For 6-fold coordination the d(Na-O) values range from 2.49 to 2.60 Å.[325] This suggests that both Na(**a**) and Na(**b**) sites are involved in 6-fold coordination. However, the δ_{iso} ranges between -1.8 and 3.8 ppm lie in the 5- and 6-fold coordination region. In order to distinguish between the two sites we must consider the differences in P_Q values and the effect of polyol addition. The Na(**a**) site is present in all of the hydrogels and therefore must correspond to the primary cation $\text{Na}[(\text{H}_2\text{O})_n]^+$ (n = 6 for the first coordination sphere) counterbalancing non-bridging oxygens (NBOs). If we refer to **Figure 4.10**, a P_Q value of 5 MHz would indicate an intermediate complex between a highly distorted octahedron and that with planar symmetry. The δ_{iso} and P_Q values of the Na(**b**) site are similar to that of the 5-coordinate site found in makatite. This site, detailed in **Chapter 5**, has a trigonal bipyriamidal geometry coordinating to two water molecules and three silanol oxygen groups. However, no makatite crystals can be detected by XRD (see **Chapter 5**) hence Na(**b**) is likely to resemble a geometry and coordination sphere similar, but not identical, to that of the makatite 5-coordination site. The two sites are shown with idealized geometries in **Figure 4.12**. The Na(**b**) site has a strong association with the silica surface which is reflected by a shorter *d*(Na-O) distance compared to that for the Na(**a**) site. Although the exact ligands surrounding the Na(**b**) site are not identified it most probably coordinates directly with one ≡Si-O$^-$ NBO and is associated with a silanol proton involved in hydrogen bonding with an adjacent silanol oxygen group. In the literature, this site has not been probed using ^{23}Na NMR experiments but rather inferred *via* the ^{1}H MAS NMR spectra for a variety of hydrous sodium/aluminum silicate glasses and fiber glass supports. For example, Schellar[336], Romaneko[337], Robert[300] and Cody[338] *et al.* report independently similar ^{1}H spectra, see below:

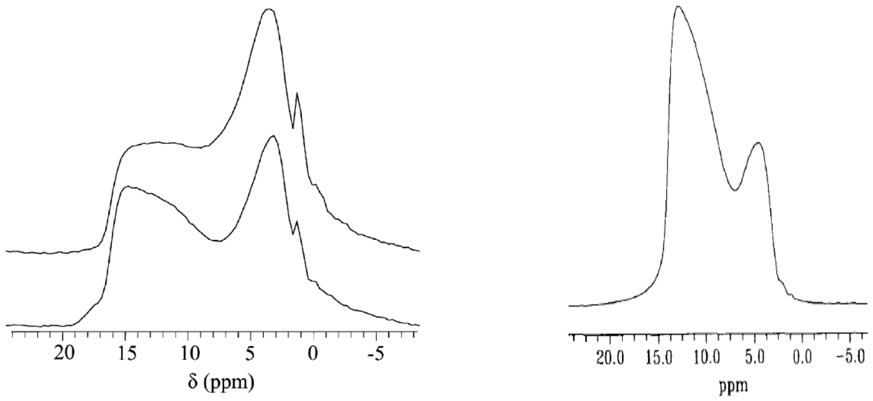

Figure 4.11 ^{1}H MAS NMR spectra of (left) alumina–sodium–silicate fiberglasses and (right) $Na_2O \cdot 4SiO_2 \cdot H_2O$ glass acquired at MAS rates of 12.5 and 10 kHz reported by Romaneko[337] and Schellar[336], respectively.

The downfield resonance is assigned to ≡Si-O**H**···O protons (see **Figure 4.12**). The spectrum is nearly identical to that of the CS2 hydrogel, which is shown in the next section. The authors do not employ ^{23}Na MQMAS NMR experiments (granted the technique was not invented when Schellar published in 1994 as MQMAS was introduced in 1995[266]) to probe the sodium environments. It would be very interesting to confirm/clarify how many sodium sites are present, certainly for the hydrous sodium silicate glasses for a comparison with the CS2 hydrogel. For example, if a second sodium site is not present in the hydrous sodium glasses, the Na(**b**) site must correspond to precursor makatite sites.

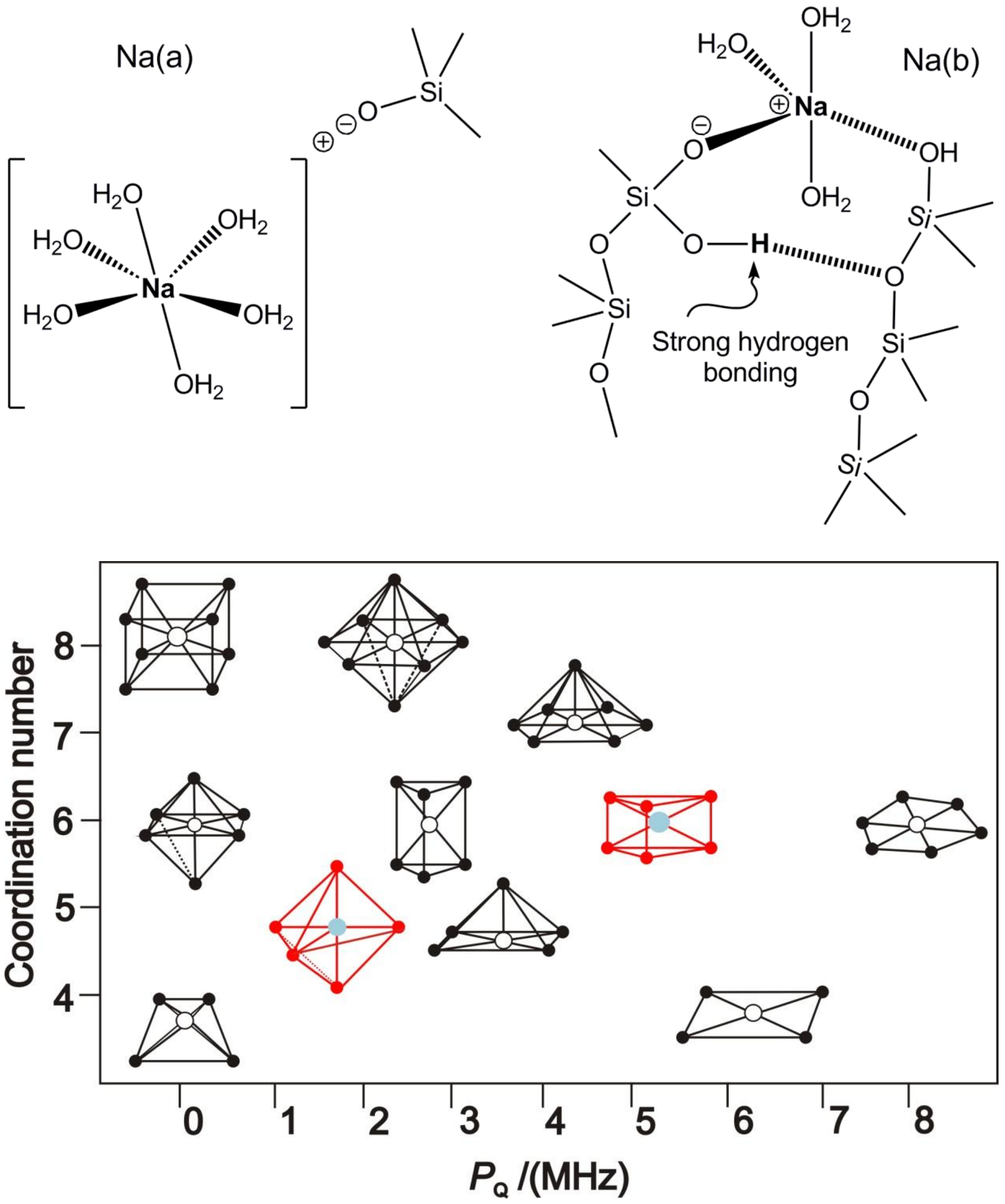

Figure 4.12 Representation of the Na(**a**) and Na(**b**) sites within the CS2 hydrogels. It is not clear as to the exact ligands making up the coordination sphere of the Na(**b**) site. The site must be balanced by one NBO and at least one silanol group. This is accompanied by a strong hydrogen bonding interaction between a proton silanol and an adjacent oxygen atom. The proton manifests as a strong resonance *ca*. 15 ppm in ^{1}H MAS NMR spectrum. The bottom figure indicates the geometry of each site based on their P_Q values.

The question to be addressed is, why do the polyols inhibit the formation of the Na(**b**) site? We postulate that in the absence of the polyols the silica clusters are in close proximity to one another and the strong –OH···O hydrogen bonding interaction is established. This would impose a steric restriction on the Na(**a**) site forcing some of these sites to transform into the Na(**b**) site. When the polyol is present, a proportion of its species acts as a buffer between the silica clusters thus inhibiting the formation of the Na(**b**) site. However, further investigation revealed that as the chain length of the polyol increases as does the intensity of the –OH···O hydrogen bonding resonance (see **Figure 4.13**). This suggests that only ethylene glycol and glycerol are small enough to act as a buffer between silica clusters.

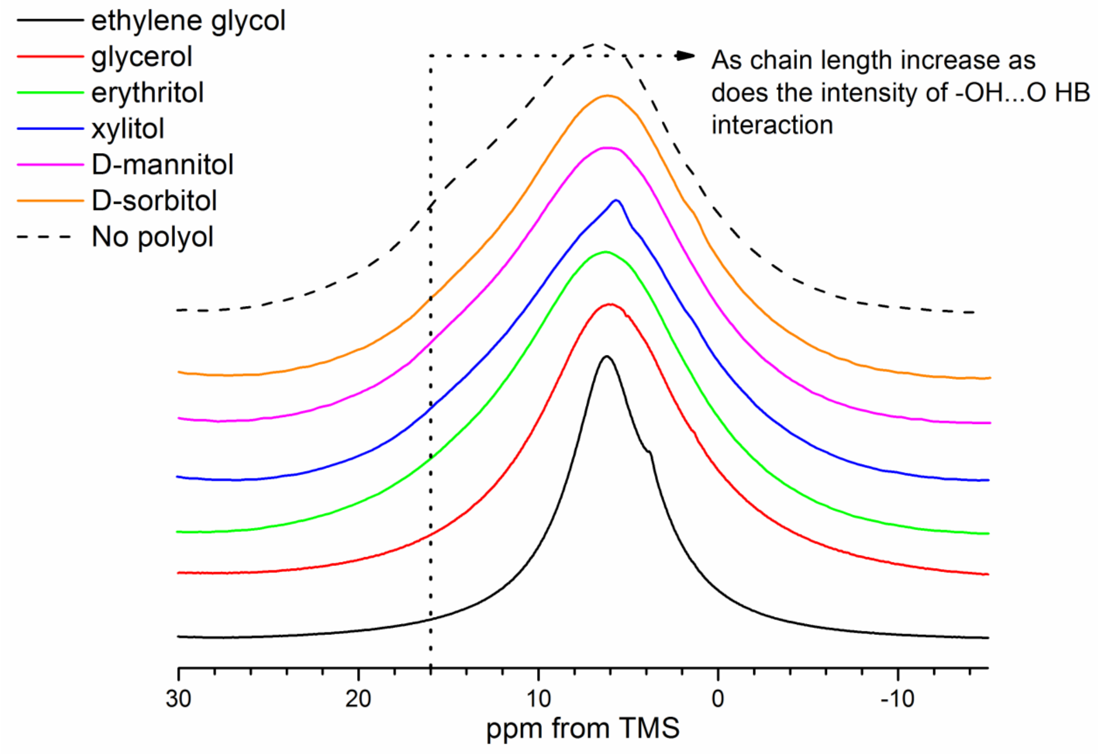

Figure 4.13 ^{1}H MAS NMR spectra of a series of CS2 hydrogels doped with polyols of increasing chain length

4.4.6 ^{1}*H MAS NMR*

As water is the major component of the hydrogels, it is expected that strong ^{1}H-^{1}H dipolar couplings will exist, undoubtedly complicating the ^{1}H NMR spectra. In an attempt to reduce the geometric dependencies of the dipolar interaction, moderate (10 kHz) and fast (30 kHz) MAS rates were applied.

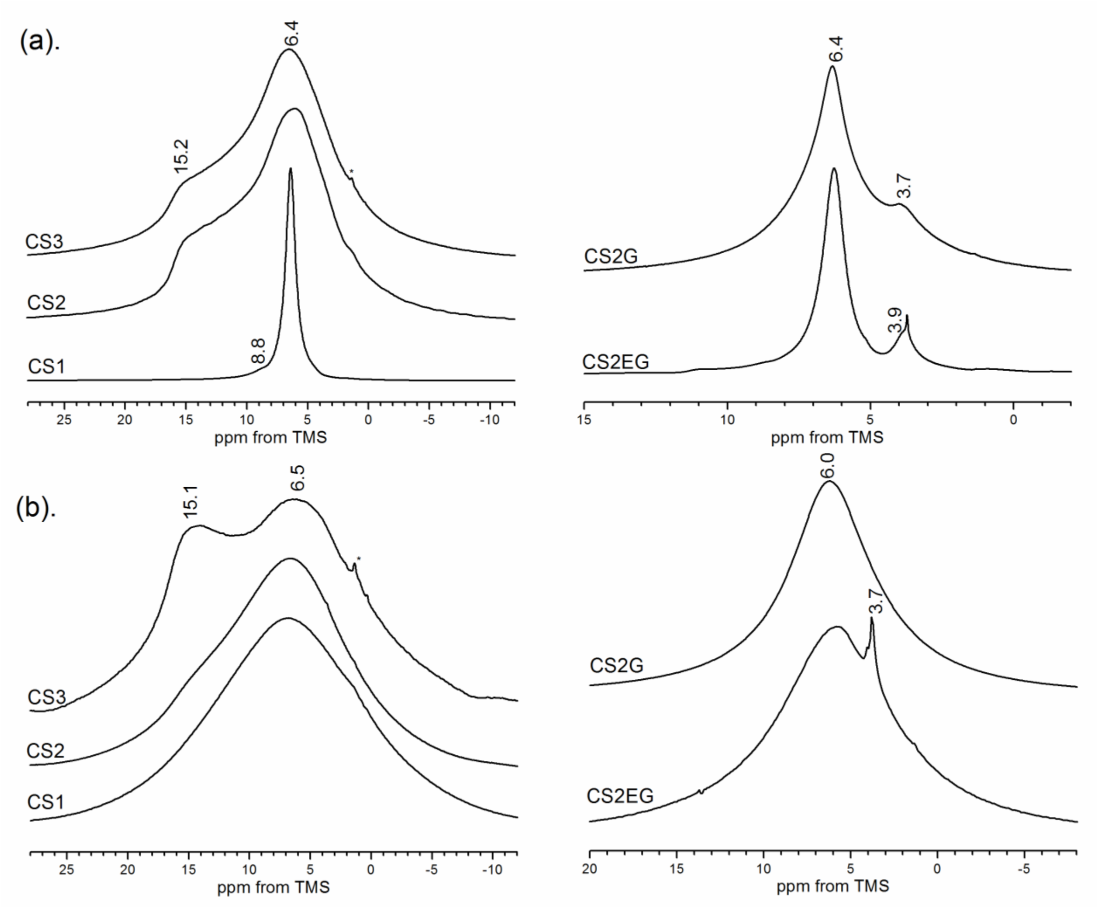

Figure 4.14 ^{1}H MAS NMR spectra acquired at an MAS rate of (a). 30 and (b). 10 kHz

Figure 4.14 (b). shows the ^{1}H MAS NMR spectra, acquired at 10 kHz. The materials display broad and featureless spectra indicating very strong ^{1}H-^{1}H dipole couplings. The polyol free hydrogels show two components at *ca.* 15 and 6.5 ppm. The intensity of the resonance at 15 ppm increases as a function of increasing Si/Na *wt.* ratio. This resonance is significantly reduced for the polyol containing hydrogels. The CS2G and CS2EG hydrogels both exhibit a single resonance at *ca*. 6 ppm. A sharp resonance at 3.7 ppm is seen for the ethylene glycol hydrogel. **Figure 4.14 (a).** shows the ^{1}H MAS NMR spectra acquired at 30 kHz. The increase in MAS rate reduces the homonuclear dipolar coupling interaction resulting in narrowing of the peaks. This is true for the CS1 hydrogel; a sharp resonance at 6.4 ppm is observed with a less intense shoulder resonance at 8.8 ppm. The spectra for the CS2 and CS3 hydrogels remain broad with no great improvement in ^{1}H resolution, indicating stronger ^{1}H-^{1}H coupling compared to the CS1 hydrogel. The spectra for the CS2G and CS2EG hydrogels show a narrowing of peaks with additional resonances at 3.7 and 3.9 ppm.

The resonance at 6.0-6.5 ppm, which is observed for all the hydrogels, can be assigned unambiguously to bulk water molecules in a network of hydrogen bonds.[5, 339-342] The resonances between 3.7 and 3.9 ppm corresponds to –CH$_2$- and –OH protons respectively, associated with the polyols but no fine structure is resolved. Resonances between 8 and 15 ppm can be attributed to hydroxyls engaged in strong hydrogen bonding. The broad resonances result from a non-uniform distribution of hydrogen bond strengths. It is established that the ^{1}H isotropic chemical shift of -OH protons increases with increasing hydrogen bonding strength. Eckert *et al.*[343] showed that a linear correlation existed between d(OH···O) distances and ^{1}H isotropic chemical shifts. A range of d(OH···O) distances between 2.5 and 2.9 Å was obtained for various silicate glasses. Therefore, if we employ this correlation to the 8.8 and 15.0 ppm resonances we obtain d(OH···O) distances of *ca.* 2.8 and 2.5 Å. The resonance at 15.0 ppm is indicative of the strongest hydrogen bonding environment and is assigned to ≡Si-O**H**···O protons between *adjacent* silica (**see Figure 4.12**)[300, 336-338] and was also confirmed using a ^{1}H-^{29}Si HETCOR experiment. For example, the presence of this environment is in good agreement with the assignment of the Na(**b**) site in the CS2 hydrogel. The remaining resonance at 8.8 ppm can be assigned to silanol protons engaged in strong hydrogen bonding.[344, 345] The absence of downfield resonances in the polyol hydrogels confirms the results from the ^{29}Si CP MAS and ^{23}Na MQMAS NMR data. These results indicate that some of the polyols are located close to the silica/water interface; the polyols inhibit the formation of the Na(**b**) sites and thus the ≡Si-OH···O environment cannot be established. Stefanescu *et al.*[346, 347] prepared oganic-inorganic gels using either ethylene glycol, glycerol, 1,2/3-propane diol with TEOS in acid catalysis. FT-IR spectroscopy showed the presence of the polyols in the silica matrix in three forms: free in the hybrid matrix pores, hydrogen bonding with the silanol groups and chemically bonded (through condensation) in the silica network. Although our materials use different routes to produce silica based gels, hydrogen bonding interactions between the polyols, water and silanols are likely to be present, but using the above techniques, the resonances have not been resolved. This is a direct result of very strong ^{1}H-^{1}H dipolar interactions and overlapping resonances arising from the high water content, the amorphous nature of the materials and the similarity in ^{1}H chemical shifts of the environments, respectively. MAS only affects the geometric term in the dipolar Hamiltonian whereas homonuclear decoupling sequences act on the spin term. Together, under CRAMPS the spatial and spin parts of the dipolar Hamiltonian are affected. DUMBO decoupling[242, 348, 349] was applied at an MAS rate of 15 kHz for direct proton detection on the CS2G hydrogel. Although there was an improvement in spectral resolution (see **Figure 4.15 (a).)** the same ^{1}H environments were observed. Another method to reduce ^{1}H-^{1}H coupling is to isotopically enrich the system with ^{2}H resulting in weaker ^{1}H-^{2}H heteronuclear couplings. Analogues of the CS2 hydrogel were prepared using D_2O and NaOD; however partial ^{1}H/^{2}H exchange occurred during the hydrogel formation. The ^{1}H MAS NMR spectra revealed that the ^{1}H dilution improved line widths (see **Figure 4.15 (b).**) but again, no additional resonances were observed. Elucidation of ^{1}H environments in these materials remain a challenge but, using new NMR hardware such as ultra-fast (65 kHz) MAS combined with FSLG, PMLG and DUMBO heteronuclear-detected proton NMR, improvements in spectral resolution could be gained.

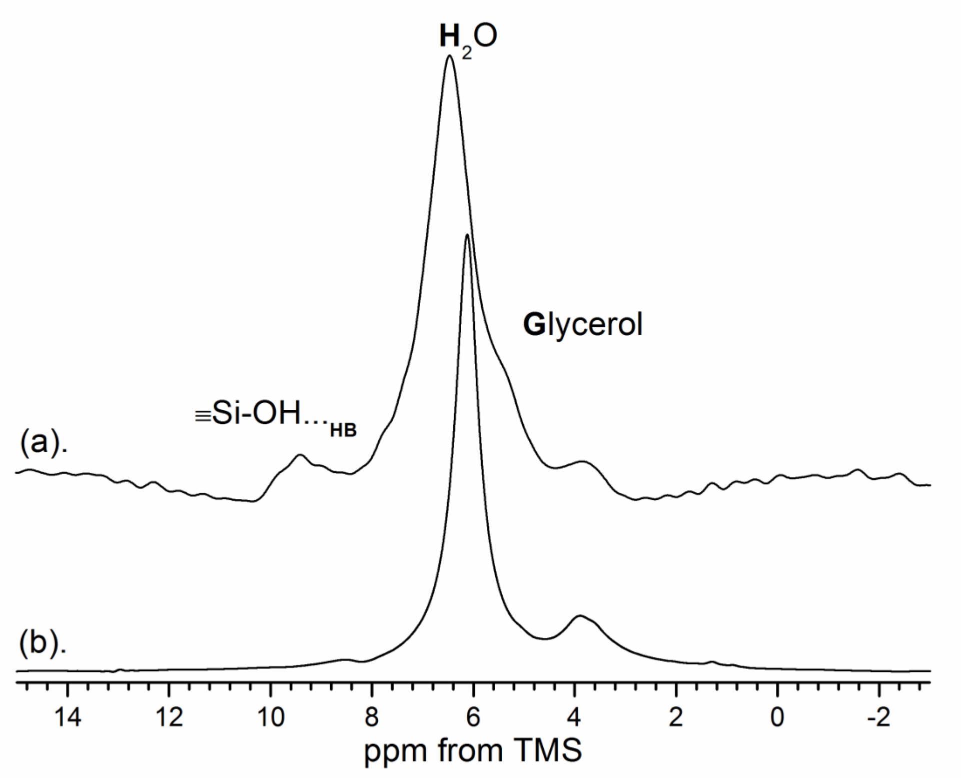

Figure 4.15 (a). ^{1}H MAS NMR spectrum of the CS2G hydrogel acquired using DUMBO decoupling at an MAS rate of 15 kHz on a 500 MHz BRUKER AVANCE III spectrometer and (b). ^{1}H MAS NMR spectrum of a deuterated CS2G analogue acquired at an MAS rate of 30 kHz on 400 MHz BRUKER DSX spectrometer

4.5 Structure and Dynamics of Water

The ^{1}H MAS NMR spectra for the CS2 hydrogels showed a broad resonance which was assigned to water molecules involved in a network of hydrogen bonds. In order to gain a better understanding of the structure and dynamics of water within the CS2 hydrogels, variable temperature T_1 and T_2 relaxation time measurements were conducted. In particular these measurements can address the following questions regarding the water networks:

1. Is the polyol distributed throughout the water network, as well as being close to the silica/water interface?

2. If statement 1 is correct, does the polyol then act to alter the hydrogen bonding networking of water?

3. Therefore, can different water phases be distinguished?

Points 1 and 2 can be addressed by variable temperature ^{1}H T_1 measurements; if an interaction exists between the polyols and water then this would be shown through different T_1 relaxation times measured for different peaks due to heterogeneous spin diffusion. The interaction would also influence the Arrhenius relationship of the molecular correlation time of the water molecules resulting in different activation energies across the hydrogel series. Point 3 is investigated using ^{1}H T_2; discriminating different types of water phases by fitting the rate of decay using exponential components. Therefore, if a biexponential decay is used to fit the decay curves it suggests two water phases are present.

4.5.1 *Variable Temperature* ^{1}H T_1 *Relaxation Measurements*

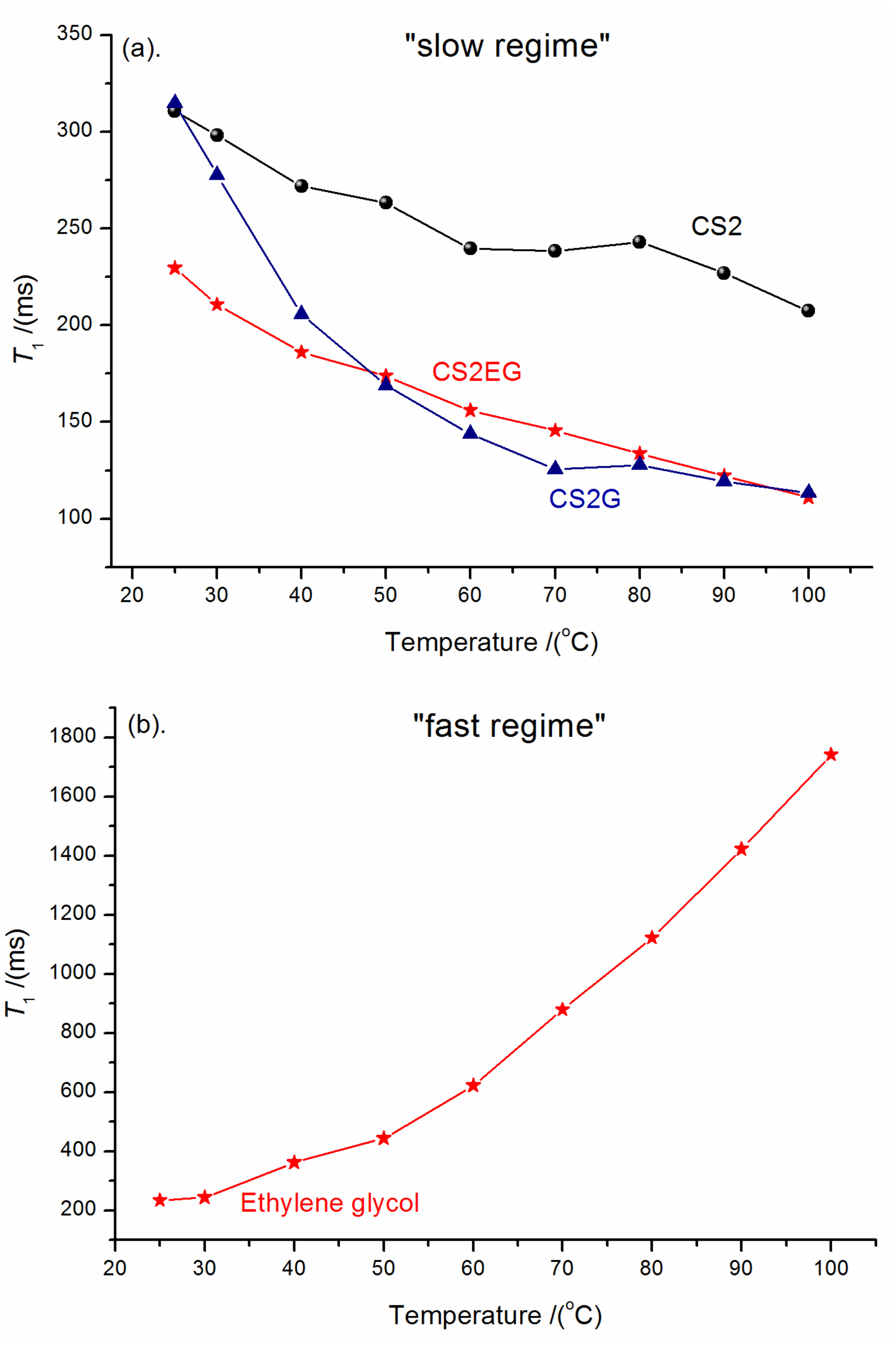

Figure 4.16 Variable temperature T_1 spin-lattice relaxation times for the protons associated with (a) water and (b) the –CH_2- protons in ethylene glycol within the CS2 hydrogels. Average error values are ± 5 to 10 ms.

Figure 4.16 (a). shows a *decrease* in T_1 relaxation times for the water protons as a function of increasing temperature across the CS2 series. The CS2 hydrogel exhibits longer ^{1}H T_1 values compared to the CS2EG/G hydrogels. For comparison, the T_1 relaxation times for the –CH_2- protons in the CS2EG hydrogel are also plotted against temperature and are shown **Figure 4.16. (b).** In this case, the –CH_2- protons show an almost linear *increase* in T_1 relaxation times with temperature.

4.5.1.1 Dynamics of the water and polyol molecules

The difference in the T_1 relaxation times for the water and –CH_2- protons can be explained using the BPP theory, which was detailed in **Chapter 2**. For a spin-1/2 nucleus, the spin-lattice relaxation is given by:

$$\frac{1}{T_1} = \frac{3\gamma^4\hbar^2}{10r^6}\left[\frac{\tau_c}{1+\omega_0^2\tau_c^2} + \frac{4\tau_c}{1+\omega_0^2\tau_c^2}\right] \qquad \textbf{Eq. 4.2}$$

Where, γ is the nuclear gyromagnetic ratio, r is the internuclear distance between a proton spin pair, ω_0 is the nuclear Larmor frequency of ^{1}H (400 MHz) , $\hbar$ is the reduced Plank's constant and τ_c is the average time taken for the molecule to rotate through one radian. **Eq. 4.2** is used typically to describe the nature of relaxation as a function of temperature whereby a T_1 curve is obtained (see **Chapter 2, Figure 2.12 (b).**). A T_1 minimum is not observed for water or for the –CH_2- protons. This simply indicates that a wider temperature range is required to modulate molecular motion to the extent whereby a new regime is entered. These regimes are:

(1). slow regime: $\omega_0^2\tau_c^2 >> 1$ (molecular motions are slower than the ω_0 *i.e.* 400 MHz for ^{1}H)

(2) intermediate regime: $\omega_0^2\tau_c^2 \sim 1$ (molecular motions are comparable to ω_0)

(3). fast regime: $\omega_0^2\tau_c^2 << 1$ (molecular motions are faster than ω_0)

The water protons can be described as being in the slow regime. As T_1 relaxation times decrease the values of τ_c become smaller and therefore mobility increases as a function of temperature. The T_1 relaxation times for the polyol hydrogels are overall *shorter* compared to the polyol free hydrogel. This implies that the water molecules in the polyol hydrogel are *more mobile* than the water molecules in the polyol free hydrogel. The fast regime accounts for the behavior of the –CH_2- protons. The rapid mobility of the –CH_2- protons reduces the efficiency of spin diffusion as the dipolar interaction is modulated. This is evidenced by the increase in T_1 relaxation times as a function of temperature. These results highlight the different motional regimes in which the water and –CH_2- protons are engaged in as a function of temperature. The response of the ethylene glycol molecules towards the change of temperature and the effect this has on the optical properties of the hydrogel is discussed in more detail in the next chapter. The relaxation times for glycerol protons could not be fitted due to the inability to resolve the resonances because of strong homonuclear couplings.

4.5.1.2 Nature of the water hydrogen bonding networks

The T_1 relaxation times for the water protons in the CS2EG and CS2G hydrogels are shorter compared to those in the polyol free hydrogel. The difference in the relaxation rates indicates different spin-diffusion processes for the water network in the presence of the polyols. This indicates that some of the polyols are distributed throughout the water network. We can gain more information on how the polyols affect the water hydrogen bonding networks by calculating the activation energy for molecular reorientation of water if we assume that the τ_c follows an Arrhenius type law.

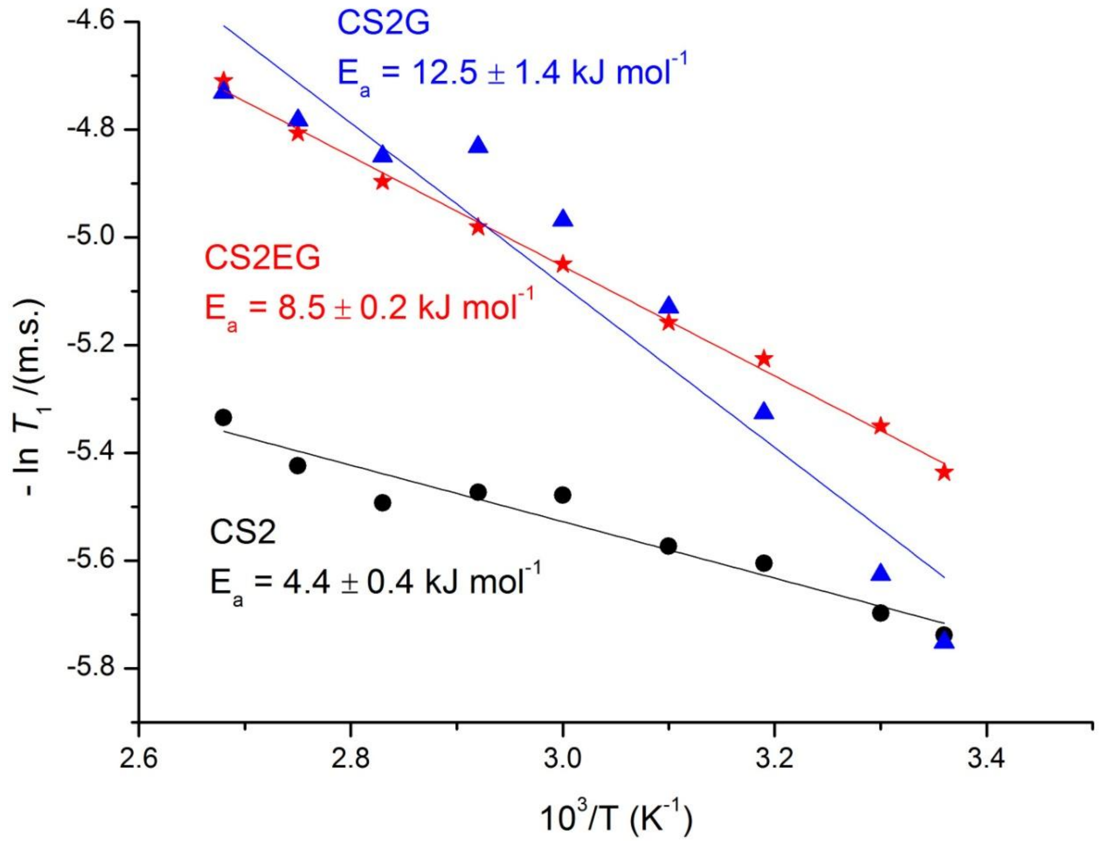

Figure 4.17 Arrhenius plots of –ln T_1 as a function of inverse temperature for the protons associated with water in the CS2 hydrogels and corresponding E_a values obtained from the gradient

Figure 4.17 shows Arrhenius plots of –ln T_1 as a function of inverse temperature for the water molecules residing in CS2, CS2EG and CS2G hydrogels with corresponding activation energies of 4.4, 8.5 and 12.5 kJ mol^{-1}. In the absence of polyols, the water molecules are assumed to be in a hydrogen bonded network separated by silica clusters and coordinated to sodium in different hydration spheres. It is also important to mention that the activation energies are not a true representation of the actual energies involved due to the effect of MAS. MAS modulates the homonuclear dipole-dipole interaction, hence values stated here are lower than if measurements were obtained under static conditions. For example, pure water has two activation energies: 15.5 to 19.0 ± 0.5 kJ mol^{-1} in the temperature ranges of 5 – 27 °C and 40 to 90 °C, respectively.[350] The two values of activation energies highlight the effect of temperature on the hydrogen bonding networks. In the high temperature range, the hydrogen bonds are weakened thus a lower E_a value is obtained.

We can assess the values across the series qualitatively and rationalise the effect of polyol addition upon the water networks. The increase in activation energies as a function of polyol addition could be due to two processes (1) the polyol interrupts the water networks by establishing different hydrogen bonding modes (2) the water molecules aggregate as a result of the hydrophobic parts of the polyols. The latter point has been confirmed by Totland *et al.*[351] who showed that the addition of 1-heptanol to pure water increases the activation energy from 19.5 to 21.5 kJ mol^{-1}. However, 1-heptanol is far more hydrophobic compared to ethylene glycol or glycerol. It is more likely that the polyols interact with the water molecules by forming hydrogen bonding networks *via.* the hydroxyl groups. The increase in activation energy of water domains as a function of hydroxyl groups was investigated further by measuring the E_a for a sorbitol doped hydrogel. Sorbitol contains 6 hydroxyl groups and was found to increase the activation energy of water to 19.2 kJ mol^{-1}.

In the literature, numerous studies investigate aqueous mixtures of glycerol or ethylene glycol as cryoprotectants agents. These mixtures are used to preserve the functionality of biological molecules and inhibit the formation of ice within membranes. The mechanisms by which the solutions penetrate the cellular membranes and function can be found in the following references.[352-354] The general hypothesis in which these agents act is by modifying the water structure, thus inhibiting ice formation. To this end, the physical properties of glycerol (to a lesser extent, ethylene glycol) and water have been studied. The majority of these studies use molecular dynamics (MD) simulations to predict the change in the hydrogen bonding network of pure water as a function of glycerol addition, usually on dilute aqueous (less than 0.100 mole fraction) glycerol solutions. However, conflicting conclusions are reported; Chen *et al.*[355] and Politi *et al.*[356] studied dilute aqueous glycerol solutions (0.06 to 0.133 mole fraction) independently. Using MD simulations they suggested that glycerol acted to diminish the hydrogen bonding ability of water molecules. Conversely, Towey *et al.*[357] used neutron diffraction experiments in conjunction with MD simulations on

0.05 mole fraction glycerol solutions. They conclude "while the local structure of water is relatively unperturbed by the presence of glycerol, the hydrogen bonded network is highly mixed between glycerol and water... the action of glycerol should focus on not just the local water structure, but the extended hydrogen bonded network in the system." Egorov *et al.*[358] studied concentrated glycerol solutions, 42.9 and 60.0 wt %, using MD simulations. They indicate that some of the glycerol exists as monomers, solvated by water whilst some form hydrogen bonded networks. The T_1 relaxation results are in good agreement with the results reported by Towey[357] and Egorov *et al.*[358]; this suggests that some of the polyol molecules are dispersed throughout the bulk water affecting the extended hydrogen bonding network, whilst the some are located close to the silica clusters.

We have shown that water in the CS2 hydrogel exhibits slower motions compared to the CS2EG and CS2G hydrogels with a corresponding decrease in the E_a values. It is expected that a reduction in mobility would require more energy for reorientation processes to occur but is not observed here. The discrepancy between water mobility and E_a energies in the polyol containing hydrogels could be explained by the presence of *two* water phases. The main phase corresponds to bulk water whose network of hydrogen bonding is slightly different in each hydrogel. The second phase, only present in the CS2EG and CS2G hydrogels corresponds to water and polyols involved in a modified hydrogen bonding network as outlined by Towey[357] and Egorov[358]. The fact that only a single exponential component is used to interpret the T_1 relaxation times suggests an efficient exchange between the two phases. However, the phases manifest themselves through differences between T_1 relaxation rates and E_a values. This is investigated in more detail using variable temperature T_2 relaxation measurements.

4.5.2 *Variable Temperature ^1H T_2 Relaxation Measurements*

Zimmerman *et al.*[359] first demonstrated the use of variable temperature relaxation measurements for the study of adsorbed water vapour on silica gel. They showed that the T_2 decay for water on a solid surface is multiexponential, with two or more relaxation components corresponding to water in different phases. T_2 measurements yielded a double population whilst a single population was observed from T_1 measurements. The T_2 components are designated as T_2^a and T_2^b. The latter usually represents the population with the shorter relaxation time. O'Reilly *et al.* showed that this component is due to –OH groups on the adsorbent surface and that longer relaxation component (T_2^a) will be due to water physically adsorbed to the surface. Overloop and Van Gerven[360] expanded on Zimmerman's theory by studying water in uniform and nonuniform porous media using higher quantities of water. They showed that water displayed at least two environments with different relaxation rates: (1) water present in the adsorbed water layers close to the surface and (2) bulk water, *i.e.* further away from the surface. The –OH groups of the adsorbent are also considered, but due to proton exchange with adsorbed water it is difficult to observe even in materials containing smaller amounts of water. In an attempt to understand the nature and number of water domains within the CS2 hydrogels, variable temperature T_2 measurements were conducted.

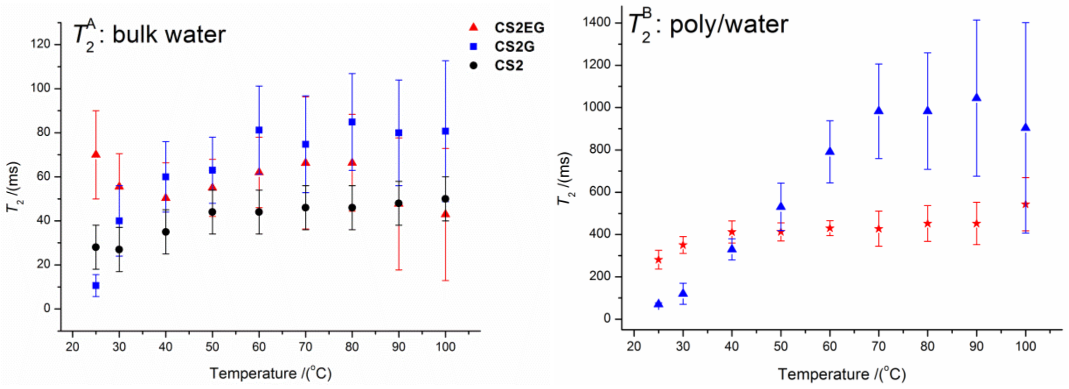

Figure 4.18 Variable temperature T_2 values for the protons associated with water in the CS2 series hydrogels. Left: T_2^a component (major) and right T_2^b component (minor). The latter component is only present in the CS2EG/G hydrogels.

Figure 4.18 shows the dependence of T_2 times of water protons as a function of temperature within the CS2 hydrogels. The water protons in the CS2G and CS2EG hydrogels are fitted using a double exponential decay, whereas a single exponential decay is used for the CS2 hydrogel. The T_2^A component can be assigned to bulk water with the T_2^B component corresponding to a poly/water phase, discussed previously. The absence of the second component for the polyol free hydrogel also confirms this assignment. The fact that there are two types of water environments in the polyol hydrogels explains why higher activation energies are obtained for the CS2EG and CS2G hydrogels. An interfacial silica/water phase will exist but because of the amount of water within the hydrogels this component cannot be distinguished. The water phases with and without polyol are represented in **Figure 4.19**.

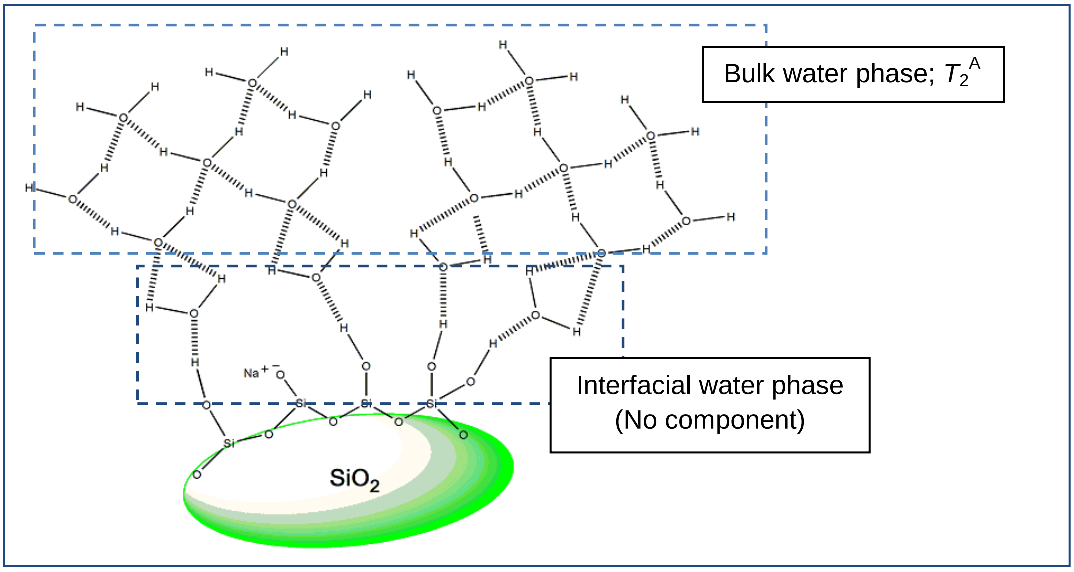

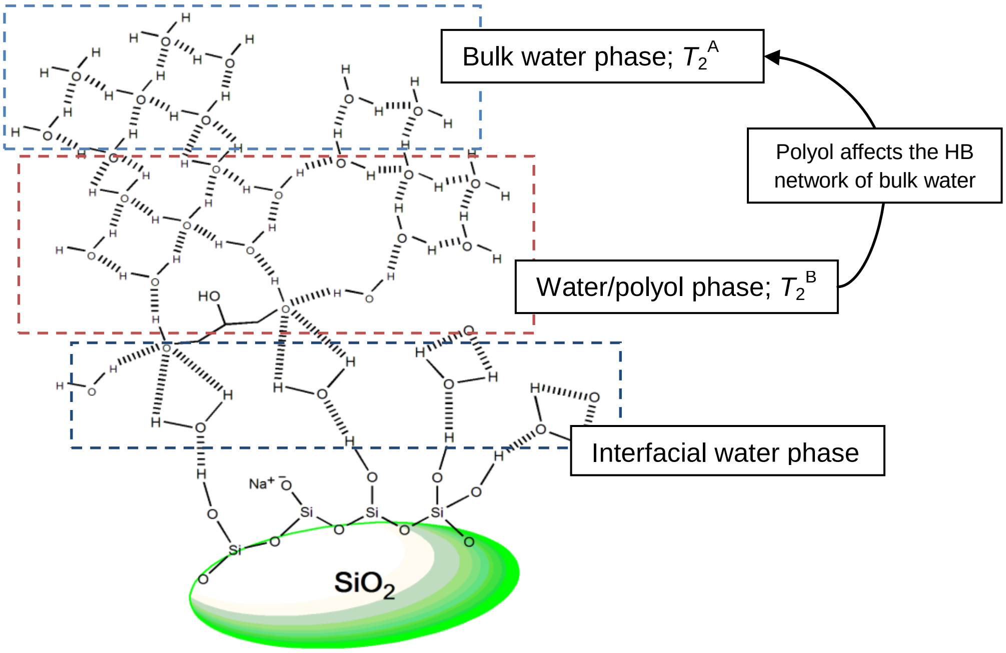
Bulk water phase; T_2^A
Polyol affects the HB network of bulk water
Water/polyol phase; T_2^B
Interfacial water phase
HO
Na^+
Si
SiO_2

Figure 4.19 Water phases present within the CS2 (top) and CS2EG/G hydrogels (bottom). *Note:* Polyols are also present at the silica/water interface but have been omitted for clarity

4.6 Distribution of polyols in hydrogels

^{1}H spin–lattice relaxation measurements of polymer blends have been reported.[230, 231] If two polymers are miscible, the relaxation decay of the mixture can be described by a mono-exponential equation, whereas if they are not miscible, relaxation decay corresponds to a bi-exponential equation. The qualitative assessment used for polymer blends can be applied in the study of glycerol distributions within the CS2G hydrogel. This is a similar approach to the T_2 measurements above whereby different domains can be distinguished:

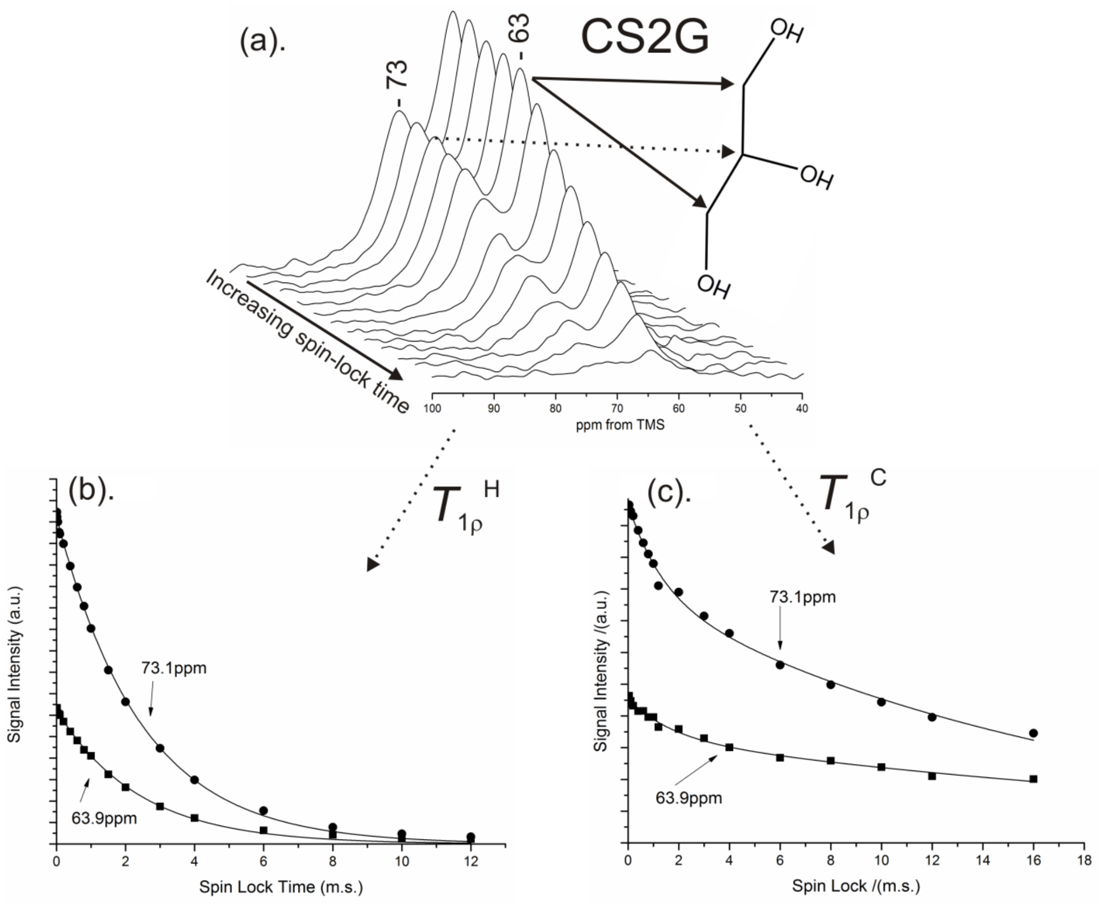

Figure 4.20 (a). The exponential decay of the glycerol carbon signals as a function of increasing spin-lock times representative within the CS2G hydrogel. The signal decay curves of the two sites are then plotted against spin-lock times to yield exponential decays (b). and (c)., from which the $T_{1\rho}$ relaxation times are calculated. We implement different pulse sequences, shown in **Chapter 3**, to obtain $T_{1\rho}^{H}$ and $T_{1\rho}^{C}$ relaxation times.

Table 4.4 $T_{1\rho}^{H}$ relaxation times obtained from a single-exponential decay fit for glycerol within the CS2G hydrogel

Resonance /δ_{iso}	**Signal Intensity /(a.u.) 1x10^7**	**$T_{1\rho}^{H}$ /(ms)**
73.1	7.11 ± 0.03	2.45 ± 0.04
63.9	3.12 ± 0.02	2.38 ± 0.06

Table 4.5 $T_{1\rho}^{C}$ relaxation times obtained from a single-exponential decay fit for glycerol within the CS2G hydrogel

Resonance /δ_{iso}	**Signal Intensity /(a.u.) 1x10^7**	**$T_{1\rho}^{C}$ /(ms)**	***Component***
63.9	0.54 ± 0.06	1.31 ± 0.25	$T_{1\rho}^{C}$(A)
	1.58 ± 0.07	17.8 ± 1.43	$T_{1\rho}^{C}$(B)
73.1	0.24 ± 0.04	1.70 ± 0.42	$T_{1\rho}^{C}$(A)
	0.67 ± 0.04	29.5 ± 4.91	$T_{1\rho}^{C}$(B)

Table 4.4 and **4.5** gives the $T_{1\rho}^{H}$ and $T_{1\rho}^{C}$ relaxation times fitted using a single and double exponential decay curves, respectively for glycerol within the CS2G hydrogel. The single exponential suggests a homogenous proton spin bath whereby relaxation on kHz motional regime is averaged efficiently across the system. The double exponential behaviour suggests two glycerol domains comprised of short (fast), $T_{1\rho}^{C}$(A) and long (slow) $T_{1\rho}^{C}$(B) times, with the former component in excess. The two domains are a result of two distinct glycerol environments with different relaxation mechanisms. Tentatively, we can assign $T_{1\rho}^{C}$(A) to glycerol molecules at the water/silica interface whilst $T_{1\rho}^{C}$(B) corresponds to the glycerol/water phase. These results are in good agreement with the ^{1}H, ^{23}Na, ^{29}Si data and the relaxation measurements. The results illustrate the heterogeneity of the polyol within the material. These results were also reproduced at different sections within an interlayer. Originally, we set out to prove that a gradient existed within a hydrogel interlayer due to the convection mixing of the solution phase during the drying stage. This would be shown by examining the level of enrichment and depletion of various species within the depth profile of the hydrogel. This led us to investigate ‘top’ and ‘bottom’ sections of the hydrogel using $T_{1\rho}$. Although differences in $T_{1\rho}$ times were observed, not enough data were

collected to confirm the presence of the polyol gradient. In light of this we propose that future work should focus on using several methodologies including NMR and Raman spectroscopy.

4.7 Conclusions

Amorphous, structurally heterogeneous hydrogels with and without polyols have been investigated using SSNMR. The ^{29}Si CP MAS NMR experiments indicate that as the *wt.* ratio of the hydrogels increases so does the extent of silica condensation. The silica networks comprise of Q^3,Q^2,Q^4 and Q^1 units. Two distinct sodium environments were revealed through ^{23}Na MQMAS and assigned on the basis of their quadrupolar coupling parameters and through comparisons with literature. The octahedral site **a**, is present in all of the hydrogels whereas the trigonal bipyriamidal site **b**, is established in the absence of polyols. This indicated that some of the polyol must be located close to the silica/water interface. The ^{1}H MAS NMR experiments showed little fine structure due to strong homonuclear dipolar couplings. However, in the CS2 hydrogel the downfield resonance corresponding to a ≡Si-OH···O interaction associated with the Na site b is clearly observed. Variable temperature T_1 and T_2 relaxation measurements showed that in each hydrogel the water networks are involved in different hydrogen bonding environments. The calculated E_a energies of the water hydrogen bonding interactions increased as a function of increasing polyol chain length. The $T_{1\rho}$ relaxation measurements showed two glycerol domains, consistent with the results obtained from the T_1 and T_2 data. Using the results, molecular level models of the CS2 hydrogels with and without polyol are presented:

CS2 Hydrogel

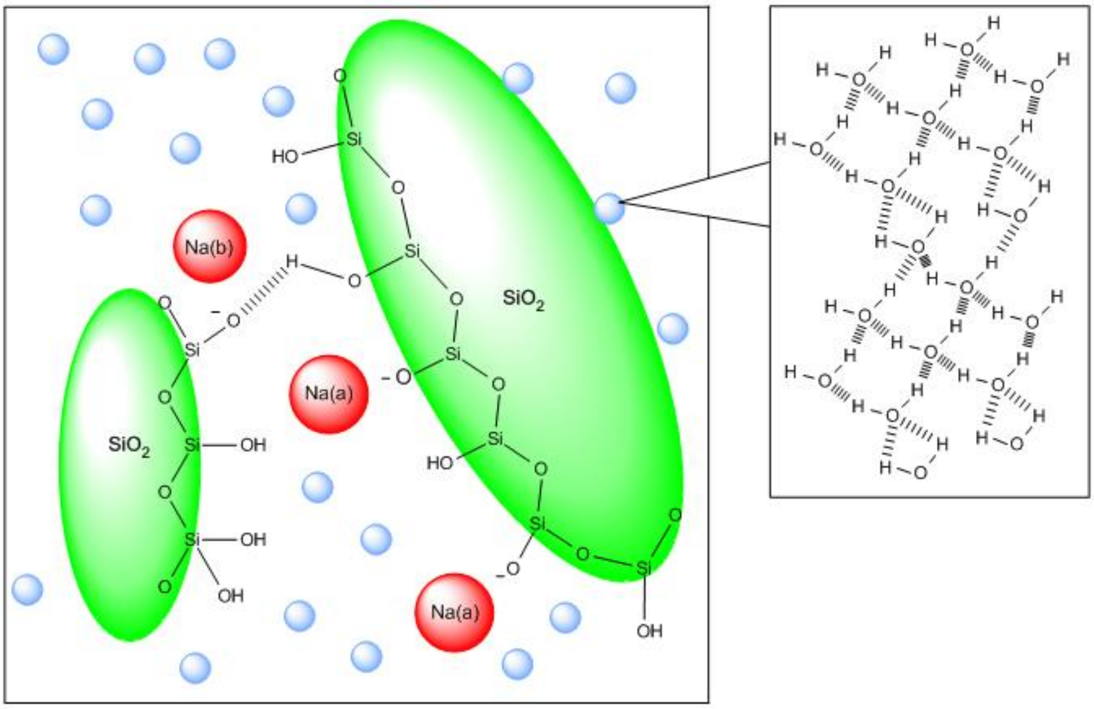
SiO2
SiO2
Na(b)
Na(a)
Na(a)
Si
O
OH
HO
H

CS2G Hydrogel

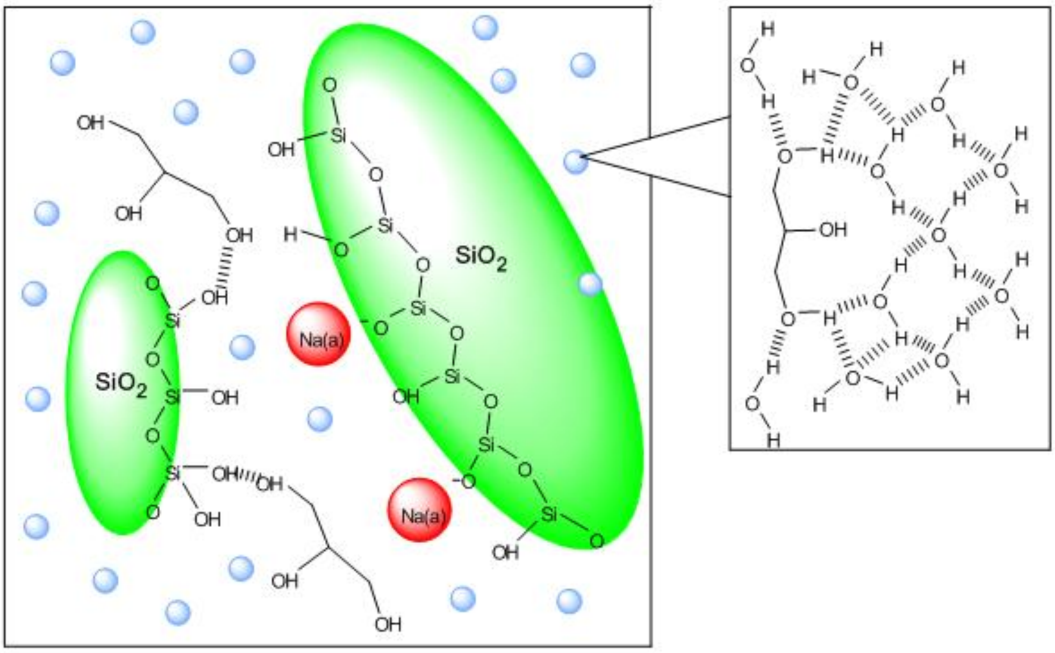
SiO2
SiO2
Na(a)
Na(a)
Si
O
OH
H

Figure 4.21 Proposed models of the CS2 and CS2G hydrogels

The hydrogels can be visualised as dynamic systems in which condensed silica units (less than 3 nm in diameter, as larger units would results in a loss of transparency) are in a sea of complex hydrated sodium/polyol/water networks. Whilst we have probed the local atomic environments and dynamics of the systems, it would be interesting to "map"/image the water networks and/or track water/polyol diffusion. For example, if a hydrogel is imaged using MRI (using either T_1 or T_2 weighted images) it would probably yield a homogenous picture of water distributions due to similarity in relaxation times. In the literature, Weerasekare *et al.*[361] show that the sol-gel transition of a peptide gel can be visualised but only when a Gd(III)-chelate contrast agent is added. These agents significantly change the relaxation times of water, which, in the images show up as different areas of brightness. Following on from this, if a Gd-polyol or a similar metal-polyol could be synthesised and doped into a hydrogel, it may be possible to map areas of water/polyol distributions for an in-situ analysis of the products. Alternatively, Salvati *et al.*[362] use MRI with chemical shift resolution to provide detailed information about the release of poly(ethylene glycol) and imidazole from a hydrogel into an external reservoir of water. However, these gradient techniques rely on well resolved ^{1}H spectra. A T_2-filter pulse can be used to separate chemical shifts based on their T_2 relaxation times. This was attempted on the hydrogels but because of the similarity in relaxation times between water and polyol the filter simply removed the majority of signal. What certainly is feasible for future work is to investigate the glycerol heterogeneity and indeed other polyols using variable temperature $T_{1\rho}^{C}$ and wide-line separation NMR experiments (WISE)[363], which correlates the dynamic information to specific carbon environments. Also the possibility of using pulse-field gradients (PFGs) combined with MAS to determine glycerol diffusion at variable temperatures could be possible.[364, 365] The ability for the system to diffuse and reorganise is investigated in the next chapter.

Chapter 5

Investigation into the thermal stability of the CS2 hydrogels

5.1 Introduction

The hydrogels serve as effective fire resistant materials. Temperatures in excess of 100°C induce the fire response which was covered in **Chapter 2**. In this chapter the effect of heating the hydrogels in a lower temperature regime; up to 100°C was investigated. The results are split into two sections according to the length of time the hydrogels were subjected to heating. Static heating was conducted using short (less than 24 hour) and long (more than 24 hour) time periods. The first section includes visual inspection and results obtained from VT ^{1}H MAS, ^{1}H-^{13}C HETCOR and DSC experiments are used to investigate the short term thermal stability of the CS2 hydrogels. The CS2 and CS2G hydrogels remain transparent between 25 and 100°C. Conversely the CS2EG hydrogel shows a reversible change of optical properties; from 30°C onwards the material is white opaque, and upon cooling transparency is restored. The visual properties were correlated with changes occurring at the molecular level using SSNMR and are used to explain the opacity of the CS2EG material. Following on from this, the second section presents the results obtained from heat ageing of the hydrogels over a period of 20 days. The hydrogels crystallise into makatite upon static heat ageing. These transparent materials become increasingly translucent and eventually opaque as a result of the crystallisation process. The irreversible degradation of optical clarity was assessed using haze measurements and visual inspections. Crystal formation and growth were tracked using X-ray diffraction. Solid-state NMR experiments based on ^{23}Na MAS, ^{1}H-^{29}Si CP/MAS and ^{23}Na MQMAS NMR provided information on the local atomic structures of the materials during the transformation. Optical measurements, XRD and NMR results indicate that the addition of glycerol can hinder the crystallisation process over the ethylene glycol and polyol free hydrogels. This is explained by the labile ethylene glycol molecules which dissociate away from the silica units when exposed to temperature above 30°C

5.2 Short term ageing

5.2.1 *Temperature-dependent transparency and structural changes in the hydrogels*

The following figures include VT ^{1}H MAS NMR spectra and full-width half maximum values of the ^{1}H resonances. Images are obtained of the hydrogels after annealing at 100°C for 4 hours.

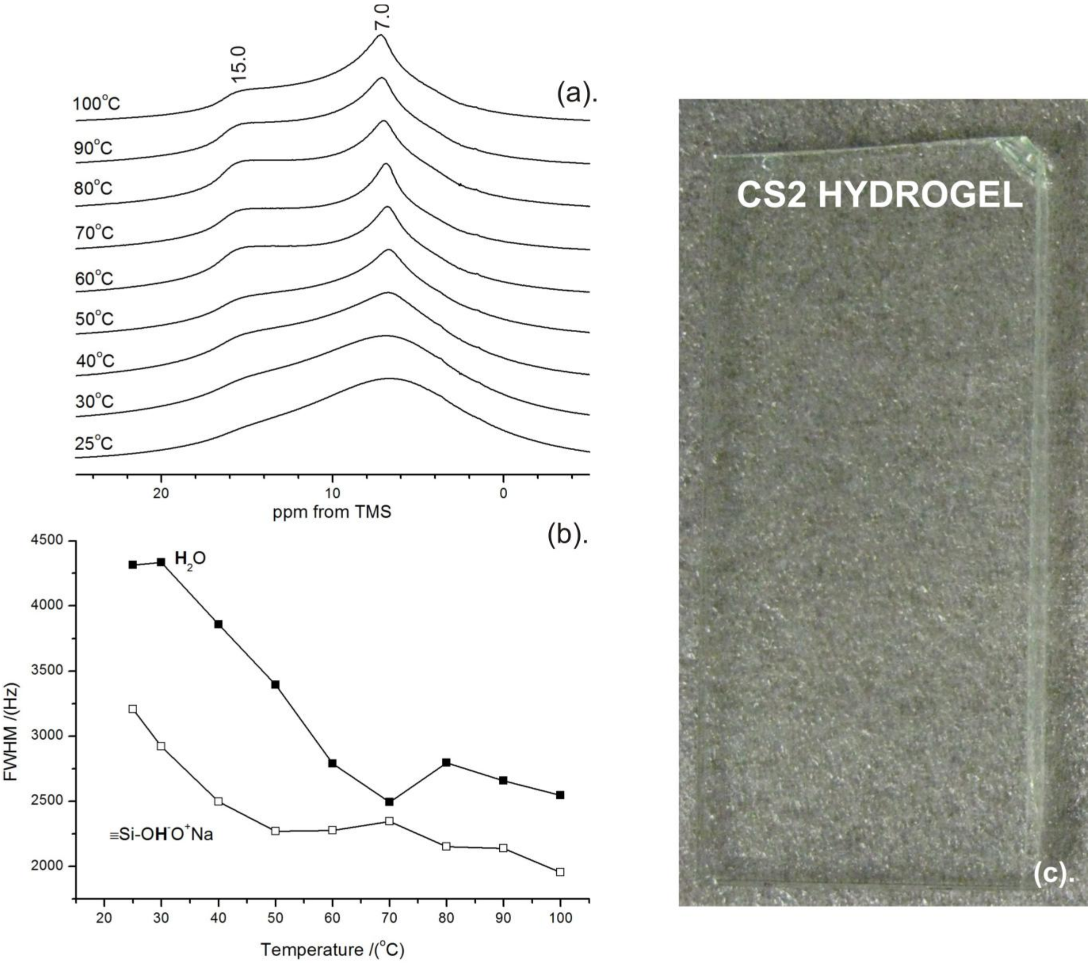

Figure 5.1 (a). Variable temperature ^{1}H MAS NMR spectra of CS2 hydrogel acquired at an MAS rate of 10 kHz (b). Temperature dependence on FWHM values for the water protons and strongly hydrogen bonded silanol protons and (c). Image of the CS2 hydrogel at 100°C. The hydrogel was subjected to heating at 100°C for 4 hours.

Figure 5.1 (a). and **(b).** shows the change in ^{1}H resonances and line widths respectively as a function of temperature for the CS2 hydrogel. The resonances for the water and silianol protons become narrow with increasing temperature, which is shown by a general decrease in FWHM values. The

^{1}H MAS NMR spectra show no additional resonances but a reduction in FWHM values as a function of temperature, indicating an increase in molecular motions. **Figure 5.1 (c).** Indicates that CS2 hydrogel remains transparent from room temperature up to 100°C.

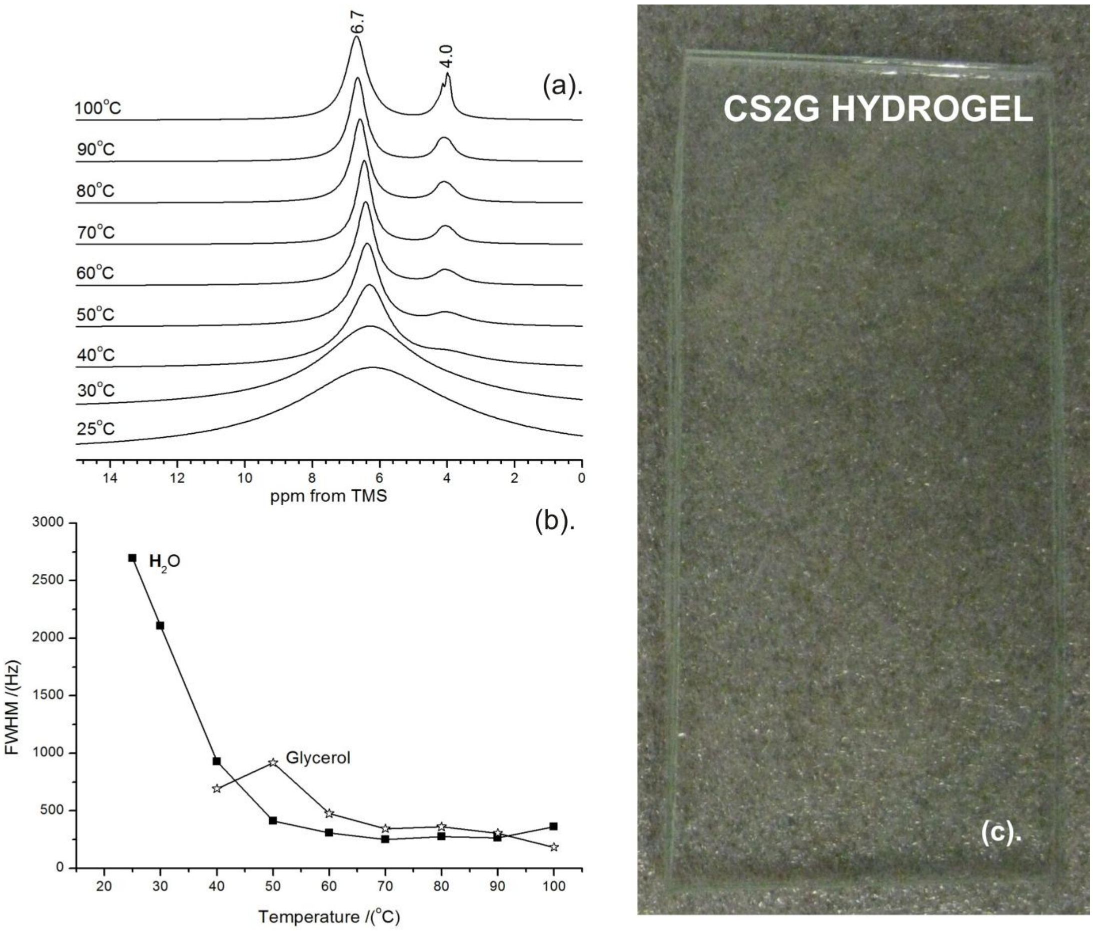

Figure 5.2 Variable temperature ^{1}H MAS NMR spectra of the CS2G hydrogel acquired at an MAS rate of 10 kHz (b). Temperature dependence on FWHM values for the water protons and glycerol protons and (c). Image of the CS2G hydrogel at 100°C. The hydrogel was subjected to 100°C heating for 4 hours.

In the glycerol hydrogel, the ^{1}H MAS NMR spectra show that two components at *ca.* 6.7 and 4.0 ppm can be resolved at temperatures above 30°C. **Figure 5.2 (b).** shows a decrease in line-widths for water and glycerol protons with increasing temperature. This indicates a rise in molecular motion and, hence, a reduction in the strength of ^{1}H-^{1}H dipolar couplings. Indeed, at 100°C, the broad resonance at 4.0 ppm shows fine structure corresponding to the different proton environments in the glycerol molecule.

The hydrogel remains transparent from room temperature to 100°C which is shown in **Figure 5.2 (c).**

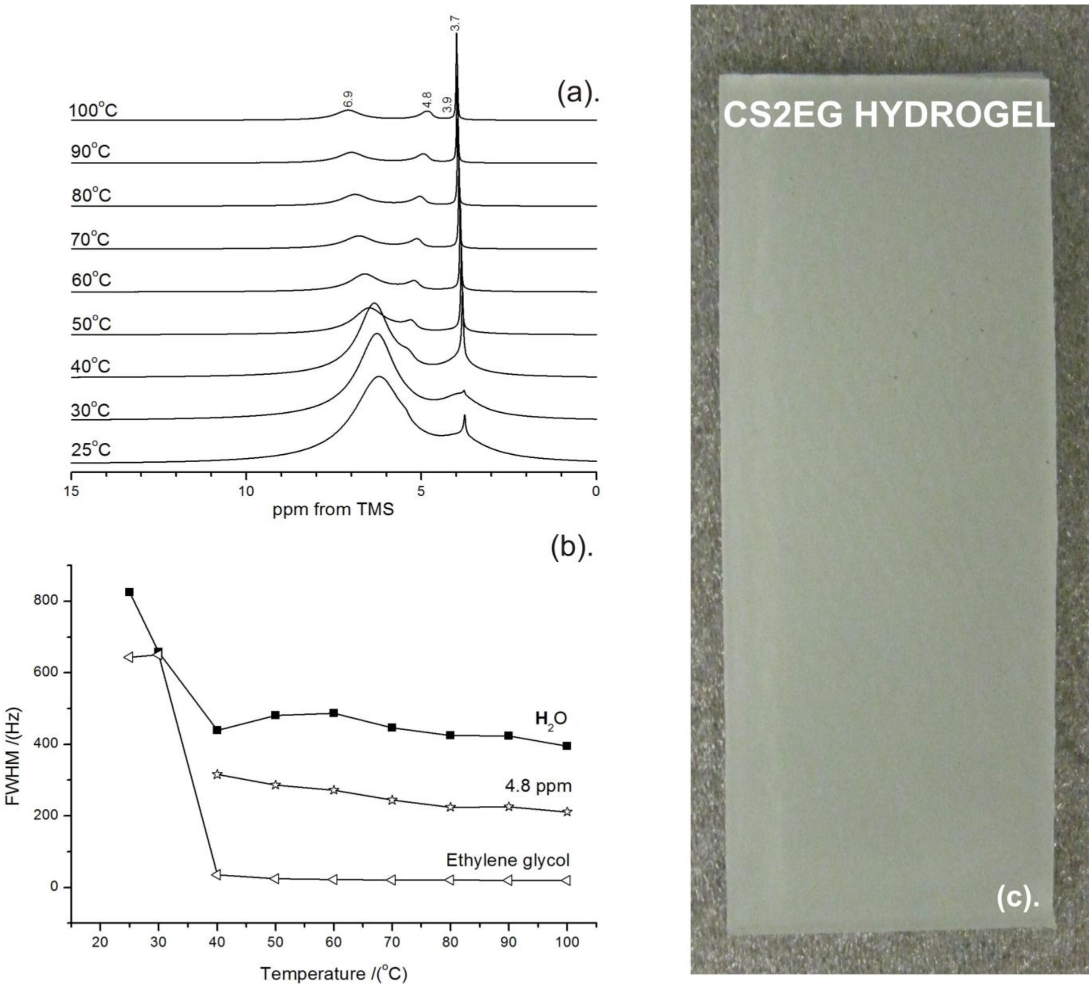

Figure 5.3 Variable temperature ^{1}H MAS NMR spectra of the CS2EG hydrogel acquired at an MAS rate of 10 kHz; (b) Temperature dependence on FWHM values for the water protons, resonance at 4.8 ppm and –CH_2-protons in ethylene glycerol; (c) Image of the CS2EG hydrogel at 100°C. The hydrogel was subjected to 100°C heating for 4 hours.

Figure 5.3 (a). and **(b).** shows the ^{1}H MAS NMR spectra and FWHM values for the CS2EG hydrogel as a function of temperature. There are significant changes in ^{1}H spectra, FWHM values and optical properties for the CS2EG hydrogel: From 30 to 40°C onwards the –CH_2- protons in ethylene glycol manifest as a sharp resonance at 3.7 ppm whose FWHM values decrease from 630 to 20 Hz indicating rapid molecular motion. This is also evidenced from the VT T_1 relaxation measurement in the previous chapter. We showed that the $–CH_2$- protons are in the "fast regime" opposed to the "slow regime" describing the mobility of water.

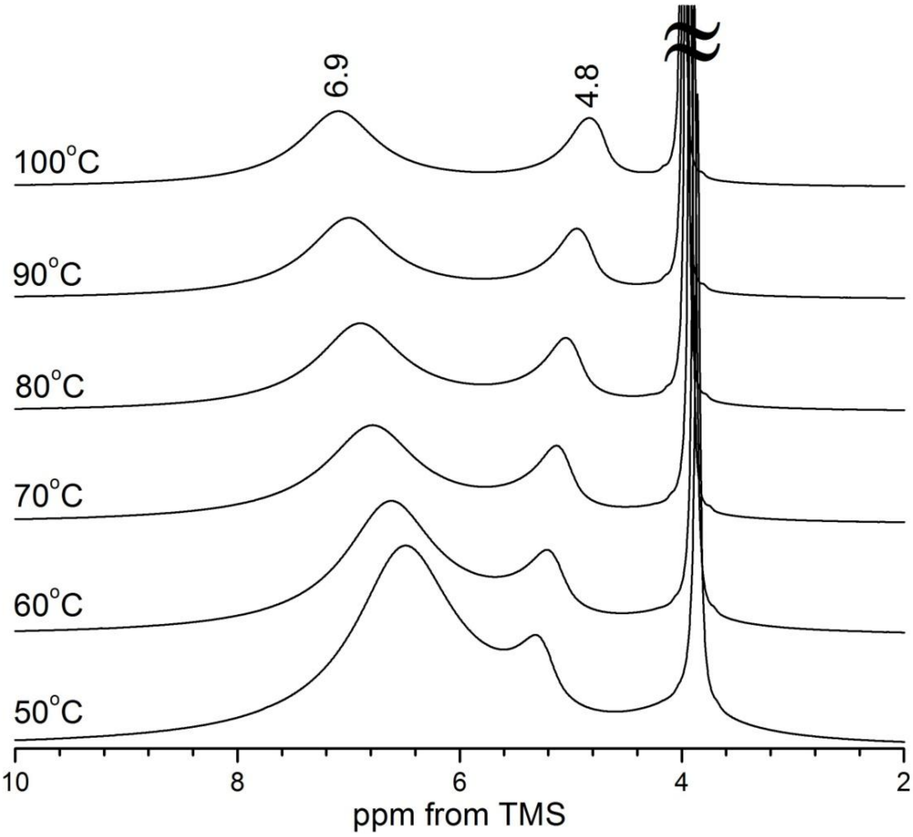

Figure 5.4 Variable temperature ^{1}H MAS NMR spectra of the CS2EG hydrogel acquired at an MAS rate of 10 kHz

Figure 5.4 shows the ^{1}H MAS NMR spectrum of the CS2EG hydrogel in more detail. There is an increase in signal intensity of the 4.8 ppm resonance as the 6.9 ppm resonance decreases as a function of temperature, on this basis, the resonance at 4.8 ppm is assigned to a second water domain, H_2O(II). This is consistent with the results of Jeong *et al*.[366] who investigated poly(vinyl butyral) (PVB) gels with different *wt* % water loadings using variable temperature ^{1}H MAS NMR and gravimetric methods. They observe sharp resonances between 5.0 and 4.9 ppm assigned to different "free" water domains. These domains are consistent with the resonance at 4.8 ppm. The resonance is apparent above 30°C and is associated with the ethylene glycol molecules resulting in an ethylene glycol/H_2O(II) component separated from the bulk water/silica phase. Therefore, the change in optical properties of the hydrogel could be explained by phase separation and is discussed later in this chapter. The process is reversible; when the hydrogel is cooled to room temperature transparency is restored. To investigate this hypothesis further, VT ^{1}H-^{13}C HETCOR experiments were used to clarify the polyol/silica proximity at room temperature and at 50°C.

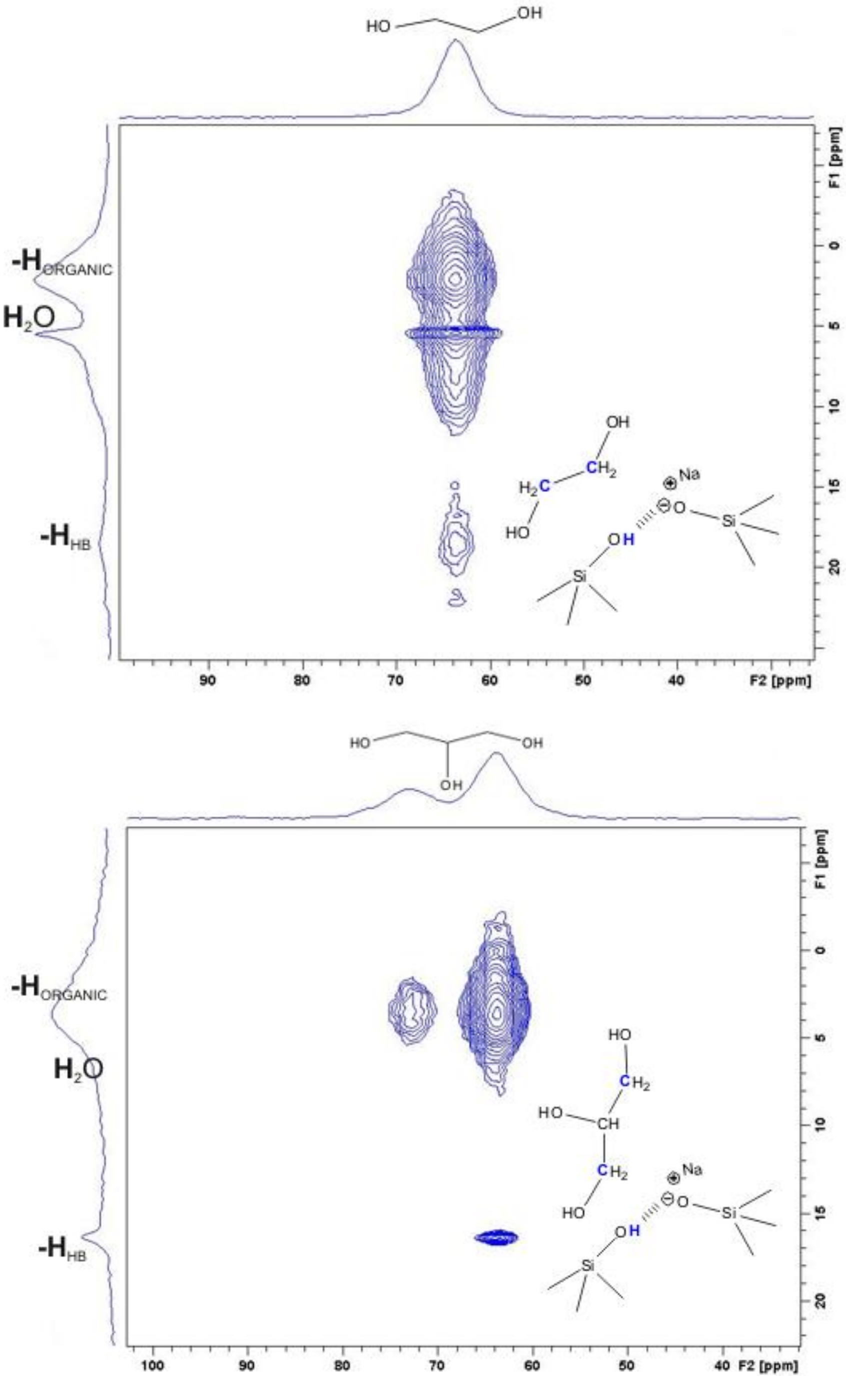

Figure 5.5 ^{1}H-^{13}C HETCOR NMR spectra of (top) CS2EG and (bottom) CS2G acquired at room temperature. The f_1 projection shows the ^{1}H indirect dimension correlating to the f_2 ^{13}C direct dimension

The HETCOR spectra is a 2D contour plot that correlates ^{1}H to ^{13}C distances of ~ 0.3 nm[367] through dipolar couplings. The spectra in **Figure 5.5** consist of ^{1}H (f_1 dimension) and ^{13}C (f_2 dimension) resonances; those of which are in close proximity to one another are represented by the blue cross peaks. In the f_1 dimension, the proton resonances in both the CS2EG and CS2G hydrogels are similar to those seen in **Chapter 4, Figure 4.14**, however, the ≡Si-OH¨O environment at 15 ppm can also be resolved. In both hydrogels the polyol and water protons show strong correlations to ethylene glycol and glycerol carbons. The ≡Si-OH¨O environment associated with silicon $Q^{2,\,3}$ sites also correlate to the polyols. This result confirms that a proportion of the polyols are located near the silica units at room temperature.

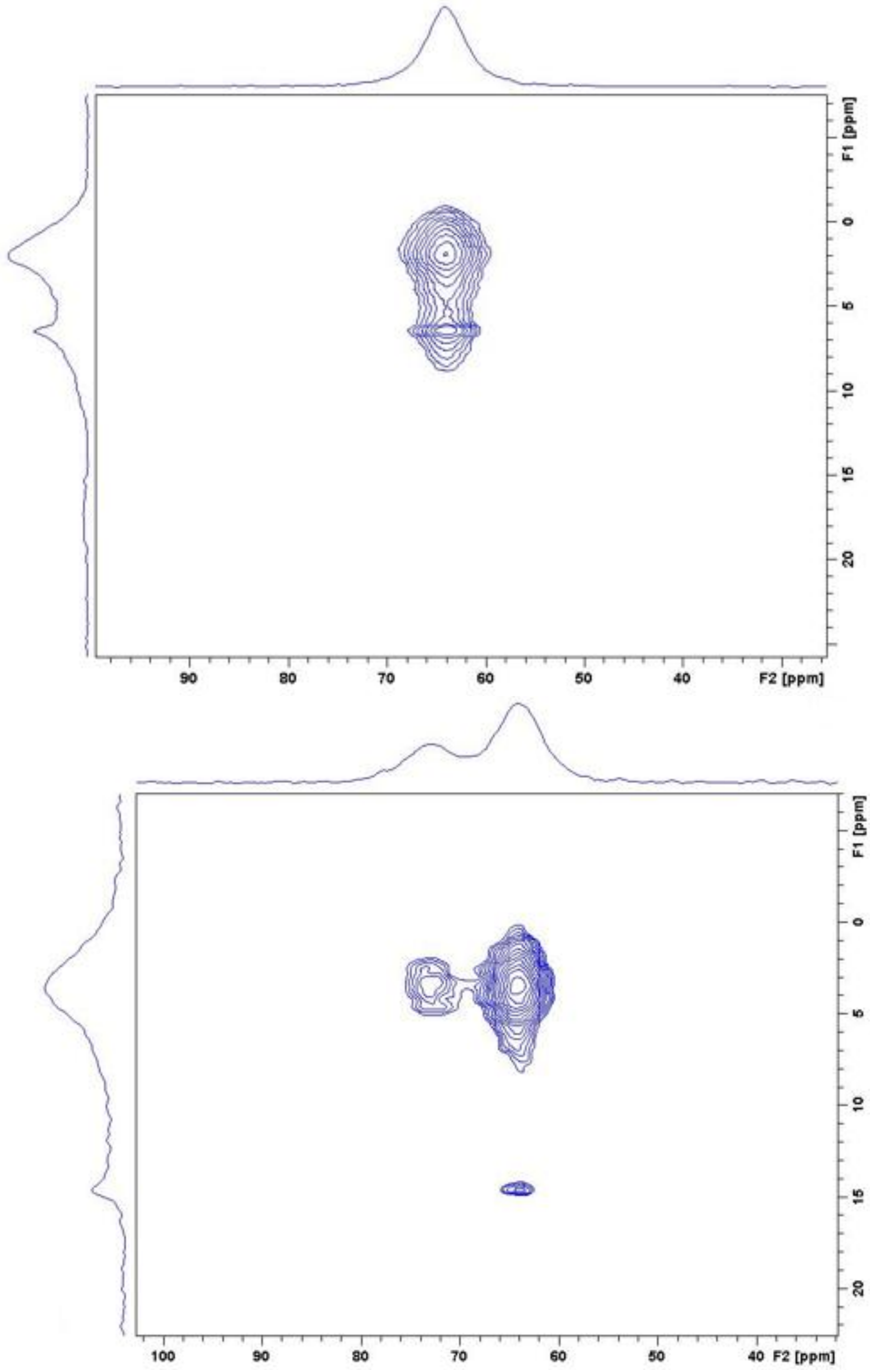

Figure 5.6 ^{1}H-^{13}C HETCOR NMR spectra of (top) CS2EG and (bottom) CS2G acquired at 50°C.

Figure 5.6 (top) shows the HETCOR spectrum of the CS2EG hydrogel acquired at 50°C. The correlation between the polyol and water protons to the ethylene glycol carbons is present, but the ≡Si-OH$^{\cdot\cdot}$O to ethylene glycol interaction has disappeared. The HETCOR experiment relies on the presence of through space ^{1}H–^{13}C heteronuclear dipolar interactions and the strength of the correlation is, therefore, dependent upon distance and mobility of the ^{1}H-^{13}C spin pair (see **Chapter 2**). Strong correlations are seen for short ^{1}H-^{13}C distances and slow mobility. Weak correlations are observed for longer distances and faster mobility. Indeed, as temperature is increased the ethylene glycol molecules become mobile and weaken the ^{1}H-^{13}C interaction but this alone does not account for the loss of correlation. There is also a physical separation between the polyol and the silica units. Conversely, a correlation between glycerol and the $\equiv$Si-OH¨O environment remains.

5.3 Differential Scanning Calorimetry

DSC is an effective analytical tool for characterising the physical properties of a material. DSC enables determination of melting, crystallisation, glass transition and other effects which show changes in heat capacity.[368, 369] DSC was used to further investigate the thermal response of the CS2G and CS2EG hydrogels.

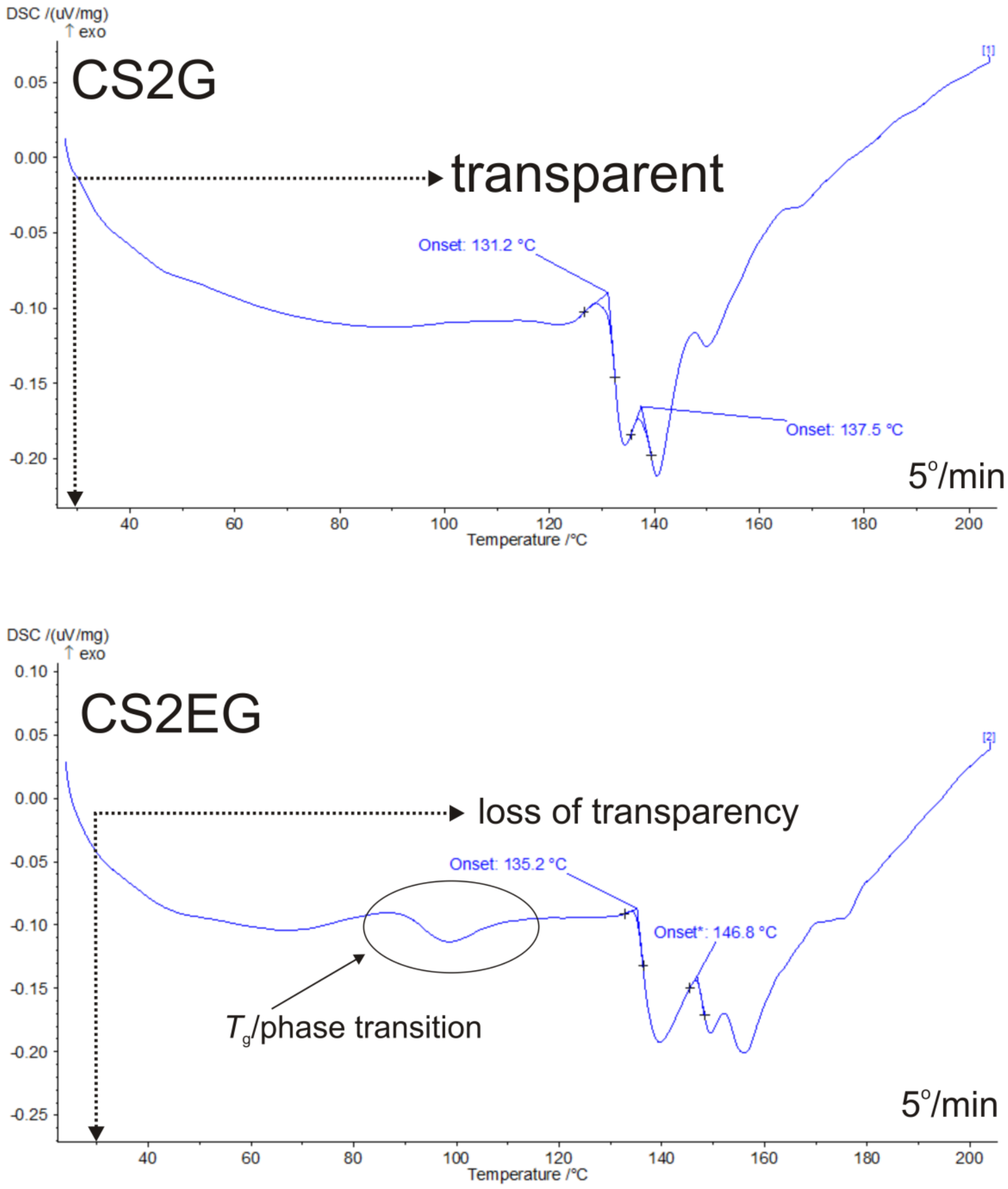

Figure 5.7 DSC thermograph of the CS2G and CS2EG hydrogels at 5° min^{-1}

The DSC heating curves at a rate of 5° min^{-1} for the CS2G and CS2EG hydrogels are shown in **Figure 5.7**. The two hydrogels display a broad endothermic event between 30-100°C and multiple melting peaks between

130-160°C. The former is probably due to transitions associated with water/polyol mobility evidenced from the VT ^{1}H MAS NMR results in **Figure 5.2 (a).** and **Figure 5.4.** The latter peaks could correspond to the bulk water, water-polyol and interfacial silica/water phases, which was elucidated from the relaxation measurements in **Chapter 4**. The CS2EG hydrogel also exhibits an additional peak *ca.* 95°C, which is heating rate dependent. This indicates a possible glass or second order phase transition; as heating rate decreases so does the onset of this peak. This result is in good agreement with the VT ^{1}H MAS and HETCOR experiments which point towards ethylene glycol in a mobile state and its dissociation away from the silica interface.

5.4 Long term ageing

5.4.1 *Tracking makatite crystallisation*

5.4.2 *Powder X-ray Diffraction*

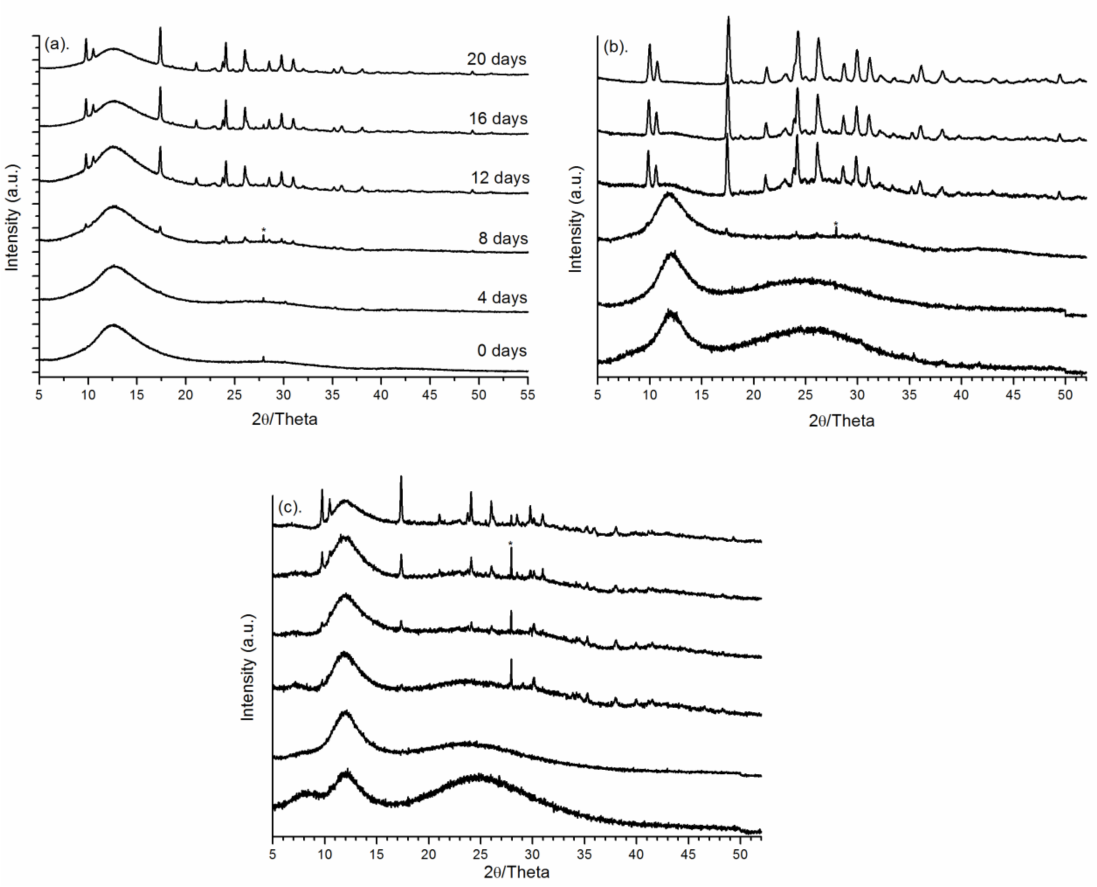

Figure 5.8 XRD patterns of (a). CS2 (b). CS2EG and (c). CS2G [* = impurity.]

Figure 5.8 shows the powder X-ray diffraction patterns of the CS2, CS2EG and CS2G hydrogels heated at 100°C and sampled at 4 day intervals. The initial materials (0 days) show no reflections indicating the absence of a crystalline phase but two features are present; the broad hump at 27° 2θ, is typical of amorphous silica whilst the stronger hump, at 12° 2θ corresponds to the background holder. At 4 days the CS2 hydrogel shows weak reflections at high 2θ indicating the onset of the formation of crystalline product. At 0-4 days the polyol hydrogels show no sign of the formation of a crystalline product as indicated by the featureless patterns. At 8 days a crystalline phase is detected, indicated by the reflections between 15° to 45° 2θ. The emerging crystal phase matches that of makatite.[204-206] The weak reflection at 9.8° 2θ is due to the interlayer spacing with a *d*-spacing value of 9.0 Å, consistent with the literature findings.[185, 204-207, 209] From 12 days onwards both the CS2 and CS2EG hydrogels show an increase in makatite crystallinity as indicated by the increase in reflection intensity with time. The CS2EG hydrogel displays broader reflections compared to the CS2 and CS2G hydrogels and suggests a difference in crystal sizes. The Scherrer equation has been used for determining crystal sizes. However, according to Gribb *et al.*[370] the equation can overestimate crystal sizes by at least 30 nm. Taking this into account, crystal sizes are calculated using the Scherrer equation by:

$$\boldsymbol{D = \frac{K\lambda}{\beta \cos\theta}}$$ **Eq. 5.1**

λ is the X-ray wavelength, K the particle shape factor, taken as 0.9, β is defined as the width at half maximum (FWHM) of the peak and θ the position (angle) of the peak.

Table 5.1 XRD parameters of the [031] reflection used to calculate average crystal sizes.

Hydrogel	**Ageing Time /(Days)**	**FWHM /(2θ)**	**Crystal size /(nm)**
CS2EG	20	0.279	28.8
CS2G	20	0.146	55.1
CS2	20	0.174	46.2

The average crystal sizes in the hydrogels at 20 days are given in **Table 5.1**. The CS2G hydrogel contains the largest crystals, following a decrease in size for the CS2 and CS2EG hydrogels. The difference in crystal sizes suggests a greater number of nucleation sites in the absence of glycerol. The XRD results show that the addition of glycerol can inhibit the formation of makatite over the ethylene glycol and the polyol free hydrogel. To confirm the crystal size calculations, SEM images were obtained.

5.4.3 *Environmental-SEM*

ESEM was conducted on the initial hydrogels and those aged for 20 days and also compared to an image of naturally occurring makatite mineral.

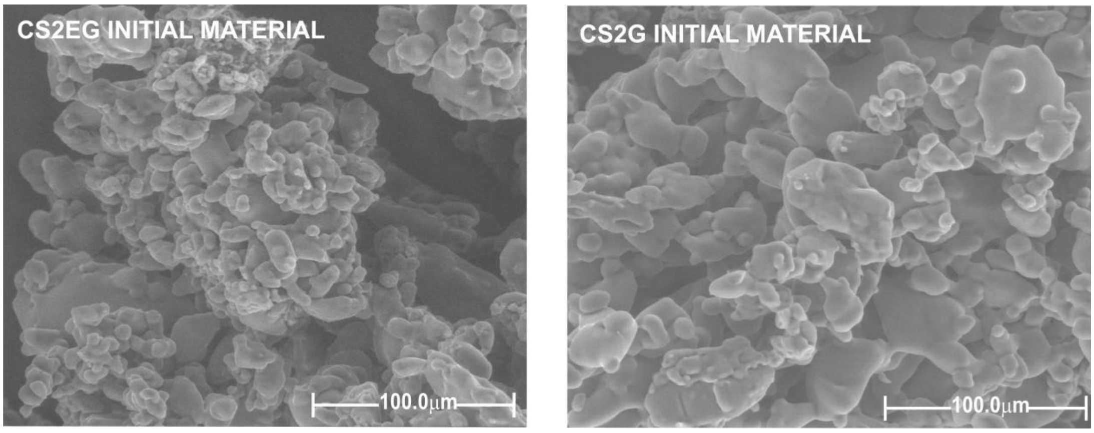
CS2EG INITIAL MATERIAL
100.0µm
CS2G INITIAL MATERIAL
100.0µm

Figure 5.9 ESEM images of the CS2EG and CS2G hydrogels without heat treatment i.e. initial material.

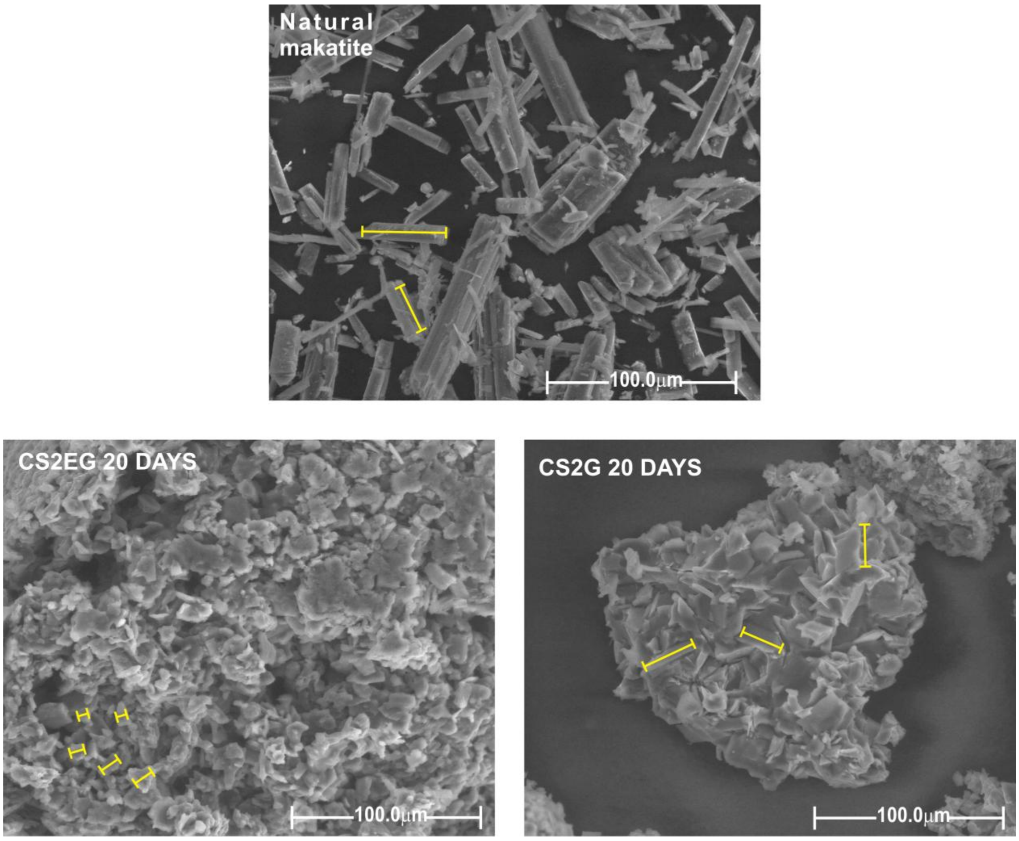
Natural makatite
100.0µm
CS2EG 20 DAYS
100.0µm
CS2G 20 DAYS
100.0µm

Figure 5.10 ESEM images of a natural occurring makatite mineral and CS2EG and CS2G hydrogels heat aged for 20 days. The yellow markers represent average crystal sizes.

The ESEM images in **Figure 5.9** show that the CS2EG and CS2G hydrogel contains ill-defined clusters with sizes larger than 100 µm. The clusters are formed from platelets of connected amorphous silica particles whose surface exhibits nodule like features with diameters of *ca.* 2 µm. The clusters aggregate together due to the sampling technique. These images are also representative of the CS2 hydrogel.

The natural occuring makatite mineral shows rectangular, rod like crystals. Upon heating the morphologies of the hydrogels have transformed into plate like stacks of crystals. They do not exhibit the same shapes as those in natural makatite but this could be because the systems require longer ageing periods to establish better crystal growth. A qualitative inspection of the hydrogel images shows that the CS2EG hydrogel does contain smaller crystallites per unit area compared to the CS2G hydrogel. This confirms the results obtained from XRD. The CS2G image is also representative of the CS2 hydrogel. It is unclear as to why, in the presence of ethylene glycol, nucleation points of makatite are increased.

5.5 Optical Properties

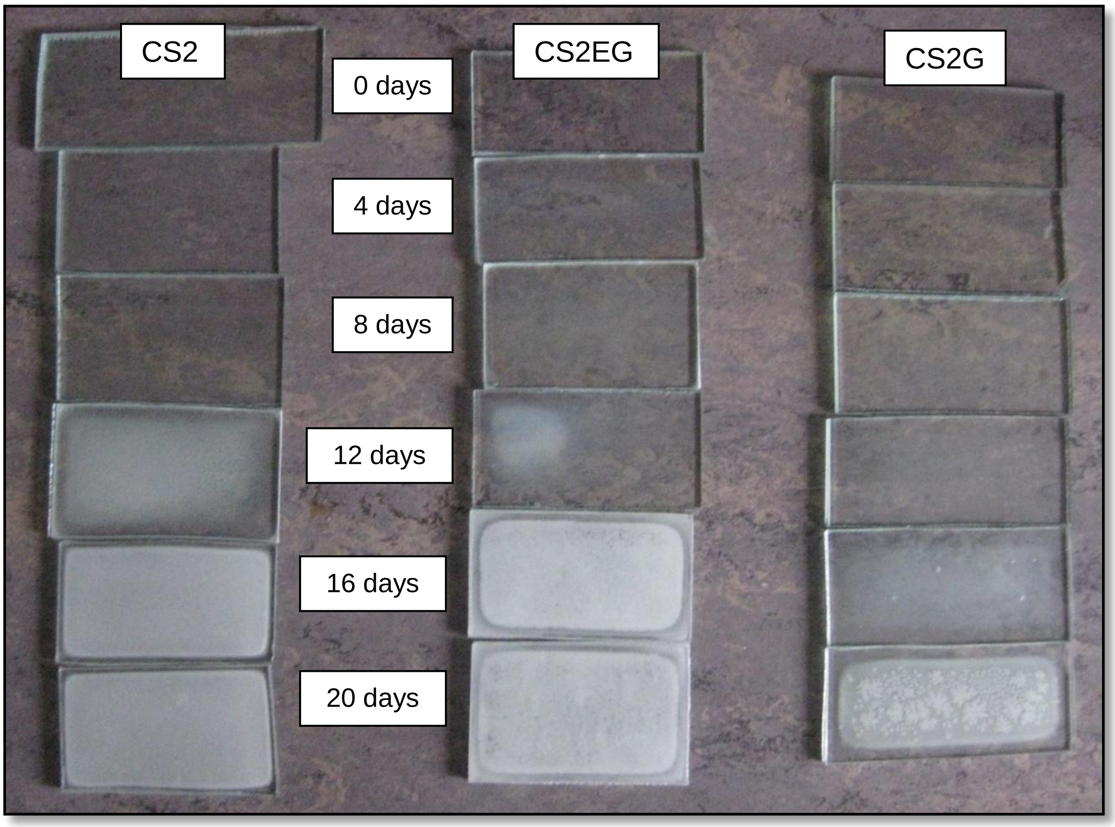
CS2
CS2EG
CS2G
0 days
4 days
8 days
12 days
16 days
20 days

Figure 5.11 Photographs showing the loss of transparency as a function of heat ageing at 100°C in the CS2 (left column), CS2EG (middle) and CS2G (right column) hydrogels.

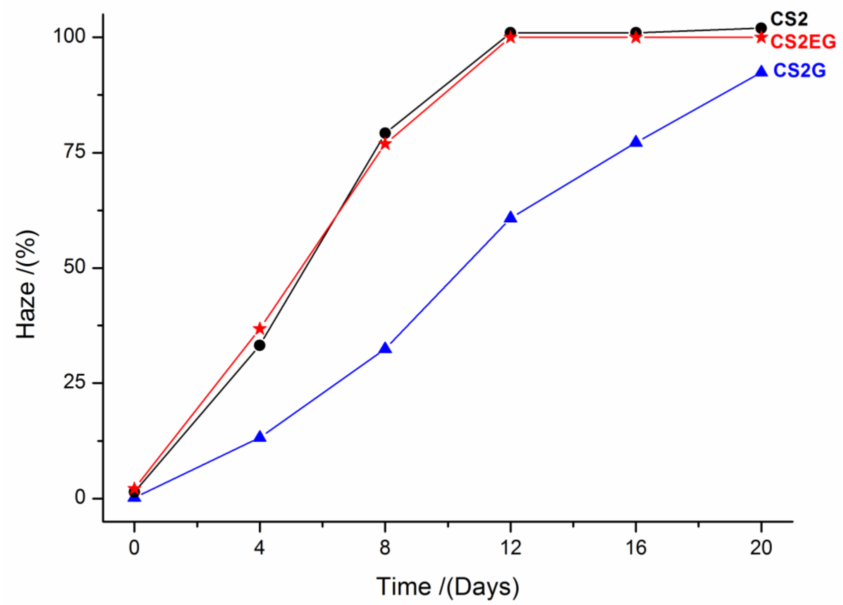

Figure 5.12 Percentage haze as a function of ageing within the CS2 hydrogels

Figure 5.11 and **5.12** show the extent of change in optical properties for each hydrogel as a function of ageing. The initial materials are transparent with hazing values less than 5 %. At 4 to 8 days no visual change in the hydrogels is observed, however there is a significant increase in hazing values. From 12 days onwards the CS2 and CS2EG hydrogels display a ‘photo-frame’ type effect with a white centre and corresponding hazing value of 100 %. The CS2G hydrogel becomes translucent with increasing hazing values. It should be noted that from 28 days onwards CS2G reaches 100% haze and displays the same ‘photo-frame’ feature as the CS2 and CS2EG hydrogels. The rate of optical change is *faster* for the CS2 and CS2EG hydrogels compared to that of the CS2G hydrogel. This is consistent with the formation and rate of makatite crystallisation from the XRD results.

5.6 The Structure of Makatite

We studied a naturally occurring specimen of makatite from Lake Chad in Kenya in order to compare the structure and composition with that of the synthetic makatite formed within the hydrogels. Makatite crystallises in a monoclinic structure with a $P2_1/c$ space group, the XRD pattern for naturally occurring makatite is shown in **Figure 5.13**.

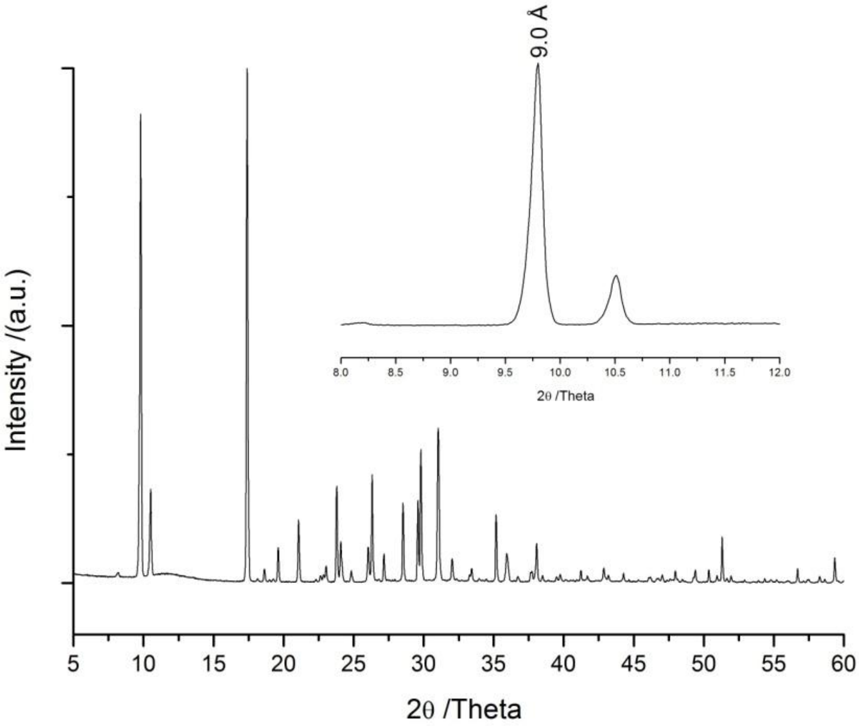

Figure 5.13 XRD pattern of naturally occurring makatite. The reflection at 9.6° 2θ corresponds to the interlayer spacing of 9.0 Å, consistent with the literature.[371]

The structure is built up of $[Si_2O_4(OH)]_n^{n-}$ (Q^3) layers, which is confirmed by the ^1H-^{29}Si CP/MAS NMR spectrum in **Figure 5.15** and consistent with the literature findings. The silicate layer is built of unbranched vierer (German for four) single chains $(Si_4O_{12})_{n.}$ in a unit cell. The chains are parallel to the *a*-axis, and all the free corners in a single chain exhibit undulation i.e. “up and down” structure:

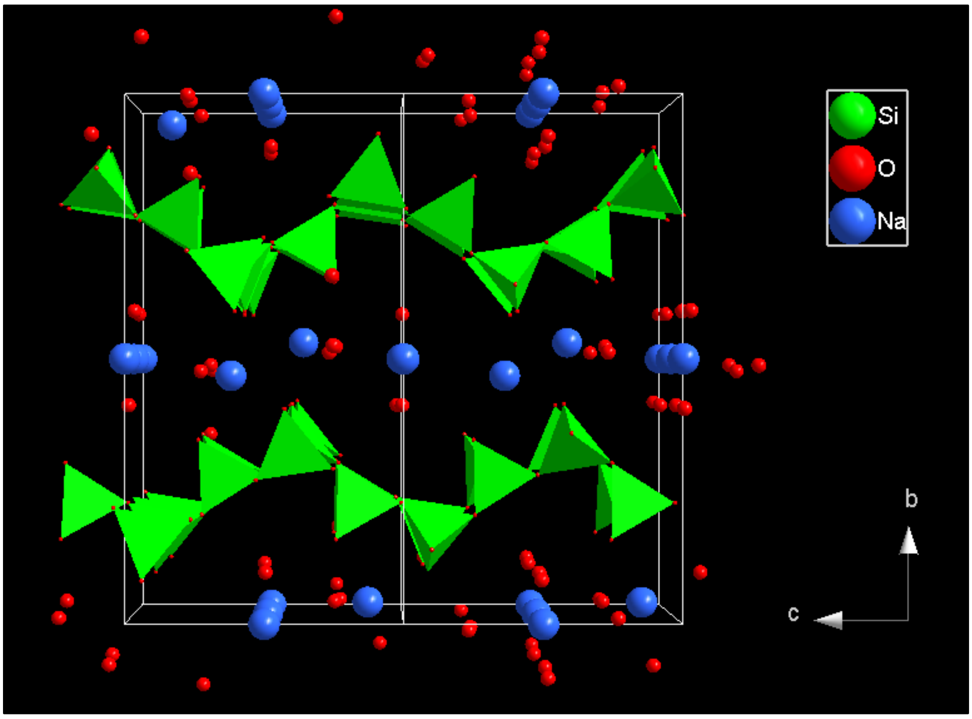

Figure 5.14 View from the a-axis showing the undulation (wave like) of the silicate layers interspaced by hydrated sodium cations in a double unit cell

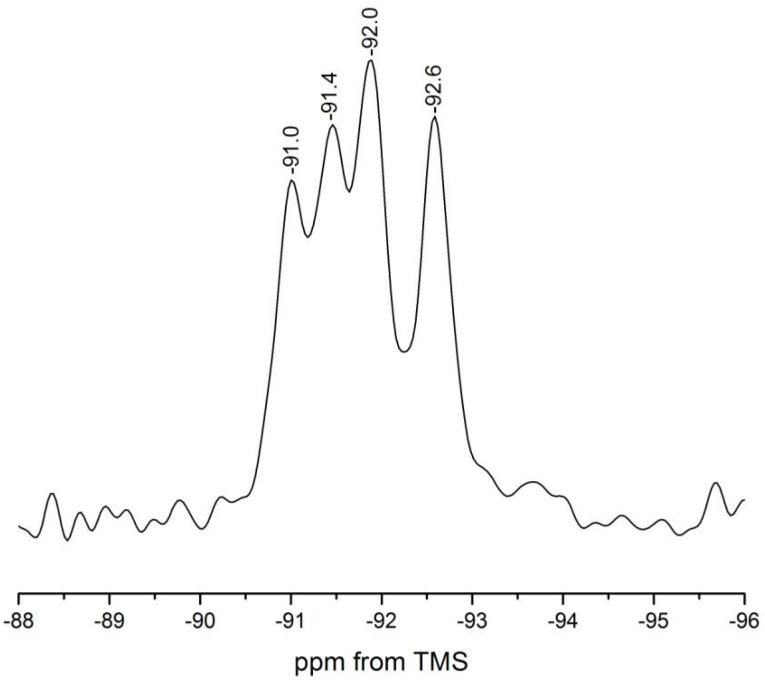

Figure 5.15 ^{1}H-^{29}Si CP NMR spectrum of naturally occurring makatite acquired at an MAS rate of 4 kHz. The resonances between -91.0 and -92.0 ppm are assigned to the three silicon atoms whose silanol groups coordinate with the Na(I) site. The resonance at -92.6 ppm is assigned to the remaining silicon environment not associated with the Na(I) site.[371]

The layers are connected by three different types of Na complexes: Na(II) and Na(III) ions are coordinated to six water oxygen atoms and form edge-sharing octahedral rods parallel to the *a*-axis; these rods are probably connected to the layers by hydrogen bonds. Na(I) is coordinated in a distorted trigonal bipyramid to two water oxygen atoms, which share corners with the octahedral rods, and to three oxygen atoms associated to silanol groups in the silicate layers, thus connecting the layers in *b*-direction. The three Na sites are shown in **Figure 5.16** and are probed using ^{23}Na{^{1}H} MQMAS NMR spectrum in **Figure 5.17**.

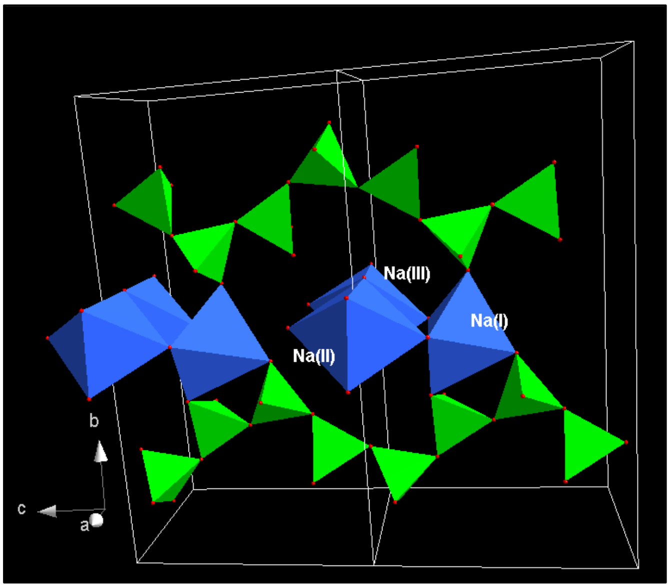

Figure 5.16 Projection of the three sodium sites present within the interlayer space of the makatite. Na(I) in a trigonal bipyramidal geometry coordinating with three oxygen atoms associated with the silanol groups. Na(II) and Na(III) in an octahedral geometry coordinating with water molecules.

The ^{23}Na{^{1}H} MQMAS NMR spectrum of makatite (**Figure 5.17**) shows three different sodium sites with a 1:1:2 intensity ratio (the signal of site I is approximately twice as intense than the other sites) which is consistent with the crystal structure. The quadrupolar parameters (**Table 5.2**) which are obtained from line-shape simulations are similar with those reported by Harris *et al.*[209] The fitting and subsequent quadrupolar parameters obtained for site I are in good agreement with Harris' work. However, there are differences in the quadrupolar parameters for sites II and III. Regarding site II, Harris comments "the spectral shape for site II is still distorted from that of theoretical expectation...simulated spectrum is not good. This is considered to be due to the overlapping of signals from sites II and III." This can be seen in **Figure 5.18** whereby the ^{23}Na MQMAS NMR spectrum of makatite shows the overlap of sites II and III. As discussed in **Chapter 2**, there exists an inverse dependence on the second-order quadrupole coupling with respect to B_0. i.e. the higher the field strength the weaker the quadrupolar interaction. The MQMAS experiment reported by Harris is conducted at 200 MHz (B_0) and our experiments are conducted at 400 MHz. Hence, greater line separation of sites II and III is achieved in our work due to the higher field. The improvement in line separation and resolution results in simulations which are more representative compared to those obtained on lower field spectrometers. Additionally, Harris does not state whether the makatite sample analysed is obtained from nature or synthetically.

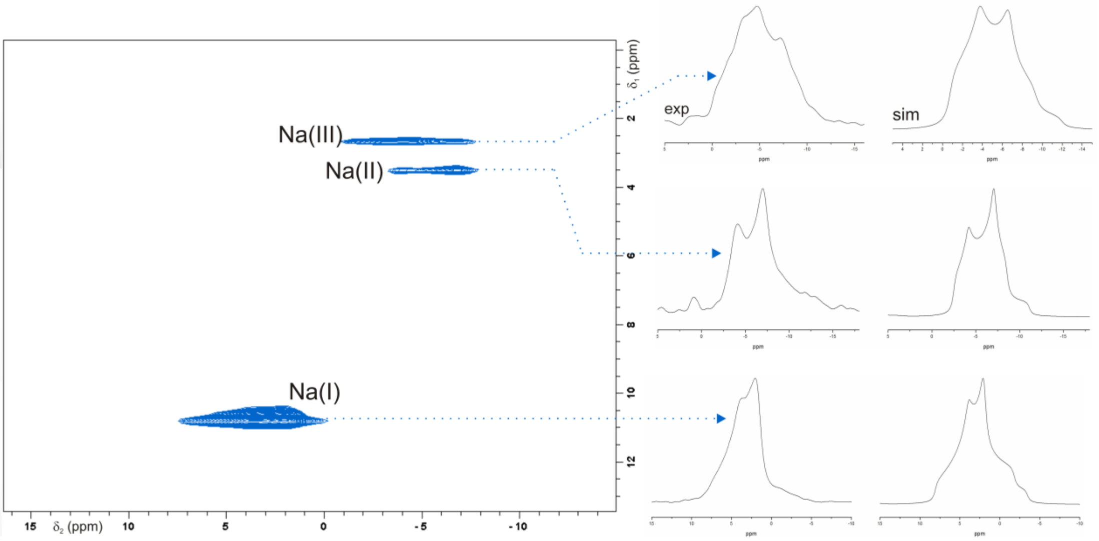

Figure 5.17 ^{23}Na{^{1}H} MQMAS NMR spectrum of makatite. To the right of the spectrum; experimental projections extracted from the MAS dimension with their corresponding simulated spectra, yielding the parameters in **Table 5.4**.

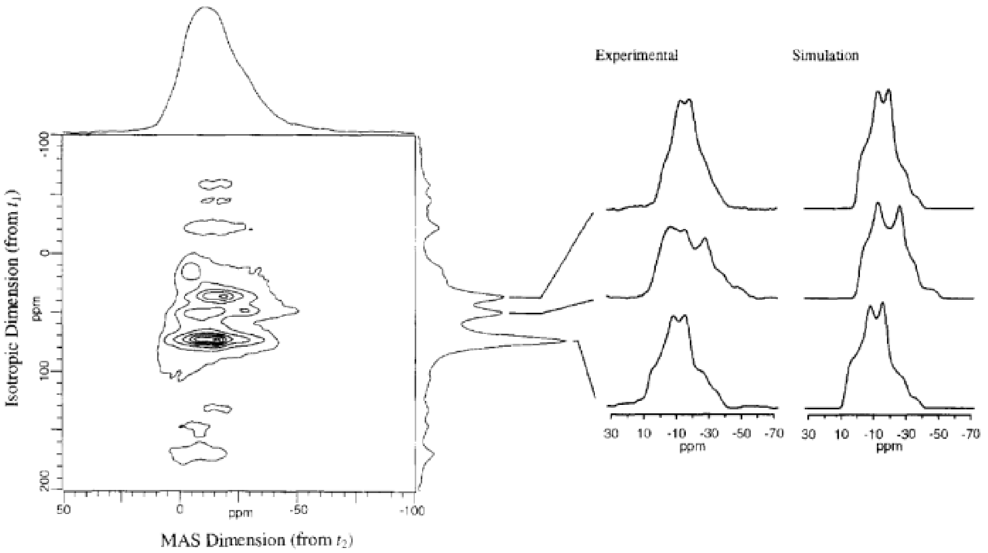

Figure 5.18 ^{23}Na{^{1}H} MQMAS NMR spectrum of makatite with extracted MAS dimensions and their corresponding simulations reported by Harris.[208]

Table 5.2 Isotropic chemical shift (δ_{iso}), quadrupolar coupling constant (C_Q) and asymmetry parameter (η) obtained from line-shape simulations extracted from **Figure 5.17** and **5.18**.

Crystal	Author	Site	δ_{iso} /ppm	C_Q /MHz	η
Makatite	Our work	I	8.3	1.4	0.67
		II	-1.9	1.2	0.32
		III	-0.3	1.4	0.46
	Harris *et al.*	I	8.0	1.4	0.60
		II	1.0	1.5	0.40
		III	0.0	1.4	0.60

5.7 Monitoring changes at the molecular level as a function of ageing

5.7.1 *^{1}H-^{29}Si CP MAS NMR*

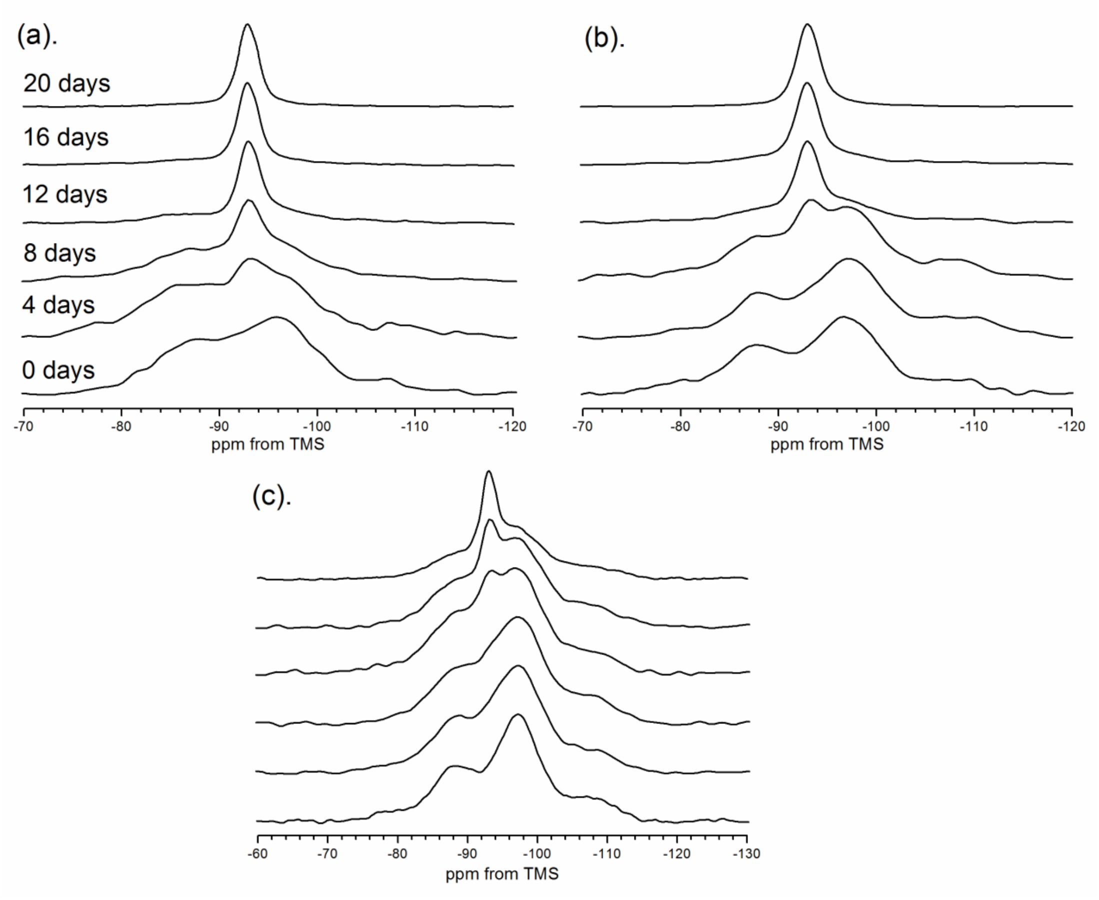

Figure 5.19 ^{1}H-^{29}Si CP/MAS NMR spectra of (a). CS2 (b). CS2EG and (c). CS2G

The ^{1}H-^{29}Si CP MAS NMR spectra of the three hydrogels show the change in silica condensation and speciation as a function of ageing. The initial hydrogels (0 days) contain amorphous $Q^{1,}$ Q^{2}, Q^{3} and Q^{4} units centred at -75 to -115 ppm. At 4 days, a new Q^{3} site at -93.3 ppm corresponding to the formation of makatite (Q^{3}_{m}) is observed for the CS2 hydrogel. This resonance appears at 8 and 12 days for CS2EG and CS2G respectively. The appearance of the makatite resonance in each hydrogel coincides with the appearance of makatite from the XRD data (**Figure 5.8**). At 20 days only a Q^{3} site is present corresponding to the crystalline silica sites in makatite for both the CS2 and CS2EG hydrogels. The progression is slower in the CS2G hydrogel as Q^{2} and Q^{3} sites from the amorphous phase are still observed. The overall reaction results in the condensation of Q^{1}, hydrolysis of Q^{4}

followed by the condensation of Q^2 units. Finally, the rearrangement of amorphous to crystalline Q^3 sites occurs.

5.7.2 *^{23}Na MAS and MQMAS NMR*

^{23}Na MAS and MQMAS NMR experiments were used to probe the sodium environment during the ageing process of the glycerol containing hydrogel.

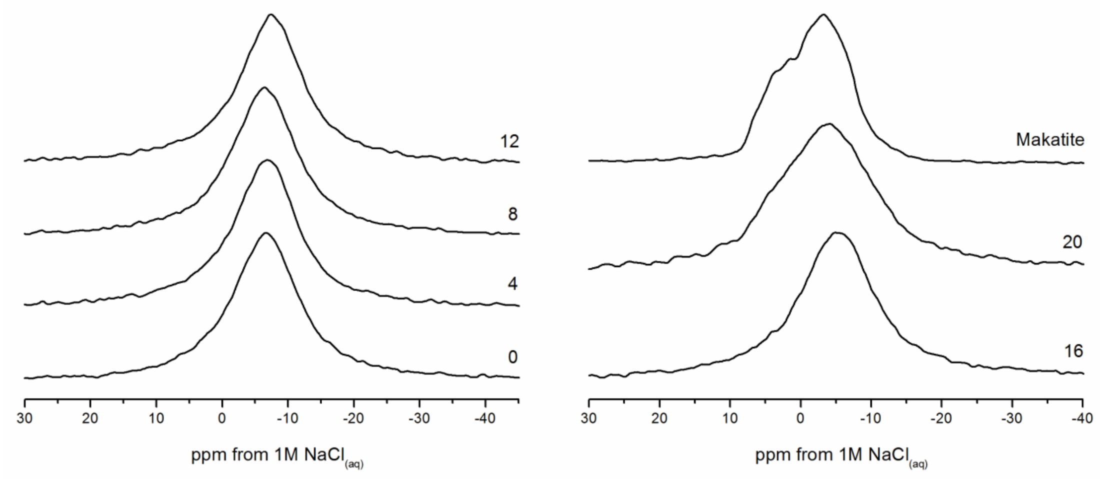

Figure 5.20 ^{23}Na MAS NMR spectra of CS2G hydrogels sampled every 4 days during a 100°C age test. The ^{23}Na MAS NMR spectrum of naturally occurring makatite is shown for comparison.

Figure 5.20 shows the ^{23}Na MAS NMR spectra of the CS2G material sampled every 4 days during a 100°C age test. The spectra for 0 to 12 days display a single resonance with similar chemical shifts and line-widths: -6 to -7 ppm, 1.0 to 1.1 kHz respectively. These broad and featureless lineshapes are typical for amorphous or disordered materials. Although the XRD results indicate the presence of makatite at 8 days, the residing amorphous sodium environments mask the makatite sodium site, hence no change in spectra is observed. From 16 days onwards the spectrum shows a downfield shift with broadening indicating that the majority of the amorphous content has become crystalline, confirmed by the XRD patterns. The spectrum for naturally occurring makatite shows a distorted line shape, consistent with the literature for ^{23}Na MAS NMR experiments.

Table 5.3 Observed chemical shift, δ_{observed}, and FWHM values obtained from the deconvolution of ^{23}Na MAS NMR spectra using Gaussian fitting

Age (Days)	δ_{observed} /(ppm)	FWHM /(kHz)
0	-6.5	1.19
4	-6.6	1.06
8	-6.3	1.24
12	-7.2	1.17
16	-5.7	1.39
20	-3.6	1.87

The spectra do not show the characteristic features of second-order quadrupolar broadening suggesting other broadening mechanisms[324, 325] similar to those reported in **Chapter 4** and therefore MQMAS is required to probe the ^{23}Na environments.

5.7.3 *^{23}Na{^{1}H} MQMAS NMR*

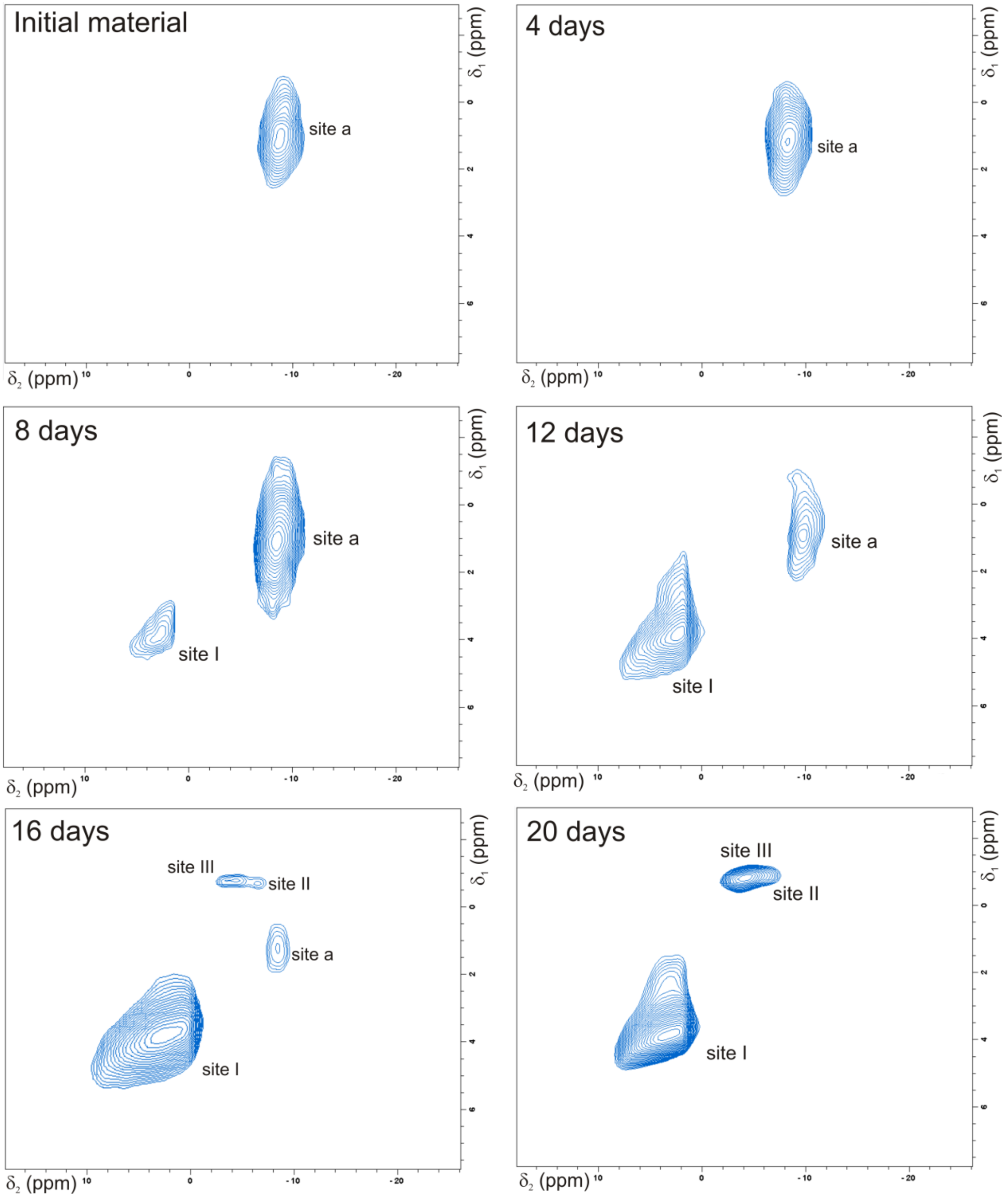

Figure 5.21 ^{23}Na{^{1}H} MQMAS NMR spectra following the change in sodium coordination within the CS2G hydrogel starting with the initial material and ending at 20 days

Figure 5.21 shows that four sodium sites can be resolved at different ageing periods. Site **a** is present in the initial amorphous material and has previously been assigned to the $Na[(H_2O)_6]^+$ cation. At 8 days a second peak is observed (site I) and at 12 days two additional lines appear (sites II and III). The intensity of sites I to III increase as a function of ageing whilst site **a**

gradually decreases and disappears at 20 days. Sites I, II and III corresponds to the 5-coordinate and to the two 6-coordinate sites in makatite respectively, see **Figure 5.16**.

Table 5.4 Isotropic chemical shift (δ_{iso}) and quadrupolar product (P_Q) obtained from **Eq. 2.37** and **2.38** using $F_{1/2}$ values for ^{23}Na during ageing process

Age /(Days)	Site	F_1 /ppm	F_2 /ppm	δ_{iso} /ppm	P_Q /MHz
0	a	1.0	-8.8	-2.6	5.2
4	a	1.0	-8.3	-2.4	4.8
8	a	1.1	-8.5	-2.5	5.2
	I	3.9	3.4	3.7	1.2
12	a	1.0	-9.2	-2.8	5.3
	I	3.9	2.9	3.5	1.6
	II	-0.8	-8.1	-3.5	4.5
	III	-0.9	-4.8	-2.3	3.3
16	a	1.2	-8.5	-2.4	5.2
	I	4.0	3.4	3.8	1.3
	II	-0.6	-6.9	-2.9	4.2
	III	-0.8	-3.6	-1.9	2.8
20	I	4.0	3.2	3.7	1.5
	II	-0.5	-5.6	-2.4	3.7
	III	-0.9	-4.4	-2.2	3.1

Table 5.4 contains the isotropic chemical shifts and quadrupolar parameters for each sodium site as a function of ageing. The δ_{iso} and P_Q values for site **a** remain the same during the ageing process but the signal intensity of this site decreases and disappears at 20 days. This indicates that sites I, II and III

are established from the initial amorphous site. The δ_{iso} and P_{Q} values for site I show little change as a function of ageing. This indicates that the chemical environment around site I is established and matches the corresponding 5-coordinate site in makatite. Sites II and III have similar δ_{iso} but higher P_{Q} values compared to those in makatite. The P_{Q} values for sites II and III decrease as a function of ageing, which reflects the ongoing crystallisation process. This is evidenced further by comparing the line shapes extracted from the MAS dimension of the MQMAS spectrum for sites I-III in makatite to the corresponding sites at 20 days of ageing.

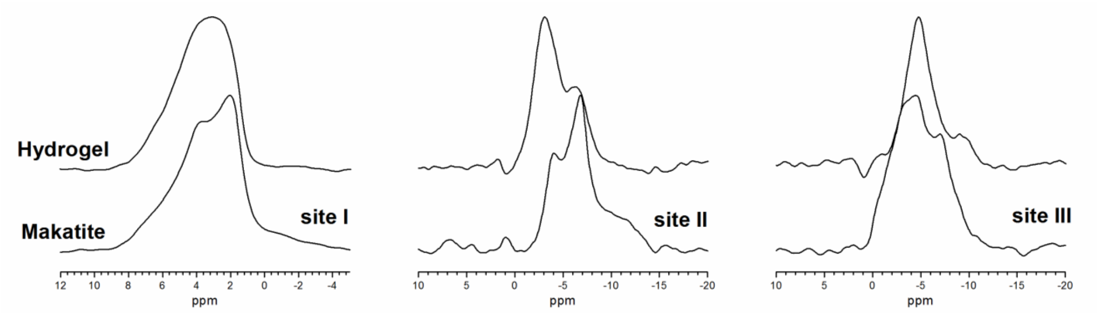

Figure 5.22 Comparing the projections of extracted spectra of the MAS dimension from the MQMAS experiment of the sodium sites at 20 days aged (top) to the sites present in naturally occurring makatite (bottom)

Figure 5.22 shows the comparison between the MAS dimension projections of the sites found in natural makatite and those in the 20 day aged hydrogel. It is clear that the lineshape for site I in the hydrogel is comparable, although broadened, to the site in makatite; this is also reflected in the similarity between the δ_{iso} and P_{Q} values. This indicates that the local environment, the ligands/geometry (electric field gradient) experienced at the Na nucleus in site I is near identical in the aged hydrogel to that of the makatite. Conversely line shapes for sites II and III in the aged hydrogel do not match those in makatite but do show a similarity in chemical shift values. This suggests the same ligands in the coordination sphere but differences in geometries. For example, the P_{Q} values for sites II and III generally decrease with ageing. This indicates a reduction in the asymmetry of the Na coordination spheres transforming towards the more symmetric sites in makatite with P_{Q}/Q_{cc} values of *ca.* 1.2 MHz. It also shows that the CS2G hydrogel requires ageing periods of more 20 days to achieve the same Na sites to those found in makatite. The results provide a unique insight not only into the appearance of crystalline Na sites but also of the change in geometries upon crystallisation.

5.7.4 *Comparison of ^{23}Na sites present within the CS2 and CS2EG hydrogels during the phase transformation: ^{23}Na MQMAS NMR*

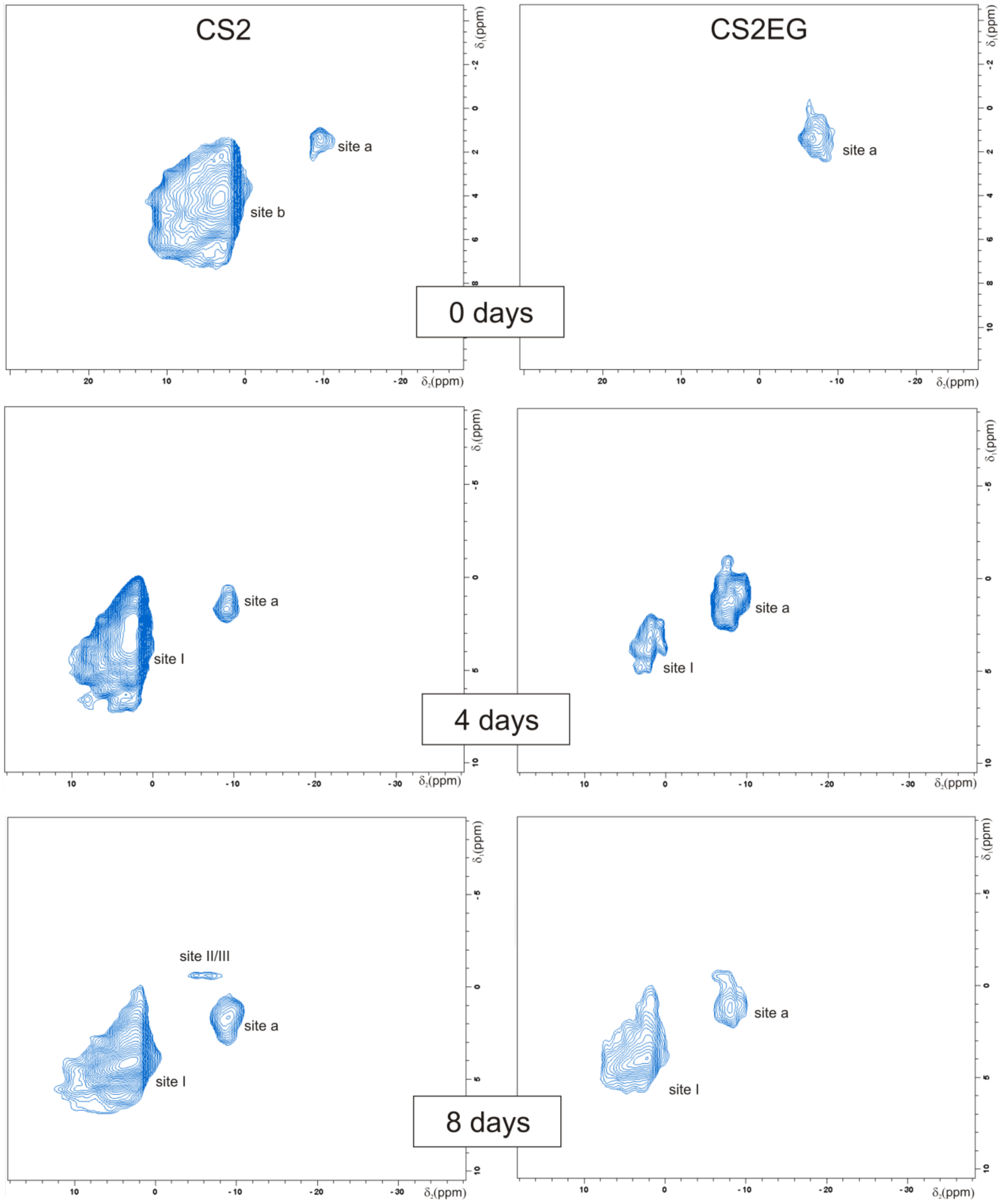

Figure 5.23 ^{23}Na{^{1}H} MQMAS NMR spectra following the change in sodium coordination within the CS2 and CS2EG hydrogels from 0, 4 and 8 days.

Figure 5.23 shows the change in sodium coordination during the initial 8 days of makatite formations for the CS2 and CS2EG hydrogels. In the CS2 hydrogel, the Na(b) site transforms into the crystalline Na(I) site within a 4 day period. At 8 days the Na(II) and (III) sites are detected. In the CS2EG hydrogel, the Na(I) site is observed from 4 days onwards and Na(II) and (III) are not present at 8 days.

5.8 Discussion

5.8.1 *Makatite Crystallisation*

Makatite crystallisation process, although occurring at different rates for each hydrogel, can be surmised into three stages:

1. Na(I) trigonal bipyramidal site is established;
2. Condensation of Q^1 and the hydrolysis of Q^4 sites follow;
3. Na (II) and (III) sites are established with the condensation of Q^2 and the rearrangement of amorphous Q^3 towards makatite Q^3 sites.

Therefore, the rate of crystallisation across the CS2 hydrogels is affected by sodium coordination, the ability for the silica/sodium sites to diffuse through the water networks, and steric effects: The CS2 hydrogel crystallises first as the Na(**b**) site is present in the initial material and is predisposed towards that of the makatite Na(I) site. The activation energies for the reorientation of the water molecules (see previous chapter) show that the polyol free hydrogel requires the *least* amount of energy for this process to occur whilst the glycerol hydrogel requires the *greatest* amount of energy. The ‘process’ can be thought in terms of the energy barrier the water molecules must overcome to reorientate by one radian defined by the correlation time. The correlation time is a measure of mobility; therefore a higher E_a indicates a reduction in mobility. The mobility of water in the hydrogels is dependent upon the strength of the hydrogen bonding networks. The ability of the silica and sodium units to diffuse throughout the water networks and form makatite would, therefore, be dependent upon the strength of such water networks. Following on from this reasoning, the calculated E_a values can be linked with the rates of crystallisation that occur in each hydrogel. For example, the CS2G hydrogel required the *highest* amount of energy for the process to occur. This was rationalised by the presence of a stronger water hydrogen bonding network compared to that in the polyol free hydrogel and, subsequently, the glycerol hydrogel showed the slowest rate of crystal growth.

The presence of glycerol, and to a lesser extent ethylene glycol, can also sterically restrict the movement of the silica units towards makatite. The XRD, ^{29}Si CP MAS and ^{23}Na MQMAS NMR results show that makatite crystallisation occurs at a faster rate in the CS2EG hydrogel compared to the CS2G hydrogel. The VT ^{1}H MAS NMR and ^{1}H-^{13}C HETCOR experiments can be used to explain why crystallisation occurs at a faster rate in the system; the ethylene glycol molecules become mobile and dissociate away from the silica units. This reduces the steric effects imposed on the silica units and allows the system to rearrange towards makatite. Conversely, in the CS2G hydrogel, the glycerol molecules remain at the silica units for a longer period inhibiting makatite formation.

5.8.2 *Origin of the Change in Optical Properties; Short and Long Term Ageing*

There are two main factors that assure the transparency of glass-ceramics (TGCs)[372, 373] and polymer blends[374, 375]; (1). crystal sizes are much smaller than the wavelength of light (2). the difference between the refractive index of a glass matrix and crystal phase is small.

The *short term ageing* results for the CS2EG hydrogel show a reversible white opaque haze throughout in response to temperature. The VT ^{1}H and ^{1}H-^{13}C HETCOR data indicate that the ethylene glycol molecules become mobile and segregate away from the silica interface. The silica units could aggregate together and form amorphous units comparable or larger than the wavelength of light thus giving rise to the loss of transparency. An alternative explanation is that phase separation could occur between the silica and ethylene glycol domains. The difference in refractive indexes of each domain would be large enough to render the material opaque. DSC was also used to assess the thermal stability of the CS2EG and CS2G hydrogels. The results indicate a possible glass-transition induced optical effect for the CS2EG hydrogel. However, the true origin for the change in optical properties of the CS2EG is yet to be established and requires further investigation. Conversely, the loss of transparency in the hydrogels as a function of *long term ageing* is explained by the nucleation and growth of makatite crystals, scattering light from within the material.

5.9 Conclusions

In summary, the hydrogels transform into makatite upon heat ageing. Polyols influence the rate at which makatite crystallises and the subsequent size of crystals that form. The crystallisation process is responsible for the loss of transparency in the products. Interestingly, the ethylene glycol hydrogel exhibits a white haze when exposed to temperatures in excess of 30°C. The VT ^{1}H and ^{1}H-^{13}C HETCOR experiments indicate a phase separation between silica/water and ethylene glycol/water domains. These results also explain why the ethylene glycol hydrogel crystallises at a faster rate than the glycerol hydrogel. Therefore this also implies that the system requires motional freedom to reorganise towards makatite. The degree of diffusivity with respect to the silica/polyol units within the hydrogels was considered to be investigated by means of ^{29}Si or ^{13}C diffusion-ordered spectroscopy (DOSY). The technique uses pulse-field gradients (PFGs) experiments to separate the NMR signals of the different components of a mixture on the basis of their diffusion characteristics.[376-378] DOSY has been applied for the study of oligomeric dimethylsilxoanes[379], sodium-silicate solutions[380] and used for an insight into the mechanisms of hydrolysis and condensation of TEOS with tetrapropylammonium hydroxide (TPAOH).[381] The results show the potential of using ^{29}Si DOSY NMR but limitations of the technique are in the difficulty of extracting diffusion data for strongly overlapping NMR signals and the need for ^{29}Si enrichment. However, the technique certainly warrants future investigation into hydrogel based materials. Finally, the transformation of the Na site **a** into the makatite Na sites was tracked using ^{23}Na MQMAS NMR experiments. The results show the use of correlating P_Q values to changes in Na geometries during the crystallisation process. This has not been reported in the literature before for amorphous materials and could potentially be useful for other systems like that of Zeolite crystallisation.

Chapter 6

Inhibiting Makatite Formation

6.1 Introduction

In the previous chapter we showed that the formation of makatite can be inhibited by the addition of polyols. This was rationalised by steric effects, water/silica mobility and the nature of the sodium sites present within the initial hydrogels. In this chapter we will demonstrate that formation of makatite can also be inhibited significantly by modifying the sodium-silicate solutions used to prepare the hydrogels. The chapter is broadly divided into two sections; firstly the commercial solutions (CS1, CS2 and CS2) and the synthetic analogues (sCS2 and sCS2G) are analysed using ^{29}Si solution NMR and Lentz-GC analysis. In the second part, the sCS2 and sCSG solutions are dried to form hydrogels, heat aged at 100°C and the ageing performance compared to their standard counterparts; CS2 and CS2G. Possible reasons as to why the synthetic system inhibits makatite formation are discussed.

6.2 Experimental Part

6.2.1 *Commerical Solutions, CS1, CS2 and CS3*

The compositions of these solutions are given in **Chapter 4**. These materials have been used as received without further purification.

6.2.2 *Synthesis of the sCS2 analogue*

A synthetic analogue of the commercial CS2 solution was prepared by dissolving 21.8 g of an aqueous suspension of 50 nm colloidal silica into the CS1 solution (55.0 g) with additional water (23.2 g). Initially, the solution has a cloudy white appearance due to the colloidal silica. The solution becomes increasingly transparent with time as the colloidal silica is gradually dissolved into the solution. The solution is left for two weeks in order to equilibrate.

Table 6.1 Bulk properties of the solutions

Solution	SiO_2:Na_2O *wt.* ratio	Viscosity (Poise, P)	pH
CS2	3.30	0.84 ± 0.10	11.4
sCS2	3.30	0.90 ± 0.10	11.2

6.2.3 *Lentz-GC Analysis*

The Lentz-method (trimethylsilyation) has been used to study silicate structures in silicate solutions or minerals. The aim of the reaction is to keep silanol condensation to a minimum so that the polyorganosiloxanes reflect the anions present in the starting material.

6.2.4 *Trimethylsilation procedure*

In a typical synthesis, a mixture of 160 ml concentrated HCl (11.6 M), 125 ml H_2O, 300 ml isopropyl alcohol and 200 ml of hexamethyldisiloxane (HMDS) was stirred at room temperature for 1 hour. A diluted aliquot of the commercial sodium-silicate was added (*i.e.* for the CS2 solution, $[SiO_2] = 6.4$ M which was diluted to *ca.* 1 M) drop wise ensuring that the reaction did not rise above room temperature. The solution was left to stir for 2 hours. The polyorganosiloxane phase was separated and washed three times with H_2O and then stirred in Amberlyst-15 (acid resin) for 16 hours. According to

Lentz[382], this reaction reduces the number of chemical species present in the mixture simplifying GC analysis. After the Amberylst reaction, the mixture was filtered and excess HMDS removed using a rotor evaporator to yield a viscous, clear product.

6.2.5 *Gas-Chromatography*

The polyorganosiloxane products were analysed by gas chromatography on Varian 6890N equipment. The products were dissolved in dichloromethane and injected (0.1 μl) onto a 25 m capillary column of BP1 bonded phase on fused quartz. The oven temperature was programmed to rise from 50 to 300°C at 10°C min^{-1}.

6.3 Analysis of Sodium-Silicate Solutions

6.3.1 *Commercial Sodium-Silicate Solutions*

The following ^{29}Si NMR spectra show the silica speciation and distributions of the commercially available sodium-silicate solutions that are used to prepare the CS1, CS2 and CS3 hydrogels.

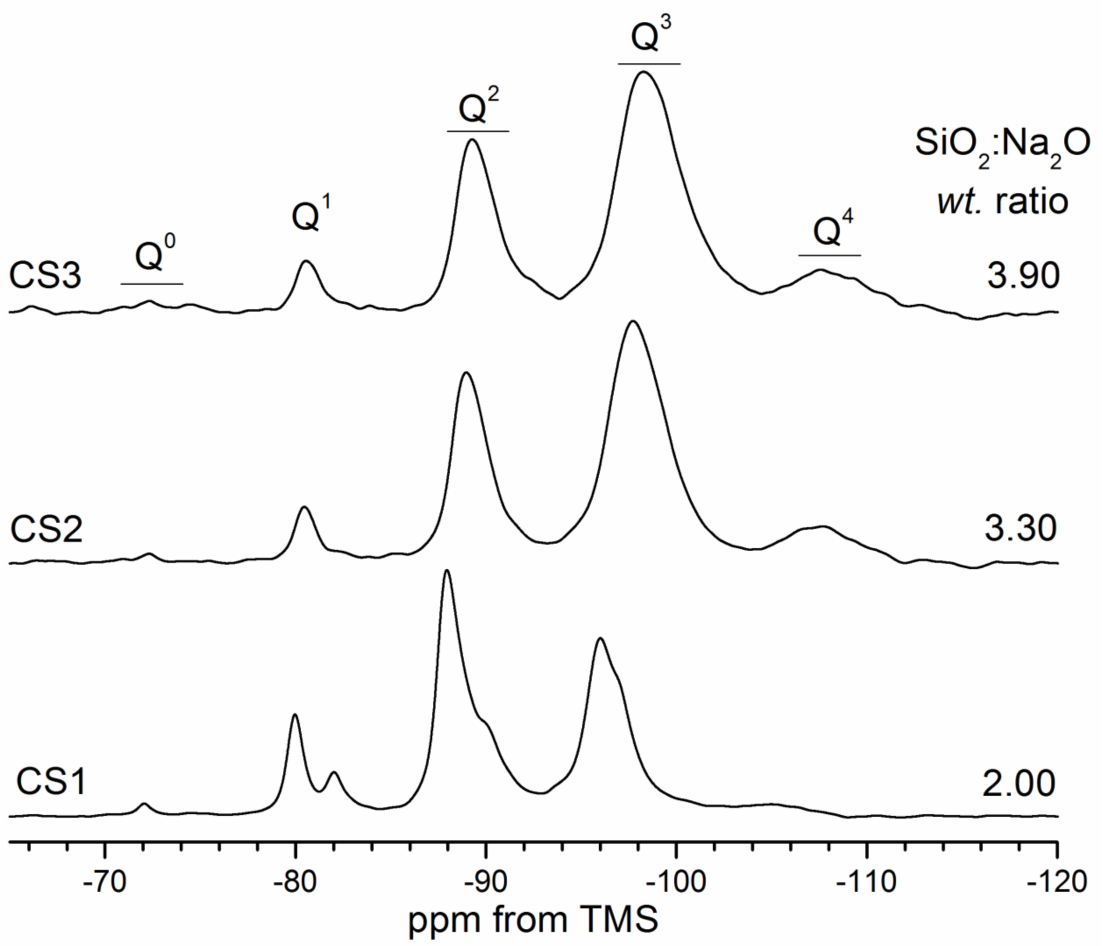

Figure 6.1 ^{29}Si{^{1}H} solution NMR spectra of the commercial sodium-silicate solutions

Table 6.2 Q-distributions for commercial sodium silicate solutions. Integration errors are ± 2.0

Solution	Q^0	Q^1	Q^2	Q^3	Q^4
CS1	1.2	14.2	43.4	37.5	3.6
CS2	0.7	6.0	29.5	54.7	9.2
CS3	0.6	4.8	26.5	57.2	10.9

The changes in silica speciation and distributions of each Q site in the CS solutions are presented in **Figure 6.1** and **Table 6.2**. In the CS1 solution the Q^1 to Q^3 resonances are split. The Q^2 anions dominate followed by the Q^3, Q^1, Q^4 and Q^0 units. Conversely, in the the CS3 solution the resonances broaden with the Q^3 site dominating followed by Q^2, Q^4, Q^1 and Q^0. In **Chapter 4** the deconvolution of sites Q^3 and Q^4 for the CS2 and CS3 hydrogels showed similar distributions due to overlapping resonances. Here, we show that the CS3 solution does contain higher proportions of Q^3/Q^4 units compared to the CS2 solution and therefore, this also holds for the hydrogels.

6.3.2 *Commercial vs. Synthetic Sodium-Silicate Solutions*

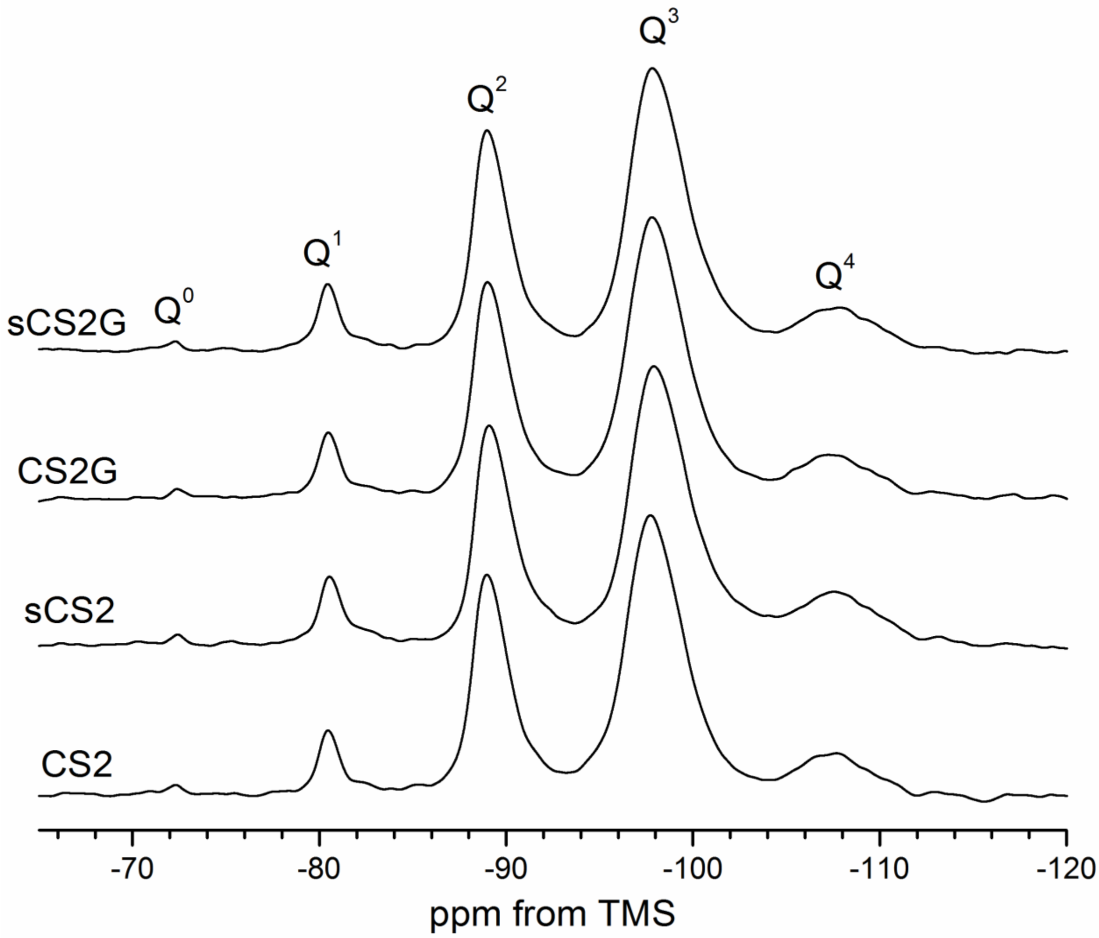

Figure 6.2 $^{29}Si\{^1H\}$ NMR spectra of the CS2, sCS2, CS2G and sCS2G solutions

Table 6.3 Q-distributions for the standard and synthetic solutions with and without glycerol. Integration errors are ± 2.0

Solution	**Q^0**	**Q^1**	**Q^2**	**Q^3**	**Q^4**
CS2	0.70	6.0	29.5	54.7	9.2
sCS2	0.40	5.8	28.3	54.8	10.5
CS2G	0.60	6.2	28.6	53.7	10.8
sCS2G	0.50	5.9	28.3	54.8	10.5

The ^{29}Si NMR spectra in **Figure 6.2** show that the synthetic solution has the same silica speciation and distribution (**Table 6.3**) as the standard. The Q^3 units dominate followed by Q^2, Q^4, Q^1 and Q^0. The addition of glycerol to both the CS2 and sCS2 solutions does not affect of the distribution of silica species. The spectra also indicate the successful dissolution of the colloidal silica and that subsequent equilibration has occurred within the synthetic system.

6.4 Lentz-GC Analysis

The ^{29}Si solution NMR results provide the change in distributions of Q-species as a function of $SiO_2 : Na_2O$ *wt.* ratio but is unable to discriminate individual silicate oligomers. However, these species in the CS1, CS2, sCS2 and CS3 solutions can be isolated and analysed using the Letnz-GC method.

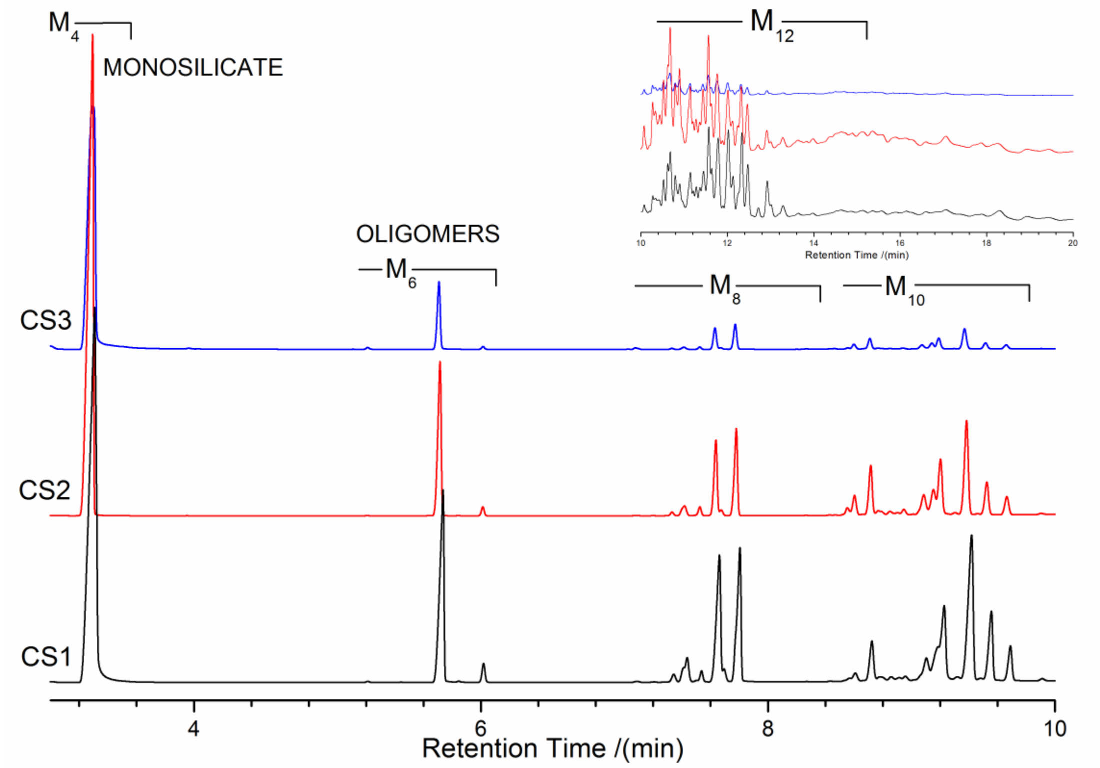

Figure 6.3 Chromatograms of trimethylsilylated silicate ions in the commercial solutions. For clarity, the top right shows the area of retention from 10 minutes onwards and is assigned to the higher M_{12} oligomers.

Figure 6.3 shows the chromatograms of the trimethylsilylated silicate ions in the commercial solutions. There exists five, well-separated areas of retention corresponding to the M_4, M_6, M_8, M_{10} and M_{12} groups. A qualitative inspection of the chromatograms indicates that as the $SiO_2 : Na_2O$ *wt.* ratio of the solution increases from CS1 to CS3, the amount of monosilicate and oligomers decreases. The amount of M_{10} and M_{12} oligomers in the CS3 solution are significantly reduced. This is in good agreement with results obtained in the literature[152, 154, 158, 382] and is consistent with the ^{29}Si solution NMR. The relationship between SiO_2 : Na_2O *wt.* ratio, pH and subsequent silicate speciation is detailed in the discussion section.

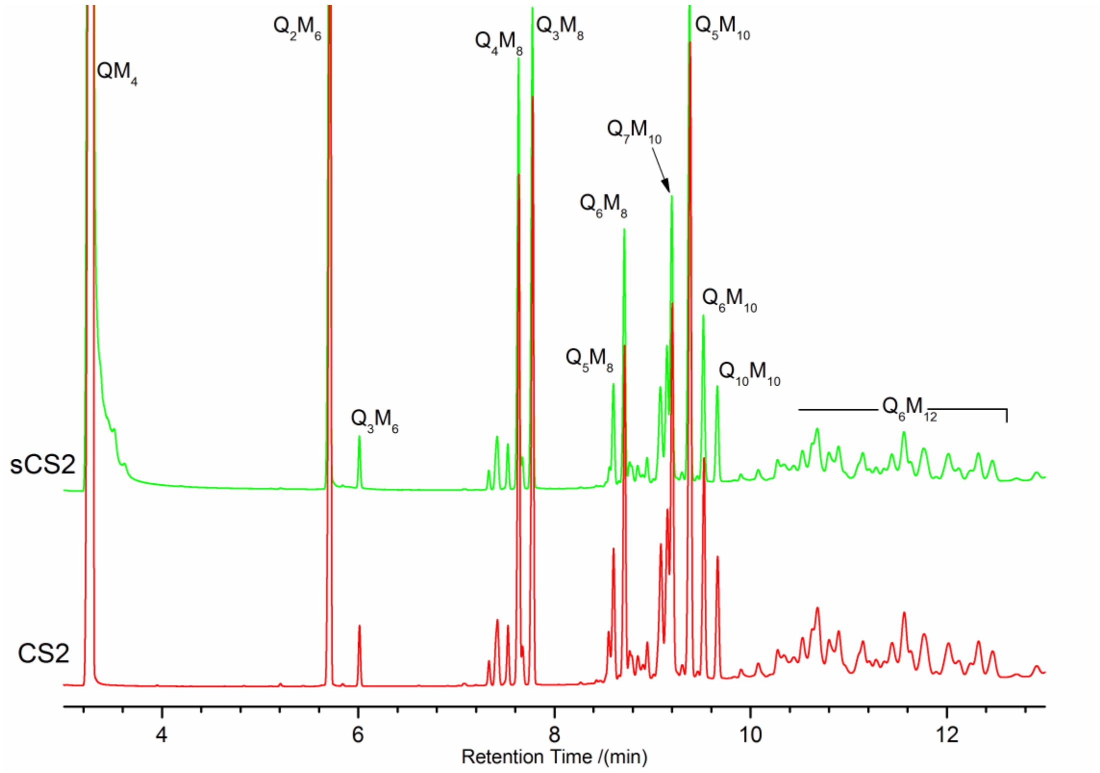

Figure 6.4 Chromatograms of trimethylsilylated silicate ions in the commercial CS2 and the synthetic sCS2 solutions. Where possible, peak assignments have been made.

The chromatograms of the commercial and synthetic solutions (**Figure 6.4**) are very similar but show some slight differences. This indicates that although the sCS2 and CS2 solutions are prepared differently, subsequent equilibration yields similar silicate distribution of oligomers. The unassigned peaks are a combination of isomers and of partially trimethylsilylated silicate ions. For example, according to Lentz[382] both the $[(CH_3)_3SiO]_3SiOSi[OSi(CH_3)_3]$ compound and its partially silylated derivative $[(CH_3)_3SiO]_3SiOSi($**OH**$)$-$[OSi(CH_3)_2]$ will give rise to two peaks in the M_6 region due to the slight differences in polarity, Therefore, the case becomes more complicated as the number of Q_xM_y increases. In fact, Garzo *et al.*[154] claim that by combining 1,2,3...12 silicon atoms and 4,6,8,10, 12-M groups gives more than 250 species/isomers. The assignable peaks are schematically represented in the figure below:

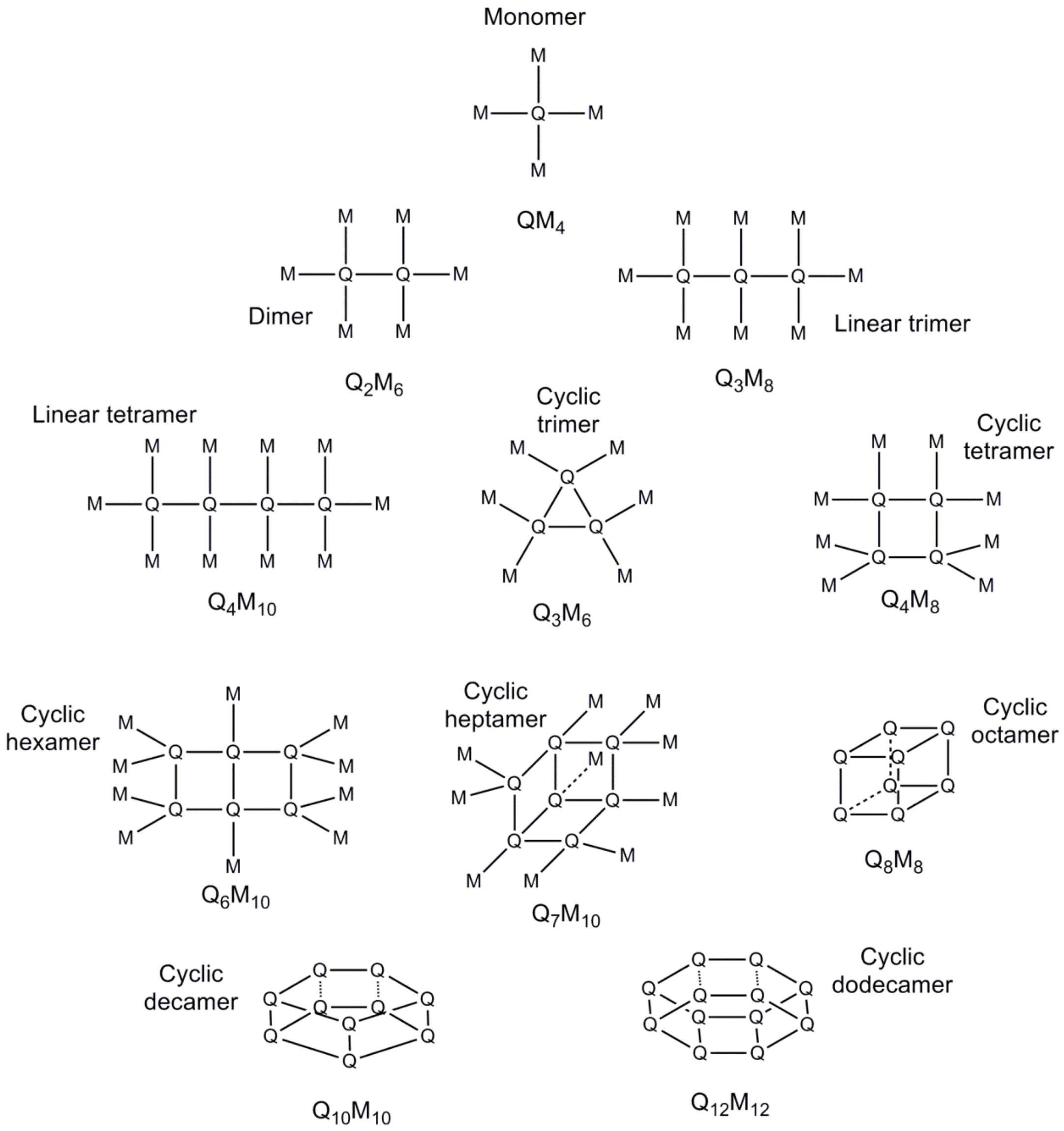
Monomer
QM_4
Dimer
Q_2M_6
Linear trimer
Q_3M_8
Linear tetramer
Q_4M_{10}
Cyclic trimer
Q_3M_6
Cyclic tetramer
Q_4M_8
Cyclic hexamer
Q_6M_{10}
Cyclic heptamer
Q_7M_{10}
Cyclic octamer
Q_8M_8
Cyclic decamer
$Q_{10}M_{10}$
Cyclic dodecamer
$Q_{12}M_{12}$

Figure 6.5 Structures of some trimethylsilylated derivatives of silicate anions in the CS and sCS solutions. (M = $-Si(CH_3)_3$).

The $Q_{12}M_{12}$ species with a molecular weight of 2664, is the upper limit of detection of the GC. Therefore, the polysilicate or colloidal fraction also present in the sodium-silicate solutions cannot be analysed using this method. Gel permeation chromatography (GPC) can be used to analyse the polysilicate fraction. However, the results obtained by Hill *et al.*[203] show that this method simply gives the % of polysilcates present rather than any structural information.

6.5 Ageing Performance

The sCS2 and sCS2G solutions were dried to form hydrogels analogous to their standard counterparts, CS2 and CS2G. The hydrogels were heat aged at 100°C and sampled every 4 days for visual inspection, hazing measurements, XRD and NMR analysis.

6.5.1 *Visual Observations*

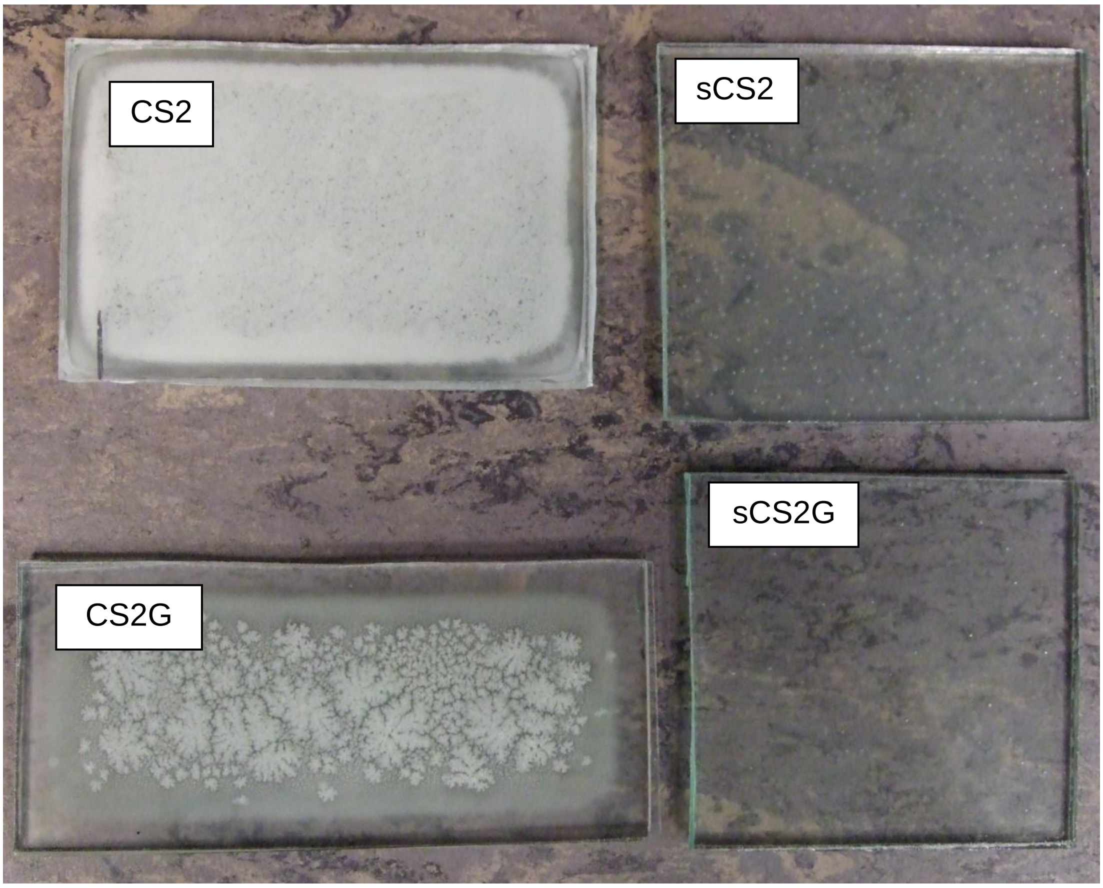

Figure 6.6 Photograph of the commercial and synthetic hydrogels at heat aged at 100°C for 20 days

At 20 days the sCS2 hydrogel has a light haze throughout and small trapped bubbles of oxygen whilst the sCS2G hydrogel remains transparent. The commercial products show significant hazing and loss of transparency. In both the commercial and synthetic systems the addition of glycerol improves the visual properties.

6.5.2 *Hazing Measurements*

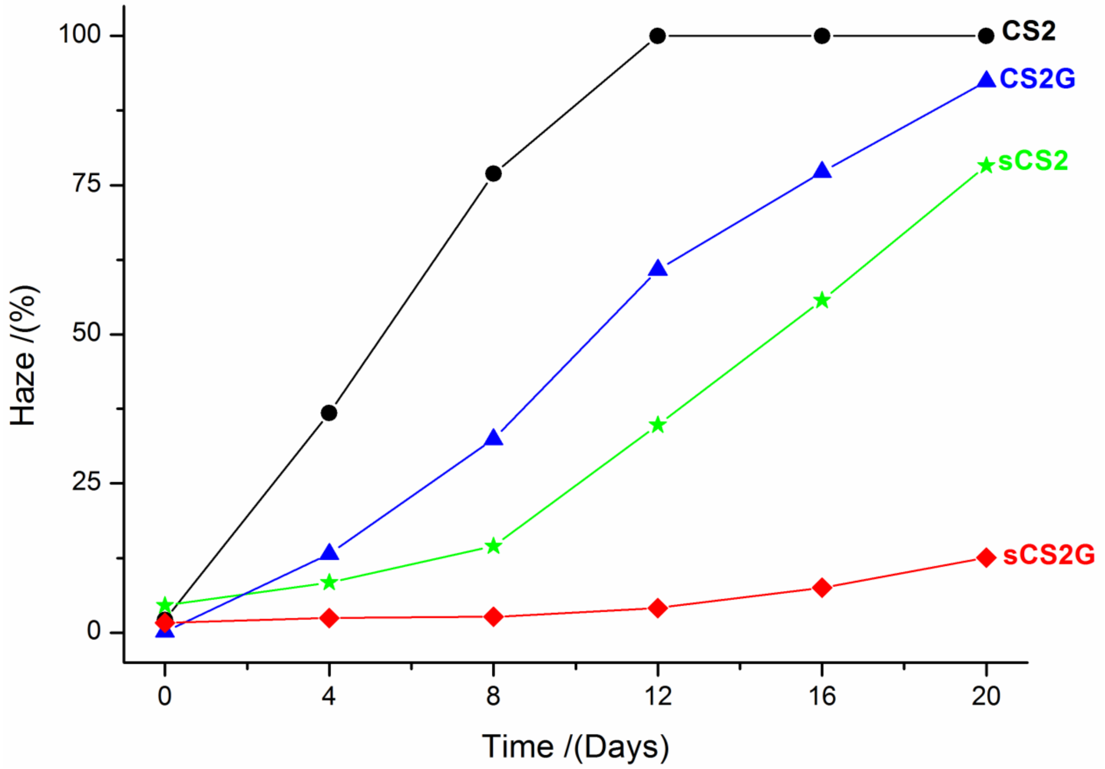

Figure 6.7 Hazing measurements comparing the CS2 and sCS2 hydrogels with and without glycerol

The hazing measurements show a clear reduction in haze for the synthetic analogues compared to their standard counterparts. The decrease in haze for the hydrogels follows; CS2, CS2G, sCS2 and sCS2G. The addition of glycerol to both the standard and synthetic hydrogels can reduce haze and prolong transparency. Moreover, the extent of hazing in the sCS2G hydrogel is reduced dramatically. For example, at 20 days, the sCS2G hydrogel only has a hazing value of 12.6 % compared to 92.4 % haze for the CS2G hydrogel.

6.5.3 *Powder X-ray Diffraction*

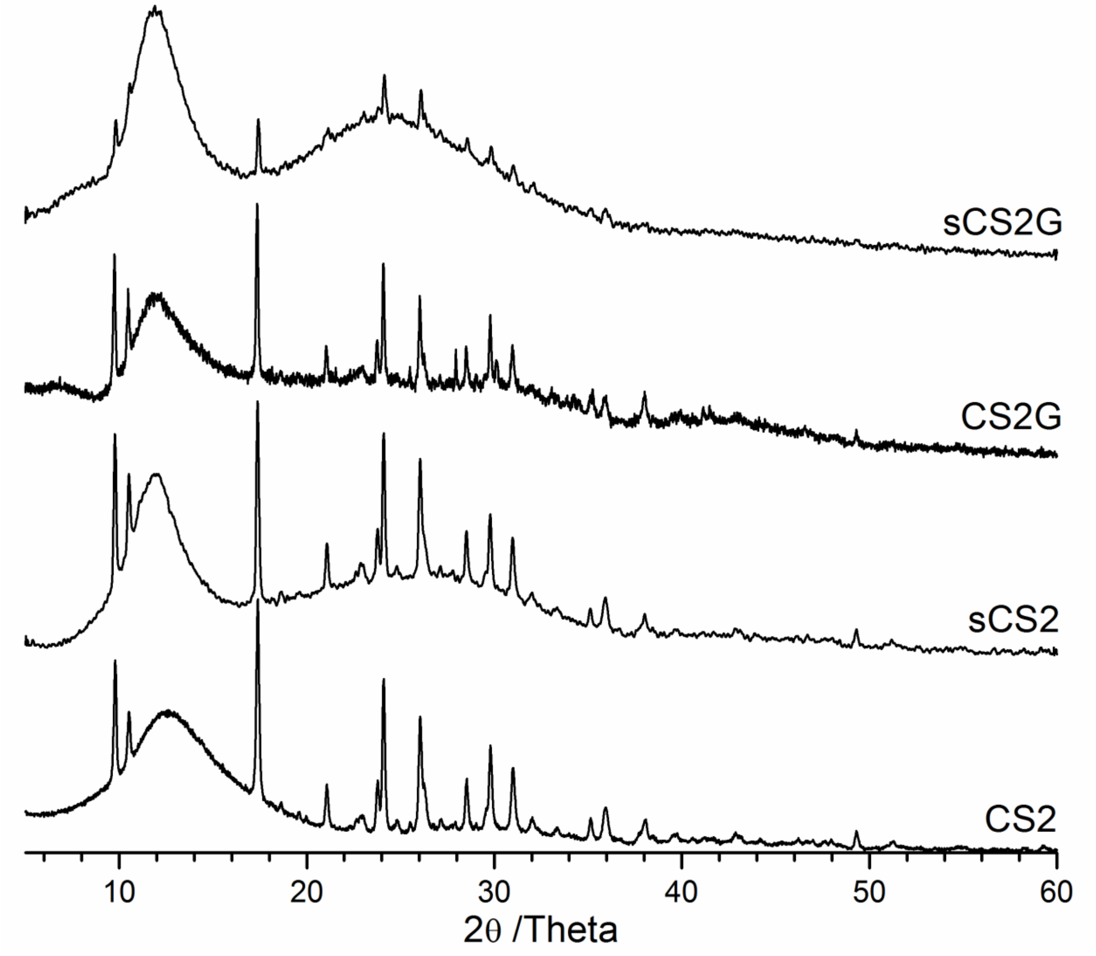

Figure 6.8 XRD patterns showing the comparison between the CS2 and sCS2 hydrogels with and without glycerol aged at 100°C for 20 days

The XRD patterns for the synthetic hydrogels with and without glycerol indicate a transformation into the makatite phase similar to their commercial counterparts. The reflections for the CS2 and sCS2 hydrogels are similar indicating that the crystallinity of makatite in both is comparable. However, from the visual and haze measurements, more makatite crystals have nucleated and grown in the CS2 hydrogel compared to the sCS2 hydrogel. Additionally, the strong hump from 20 to 30 °2θ reflects that a large proportion of amorphous silica is still present in the sCS2 hydrogel. The sCS2G hydrogels shows significantly weaker reflections compared to the other three hydrogels. This is in good agreement with the visual and hazing measurements.

6.6 Comparison of the local environments in the commercial and synthetic hydrogels

6.6.1 *^{29}Si SP MAS NMR*

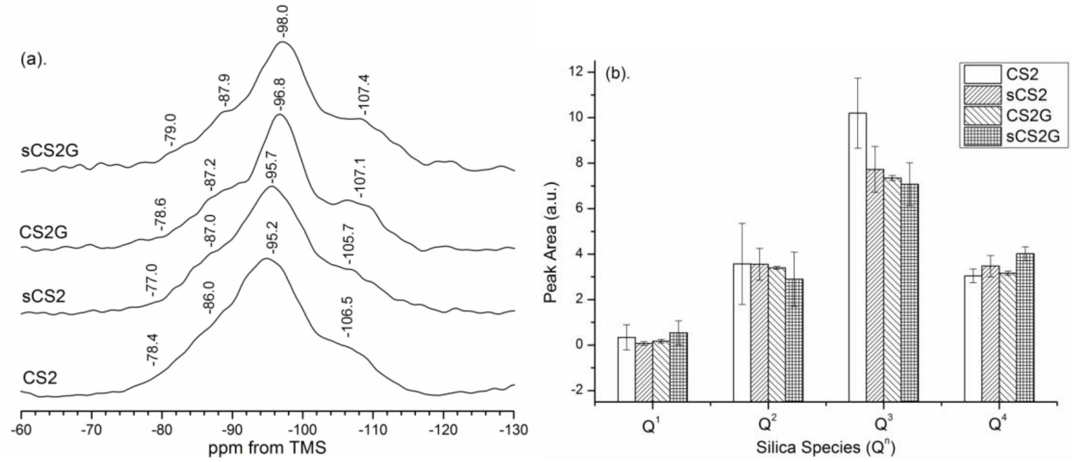

Figure 6.9 (a). ^{29}Si SP NMR spectra comparing the composition of the CS2, sCS2, CS2G and sCS2G hydrogels (b). Bar chart with errors showing the normalised peak areas for silica Q-sites obtained from Gaussian deconvolution.

Figure 6.9 (a). shows the ^{29}Si SP NMR spectra for the CS2 and sCS2 hydrogels with and without glycerol. There are slight differences in chemical shifts and for each hydrogel. The peak areas in **Figure 6.9 (b).** show similar distributions of Q-sites in the standard and synthetic hydrogels.

6.6.2 *^{23}Na{^{1}H} MQMAS NMR*

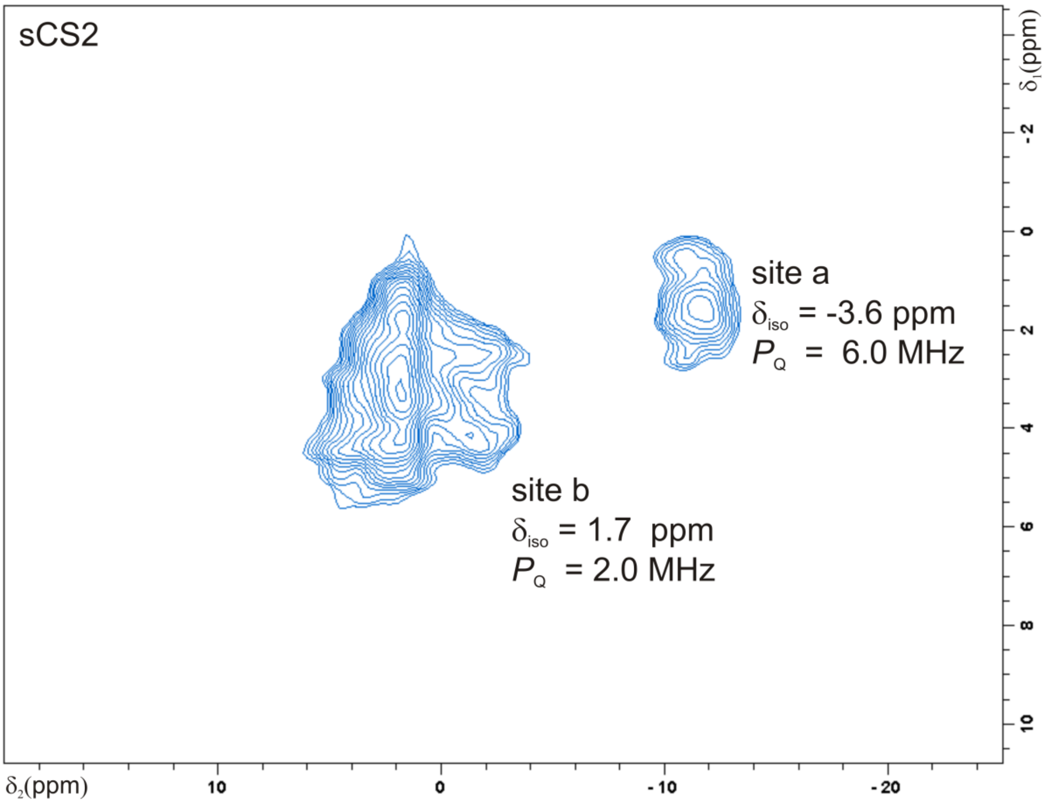

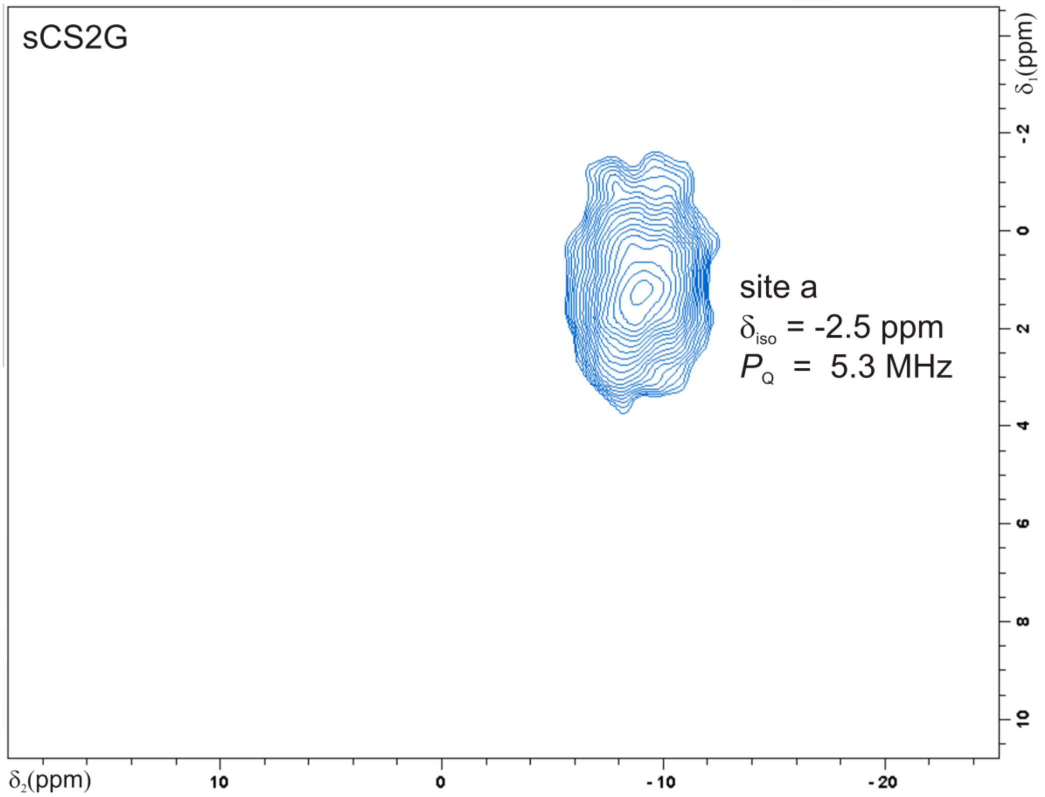

Figure 6.10 ^{23}Na{^{1}H} MQMAS NMR spectra of the sCS2 and sCS2G hydrogels

Figure 6.10 shows the MQMAS NMR spectra of the sCS2 and sCS2G hydrogels, which display similar sodium environments compared to the CS2 and CS2G hydrogels reported in **Chapter 4**. There are slight deviations between the δ_{iso} and P_{Q} values compared to the CS2 and CS2G hydrogels. The ^{29}Si SP and ^{23}Na MQMAS NMR experiments indicate that the silica and sodium environments are very similar in the standard and synthetic hydrogels.

6.7 Discussion

The synthetic solution was prepared *via* the dissolution of a suspension of aqueous 50 nm colloidal silica into a 2.00 *wt.* ratio sodium-silicate to give the same *wt.* ratio and solids content to that of the commercial CS2 solution. The CS2 solution is obtained from the traditional method of hydrothermally dissolving a glass cullet (see **Chapter 1**). The pH, viscosity, silica speciation, concentration and the distribution of silicate monomer and oligomers of the two solutions are very similar. This indicates that although the solutions are prepared differently, the resulting macroscopic and molecular level properties are the same. Therefore, it comes as a surprise that the crystallisation of makatite is inhibited in the synthetic hydrogels as no discernible differences are observed between the synthetic and standard solutions or hydrogels.

This led us to propose possible differences in the colloidal fraction of the two solutions. The colloidal silica in solution and hydrogel is evidenced from the ^{29}Si solution and solid NMR experiments by the Q^3 and Q^4 resonances. We can gain additional information about the nature of the solutions from literature. Iler[383] reports that as the $SiO_2 : Na_2O$ *wt.* ratio of increases there is a corresponding increase in the proportion of silica present as highly “polymeric” or “colloidal”. These particles are in equilibrium with monomeric and oligomeric silicates ions containing up to *ca*. 12 silicon atoms (we confirm the latter point using the Lentz method). Iler[383] and Dietzel *et al.*[163] study a 3.10 *wt.* ratio sodium-silicate solution (25.2 wt% SiO_2) using molybdic acid and ultrafiltration methods. The reaction of molybdic acid *with only* monomeric silica to form the yellow silicomolybdate ion has been used not only to determine soluble silica but also to characterize oligomers and colloidal silica particles. The rate at which the oligomers and colloidal silica depolymerise or dissolve to form the monomer, which then reacts with the molybdic acid reagent, determines their respective content in solution[162]. The results indicate that the solution consists of 10 *wt.* % monomer, 15 *wt.* % oligomers and 75 *wt.* % colloids. The average diameter of the colloid fraction is between 1.8 to 1.9 nm. Otterstedt *et al.*[384] investigated the particle size of colloidal silica in solutions ranging from 1.5 to 20 moles of SiO_2 per mole of

M_2O, (M = Li, Na, K and Cs) and 1 to 5 M SiO_2, using molybdic acid and Sears titration[385]. They calculated particle sizes between 1.0 and 4.5 nm as a function of increasing ratio but the sizes did not depend on the type of alkali-metal cation. A more recent report, by Böschel *et al.*[386] investigated the size distribution of colloidal silica in sodium silicate solutions by dynamic light scattering (DLS) measurements. The authors study SiO_2 : Na_2O solutions with *wt.* ratios between 2.00 and 4.00 and dilutions from 0.5 to 15 *wt.* %. The results indicate at least three size classes of colloidal particles: 0.4 to 0.6 nm, 2.5 to 13 nm and 75 to 85 nm. It should be noted that, as with the Lentz method, DLS requires the dilution of concentrated SiO_2:Na_2O solutions (concentrated: 5 to 6 M, diluted: 0.5 to 1 M with respect to SiO_2). Hence, many reports on the nature of oligomers and colloidal components in sodium-silicate solutions show some discrepancies. However, we can use these findings to assume that the commercial and synthetic solutions contain similar *wt.* % distributions of monomer, oligomer and colloidal fractions reported by Iler and Dietzel[163]. We can also assume that in the CS2 solution, the majority of colloids have average diameters of 1.8 to 1.9 nm, with the possibility of larger colloid sizes existing as to satisfy those reported by Boschel[386] and Otterstedt[384] because they are prepared using the same hydrothermal route. However, the method of producing the synthetic analogue is *different* to the CS2 solutions. Hence, we propose that there exists a mixture of colloidal fractions in the sCS2 solution. We believe that the additional colloids present have dimensions larger than 1.9 nm and/or different morphologies. The rationale for this is represented schematically in **Figure 6.11**. We start by dissolving (1). stable suspensions of non-agglomerated and non-porous spherical 50 nm particles of SiO_2 (pH 9) into (2). strongly alkaline 2.00 *wt.* SiO_2: Na_2O solution. We know from ^{29}Si NMR and Lentz-GC analysis that the solution contains high amounts of monomeric and oglimeric silicate anions in equilibrium with one another and the colloidal fraction. We shall designate this fraction as “colloidal 1” with diameters *ca.* 1.8-1.9 nm. During dissolution the spherical SiO_2 particles depolymerise into smaller colloidals and/or oligomers.

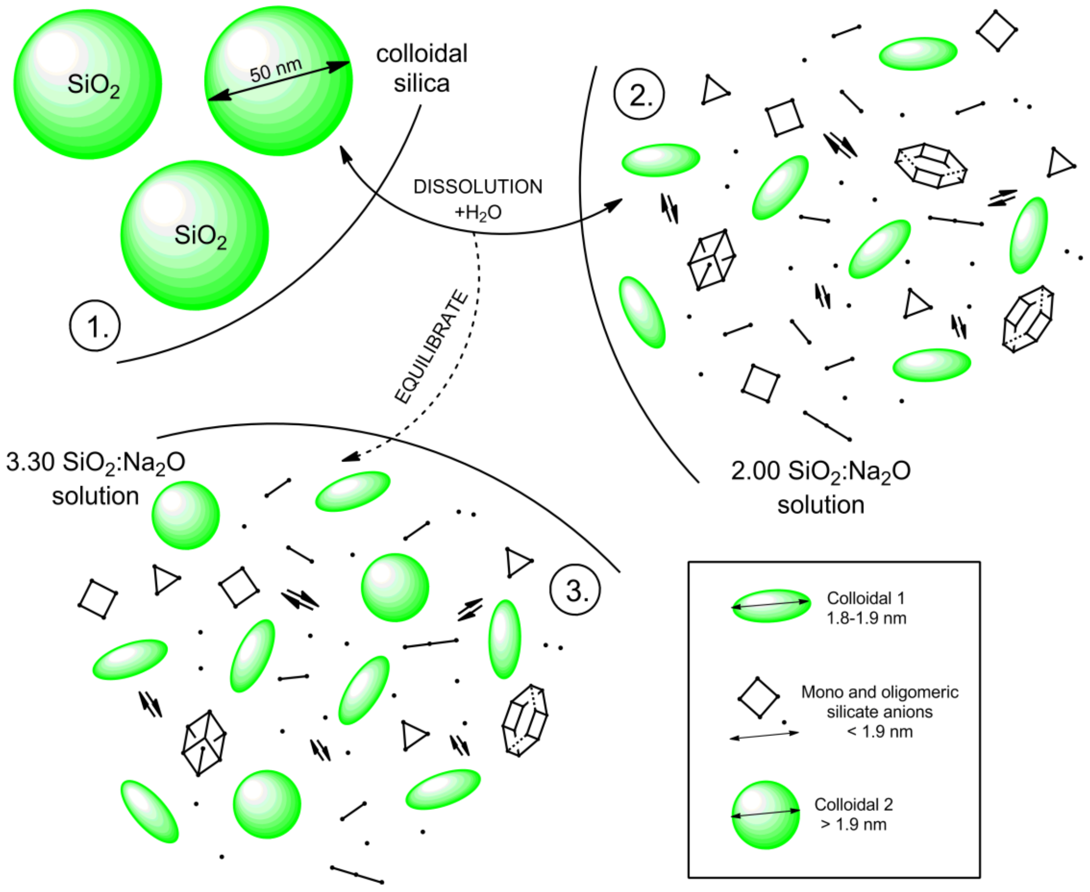
SiO_2
50 nm
SiO_2
colloidal silica
SiO_2
1.
DISSOLUTION
$+H_2O$
EQUILIBRATE
2.
$2.00\ SiO_2:Na_2O$ solution
$3.30\ SiO_2:Na_2O$ solution
3.
Colloidal 1
1.8-1.9 nm
Mono and oligomeric silicate anions
< 1.9 nm
Colloidal 2
> 1.9 nm

Figure 6.11 Method of preparing the synthetic, sCS2 solution.

At stage (3). the solution has reached "equilibrium." The solution contains the original collodial fraction 1; present from the 2.00 *wt.* solution but also remnants of the depolymerised 50 nm colloidal silica. These particles, designated as "colloidal 2" could have diameters greater than "colloid 1" with spherical morphologies. Conversely, **Figure 6.12**, shows the method of producing the commercial solution. Simply, a glass cullet is dissolved hydrothermally to produce the desired Si/Na *wt.* ratio. The colloids here, we assume, are similar in size to those present in the 2.00. *wt.* ratio solution.

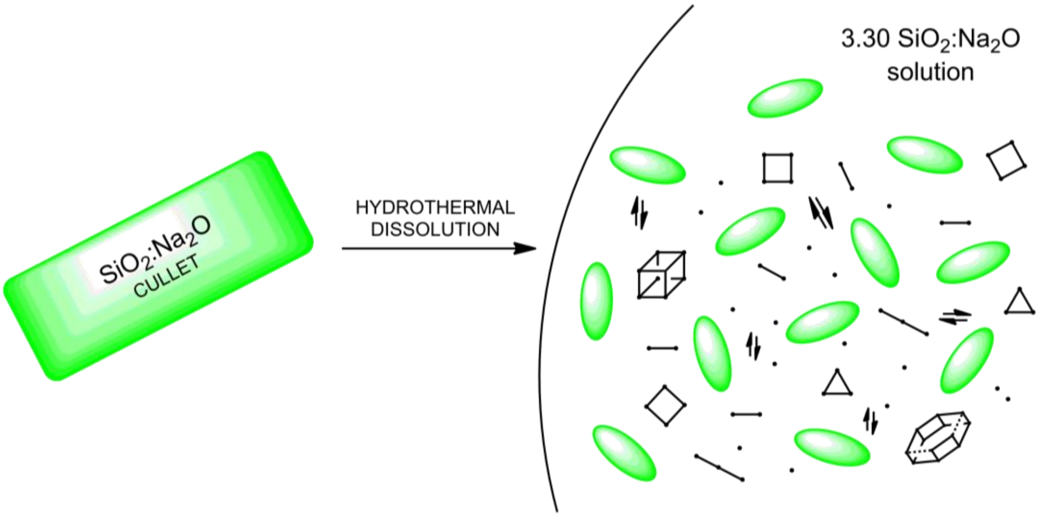

Figure 6.12 Method of preparing the commercial, CS2 solutions.

We also believe that the presence of larger colloids with spherical morphologies in the synthetic solution could explain why makatite crystallisation is inhibited. Recall that the crystal structure of makatite is composed of single layered Q^3 silicate sheets. The ability for the amorphous silica to structurally rearrange towards makatite is therefore dependent upon their size and morphology. Therefore, smaller, linear type species, present in the commercial systems, would require less energy for the transformation opposed to larger, bulkier colloids like those found in the synthetic system.

6.7.1 *The Effect of SiO_2 : Na_2O ratio on silica speciation*

The solubility curve of silica as a function of pH (**Chapter 1**) can be used to explain the relationship between Q-speciation as a function of SiO_2 : Na_2O *wt.* ratio. As the *wt.* ratio decreases the pH of the systems increases (high concentration of ^-OH anions) which catalyses the hydrolysis of siloxane bonds through the following mechanism:

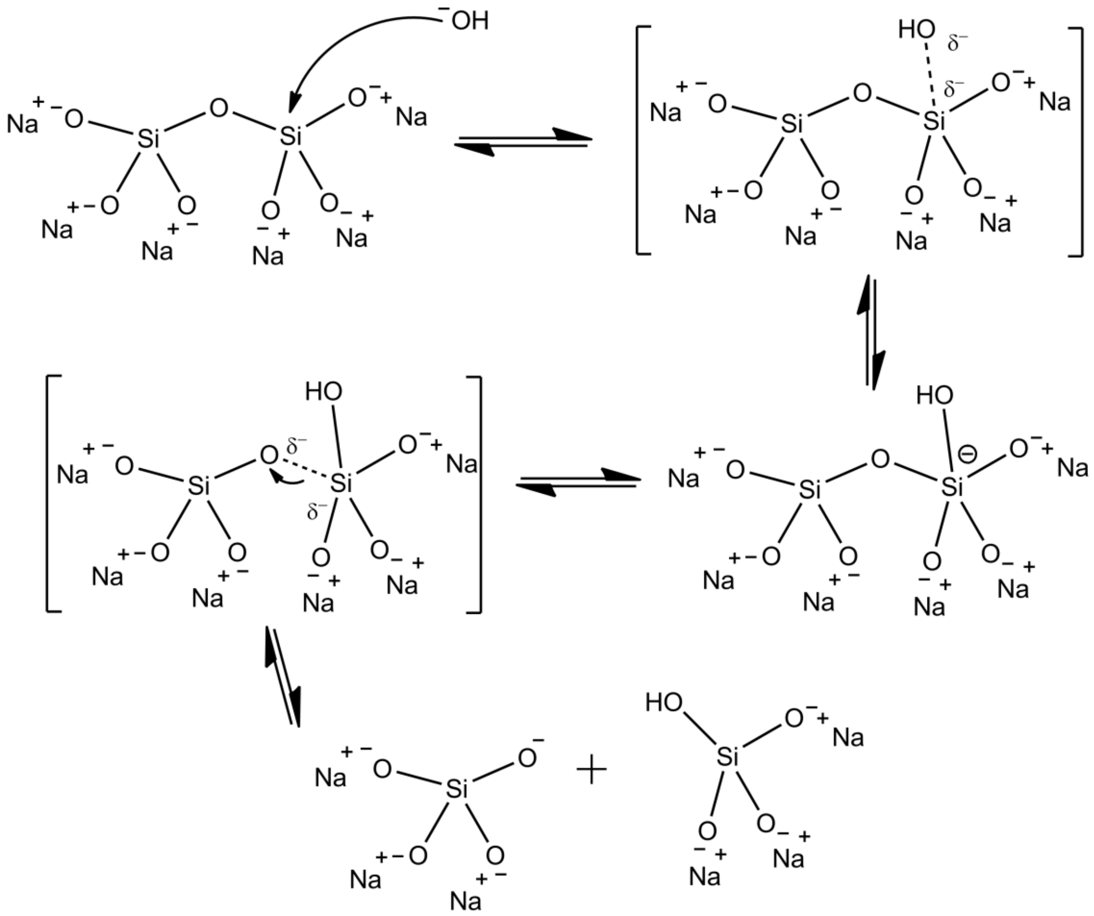

Scheme 6.1 Example of base catalysed hydrolysis of a dimer species to produce two monomer units through S_n2 mechanism

Under basic conditions water dissociates to produce nucleophilic hydroxyl anions in a rapid first step. The hydroxyl anion then attacks the silicon atom within the dimer to form a five-coordinate transition state. The silicon atom acquires a formal negative charge in the intermediate state and decays to a second transition state. The negative charge is drawn towards the Si-O---Si oxygen atom resulting bond cleavage to form the two monomer units. As the pH of the solutions increases as does the rate of hydrolysis.[87, 92, 387] This is shown in both the ^{29}Si sol NMR and Lentz-GC analysis; as the *wt.* ratio decreases the amount of monosilicate and oligomeric silicate anions in solution increases. Additionally, at high pH (>11) surface charges on the oligomers increase, and the resulting electrostatic repulsive forces reduce the rate at which the oligomers can condense back together. This is seen from the ^{29}Si sol NMR spectrum of the CS1 solution (pH > 12); whereby resonances of Q^1, Q^2 and Q^3 are split. For example, the Q^2 region shows two resonances which are assigned to the cyclic trimer and cyclic tetramer.[388] The exchange between these two species is slow because of the repulsive forces; on the other hand, in the CS3 solution (pH 10.8), fast equilibrium between species results in broad resonances.

6.8 Conclusions

The crystallisation of makatite can be inhibited by altering the silica source of the precursor solutions. In the presence of glycerol, makatite crystallisation can be *significantly* retarded with haze levels staying less than 20 % over 20 days of heat ageing. Interestingly, the bulk properties, silica distributions and sodium environments in the synthetic and commercial materials are the same. However, we propose that the colloidal fractions are different in the two solutions. Although we have not proved nor disproved this theory there exist several methodologies that can investigate this hypothesis. As with those reported in the literature, the commercial and synthetic systems could be analysed using DLS measurements. Alternatively, the colloidal fractions can be precipitated out of solution using sulphuric acid and extracted using THF or BuOH.[383, 384, 389, 390] Once extracted, the morphology and microstructure can be assed using scanning electron microscopy (SEM). Another method would be to synthetically produce a variety of 3.30 *wt.* ratio solutions using colloidal silica with diamaters from 10 to 40 nm. One would expect that as diameter size decreases the rate of makatite crystallisation would increase.

Chapter 7

Investigating makatite/glycerol interactions

7.1 Introduction

Insight into makatite formation and interlayer reactivity is important to gain a deeper understanding of how the hydrogels transform into this mineral. Therefore, in this chapter we ‘reverse’ the hydrogel process, that is we synthesise a makatite hydrogel containing the same water and glycerol contents to those in the initial amorphous silica based hydrogels. Through this process the interactions occurring between glycerol and makatite are investigated using TGA and NMR techniques. The question of where glycerol is located during the crystallisation process is addressed. We also highlight the difficulty in synthesising makatite hydrothermally and its resistance towards intercalation compared to other layered silicates.

7.2 Experimental Part

7.2.1 *Makatite Synthesis*

The synthesis of makatite was attempted *via* the hydrothermal route reported in the literature. The SiO_2:Na_2O:H_2O molar ratios used were 3.40 : 1.00 : 26.2 (hydrogel composition) and 3.60 : 2.00 : 13.3 as reported by Schwieger *et al.*[206] Fumed silica was dissolved in NaOH and transferred to Teflon Liners. The solutions were treated hydrothermally over a period of 19 days. The contents of the vessels were inspected every several days but did not yield any precipitate. The temperature was also varied; makatite solutions exposed to temperatures in excess of 200°C for several days yielded an amorphous white product. Those treated at lower temperatures (*ca.* 100°C) preferentially formed magadiite. The “seeding” method was also employed. Makatite crystals (naturally occurring from Lake Chad in Kenya) were placed in sodium-silicate solutions with the intention to act as nucleation centres for makatite. The resulting product was magadiite. As the hydrothermal route failed, the mineral used in this work was obtained from heating a CS2 hydrogel in excess of one year at 100°C. The material was thoroughly washed in water and left to dry overnight to yield a fine, white power.

7.2.2 *Synthesis of makatite/glycerol composite*

Typically, 300 mg of makatite was added to 10 ml of glycerol and stirred at room temperature for 5 days. The resulting solution was filtered under vacuum using a glass frit and then left to dry over night. We also prepared analogues using ethylene glycol and D-sorbitol.

For the purposes of this chapter, results obtained for the glycerol/makatite comosite are presented. This material, denoted as MKG is compared to its parent material, pMK, obtained from heat ageing of a CS2 hydrogel. We also compare the structures of these materials to that of a naturally occurring makatite sample, nMK and a CS2G hydrogel.

7.3 Results

7.3.1 *Composition of the Materials*

The MKG composite is a fine white powder that appears similar to the drilled CS2G hydrogel.

Table 7.1 C/H and Karl-Fisher analysis on pMK, MKG and CS2G

Material	C (%)	H (%)	H_2O /(%)
pMK	0.19	2.19	20.54 ± 0.41
MKG	1.64	2.32	20.14 ± 0.33
CS2G	4.97	2.58	20.43 ± 0.52

Table 7.1 shows the C and H content of pMK, MKG and CS2G. There is a considerable increase in carbon content in MKG when compared to the host, sMK, and greater still for the CS2G hydrogel. There is also an associated increase in hydrogen content. The idealised molecular formula for natural makatite has been reported to be $4.0\ SiO_2$: $1.0\ Na_2O$: $5.0\ H_2O$[185, 207], although the water content can be variable. Assuming that the main hydrogen contributor in makatite is water, the molecular formula of makatite in the current study is $4.0\ SiO_2$: $1.0\ Na_2O$: $4.3\ H_2O$ which is in good agreement with the idealised formula. The C:H mass ratio of MKG is 0.71 which is much lower than 4.5 for neat glycerol. This result indicates that there must be still a large proportion of water remaining in the interlayer region. This is also confirmed from the Karl-Fisher analysis. Furthermore, producing covalently grafted glycerol to the surface would increase the C:H mass ratio above 4 rather than decrease it. The substantially low value of 0.71 strongly suggests that there is negligible if any covalent grafting to the Q^3 surface sites of makatite. The CS2G hydrogel contains more glycerol but also has the same water contents to that of the pMK and MKG. To gain more information on the nature of interactions of the water molecules and glycerol with the mineral phase in these materials, thermogravimetric (TGA) analysis was conducted.

7.3.2 *TGA*

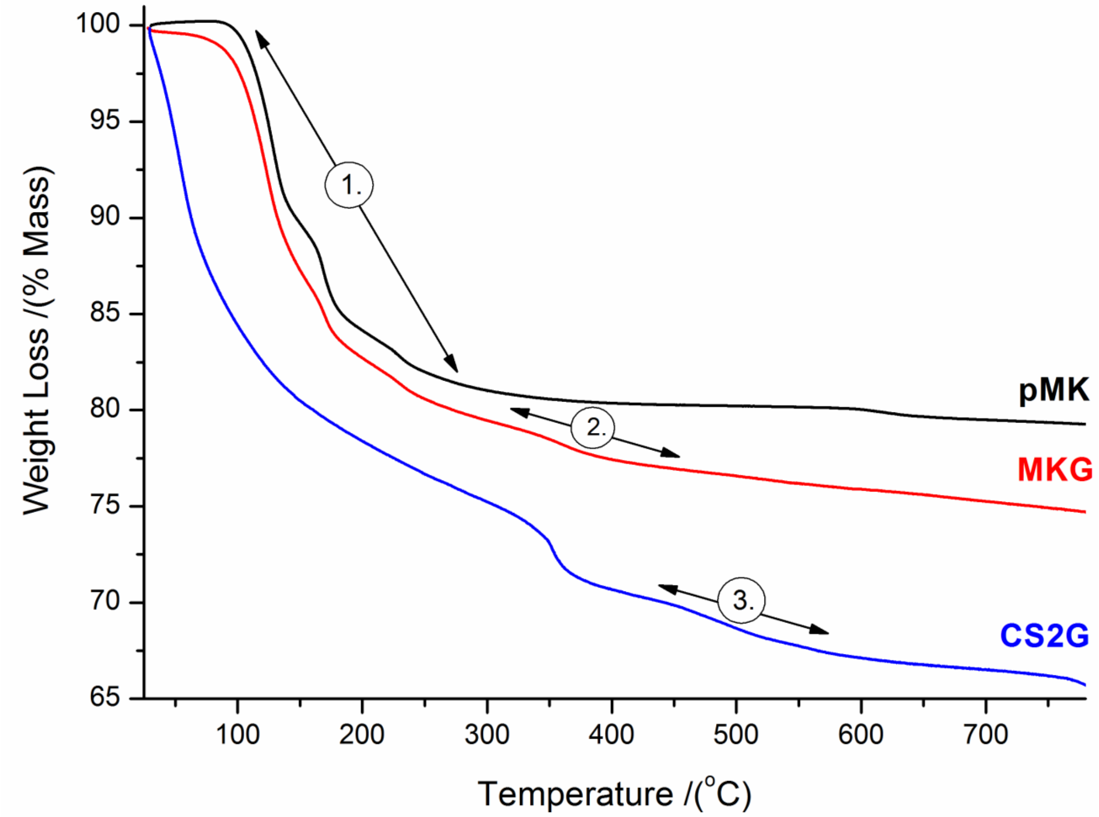

Figure 7.1 TGA curves of pMK (black), MKG (red) and CS2G hydrogel (blue).

Figure 7.1 shows the TGA curves for a CS2G hydrogel, pMK and MKG. The three materials show a weight loss of *ca.* 20 % between RT and 250°C. These losses are attributable to water molecules with different strengths of hydrogen bonding. The total mass loss is in agreement with the water contents analysed using Karl-Fisher method. The pMK material shows negligible weight loss above 250°C. Closer inspection of this region reveals that the CS2G hydrogel losses more mass compared to pMK and MKG. This suggests that the water molecules are involved in weaker hydrogen bonding environments than those in pMK or MKG. The MKG composite and CS2G hydrogel display two additional mass losses between 300 and 430°C and 450 to 550°C. The first mass loss region coincides with the boiling point of glycerol and is therefore attributed to the loss of glycerol molecules. The second loss may correspond to stronger glycerol interactions between the silica interfaces but does necessarily point towards grafting or intercalation. To investigate this further, XRD and NMR experiments are conducted.

7.3.3 *Powder X-ray diffraction*

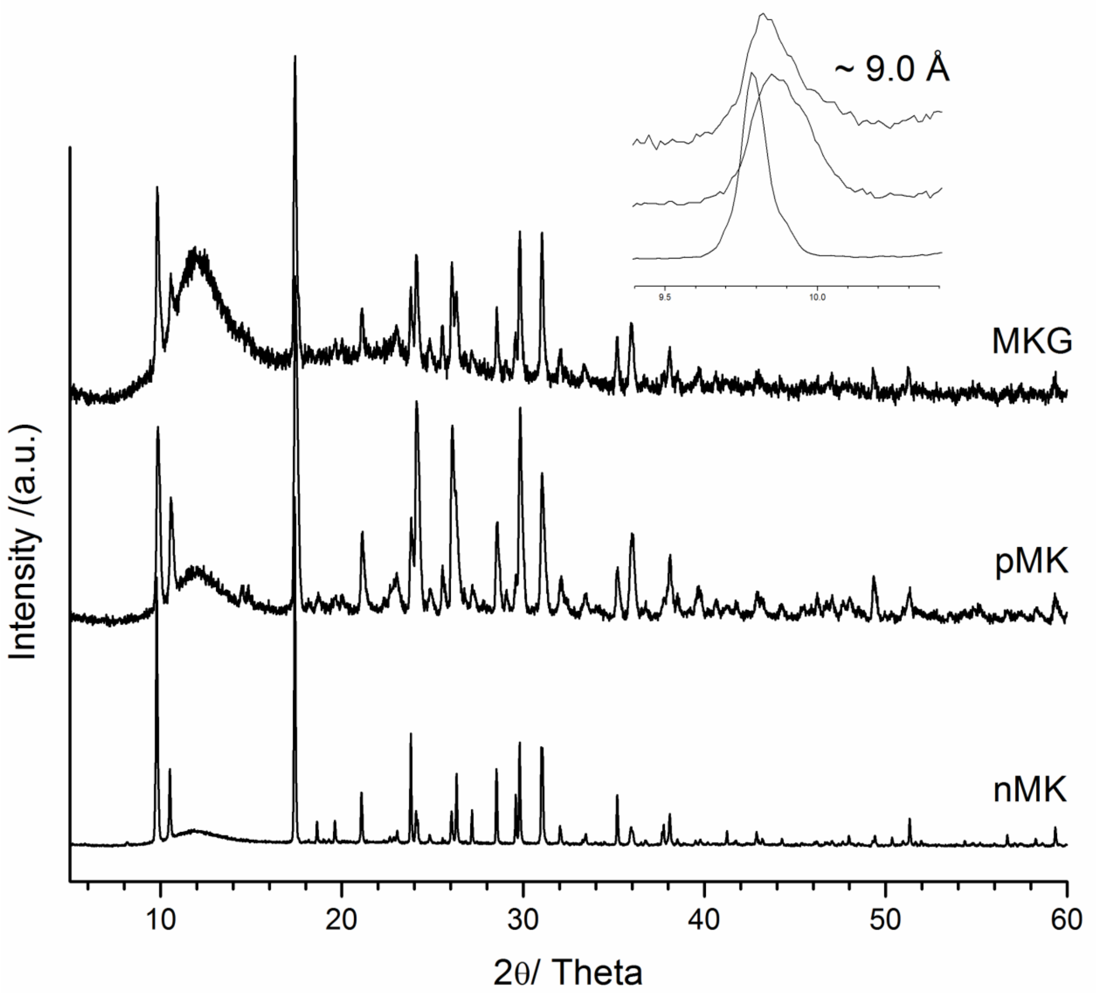

Figure 7.2 XRD patterns for naturally occurring nMK, pMK and MKG. Region between 9.5 to 10.0 °2θ indicates the *d*-spacing of the interlayer region.

Figure 7.2 shows the XRD patterns for nMK, pMK and MKG. The patterns for the pMK and MKG match that of nMK indicating the same crystal structures. However, the broader peaks observed for sMK and MKG suggest a reduction in crystallinity compared to their natural occurring counterpart. The reflection at 9.8 °2θ is for observed for each material and is due to the interlayer spacing between the silicate sheets corresponding to a *d*-spacing value of 9.0 Å, consistent with the literature. No change in *d*-spacing upon glycerol addition, unambiguously confirms that intercalation or grafting has not occurred between the silicate layers, consistent with the microanalysis and TGA data (there was also no change in *d*-spacing when using ethylene glycol through to *D*-sorbitol).

7.4 Probing the local structure

7.4.1 *^{1}H-^{29}Si CP MAS NMR*

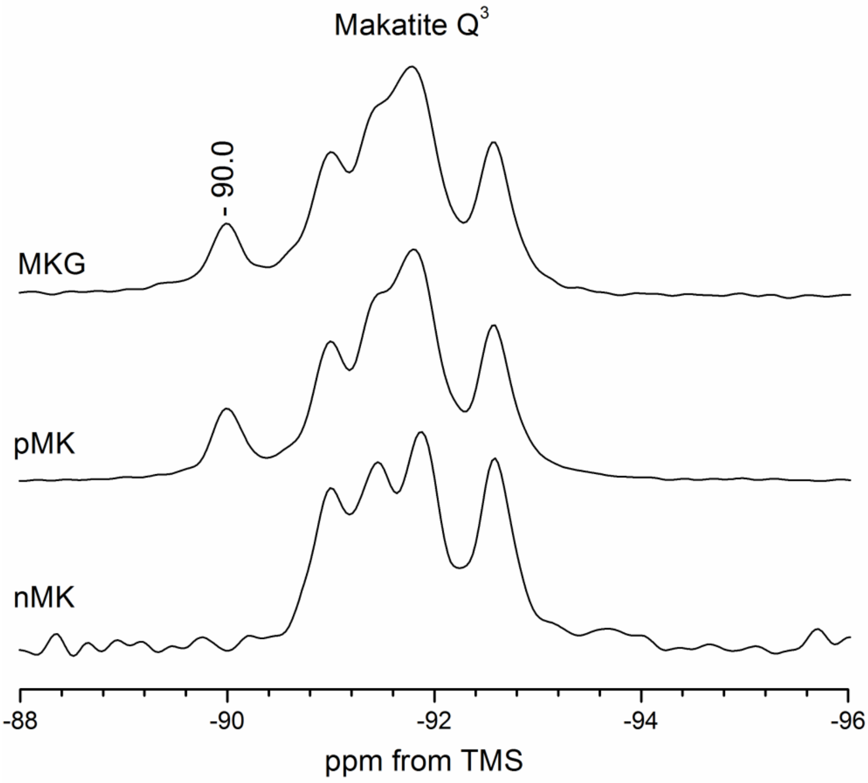

Figure 7.3 ^{1}H-^{29}Si CP MAS NMR spectra of nMK, pMK and MKG

It was shown in **Chapter 5, Figure 5.15**, that makatite consists of four crystallographic distinct Q^3 environments. The sMK and MKG materials also exhibit these resonances but contain an additional Q^3 site centered at -90 ppm. The lines for the four Q^3 sites are less defined than those for natural makatite indicating a reduction in crystallinity, in agreement with the XRD data. The resonance at -90 ppm could correspond to Q^3 site associated with terminated makatite sheets.

7.4.2 *^{1}H MAS NMR*

The local structures of the water and glycerol domains in the MKG composite have been investigated using ^{1}H and ^{13}C{^{1}H} MAS NMR experiments. The spectra are compared to those acquired for a CS2G hydrogel and a material that has been heat aged at 100°C for 28 days.

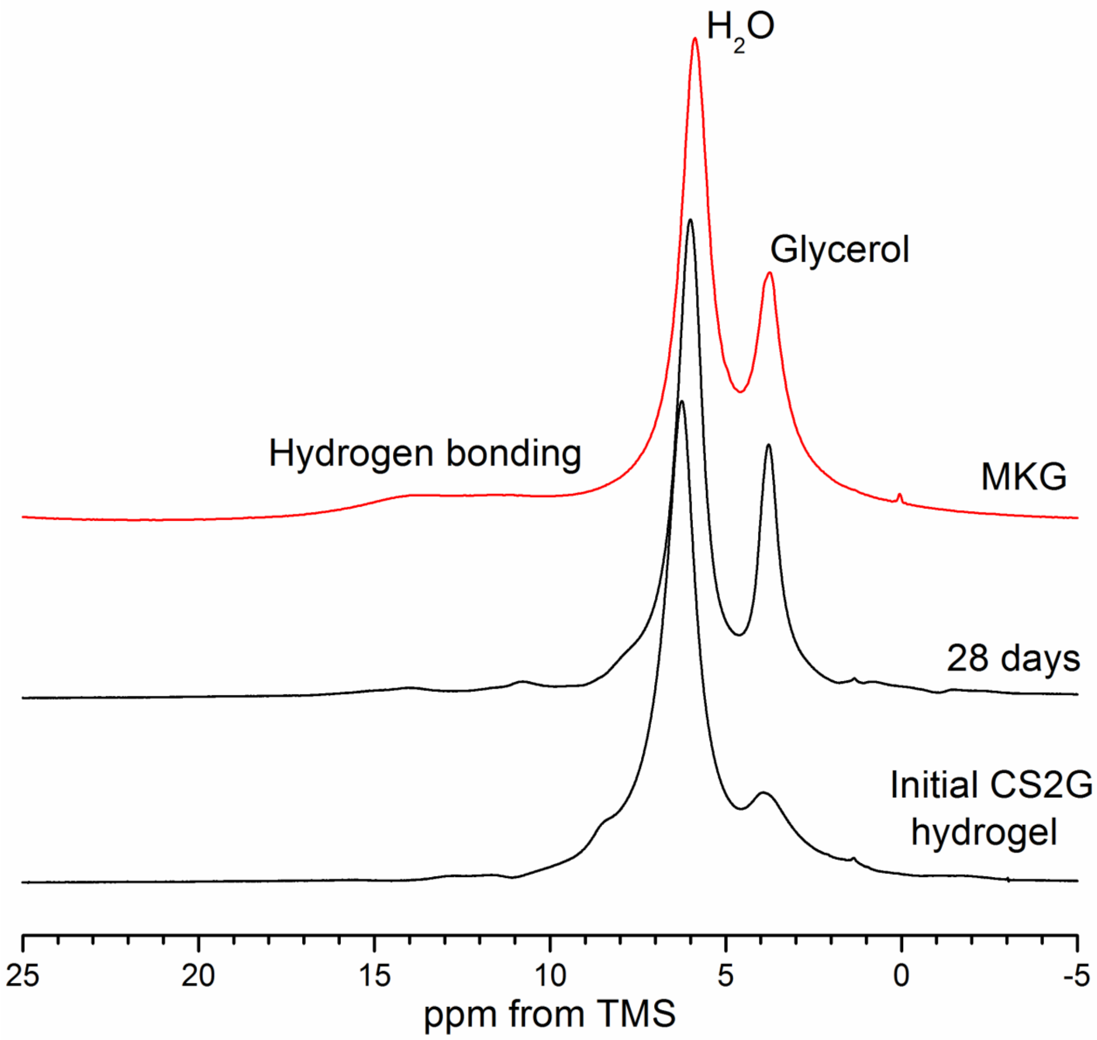

Figure 7.4 ^{1}H MAS NMR spectra of the CS2G hydrogel, 100 °C aged CS2G hydrogel and the MKG composite. The spectra were acquired at an MAS rate of 30 kHz.

Figure 7.4 shows the ^{1}H environments in the initial CS2G hydrogel and at 28 days heat aged with those in the MKG material. The resonances for water and glycerol get narrower and separate away from each other as interlayer hydrogen bonding environment is established as function of ageing. The ^{1}H spectrum for 28 day aged hydrogel is very similar to that of the MKG composite.

7.4.3 *^{13}C{^{1}H} MAS NMR*

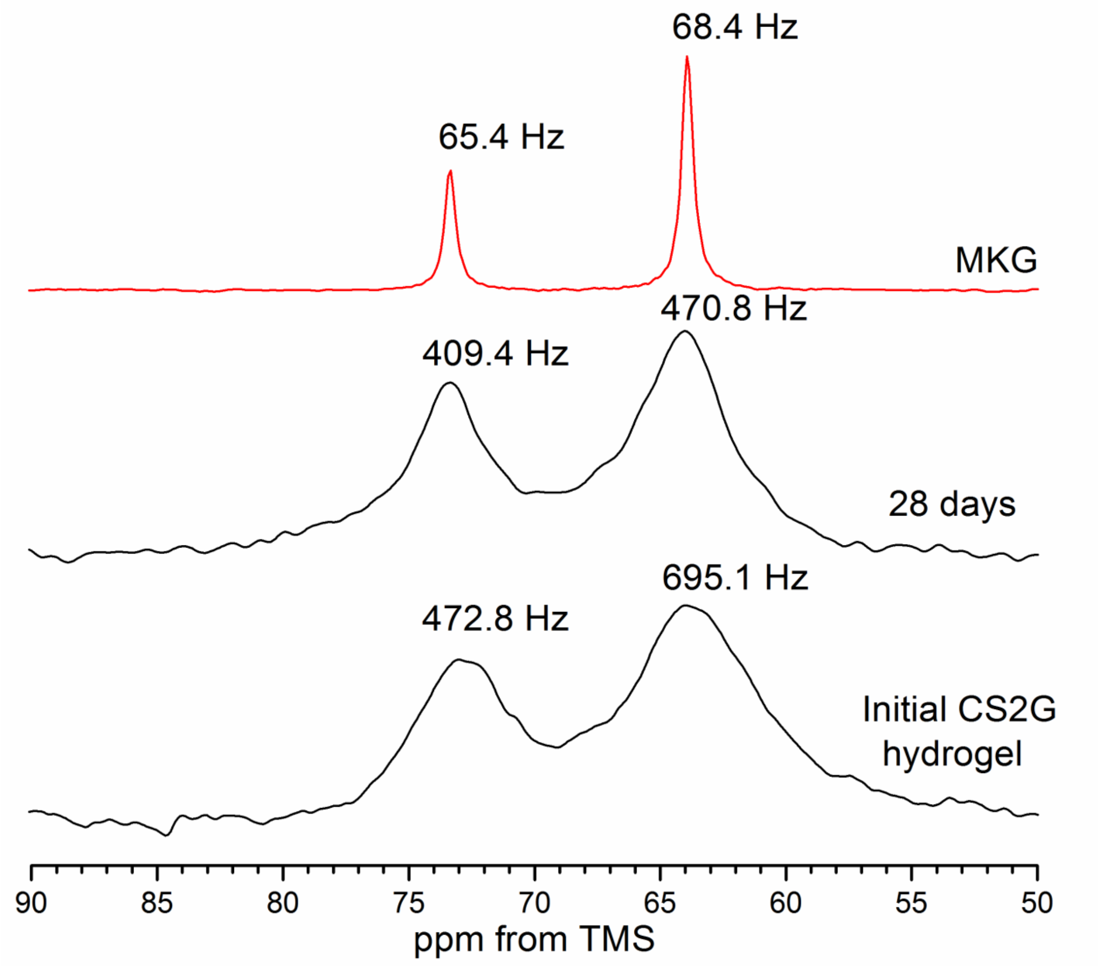

Figure 7.5 ^{13}C{^{1}H} MAS NMR spectra showing the glycerol carbon environments and FWHM values for the initial CS2G hydrogel, aged for 28 days and the MKG composite.

Figure 7.5 shows the ^{13}C{^{1}H} MAS NMR spectra of the initial CS2G hydrogel, aged for 28 days and the MKG composite with corresponding FWHM values. The ^{13}C spectrum shows two resonances at 73.3 and 63.8 ppm corresponding to the two carbon environments present in glycerol. The absence of additional carbon resonances indicates that grafting has not occurred. In the initial CS2G hydrogel the carbon resonances are broad reflecting the amorphous nature of the system. Upon heating for 28 days the resonances narrow. The MKG composite shows resonances with low FWHM values. A reduction in line widths can arise from either fast molecular motion or increasing structural orderring. The ^{13}C spectrum of the MKG composite acquired using ^{1}H-^{13}C CP MAS NMR shows poor signal-to-noise and suggests that the glycerol molecules are very mobile resulting in modulation of the ^{1}H-^{13}C heteronuclear dipolar interaction. These features are also seen for the hydrogel aged for 28 days. The fact that the resonances narrow in the ^{1}H and ^{13}C NMR spectra for the 28 day aged hydrogel indicates that the water and glycerol molecules are being forced away from the silica units as makatite crystallises, and is discussed in more detail later.

7.4.4 *^{23}Na{^{1}H} MQMAS NMR*

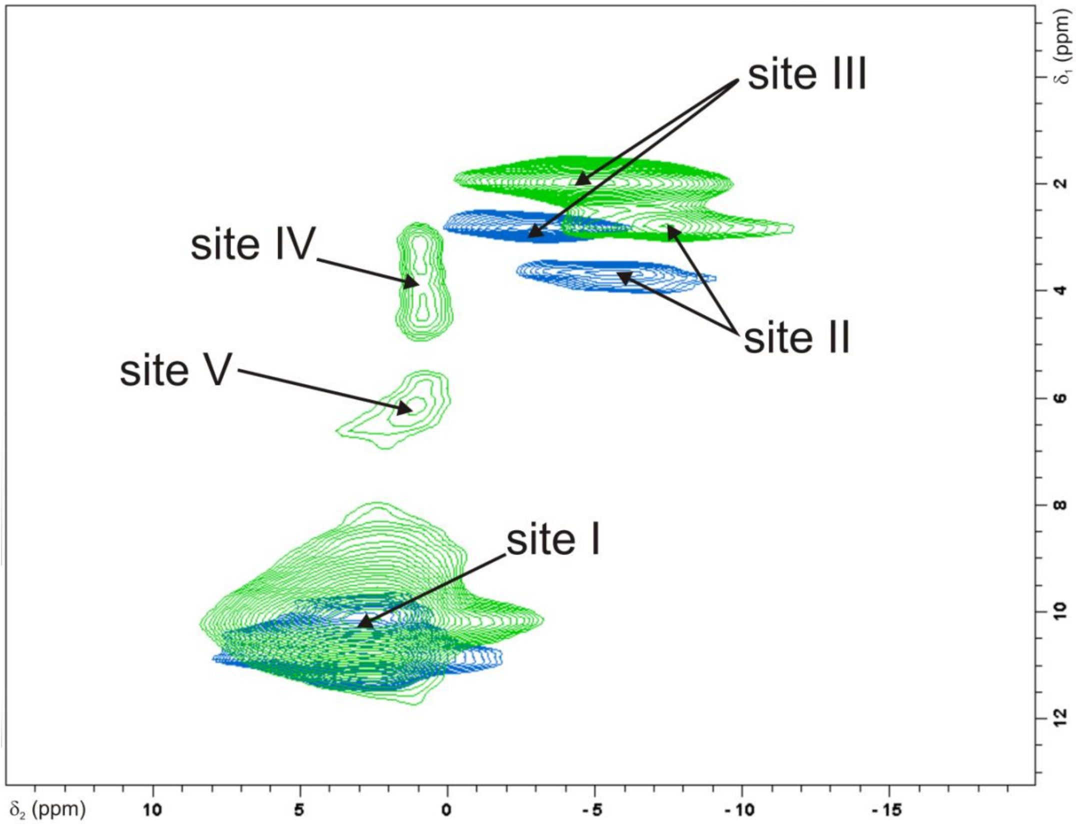

Figure 7.6 ^{23}Na{^{1}H} MAS NMR spectra showing the (blue) sodium environments in pMK and overlaid with (green) the sodium sites present in MKG

Figure 7.6 shows the comparison of sodium sites within the pMK and MKG materials represented by the blue and green contours respecively. The pMK shows the three sodium sites that are present in naturally occurring makatite, see **Chapter 5, Figure 5.16**. The MKG composite also exhibits these sites this but with a slight change in δ_{iso} values for sites II and III compared to the host. The composite also contains additional sodium sites.

This result provides the only evidence that a structural change has occurred in the host as due to the presence of glycerol. The XRD showed no change in interlayer spacing upon the addition of glycerol. However, there could be some exchange of water molecules for glycerol in the interlayer space. For example, the interlayer spacing is *ca*. 9.0 Å, the average diameter and length of a glycerol molecule is reported to be 4.7 and 5.2 Å respectively[391].

Table 7.2 Quadrupolar parameters calculated from **Eq. 2.37** and **2.38** giving the δ_{iso} *and* P_Q values for the pMK and MKG materials

Material	**Site**	**δ_{iso} /ppm**	**P_Q /(MHz)**
pMK	I	8.0	1.5
	II	0.1	1.6
	II	0.7	1.3
MKG	I	7.4	1.5
	II	-1.1	1.7
	III	-0.7	1.4
	IV	2.8	1.0
	V	4.2	1.2

The XRD pattern for the MKG material indicates a reduction in crystallinity compared to that of its parent material. Therefore, polyol mixing may simply affect the crystal structure resulting in the interlayer sodium ions being washed out and hence the appearance of new sodium sites. The location of the polyol with respect to the interlayer region could be probed using ^{1}H-^{13}C HETCOR experiments.

7.5 Discussion

7.5.1 *Structural representation of the MKG composite*

The MKG composite and CS2G hydrogel are both fine, white powders with similar amounts of carbon and water. However, the TGA results indicate that the water molecules in MKG are held more tightly than in the hydrogel. The XRD confirms no change in interlayer spacing indicating unsuccessful intercalation of polyols. This is also confirmed by the absence of additional resonances in the ^{29}Si or ^{13}C NMR spectra. The ^{1}H and ^{13}C NMR spectra display narrow resonances for MKG suggesting mobile and/or ordered domains of water and glycerol. The hydrogel shows broader resonances, which, upon heat ageing begin to narrow as makatite formation occurs. This suggests that the water molecules rearrange towards more ordered structures. Additionally, glycerol, which is not part of the makatite crystal structure, segregates away from the silica interface forming water/glycerol domains. Essentially the end product of the CS2G hydrogel crystallisation is analogous to the MKG composite. Taking into account the results, the proposed structure of the MKG composite is given in **Figure 7.7**:

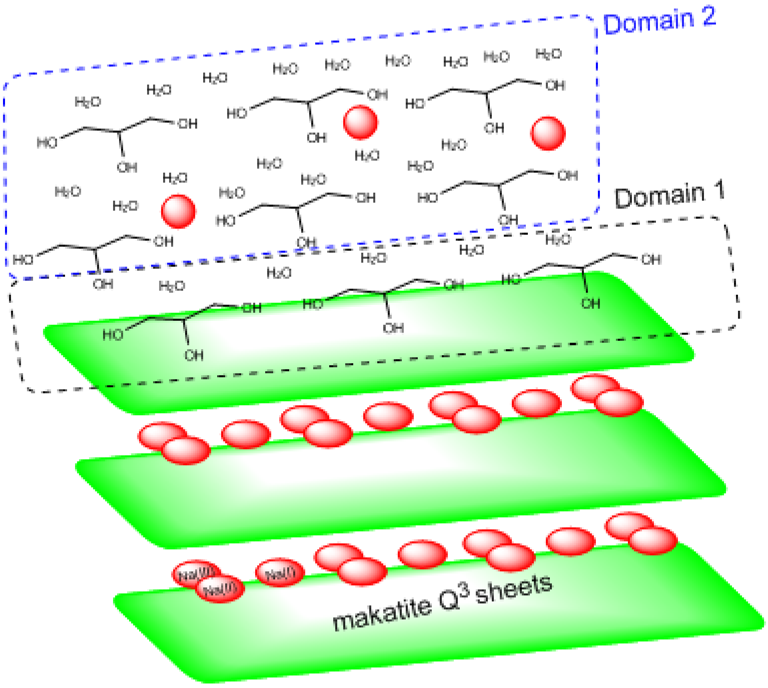

Figure 7.7 Structural representation of the MKG composite

The makatite structure is retained but we believe that glycerol and water domains encase the crystals. Domain 1 could correspond to glycerol/water interacting with terminated sheets. This is possible because there is an additional Q^3 resonance present in the ^{29}Si CP MAS NMR spectra in **Figure 7.3**. Additionally, the TGA shows a mass loss between 450 and 550°C which would indicate some glycerol species involved in stronger bonding interactions. Domain 2 constitutes bulk glycerol/water domains, with stronger intermolecular hydrogel bonding interactions than the CS2G hydrogel. This is justified because the CS2G hydrogel shows a faster rate of mass loss from RT to 250°C compared to the MKG composite, and therefore indicates weaker water/glycerol interactions. In fact, if we refer back to the proposed models of the hydrogel in **Chapter 4**, it coincides with the notion of a heterogeneous system; the water/glycerol domains are interrupted by silica oligomers and colloids thus reducing long range intermolecular bonding.

7.5.2 *Makatite Synthesis*

Our attempts to produce makatite hydrothermally resulted in the formation of magadiite. The crystal structure of magadiite is unresolved, but from ^{29}Si NMR and powder XRD it is composed of multilayer Q^4/Q^3 sheets separated with hydrated sodium ions giving a basal spacing of *ca.* 15.0 Å. It is likely that a more condensed silica phase is preferentially formed over time during hydrothermal conditions. This is exemplified by the presence of the kenyaite phase forming after 13 days, which was derived from magadiite. Kenyaite has an interlayer spacing of 20.0 Å. Similarly, the “seeding” method employed to influence crystal formation seemed independent in the presence of the naturally obtained makatite crystals, which formed the magadiite phase. We could only obtain synthetic makatite through the heat ageing of the CS2 hydrogels between glass sheets. The question as to why this occurs is still being addressed and warrants future investigation.

7.5.3 *Intercalation Chemistry*

The microanalysis, TGA, XRD and NMR results .unambiguously show that makatite does not intercalate nor graft short to long chained polyols. Conversely, magadiite and kenyaite readily graft and intercalate a variety of organic molecules. We postulate that intercalation reactivity between makatite and magadiite/kenyaite can be explained by differences in interlayer spacing and stabilities. Firstly, makatite has the smallest interlayer gallery, followed by magadiite and kenyaite; 9.0, 15.0 and 20.0 Å respectively. A small gallery spacing would simply restrict the amount of organic species that can enter. However, no intercalation is observed for makatite, suggesting there are more than just size exclusion effects occurring.

Secondly, the ^{23}Na MQMAS NMR experiments on magadiite and kenyaite reported by Harris (we also have reproduced their results) find one sodium site for each mineral with similar chemical shifts and quadrupolar coupling constants indicating sodium in a six-fold coordination sphere with water molecules. It is suggested that these environments are involved in hydrogen bonding with silanol groups, which can readily be exchanged for organics. Recall that in makatite there are three distinct sodium sites, two of which are involved in hydrogen bonding with water and silanol groups; sites II and III. The remaining site (site I) is involved in bonding with oxygen atoms associated with silicon atoms *i.e*. siloxide (Si-O^-) in nature. We postulate this “formal” bonding $\equiv\text{Si-O}^{-+}\text{Na}$ interaction is thought to be responsible for makatites resilience towards intercalation or grafting.

7.6 Conclusions

In summary, a makatite/glycerol hydrogel has been synthesised. Upon mixing with glycerol/water the makatite crystal structure remains largely intact with a small proportion of interlayer sodium ions being leached out. These ions are probably located in the glycerol/water domains. The synthesised composite is analogous to the end product of heat ageing a CS2 series hydrogel. Unlike other layered silicates, makatite does not intercalate or graft short to long chained polyols.

Chapter 8

General Conclusions and Outlook

8.1 General Conclusions and Outlook

A detailed investigation into the characterisation, thermal stability and methodologies to improve commercial fire resistant glasses has been presented. The chemical transformation and mechanical properties of these materials, above a temperature of 150°C, has been thoroughly documented and is well understood. Therefore, in this report we have focused on the molecular level understanding and the response of these products at temperatures up to 100°C. The research presented here highlights various methodologies available for the study of complex materials that lack long range order. Solid-state NMR has provided a unique insight into these previously unstudied materials. Throughout the report, the limitations of these techniques when applied to amorphous systems with high concentrations of water have also been highlighted.

From an industrial standpoint, no knowledge existed on the effect of the polyols on the silica, sodium and water environments in such complex materials (**Chapter 4**). For example, the polyol blocks hydrogen bonding between adjacent silica clusters, as shown by the absence of a resonance at 15 ppm in the ^{1}H MAS experiments. This also inhibits the formation of the Na(**b**) site. These results show that the polyols are located at the silica/water interface. T_1 and T_2 variable temperature measurements confirmed these findings, but also indicated that a proportion of the polyols are distributed throughout the water networks. The E_a required to modulate water motion increases as a function of polyol chain length. Therefore, the polyol acts as a plasticiser and also as a positive azeotrope. Preliminary work also pointed towards a glycerol gradient throughout the hydrogel as a result of the drying processing, which was previously hypothesised. However, further work is needed to clarify this effect, see conclusion section in **Chapter 4**.

The hydrogels were subjected to heating at 100°C for short and long periods. The products, when installed in buildings, will not be exposed to such elevated temperatures. However, storage at this elevated temperature was used to accelerate the crystallisation process and track the molecular level changes that occur within a realistic timeframe. The hydrogels are metastable, therefore the propensity for the materials to form further kinetic products at temperatures of 30 to 70°C is not surprising. Additional heat ageing experiments (not included in this report) show that the decrease in temperature inhibits the rate of crystallisation of makatite. Glazing installations in certain countries have the propensity to regularly reach temperatures in excess of 40°C. With this in mind, understanding and being able to control the crystallisation process is very important for the longevity of the product. This was the driving force behind **Chapters 5** and **6**. Short term ageing showed that the CS2G and CS2 hydrogels remain transparent whereas the CS2EG hydrogel showed a reversible white hazing throughout when exposed to temperatures above 30°C. VT ^{1}H MAS, ^{1}H-^{13}C HETCOR and DSC measurements indicate that the ethylene glycol/water networks become very mobile resulting in phase segregation from the silica/water units causing a loss of transparency. XRD and NMR experiments tracked the crystallisation of makatite as a function of long term ageing.

The results obtained from the short term ageing and those in **Chapter 4**, were used to rationalise the differing rates of makatite crystallisation for each hydrogel. The CS2G hydrogel shows inhibited makatite nucleation and growth; this ultimately prolongs its transparency over the CS2EG and CS2 hydrogels. Combining the results from **Chapters 4** and **5**, on a macroscopic level, the CS2G hydrogel provides better optical and structural integrity and has a longer “shelf-life” over the CS2 and CS2EG hydrogels. The substitution of glycerol for polyols with similar dimensions i.e. ethylene glycerol, sorbitol *etc.* can significantly influence the molecular and macrolevel properties of the resulting hydrogels.

Makatite crystallisation can also be influenced by the nature of the starting sodium-silicate solutions used for hydrogel synthesis. The use of a synthetic analogue of the commercial 3.30 *wt.* ratio solution with and without glycerol slowed down makatite formation and prolonged transparency of the hydrogel at elevated temperatures. Despite this, no differences between the synthetic and commercial solutions/hydrogels could be distinguished at the molecular level. Therefore, we concluded that the synthetic system must contain different colloidal components, affecting the crystallisation process.

The research, particularly from **Chapter 6**, has led to further studies based on similar hydrogel systems using different network modifiers and formers based on Ti, Zr and Al.

Focusing more on the academic nature of the project, the use of ^{23}Na MQMAS experiments have been used to investigate Zeolite crystallisation[324, 325] and focused mainly on correlating Na-O distances to δ_{iso} values. Based on the work from **Chapters 4** and **5**, it would be very interesting to see if a correlation existed between *wt.* ratio/water content in hydrogels and the subsequent effect this has on the sodium environments. Also, no reports exist on using alternative MQMAS pulse sequences on amorphous materials. For example, RIACT[392] (Rotation-Induced Adiabatic Coherence Transfer), DFS[393] (Double Frequency Sweeps) and the FAM[394] (Fast Amplitude Modulation) are methods that can improve the efficiency of 3Q to 1Q transfer. Therefore it would certainly be interesting to investigate the effect of these different pulse sequences have on such materials. The synthesis of a makatite/glycerol hydrogel gave further insight into the chemistry and reactivity of the starting hydrogels

References

1. *PQ Sodium-Silicates*, http://www.pqcorp.com/pc/NorthAmerica/Products/SodiumSilicateLiquids.aspx.
2. B. Research, *The Global Market for Flame Retardant Chemicals*, http://www.bccresearch.com/aboutus/contactus/.
3. B. J. Hughes, J. B. Guilbaud, M. Allix and Y. Z. Khimyak, *Journal of Materials Chemistry*, 2005, **15**, 4728-4733.
4. L. Sierra, B. Lopéz, H. Gil and J.-L. Guth, *Advanced Materials*, 1999, **11**, 307-311.
5. J. Trebosc, J. W. Wiench, S. Huh, V. S. Y. Lin and M. Pruski, *J. Am. Chem. Soc.*, 2005, **127**, 3057-3068.
6. C. Vercaemst, M. Ide, P. V. Wiper, J. T. A. Jones, Y. Z. Khimyak, F. Verpoort and P. Van Der Voort, *Chemistry of Materials*, 2009, **21**, 5792-5800.
7. A. S. Dorcheh and M. H. Abbasi, *Journal of Materials Processing Technology*, 2008, **199**, 10-26.
8. A. Pons, L. Casas, E. Estop, E. Molins, K. D. M. Harris and M. Xu, *Journal of Non-Crystalline Solids*, 2011, **358**, 461-469.
9. F. Bentivegna, M. Canva, P. Georges, A. Brun, F. Chaput, L. Malier and J. P. Boilot, *Applied Physics Letters*, 1993, **62**, 1721-1723.
10. T. Khonina, E. Shadrina, A. Boyko, O. Chupakhin, L. Larionov, V. A. and V. Burda, 2010, 75-80.
11. H. Roggendorf, D. Böschel and J. Trempler, *Journal of Non-Crystalline Solids*, 2001, **293-295**, 752-757.
12. Q. Zhao, M. Guerette and L. Huang, *Journal of Non-Crystalline Solids*, 2012, **358**, 652-657.
13. R. Sawyer, H. W. Nesbitt and R. A. Secco, *Journal of Non-Crystalline Solids*, 2012, **358**, 290-302.
14. A. Goel, J. S. McCloy, K. M. Fox, C. J. Leslie, B. J. Riley, C. P. Rodriguez and M. J. Schweiger, *Journal of Non-Crystalline Solids*, 2012, **358**, 674-679.
15. W. Holderich, M. Hesse and F. Naumann, *Angewandte Chemie-International Edition in English*, 1988, **27**, 226-246.
16. M. E. Davis and R. F. Lobo, *Chemistry of Materials*, 1992, **4**, 756-768.
17. C. S. Cundy and P. A. Cox, *Chemical Reviews*, 2003, **103**, 663-701.
18. Y.-R. Wang, S.-F. Wang and L.-C. Chang, *Applied Clay Science*, 2006, **33**, 73-77.
19. Y. Wang, Y. Shang, J. Zhu, J. Wu, S. Ji and C. Meng, *Journal of Chemical Technology and Biotechnology*, 2009, **84**, 1894-1898.
20. O. Y. Kwon and K. W. Park, *Bulletin of the Korean Chemical Society*, 2004, **25**, 25-26.
21. T. Iwasaki, T. Kuroda, S. Ichio, M. Satoh and T. Fujita, *Chemical Engineering Communications*, 2006, **193**, 69-76.
22. R. M. Hazen, L. W. Finger, R. J. Hemley and H. K. Mao, *Solid State Communications*, 1989, **72**, 507-511.
23. F. Hoffmann, M. Cornelius, J. Morell and M. Froeba, *Angewandte Chemie-International Edition*, 2006, **45**, 3216-3251.
24. C. Sanchez, B. Julian, P. Belleville and M. Popall, *Journal of Materials Chemistry*, 2005, **15**, 3559-3592.
25. K. Cabrera, *Journal of Separation Science*, 2004, **27**, 843-852.
26. J. E. Fesmire, *Cryogenics*, 2006, **46**, 111-117.
27. *Industrial Ceramics*, 1998, **18**, 114-114.
28. W. F. McDonough and S. S. Sun, *Chemical Geology*, 1995, **120**, 223-253.
29. W. O. R. Horacio E. Bergna, *Colloidal Silica: Fundamentals and Applications*, CRC Press, 2005.

30. J. F. Ma and N. Yamaji, *Trends in Plant Science*, 2006, **11**, 392-397.
31. V. Martin-Jezequel, M. Hildebrand and M. A. Brzezinski, *Journal of Phycology*, 2000, **36**, 821-840.
32. C. C. Perry and T. Keeling-Tucker, *Journal of Biological Inorganic Chemistry*, 2000, **5**, 537-550.
33. E. Maciel Gary, in *Solid-State NMR Spectroscopy of Inorganic Materials*, American Chemical Society, Editon edn., 1999, vol. 717, pp. 326-356.
34. G. J. Copley, *Materials Science and Engineering*, 1971, **8**, 1-&.
35. J. A. Duffy and D. E. Macphee, *The Journal of Physical Chemistry B*, 2007, **111**, 8740-8745.
36. T. L. Weeding, B. H. W. S. de Jong, W. S. Veeman and B. G. Aitken, *Nature*, 1985, **318**, 352-353.
37. J. F. Stebbins and P. McMillan, *Journal of Non-Crystalline Solids*, 1993, **160**, 116-125.
38. S. D. Kinrade, J. W. Del Nin, A. S. Schach, T. A. Sloan, K. L. Wilson and C. T. G. Knight, *Science*, 1999, **285**, 1542-1545.
39. A. A. Lebedev, *Trudy Gos. Opt. Inst.* , 1921, **2**, 1-20.
40. J. T. Randell, H. P. Rooksby and B. S. Cooper, *Z. Kristalogr*, 1930, **75**, 196-214.
41. W. H. Zachariasen, *J. Am. Chem. Soc.*, 1932, **54**, 3841-3850.
42. B. E. Warren, *Phys. Rev.*, 1934, **45**, 657-661.
43. G. S. Henderson, *The Canadian Mineralogist*, 2005, **43**, 1921-1958.
44. G. N. Greaves and S. Sen, *Advances in Physics*, 2007, **56**, 1-166.
45. G. N. Greaves, A. Fontaine, P. Lagarde, D. Raoux and S. J. Gurman, *Nature*, 1981, **293**, 611-616.
46. G. N. Greaves, *J. Non-Cryst. Solid*, 1985, **71**, 203-217.
47. F. M. E. Eldin and N. A. El Alaily, *Materials Chemistry and Physics*, 1998, **52**, 175-179.
48. S. Balasubramanian and K. J. Rao, *Journal of Non-Crystalline Solids*, 1995, **181**, 157-174.
49. A. Bunde, M. D. Ingram and P. Maass, *Journal of Non-Crystalline Solids*, 1994, **172-174, Part 2**, 1222-1236.
50. D. Wilmer, T. Kantimm, O. Lamberty, K. Funke, M. D. Ingram and A. Bunde, *Solid State Ionics*, 1994, **70-71, Part 1**, 323-327.
51. J. Habasaki and K. L. Ngai, *Physical Chemistry Chemical Physics*, 2007, **9**, 4673-4689.
52. J. Zarzycki, *Glasses and the Vitreous State*, Cambridge University, 1991.
53. E. D. Zanotto and F. A. B. Coutinho, *Journal of Non-Crystalline Solids*, 2004, **347**, 285-288.
54. G. Prabhat K, *Journal of Non-Crystalline Solids*, 1996, **195**, 158-164.
55. S. Hiroshi, *Journal of Molecular Liquids*, 1999, **81**, 25-36.
56. S. R. Elliott, *Physics of Amorphous Materials*, Longman Scientific & Technical, 1990.
57. A. Salekigerhardt, J. G. Stowell, S. R. Byrn and G. Zografi, *Journal of Pharmaceutical Sciences*, 1995, **84**, 318-323.
58. B. Shah, V. K. Kakumanu and A. K. Bansal, *Journal of Pharmaceutical Sciences*, 2006, **95**, 1641-1665.
59. M. J. Pikal and D. R. Rigsbee, *Pharmaceutical Research*, 1997, **14**, 1379-1387.
60. R. J. Lloyd, X. D. Chen and J. B. Hargreaves, *International Journal of Food Science and Technology*, 1996, **31**, 305-311.
61. D. Q. M. Craig, P. G. Royall, V. L. Kett and M. L. Hopton, *International Journal of Pharmaceutics*, 1999, **179**, 179-207.
62. J. F. Willart, A. De Gusseme, S. Hemon, G. Odou, F. Danede and M. Descamps, *Solid State Communications*, 2001, **119**, 501-505.
63. H. K. Poswal, A. K. Tyagi, A. Lausi, S. K. Deb and S. M. Sharma, *Journal of Solid State Chemistry*, 2009, **182**, 136-140.

64. G. Floudas, Paluch, M., Grzybowski, A., Ngai, K., *Molecular Dynamics of Glass-Forming Systems*, Springer, 2011.
65. E. Hellmut, *Progress in Nuclear Magnetic Resonance Spectroscopy*, 1992, **24**, 159-293.
66. M. Lancry, E. Régnier and B. Poumellec, *Progress in Materials Science*, 2012, **57**, 63-94.
67. B. C. Hancock and G. Zografi, *Journal of Pharmaceutical Sciences*, 1997, **86**, 1-12.
68. H. Rawson, *Physical Science, Measurement and Instrumentation, Management and Education - Reviews, IEE Proceedings A*, 1988, **135**, 325-345.
69. P. Atkins and P. Paul De, *Atkins' Physical Chemistry*, 8 edn., 2006.
70. J. A. Forrest, K. Dalnoki-Veress and J. R. Dutcher, *Physical Review E*, 1997, **56**, 5705-5716.
71. R. O. Ebewele, *Polymer Science and Technology* CRC Press, 2000.
72. M. J. Ojovan, *Entropy*, 2008, **10**, 334-364.
73. M. D. Ediger, C. A. Angell and S. R. Nagel, *The Journal of Physical Chemistry*, 1996, **100**, 13200-13212.
74. P. G. Debenedetti and F. H. Stillinger, *Nature*, 2001, **410**, 259-267.
75. J. Dudowicz, K. F. Freed and J. F. Douglas, *Journal of Chemical Physics*, 2006, **124**.
76. S. Hans, *Journal of Non-Crystalline Solids*, 1999, **243**, 81-108.
77. D. J. Wales and J. P. K. Doye, *Physical Review B*, 2001, **63**.
78. M. A. Beckett, M. P. Rugen-Hankey and K. S. Varma, *Journal of Sol-Gel Science and Technology*, 2006, **39**, 95-101.
79. Z. Deng, E. Breval and C. G. Pantano, *Journal of Non-Crystalline Solids*, 1988, **100**, 364-370.
80. A. Ghosh and D. Chakravorty, *Applied Physics Letters*, 1991, **59**, 855-856.
81. M. Nogami, K. Miyamura and Y. Abe, *Journal of the Electrochemical Society*, 1997, **144**, 2175-2178.
82. S. Sen and R. E. Youngman, *Journal of Physical Chemistry B*, 2004, **108**, 7557-7564.
83. R. Rustum, *Science*, 1987, **238**, 1664-1669.
84. G. D. Soraru̇, A. Karakuscu, C. Boissiere and F. Babonneau, *Journal of the European Ceramic Society*, 2012, **32**, 627-632.
85. J. T. A. Jones, C. D. Wood, C. Dickinson and Y. Z. Khimyak, *Chemistry of Materials*, 2008, **20**, 3385-3397.
86. B. A. Treuherz and Y. Z. Khimyak, *Microporous and Mesoporous Materials*, 2007, **106**, 236-245.
87. N. N. Khimich, *Glass Physics and Chemistry*, 2004, **30**, 430-442.
88. A. V. C. J. Alemán, J. He, M. Hess, K. Horie, R. G. Jones, P. Kratochvíl, I. Meisel, I. Mita, G. Moad, S. Penczek and R. F. T. Stepto, *Pure Appl. Chem.*, 2007, **79**, 1801-1829.
89. G. H. Bogush and C. F. Zukoski Iv, *Journal of Colloid and Interface Science*, 1991, **142**, 1-18.
90. P. Colomban, *Ceramics International*, 1989, **15**, 23-50.
91. J. Wen and G. L. Wilkes, *Chemistry of Materials*, 1996, **8**, 1667-1681.
92. B. J. J. Zelinski and D. R. Uhlmann, *Journal of Physics and Chemistry of Solids*, 1984, **45**, 1069-1090.
93. I. G. Khaskin, *Dokl. Akad. Nauk SSSR*, 1952, **85**, 129-132.
94. D. Arcos and M. Vallet-Regi, *Acta Biomaterialia*, 2010, **6**, 2874-2888.
95. J. Ma, C. Z. Chen, D. G. Wang and J. Z. Shi, *Materials Science and Engineering: C*, 2010, **30**, 886-890.
96. M. Zhu, H. Wang, J. Liu, H. He, X. Hua, Q. He, L. Zhang, X. Ye and J. Shi, *Biomaterials*, 2010, **32**, 1986-1995.
97. Y. E. Shapiro, *Progress in Polymer Science*, 2011, **36**, 1184-1253.

98. M. Lin, P. Xu and W. Zhong, *Journal of Biomedical Materials Research Part B: Applied Biomaterials*, 2012, **100B**, 1114-1120.
99. J. Gu, F. Xia, Y. Wu, X. Qu, Z. Yang and L. Jiang, *Journal of Controlled Release*, 2007, **117**, 396-402.
100. A. C. Pierre, *Biocatalysis and Biotransformation*, 2004, **22**, 145-170.
101. D. Brady and J. Jordaan, *Biotechnology Letters*, 2009, **31**, 1639-1650.
102. G. B. Alexander, W. M. Heston and R. K. Iler, *Journal of Physical Chemistry*, 1954, **58**, 453-455.
103. R. Siever, *Journal of Geology*, 1962, **70**, 127-150.
104. C. E. Manning, *Geochimica Et Cosmochimica Acta*, 1994, **58**, 4831-4839.
105. R. O. Fournier and J. J. Rowe, *American Mineralogist*, 1977, **62**, 1052-1056.
106. J. Šefčík and A. V. McCormick, *AIChE Journal*, 1997, **43**, 2773-2784.
107. C. T. G. Knight, S. D. Kinrade, G. H. S. L.E. Datnoff and G. H. Korndörfer, in *Studies in Plant Science*, Elsevier, Editon edn., 2001, vol. Volume 8, pp. 57-84.
108. R. K. Iler, John Wiley & Sons, Editon edn., 1979.
109. J. Falcone, in *Kirk-Othmer Encyclopedia of Chemical Technology*, John Wiley & Sons, Inc., Editon edn., 2000.
110. M. Fawer, M. Concannon and W. Rieber, *The International Journal of Life Cycle Assessment*, 1999, **4**, 207-212.
111. F. Gaboriaud, A. Nonat, D. Chaumont, A. Craievich and B. Hanquet, *The Journal of Physical Chemistry B*, 1999, **103**, 2091-2099.
112. I. Sivanesan, M. S. Son, C. S. Lim and B. R. Jeong, *African Journal of Biotechnology*, 2011, **10**, 6743-6749.
113. E. Prud'homme, P. Michaud, E. Joussein, J. M. Clacens and S. Rossignol, *Journal of Non-Crystalline Solids*, 2011, **357**, 1270-1278.
114. M. T. Tognonvi, J. Soro and S. Rossignol, *Journal of Non-Crystalline Solids*, 2012, **358**, 81-87.
115. A. V. McCormick, A. T. Bell and C. J. Radke, *The Journal of Physical Chemistry*, 1989, **93**, 1733-1737.
116. P. W. J. G. Wijnen, T. P. M. Beelen, K. P. J. Rummens, H. C. P. L. Saeijs and R. A. Van Santen, *Journal of Applied Crystallography*, 1991, **24**, 759-764.
117. I. Hasegawa, S. Sakka, Y. Sugahara, K. Kuroda and C. Kato, *Journal of the Chemical Society, Chemical Communications*, 1989, 208-210.
118. N. Goudarzi, M. A. Chamjangali and G. Bagherian, *Journal of Molecular Structure*, 2010, **982**, 127-132.
119. B. Harald, in *Handbook of Detergents, Part F*, CRC Press, Editon edn., 2008, pp. 387-419.
120. J. L. Provis, A. Kilcullen, P. Duxson, D. G. Brice and J. S. J. van Deventer, *Industrial & Engineering Chemistry Research*, 2012, **51**, 2483-2486.
121. J. H. Wills, *The Journal of Physical and Colloid Chemistry*, 1950, **54**, 304-310.
122. C. S. Gittleman, A. T. Bell and C. J. Radke, *Catalysis Letters*, 1996, **38**, 1-9.
123. H. Kalipcilar and A. Culfaz, *Crystal Research and Technology*, 2000, **35**, 933-942.
124. J. C. Vartuli, G. J. Kennedy, B. A. Yoon and A. Malek, *Microporous and Mesoporous Materials*, 2000, **38**, 247-254.
125. V. Meynen, P. Cool and E. F. Vansant, *Microporous and Mesoporous Materials*, 2009, **125**, 170-223.
126. P. B. Sarawade, J.-K. Kim, A. Hilonga, Q. Dang Viet and H. T. Kim, *Applied Surface Science*, 2011, **258**, 955-961.
127. H. Setyawan and R. Balgis, *Asia-Pacific Journal of Chemical Engineering*, 2010, n/a-n/a.
128. G. Canosa, P. V. Alfieri and C. A. Giudice, *Progress in Organic Coatings*, 2011, **73**, 178-185.

129. A. Pfeffer, C. Mai and H. Militz, *European Journal of Wood and Wood Products*, 2012, **70**, 165-176.
130. J. K. Borchardt, *Colloids and Surfaces*, 1992, **63**, 189-199.
131. A. A. H. Elsayed and M. S. Almalik, *Journal of Canadian Petroleum Technology*, 1995, **34**, 19-24.
132. U. Turksoy and S. Bagci, *Journal of Petroleum Science and Engineering*, 2000, **26**, 105-119.
133. V. A. Lotov, *Glass and Ceramics*, 2011, **68**, 234-235.
134. F. S. Pratama, H. F. Robinson and J. J. Pagano, *Colloids and Surfaces a-Physicochemical and Engineering Aspects*, 2011, **389**, 127-133.
135. J. H. E. Cartwright, J. M. Garcia-Ruiz, M. L. Novella and F. Otalora, *Journal of Colloid and Interface Science*, 2002, **256**, 351-359.
136. J. H. E. Cartwright, B. Escribano, C. Ignacio Sainz-Diaz and L. S. Stodieck, *Langmuir*, 2011, **27**, 3294-3300.
137. J. H. E. Cartwright, B. Escribano and C. Ignacio Sainz-Diaz, *Langmuir*, 2011, **27**, 3286-3293.
138. L. M. Barge, I. J. Doloboff, L. M. White, G. D. Stucky, M. J. Russell and I. Kanik, *Langmuir*, 2012, **28**, 3714-3721.
139. Unknown, *Journal of the American Oil Chemists' Society*, 1987, **64**, 1480-1484.
140. E. Blank, *Journal of the American Oil Chemists' Society*, 1942, **19**, 110-113.
141. R. W. Harman, *Journal of Physical Chemistry*, 1925, **29**, 1155-1168.
142. R. W. Harman, *Journal of Physical Chemistry*, 1926, **30**, 359-368.
143. R. W. Harman, *Journal of Physical Chemistry*, 1926, **30**, 917-924.
144. R. W. Harman, *Journal of Physical Chemistry*, 1926, **30**, 1100-1111.
145. R. W. Harman, *Journal of Physical Chemistry*, 1927, **31**, 355-373.
146. R. W. Hardman, *Journal of Physical Chemistry*, 1927, **31**, 511-518.
147. R. W. Harman, *Journal of Physical Chemistry*, 1927, **31**, 616-625.
148. G. Lagerstrom, *Acta Chem. Scand*, 1959, **13** 722-736.
149. H. Ukihashi, *Bulletin of the Chemical Society of Japan*, 1957, **30**, 470-476.
150. P. Debye and R. V. Nauman, *Journal of Physical Chemistry*, 1961, **65**, 5-&.
151. P. Debye and R. V. Nauman, *Journal of Physical Chemistry*, 1961, **65**, 8-&.
152. M.-C. Pan, W.-J. Deng, Y.-X. Yang and Y.-R. Chen, *Glass Physics and Chemistry*, 2007, **36**, 110-115.
153. I. Hasegawa, S. Sakka, K. Kuroda and C. Kato, *Journal of Chromatography* 1987, **410**, 137-143.
154. G. Garzó, D. Hoebbel, Z. J. Ecsery and K. Ujszászi, *Journal of Chromatography A*, 1978, **167**, 321-336.
155. G. Garzó and D. Hoebbel, *Journal of Chromatography A*, 1976, **119**, 173-179.
156. V. D. Hobbel and W. W., *Z. anorg. allg. Chem.*, 1974, **405**, 163-166.
157. K. Kuroda and C. Kato, *Clays and Clay Materials*, 1977, **25**, 407-410.
158. N. H. Ray and R. J. Plaisted, *Journal of the Chemical Society, Dalton Transactions*, 1983, 475-481.
159. L. S. D. Glasser and E. E. Lachowski, *Journal of the Chemical Society, Dalton Transactions*, 1980, 393-398.
160. G. J. Bratton, B. R. Currell, J. R. Parsonage and M. J. K. Thomas, *Journal of Materials Chemistry*, 1993, **3**, 343-346.
161. L. S. D. Glasser and E. E. Lachowski, *Journal of the Chemical Society, Dalton Transactions*, 1980, 399-402.
162. R. K. Iler, *Journal of Colloid and Interface Science*, 1980, **75**, 138-148.
163. M. Dietzel and E. Usdowski, *Colloid & Polymer Science*, 1995, **273**, 590-597.
164. H. Jancke, G. Engelhardt, M. Magi and E. Lippmaa, *Z. Chem.*, 1973, **13**, 392-393.
165. H. C. Marsmann, *Chem. Ztg.*, 1973, **97**, 128-133.

166. Engelhard.G, R. Radeglia, H. Jancke, E. Lippmaa and M. Magi, *Organic Magnetic Resonance*, 1973, **5**, 561-566.
167. E. Lippmaa, M. Magi, A. Samoson, G. Engelhardt and A. R. Grimmer, *J. Am. Chem. Soc.*, 1980, **102**, 4889-4893.
168. S. D. Kinrade, C. T. G. Knight, D. L. Pole and R. T. Syvitski, *Inorganic Chemistry*, 1998a, **37**, 4272-4277.
169. S. D. Kinrade, C. T. G. Knight, D. L. Pole and R. T. Syvitski, *Inorganic Chemistry*, 1998b, **37**, 4278-4283.
170. S. D. Kinrade and T. W. Swaddle, *Inorganic Chemistry*, 1988, **27**, 4259-4264.
171. C. T. G. Knight, *Journal of the Chemical Society, Dalton Transactions*, 1988, 1457-1460.
172. C. T. G. Knight, R. J. Kirkpatrick and E. Oldfield, *Journal of the Chemical Society, Chemical Communications*, 1989, 919-921.
173. C. J. Creswell, R. K. Harris and P. T. Jageland, *Journal of the Chemical Society, Chemical Communications*, 1984, 1261-1263.
174. R. K. Harris and C. T. G. Knight, *Journal of the Chemical Society, Faraday Transactions 2: Molecular and Chemical Physics*, 1983, **79**, 1525-1538.
175. R. K. Harris and C. T. G. Knight, *Journal of the Chemical Society, Faraday Transactions 2: Molecular and Chemical Physics*, 1983, **79**, 1539-1561.
176. R. K. Harris, C. T. G. Knight and D. N. Smith, *Journal of the Chemical Society, Chemical Communications*, 1980, 726-727.
177. C. T. G. Knight, R. J. Balec and S. D. Kinrade, *Angewandte Chemie International Edition*, 2007, **46**, 8148-8152.
178. M. Haouas and F. Taulelle, *The Journal of Physical Chemistry B*, 2006, **110**, 3007-3014.
179. H. Cho, A. R. Felmy, R. Craciun, J. P. Keenum, N. Shah and D. A. Dixon, *J. Am. Chem. Soc.*, 2006, **128**, 2324-2335.
180. T. T. Trinh, A. P. J. Jansen, R. A. van Santen and E. J. Meijer, *The Journal of Physical Chemistry C*, 2009, **113**, 2647-2652.
181. X.-Q. Zhang, T. T. Trinh, R. A. van Santen and A. P. J. Jansen, *J. Am. Chem. Soc.*, 2011, **133**, 6613-6625.
182. I. Halasz, A. Kierys, J. Goworek, H. Liu and R. E. Patterson, *The Journal of Physical Chemistry C*, 2011, **115**, 24788-24799.
183. D. Sebag, E. P. Verrecchia, S.-J. Lee and A. Durand, *Sedimentary Geology*, 2001, **139**, 15-31.
184. R. L. Hay, *Contributions to Mineralogy and Petrology*, 1968, **17**, 255-274.
185. G. G. Almond, R. K. Harris and K. R. Franklin, *Journal of Materials Chemistry*, 1997, **7**, 681-687.
186. K. R. Iler, *J. Coll. Sci*, 1964, **19648**.
187. U. Brenn, H. Ernst, D. Freude, R. Herrmann, R. Jahnig, H. G. Karge, J. Karger, T. Kanig, B. Madler, U. T. Pingel, D. Prochnow and W. Schwieger, *Microporous and Mesoporous Materials*, 2000, **40**, 43-52.
188. S. Wilhelm and L. Gerhard, in *Handbook of Layered Materials*, CRC Press, Editon edn., 2004.
189. H. H. Kruse, K. Beneke and G. Lagaly, *Colloid & Polymer Science*, 1989, **267**, 844-852.
190. Z. Wang and T. J. Pinnavaia, *Journal of Materials Chemistry*, 2003, **13**, 2127-2131.
191. C. Breen and R. Watson, *Applied Clay Science*, 1998, **12**, 479-494.
192. Z. Wang, T. Lan and T. J. Pinnavaia, *Chemistry of Materials*, 1996, **8**, 2200-2204.
193. D. Porter, E. Metcalfe and M. J. K. Thomas, *Fire and Materials*, 2000, **24**, 45-52.
194. Y. K. A.Usuki, M. Kawasumi, A. Okada, Y. Fukushima, T. Kurauchi and O. Kamigaito, *Journal of Materials Research*, 1993, **8**, 1179-1184.

195. W. L. Ijdo and T. J. Pinnavaia, *Green Chemistry*, 2001, **3**, 10-12.
196. M. C. Hermosin and J. Cornejo, *Chemosphere*, 1992, **24**, 1493-1503.
197. K. Beneke and G. Lagaly, *American Mineralogist*, 1983, **68**, 818-826.
198. K. Beneke and G. Lagaly, *American Mineralogist*, 1977, **62**, 763-771.
199. G. Lagaly, K. Beneke and A. Weiss, *American Mineralogist*, 1975, **60**, 642-649.
200. G. Lagaly, K. Beneke and A. Weiss, *American Mineralogist*, 1975, **60**, 650-658.
201. L. Mercier, G. A. Facey and C. Detellier, *Journal of the Chemical Society, Chemical Communications*, 1994, 2111-2112.
202. Y. K. Mitamura, Y; Hayashi, S; Sugahara, Y; Kuroda, K, *Chemistry of Materials*, 2001, **13**, 3747 - 3753.
203. D. Hirsemann, T. K. J. Köster, J. Wack, L. van Wüllen, J. Breu and J. r. Senker, *Chemistry of Materials*, 2011, **23**, 3152-3158.
204. R. A. Sheppard, A. J. Gude and R. L. Hay, *American Mineralogist*, 1970, **55**, 358-&.
205. H. Annehed, L. Falth and F. J. Lincoln, *Zeitschrift Fur Kristallographie*, 1982, **159**, 203-210.
206. W. Schwieger, K. H. Bergk, D. Heidemann, G. Lagaly and K. Beneke, *Zeitschrift Fur Kristallographie*, 1991, **197**, 1-12.
207. G. G. Almond, R. K. Harris, E. K. Franklin and P. Graham, *Journal of Materials Chemistry*, 1996, **6**, 843-847.
208. M. Hanaya and R. K. Harris, *Solid State Nuclear Magnetic Resonance*, 1997, **8**, 147-151.
209. M. Hanaya and R. K. Harris, *Journal of Materials Chemistry*, 1998, **8**, 1073-1079.
210. P. Piekarz, M. Derzsi, P. T. Jochym, J. Lazewski, M. Sternik, K. Parlinski and E. M. Serwicka, *Physical Review B*, 2009, **79**.
211. H. Tamura, D. Mochizuki, T. Kimura and K. Kuroda, *Chemistry Letters*, 2007, **36**, 444-445.
212. DirectGov, *Fire and Emergencies*, http://www.communities.gov.uk.
213. D. P. Goldenberg, *Concepts in Magnetic Resonance Part A*, 2010, **36A**, 49-83.
214. O. Sørensen, *Progress in Nuclear Magnetic Resonance Spectroscopy*, 1984, **16**, 163-192.
215. T. D. W. Claridge and D. W. C. Timothy, in *Tetrahedron Organic Chemistry Series*, Elsevier, Editon edn., 2009, vol. Volume 27, pp. 1-10.
216. T. D. W. Claridge and D. W. C. Timothy, in *Tetrahedron Organic Chemistry Series*, Elsevier, Editon edn., 2009, vol. Volume 27, pp. 11-34.
217. T. D. W. Claridge and D. W. C. Timothy, in *Tetrahedron Organic Chemistry Series*, Elsevier, Editon edn., 2009, vol. Volume 27, pp. 35-98.
218. S. R. Macomber, *A Complete Introduction to Modern NMR Spectroscopy*
John Wiley & Sons, INC. , Cincinnati 1998.
219. B. J. Lambert and P. E. Mazzola, *Nuclear Magnetic Resonance Spectroscopy: An Introduction to Principles, Applications, and Experimental Methods*, Pearson Education Inc., New Jersey, 2003.
220. D. D. Laws, H.-M. L. Bitter and A. Jerschow, *Angewandte Chemie International Edition*, 2002, **41**, 3096-3129.
221. A. Borisov, P. Hazendonk and P. Hayes, *Journal of Inorganic and Organometallic Polymers and Materials*, 2010, **20**, 183-212.
222. J. Keeler, *Understanding NMR Spectroscopy*, 2 edn., John Wiley & Sons, 2010.
223. E. A. Derome, *Modern NMR Techniques for Chemistry Research*, Pergamon Oxford, 1987.
224. R. G. Bryant, *Annual Review of Physical Chemistry*, 1978, **29**, 167-188.
225. R. Cai, H. Yang, J. He and W. Zhu, *Journal of Molecular Structure*, 2009, **938**, 15-19.
226. A. R. Lim, G. T. Schueneman and B. M. Novak, *Solid State Communications*, 1999, **109**, 465-470.

227. R. E. Taylor, A. D. Bacher and C. Dybowski, Elsevier, Editon edn., 2007.
228. E. R. Andrew, K. Jurga, J. M. Radomski and E. C. Reynhardt, *Solid State Nuclear Magnetic Resonance*, 1992, **1**, 121-125.
229. R. E. Taylor and C. Dybowski, *Journal of Molecular Structure*, 2008, **889**, 376-382.
230. A. Asano and G. A. Webb, Springer Netherlands, Editon edn., 2006, pp. 631-635.
231. Y. Aso, S. Yoshioka, T. Miyazaki, T. Kawanishi, K. Tanaka, S. Kitamura, A. Takakura, T. Hayashi and N. Muranushi, *Chemical and Pharmaceutical Bulletin*, 2007, **55**, 1227-1231.
232. P. C. M. M. Magusin, B. Mezari, L. van der Mee, A. R. A. Palmans and E. W. Meijer, *Macromolecular Symposia*, 2005, **230**, 126-132.
233. D. Suter and R. R. Ernst, *Physical Review B*, 1985, **32**, 5608-5627.
234. E. R. Andrew, *Philosophical Transactions of the Royal Society of London Series a-Mathematical Physical and Engineering Sciences*, 1981, **299**, 505-520.
235. S. P. Brown, *Solid State Nuclear Magnetic Resonance*, 2012, **41**, 1-27.
236. U. Haeberlen and J. S. Waugh, *Phys. Rev.*, 1968, **175**.
237. F. Bloch, *Phys. Rev.* , 1958, **111**.
238. A. E. Bennett, C. M. Rienstra, M. Auger, K. V. Lakshmi and R. G. Griffin, *J. Chem. Phys.* , 1995, **103**.
239. C. Vinod Chandran, P. K. Madhu, N. D. Kurur and T. Bräuniger, *Magnetic Resonance in Chemistry*, 2008, **46**, 943-947.
240. P. Subhradip and P. K. Madhu, *ChemInform*, 2011, **42**.
241. M. Lee and Goldburg, W. I. , *Phys. Rev. A.*, 1965, **140**, 1261-1271.
242. D. Sakellariou, A. Lesage, P. Hodgkinson and L. Emsley, *Chemical Physics Letters*, 2000, **319**, 253-260.
243. A. Bielecki, A. C. Kolbert and M. H. Levitt, *Chemical Physics Letters*, 1989, **155**, 341-346.
244. E. Vinogradov, P. K. Madhu and S. Vega, *Chemical Physics Letters*, 1999, **314**, 443-450.
245. R. Siegel, L. Mafra and J. Rocha, *Solid State Nuclear Magnetic Resonance*, 2011, **39**, 81-87.
246. Z. Gan, P. K. Madhu, J.-P. Amoureux, J. Trebosc and O. Lafon, *Chemical Physics Letters*, 2010, **503**, 167-170.
247. M. Leskes, S. Steuernagel, D. Schneider, P. K. Madhu and S. Vega, *Chemical Physics Letters*, 2008, **466**, 95-99.
248. J.-P. Amoureux, B. Hu and J. Trebosc, *Journal of Magnetic Resonance*, 2008, **193**, 305-307.
249. K. Suzuki, C. Martineau, G. Fink, S. Steuernagel and F. Taulelle, *Magnetic Resonance in Chemistry*, 2012, **50**, 159-168.
250. A. Pines, M. G. Gibby and J. S. Waugh, *The Journal of Chemical Physics*, 1973, **59**, 569-590.
251. D. Rovnyak, *Concepts in Magnetic Resonance Part A*, 2008, **32A**, 254-276.
252. S. R. Hartmann and E. L. Hahn, *Physical Review*, 1962, **128**, 2042-2053.
253. G. Metz, M. Ziliox and S. O. Smith, *Solid State Nuclear Magnetic Resonance*, 1996, **7**, 155-160.
254. P. P. Man, in *Encyclopedia of Analytical Chemistry*, John Wiley & Sons, Ltd, Editon edn., 2006.
255. C. Fernandez and M. Pruski, *Top. Curr. Chem.*, 2012, **306**.
256. S. E. Ashbrook and M. J. Duer, *Concepts in Magnetic Resonance Part A*, 2006, **28A**, 183-248.
257. M. J. Duer, *Solid-state NMR spectroscopy. Principles and applications. Blackwell Science, Oxford, 2002, pp. 592. ISBN 0 632 05 3518*, Blackwell Science Oxford, 2002.

258. M. E. S. K. J. D. Mackenzie, *Multinuclear solid-state NMR of Inorganic Materials*, Pergamon, 2002.
259. D. Massiot, V. Montouillout, C. Magnenet, C. Bessada, J.-P. Coutures, H. Forster, S. Steuernagel and D. Mueller, *Comptes Rendus de l'Academie des Sciences - Series IIC - Chemistry*, 1998, **1**, 157-162.
260. B. F. Chmelka, K. T. Mueller, A. Pines, J. Stebbins, Y. Wu and J. W. Zwanziger, *Nature*, 1989, **339**, 42-43.
261. A. P. M. Kentgens, *Geoderma*, 1997, **80**, 271-306.
262. F. A. Perras, I. Korobkov and D. L. Bryce, *Physical Chemistry Chemical Physics*, 2012, **14**, 4677-4681.
263. F. A. Perras and D. L. Bryce, *Journal of Magnetic Resonance*, 2011, **211**, 234-239.
264. K. T. Mueller, B. Q. Sun, G. C. Chingas, J. W. Zwanziger, T. Terao and A. Pines, *Journal of Magnetic Resonance*, 1990, **86**, 470-487.
265. P. J. Grandinetti, J. H. Baltisberger, I. Farnan, J. F. Stebbins, U. Werner and A. Pines, *Journal of Physical Chemistry*, 1995, **99**, 12341-12348.
266. A. Medek, J. S. Harwood and L. Frydman, *J. Am. Chem. Soc.*, 1995, **117**, 12779-12787.
267. R. Hajjar, Y. Millot and P. P. Man, *Progress in Nuclear Magnetic Resonance Spectroscopy*, 2010, **57**, 306-342.
268. J. Kanellopoulos, D. Freude and A. Kentgens, *Solid State Nuclear Magnetic Resonance*, 2007, **32**, 99-108.
269. S. Wimperis and G. A. Webb, Springer Netherlands, Editon edn., 2006, pp. 1507-1514.
270. A. Goldbourt and P. K. Madhu, *Monatshefte für Chemie / Chemical Monthly*, 2002, **133**, 1497-1534.
271. G. Engelhardt, A. P. M. Kentgens, H. Koller and A. Samoson, *Solid State Nuclear Magnetic Resonance*, 1999, **15**, 171-180.
272. M. R. Truter, *Journal of the Chemical Society (Resumed)*, 1955, 3064-3072.
273. D. Massiot, F. Fayon, M. Capron, I. King, S. Le Calvé, B. Alonso, J.-O. Durand, B. Bujoli, Z. Gan and G. Hoatson, *Magnetic Resonance in Chemistry*, 2002, **40**, 70-76.
274. S. P. Brown, Oxfrod 1997.
275. Z. Gan, *J. Am. Chem. Soc.*, 2000, **122**, 3242-3243.
276. C. Huguenard, F. Taulelle, B. Knott and Z. H. Gan, *Journal of Magnetic Resonance*, 2002, **156**, 131-137.
277. S. E. Ashbrook and S. Wimperis, *Progress in Nuclear Magnetic Resonance Spectroscopy*, 2004, **45**, 53-108.
278. S. Ganapathy, L. Delevoye, J. P. Arnoureux and P. K. Madhu, *Magnetic Resonance in Chemistry*, 2008, **46**, 948-954.
279. M. J. Thrippleton, T. J. Ball and S. Wimperis, *Journal of Chemical Physics*, 2008, **128**.
280. K. A.P.M, *Geoderma*, 1997, **80**, 271-306.
281. N. El-Kabany, *Physica B: Condensed Matter*, 2011, **407**, 817-821.
282. K. Kamiya, T. Dohkai, M. Wada, T. Hashimoto, J. Matsuoka and H. Nasu, *Journal of Non-Crystalline Solids*, 1998, **240**, 202-211.
283. J. S. Falcone, Jr., J. L. Bass, P. H. Krumrine, K. Brensinger and E. R. Schenk, *Journal of Physical Chemistry A*, 2010, **114**, 2438-2446.
284. I. Halasz, M. Agarwal, R. Li and N. Miller, *Catalysis Today*, 2007, **126**, 196-202.
285. G. Spiekermann, M. Steele-MacInnis, C. Schmidt and S. Jahn, *Journal of Chemical Physics*, 2012, **136**.
286. I. Halasz, M. Agarwal, R. Li and N. Miller, *Microporous and Mesoporous Materials*, 2007, **135**, 74-81.
287. S. M. Chemtob, G. R. Rossman and J. F. Stebbins, *American Mineralogist*, 2012, **97**, 203-211.

288. D. A. McKeown, A. C. Buechele, C. Viragh and I. L. Pegg, *Journal of Nuclear Materials*, 2010, **399**, 13-25.
289. H. Aguiar, J. Serra, P. Gonzalez and B. Leon, *Journal of Non-Crystalline Solids*, 2009, **355**, 475-480.
290. R. A. Dunlap and J. D. McGraw, *Journal of Non-Crystalline Solids*, 2007, **353**, 2201-2205.
291. T. Nishida, *Journal of Non-Crystalline Solids*, 1994, **177**, 257-268.
292. S. Y. Park and S. K. Lee, *Geochimica Et Cosmochimica Acta*, 2011, **80**, 125-142.
293. S. H. Santagneli, J. Ren, M. T. Rinke, S. J. L. Ribeiro, Y. Messaddeq and H. Eckert, *Journal of Non-Crystalline Solids*, 2011, **358**, 985-992.
294. J. W. Wiench, V. S. Y. Lin and M. Pruski, *Journal of Magnetic Resonance*, 2008, **193**, 233-242.
295. S. Borsacchi, M. Geppi, L. Ricci, G. Ruggeri and C. A. Veracini, *Langmuir*, 2007, **23**, 3953-3960.
296. C. Bischoff, H. Eckert, E. Apel, V. M. Rheinberger and W. Hoeland, *Physical Chemistry Chemical Physics*, 2011, **13**, 4540-4551.
297. S. E. Ashbrook, A. J. Berry, D. J. Frost, A. Gregorovic, C. J. Pickard, J. E. Readman and S. Wimperis, *J. Am. Chem. Soc.*, 2007, **129**, 13213-13224.
298. S. E. Ashbrook and M. E. Smith, *Chemical Society Reviews*, 2006, **35**, 718-735.
299. S. K. Lee, G. D. Cody, Y. Fei and B. O. Mysen, *Chemical Geology*, 2006, **229**, 162-172.
300. E. Robert, A. Whittington, F. Fayon, M. Pichavant and D. Massiot, *Chemical Geology*, 2001, **174**, 291-305.
301. G. G. Almond, R. K. Harris and K. R. Franklin, *Solid State Nuclear Magnetic Resonance*, 1996, **6**, 31-38.
302. A. Goldbourt, E. Vinogradov, G. Goobes and S. Vega, *Journal of Magnetic Resonance*, 2004, **169**, 342-350.
303. M. Eden, *Physical Chemistry Chemical Physics*, 2006, **8**, 1994-1999.
304. J. W. Mullen, *Crystallization Process Systems*, 4 edn., Butterworth-Heinemann, Oxford, 2001.
305. D. Schwarzenbach, *Crystallography*, John WIley & Sons, Toledo, 1996.
306. V. K. Pecharsky and P. Y. Zavalij, *Fundamentals of Powder Diffraction ans Structural Characterization of Materials*, 2 edn., Spinger, 2009.
307. R.-J. Zhou and T. Burkhart, *Journal of Thermoplastic Composite Materials*, 2009.
308. L. Wang, M. R. Kamal and A. D. Rey, *Polymer Engineering & Science*, 2001, **41**, 358-372.
309. E. Andreassen, Å. Larsen, K. Nord-Varhaug, M. Skar and H. Øysæd, *Polymer Engineering & Science*, 2002, **42**, 1082-1097.
310. Z. Ahmad, K. D. Kumar, M. Saroop, N. Preschilla, A. Biswas, J. R. Bellare and A. K. Bhowmick, *Polymer Engineering & Science*, 2009, **50**, 331-341.
311. G. Metz, X. L. Wu and S. O. Smith, *Journal of Magnetic Resonance, Series A*, 1994, **110**, 219-227.
312. I. Pelczer and B. G. Carter, Editon edn., 1997, vol. 60, pp. 71-155.
313. A. G. Redfield and S. D. Kunz, *Journal of Magnetic Resonance (1969)*, 1975, **19**, 250-254.
314. M. Pruski, D. P. Lang, C. Fernandez and J. P. Amoureux, *Solid State Nuclear Magnetic Resonance*, 1997, **7**, 327-331.
315. J.-P. Amoureux, C. Fernandez and S. Steuernagel, *Journal of Magnetic Resonance, Series A*, 1996, **123**, 116-118.
316. H. Y. Carr and E. M. Purcell, *Physical Review*, 1954, **94**, 630-638.
317. L. F. Gladden, *Chemical Engineering Science*, 1994, **49**, 3339-3408.
318. S. Harrison, X. Xie, K. J. Jakubenas and H. L. Marcus, *Journal of the American Ceramic Society*, 1999, **82**, 3221-3224.

319. I. S. Chuang and G. E. Maciel, *The Journal of Physical Chemistry B*, 1997, **101**, 3052-3064.

320. C. E. Tambelli, J. F. Schneider, N. P. Hasparyk and P. J. M. Monteiro, *Journal of Non-Crystalline Solids*, 2006, **352**, 3429-3436.

321. M. Criado, A. Fernandez-Jimenez, A. Palomo, I. Sobrados and J. Sanz, *Microporous and Mesoporous Materials*, 2008, **109**, 525-534.

322. A. V. McCormick, A. T. Bell and C. J. Radke, *Zeolites*, 1987, **7**, 183-190.

323. J. L. Bass and G. L. Turner, *Journal of Physical Chemistry B*, 1997, **101**, 10638-10644.

324. H. X. Yang, R. I. Walton, S. Antonijevic, S. Wimperis and A. C. Hannon, *Journal of Physical Chemistry B*, 2004, **108**, 8208-8217.

325. S. Antonijevic, S. E. Ashbrook, R. I. Walton and S. Wimperis, *Journal of Materials Chemistry*, 2002, **12**, 1469-1474.

326. X. Ai, F. Deng, J. Dong, L. Chen and C. Ye, *The Journal of Physical Chemistry B*, 2002, **106**, 9237-9244.

327. F. Angeli, J. M. Delaye, T. Charpentier, J. C. Petit, D. Ghaleb and P. Faucon, *Journal of Non-Crystalline Solids*, 2000, **276**, 132-144.

328. A. M. George and J. F. Stebbins, *American Mineralogist*, 1995, **80**, 878-884.

329. X. Xue and J. F. Stebbins, *Physics and Chemistry of Minerals*, 1993, **20**, 297-307.

330. F. Angelia, O. Villain, S. Schuller, S. Ispas and T. Charpentier, *Geochimica Et Cosmochimica Acta*, 2011, **75**, 2453-2469.

331. S. K. Lee and J. F. Stebbins, *The Journal of Physical Chemistry B*, 2000, **104**, 4091-4100.

332. P. S. Neuhoff, P. Zhao and J. F. Stebbins, *Microporous and Mesoporous Materials*, 2002, **55**, 239-251.

333. H. Koller, G. Engelhardt, A. P. M. Kentgens and J. Sauer, *Journal of Physical Chemistry*, 1994, **98**, 1544-1551.

334. H. Masui, D. P. Chen, T. Akai and T. Yazawa, *Zeitschrift Fur Naturforschung Section a-a Journal of Physical Sciences*, 2002, **57**, 473-478.

335. T. Ohkubo, K. Saito, K. Kanehashi and Y. Ikeda, *Science and Technology of Advanced Materials*, 2004, **5**, 693-696.

336. T. Schaller and A. Sebald, *Solid State Nuclear Magnetic Resonance*, 1995, **5**, 89-102.

337. K. V. Romanenko, O. B. Lapina, L. G. Simonova and J. Fraissard, *Physical Chemistry Chemical Physics*, 2003, **5**, 2686-2691.

338. G. D. Cody, B. O. Mysen and S. K. Lee, *Geochimica Et Cosmochimica Acta*, 2005, **69**, 2373-2384.

339. G. H. Findenegg, S. Jähnert, D. Akcakayiran and A. Schreiber, *ChemPhysChem*, 2008, **9**, 2651-2659.

340. B. Grünberg, T. Emmler, E. Gedat, I. Shenderovich, G. H. Findenegg, H.-H. Limbach and G. Buntkowsky, *Chemistry – A European Journal*, 2004, **10**, 5689-5696.

341. E. Leonova, I. Izquierdo-Barba, D. Arcos, A. Lopez-Noriega, N. Hedin, M. Vallet-Regi and M. Eden, *The Journal of Physical Chemistry C*, 2008, **112**, 5552-5562.

342. S. Sklari, H. Rahiala, V. Stathopoulos, J. Rosenholm and P. Pomonis, *Microporous and Mesoporous Materials*, 2001, **49**, 1-13.

343. H. Eckert, J. P. Yesinowski and E. M. Stolper, *Solid State Ionics*, 1989, **32-33, Part 1**, 298-313.

344. C. C. Liu and G. E. Maciel, *J. Am. Chem. Soc.*, 1996, **118**, 5103-5119.

345. L. Zemnukhova, T. Babushkina and T. Klimova, *Russian Journal of General Chemistry*, 2007, **77**, 1008-1013.

346. M. Ştefănescu, M. Stoia, O. Ştefănescu, A. Popa, M. Simon and C. Ionescu, *Journal of Thermal Analysis and Calorimetry*, 2007, **88**, 19-26.

347. M. Stefanescu, M. Stoia and O. Stefanescu, *Journal of Sol-Gel Science and Technology*, 2007, **41**, 71-78.

348. S. Paul, R. S. Thakur, M. Goswami, A. C. Sauerwein, S. Mamone, M. Concistrèb, H. Förster, M. H. Levitt and P. K. Madhu, *Journal of Magnetic Resonance*, 2009, **197**, 14-19.
349. A. Lesage, D. Sakellariou, S. Hediger, B. Elénaa, P. Charmont, S. Steuernagel and L. Emsley, *Journal of Magnetic Resonance*, 2003, **163**, 105-113.
350. T. A. Babushkina, T. P. Klimova, I. A. Yamskov and V. P. Yamskova, *Journal of Molecular Liquids*, 2005, **122**, 84-86.
351. C. Totland, S. Steinkopf, A. M. Blokhus and W. Nerdal, *Langmuir*, 2011, **27**, 4690-4699.
352. P. Mazur, I. I. Katkov, N. Katkova and J. K. Critser, *Cryobiology*, 2000, **40**, 187-209.
353. J. M. Storey and K. B. Storey, *Journal of Comparative Physiology B: Biochemical, Systemic, and Environmental Physiology*, 1983, **149**, 495-502.
354. S. N. Thompson, *Insect Biochemistry*, 1990, **20**, 223-237.
355. C. Chen, W. Z. Li, Y. C. Song and J. Yang, *Journal of Molecular Liquids*, 2009, **146**, 23-28.
356. R. Politi, L. Sapir and D. Harries, *The Journal of Physical Chemistry A*, 2009, **113**, 7548-7555.
357. J. J. Towey and L. Dougan, *The Journal of Physical Chemistry B*, 2011, **116**, 1633-1641.
358. A. V. Egorov, A. P. Lyubartsev and A. Laaksonen, *The Journal of Physical Chemistry B*, 2011, **115**, 14572-14581.
359. J. R. Zimmerman and J. A. Lasater, *The Journal of Physical Chemistry*, 1958, **62**, 1157-1163.
360. K. Overloop and L. Vangerven, *Journal of Magnetic Resonance, Series A*, 1993, **101**, 147-156.
361. M. Weerasekare, M. B. Taraban, X. Shi, E.-K. Jeong, J. Trewhella and Y. B. Yu, *Peptide Science*, 2011, **96**, 734-743.
362. A. Salvati, I. Lynch, C. Malmborg and D. Topgaard, *Journal of Colloid and Interface Science*, 2007, **308**, 542-550.
363. D. Radloff, C. Boeffel and H. W. Spiess, *Macromolecules*, 1996, **29**, 1528-1534.
364. C. Chmelik, D. Freude, H. Bux and J. Haase, *Microporous and Mesoporous Materials*, 2011, **147**, 135-141.
365. A. Pampel, M. Fernandez, D. Freude and K. Jörg, *Chemical Physics Letters*, 2005, **407**, 53-57.
366. S. Y. Jeong and O. H. Han, *Bull. Korean Chem. Soc.*, 2007, **28**, 662-666.
367. S. Kaplan, *Bull. Magn. Reson.*, 1992, **14**, 153-155.
368. C. Schick, *Analytical and Bioanalytical Chemistry*, 2009, **395**, 1589-1611.
369. B. B. Sauer, R. Beckerbauer and L. X. Wang, *Journal of Polymer Science Part B-Polymer Physics*, 1993, **31**, 1861-1872.
370. A. A. Gribb and J. F. Banfield, *American Mineralogist*, 1997, **82**, 717-728.
371. E. Burzo, in *Phyllosilicates*, Springer-Verlag Berlin Heidelberg, Editon edn., 2009, vol. 27I5b.
372. T. Berthier, V. M. Fokin and E. D. Zanotto, *Journal of Non-Crystalline Solids*, 2008, **354**, 1721-1730.
373. G. H. Beall and D. A. Duke, *Journal of Materials Science* 1969, **4**, 340-352.
374. I. Hermant and G. C. Meyer, *European Polymer Journal*, 1984, **20**, 85-89.
375. D. Jehl, J. M. Widmaier and G. C. Meyer, *European Polymer Journal*, 1983, **19**, 597-600.
376. K. Nicolay, K. P. J. Braun, R. A. de Graaf, R. M. Dijkhuizen and M. J. Kruiskamp, *Nmr in Biomedicine*, 2001, **14**, 94-111.
377. S. Matsukawa, H. Yasunaga, C. Zhao, S. Kuroki, H. Kurosu and I. Ando, *Progress in Polymer Science*, 1999, **24**, 995-1044.

378. C. S. Johnson, *Progress in Nuclear Magnetic Resonance Spectroscopy*, 1999, **34**, 203-256.
379. M. J. Stchedroff, A. M. Kenwright, G. A. Morris, M. Nilsson and R. K. Harris, *Physical Chemistry Chemical Physics*, 2004, **6**, 3221-3227.
380. R. K. Harris, K. A. Kinnear, G. A. Morris, M. J. Stchedroff, A. Samadi-Maybodi and N. Azizi, *Chemical Communications*, 2001, 2422-2423.
381. D. P. Petry, M. Haouas, S. C. C. Wong, A. Aerts, C. E. A. Kirschhock, J. A. Martens, S. J. Gaskell, M. W. Anderson and F. Taulelle, *The Journal of Physical Chemistry C*, 2009, **113**, 20827-20836.
382. C. W. Lentz, *Inorganic Chemistry*, 1964, **3**, 574-579.
383. R. K. Iler, *Colloidal components in solutions of sodium silicate*, American ChemicalSociety, 1984.
384. J.-E. A. Otterstedt, M. Ghuzel and J. P. Sterte, *Journal of Colloid and Interface Science*, 1987, **115**, 95-103.
385. G. W. Sears, *Analytical Chemistry*, 1956, **28**, 1981-1983.
386. D. Böschel, M. Janich and H. Roggendorf, *Journal of Colloid and Interface Science*, 2003, **267**, 360-368.
387. C. Brinker, *Journal of Non-Crystalline Solids*, 1988, **100**, 31-50.
388. K. J. Piotrowski and I. L. Svensson, *Journal of Non-Crystalline Solids*, 1986, **85**, 217-227.
389. T. Jesionowski, *Colloids and Surfaces A: Physicochemical and Engineering Aspects*, 2001, **190**, 153-165.
390. T. Jesionowski, *Journal of Materials Processing Technology*, 2008, **203**, 121-128.
391. O. I. Gordiyenko, T. P. Linnik and E. O. Gordiyenko, *Bioelectrochemistry*, 2004, **62**, 115-118.
392. G. Wu, D. Rovnyak and R. G. Griffin, *J. Am. Chem. Soc.*, 1996, **118**, 9326-9332.
393. A. P. M. Kentgens and R. Verhagen, *Chemical Physics Letters*, 1999, **300**, 435-443.
394. P. K. Madhu, A. Goldbourt, L. Frydman and S. Vega, *Journal of Chemical Physics*, 2000, **112**, 2377-2391.